ISSN 0587-4246

POLISH ACADEMY OF SCIENCES

INSTITUTE OF PHYSICS
AND
POLISH PHYSICAL SOCIETY

ACTA PHYSICA POLONICA A

JANUARY 1998

Proceedings of the International Conference
"Quantum Optics IV"
Jaszowiec, Poland, June 17–24, 1997

RECOGNIZED BY THE EUROPEAN
PHYSICAL SOCIETY

Vol. 93 - No. 1
WARSAW

APTLB 93 (1) 1–252 (1998)

WARUNKI PRENUMERATY W 1998 ROKU

Cena prenumeraty rocznej *Acta Physica Polonica A* w 1998 roku wynosi **114.00 zł. Prenumeratę przyjmuje Wydawca.** Instytut Fizyki Polskiej Akademii Nauk, Al. Lotników 32/46, 02-668 Warszawa, konto bankowe PBK XIII/Warszawa, nr 11101053-3593-2700-1-25.

Cena prenumeraty rocznej *Acta Physica Polonica B* w 1998 roku wynosi **90.00 zł. Prenumeratę przyjmuje Wydawca:** Instytut Fizyki Uniwersytetu Jagiellońskiego, ul. Reymonta 4, 30-059 Kraków.

Chcemy zwrócić uwagę Państwa, że począwszy od 1995 roku czasopisma *APPA* i *APPB* są wydawane i sprzedawane przez oddzielnych Wydawców (adresy jak powyżej).

Termin przyjmowania prenumeraty obu czasopism: do 5 każdego miesiąca poprzedzającego okres prenumeraty. Prenumerata ze zleceniem wysyłki za granicę jest o 100% droższa od krajowej. Bieżące i archiwalne numery można zakupić w Ośrodku Rozpowszechniania Wydawnictw Naukowych PAN, Pałac Kultury i Nauki, 00-901 Warszawa, a także bezpośrednio u Wydawców, przy czym archiwalne zeszyty *APPA* oraz *APPB* z lat 1991–1994 można zakupić u Wydawcy serii *A*, Instytut Fizyki Polskiej Akademii Nauk, Al. Lotników 32/46, 02-668 Warszawa, fax 0-22-43-09-26.

SUBSCRIPTION TERMS IN 1998

The subscription price of *Acta Physica Polonica A* for 1998 is US $ 228.

The subscription price of *Acta Physica Polonica B* for 1998 is US $ 170.

Please notice that starting from 1995 *APPA* and *APPB* are published and sold by separate Publishers (addresses as below).

A subscription order for 1998 can be made through your local dealer or, directly, through the Foreign Trade Enterprise ARS POLONA, Krakowskie Przedmieście 7, 00-068 Warszawa, Poland. Bank account: Bank Handlowy S.A., Warszawa, Poland, No. 10301016-00710000.

The subscription order can be also sent directly to the Publishers:

APPA: Institute of Physics, Polish Academy of Sciences, Al. Lotników 32/46, 02-668 Warszawa, Poland. Bank account: Powszechny Bank Kredytowy, XIII/Warszawa, Poland, No. 11101053-3593-2700-1-25.

APPB: Institute of Physics, Jagiellonian University, Reymonta 4, 30-059 Kraków, Poland, e-mail: acta@ztc386a.if.uj.edu.pl.

Issues of both *Acta Physica Polonica A* and *B* from years 1991–1994 can be purchased at the Editorial Board of *Acta Physica Polonica A*, Institute of Physics, Polish Academy of Sciences, Al. Lotników 32/46, 02-668 Warszawa, Poland.

POLISH ACADEMY OF SCIENCES
INSTITUTE OF PHYSICS
AND
POLISH PHYSICAL SOCIETY

ACTA PHYSICA POLONICA A

JANUARY 1998

Vol. 93 - No. 1

Proceedings of the International Conference
"Quantum Optics IV"
Jaszowiec, Poland, June 17–24, 1997

RECOGNIZED BY THE EUROPEAN
PHYSICAL SOCIETY

WARSAW

POLISH ACADEMY OF SCIENCES
INSTITUTE OF PHYSICS

Address of the Editor: Instytut Fizyki PAN, Al. Lotników 32/46,
02-668 Warszawa, Poland. Tlx: 812468 ifpan pl. Fax: Poland 22/8430926

Printed in Poland
APLA–DRUK s.c., Zakład Poligraficzno–Usługowy
ul. Al. Niepodległości 19, Warszawa

PROCEEDINGS OF THE INTERNATIONAL CONFERENCE

QUANTUM OPTICS IV

JASZOWIEC, POLAND, JUNE 17–24, 1997

Editors of the Proceedings

Jan Mostowski
Arkadiusz Orłowski

WARSAW

POLISH ACADEMY OF SCIENCES
INSTITUTE OF PHYSICS

The Conference *Quantum Optics IV* was held in Jaszowiec, Poland from June 17 to June 24, 1997.

The Conference was organized by the Institute of Physics of the Polish Academy of Sciences and the Center for Theoretical Physics of the Polish Academy of Sciences.

PROGRAM COMMITTEE

I. Białynicki-Birula (Poland)
N. Bigelow (USA)
J.H. Eberly (USA)
M. Fedorov (Russia)
J. Mostowski (Poland)
K. Rzążewski (Poland)
L. Sirko (Poland)
H. Walther (Germany)

ORGANIZING COMMITTEE

I. Białynicki-Birula
J. Mostowski
K. Rzążewski
L. Sirko

SPONSORS

We wish to thank the following institutions for their contribution to the success of this Conference:

Committee for Scientific Research (Poland)
European Commission, Directorate General III
National Science Foundation (USA)
United States Air Force European Office of Aerospace Research and Development
Polish Physical Society
Committee of Physics of the Polish Academy of Sciences

PREFACE

This volume contains lectures presented at the Quantum Optics IV meeting which took place at Jaszowiec (Poland) from June 17 to June 24, 1997. The leading themes of the meeting were: cold atoms, strong laser field–atom interactions and quantum chaos. It turned out that the first topic got most attention. It is worth noting that our meeting took place *before* the announcement of the Nobel Prize in physics for 1997. This Nobel Prize was awarded to C. Cohen-Tannoudji, W. Philips and S. Chu for their contribution to cooling and trapping of atoms. Of particular interest were lectures on the "hot topic" of ultracold atoms forming Bose–Einstein condensate. This effect is often considered as a part of condensed matter physics but it became accessible to experiments due to progress in laser cooling of dilute atomic gases. Thus we have witnessed yet another example of a new subject encompassed by quantum optics. Some earlier examples include classical and quantum chaos. Although not directly related to quantum optics they draw from experimental possibilities provided by modern laser techniques. Our third theme: strong laser field–atom interactions is a more traditional subject of quantum optics.

Some 140 physicists from 13 countries participated in the meeting. We had 25 invited lectures, of which 18 are included in this volume. In addition there were 120 posters presented at two poster sessions. The conference offered an overview of the most important issues of quantum optics in its broad sense.

Organizers

Vol. 93 (1998) *ACTA PHYSICA POLONICA A* No. 1

Proceedings of the International Conference "Quantum Optics IV", Jaszowiec, Poland, 1997

QUANTUM IMPLICATIONS OF RAY SPLITTING

R. BLÜMEL

Fakultät für Physik, Albert-Ludwigs-Universität
Hermann-Herder-Str. 3, 79104 Freiburg, Germany

Ray splitting is a universal phenomenon that occurs in all wave systems with sharp interfaces. Quantum implications of ray splitting are: (i) the importance of non-Newtonian orbits for the density of states in the semiclassical limit, (ii) ray-splitting corrections to the average density of states and (iii) the need to include non-Newtonian orbits in trace formulas for the oscillating part of the density of states. The signatures of non-Newtonian orbits in the density of states have recently been identified experimentally (L. Sirko, P.M. Koch, R. Blümel, *Phys. Rev. Lett.* **78**, 2940 (1997)).

PACS numbers: 05.45.+b

In 1948 Feynman introduced a particularly illuminating representation of quantum mechanics [1]. According to Feynman the transition amplitude of a particle from point P to point Q in the phase space is given by a sum of complex phases computed on the basis of all possible phase-space paths connecting P with Q. In order to obtain the exact quantum transition amplitude all paths in $\mathcal{S}$ are equally important. It is, however, possible to bring out particular subclasses of $\mathcal{S}$ by a judicious choice of quantum problems. Let us focus on the class of potential problems. For such problems it is convenient to divide $\mathcal{S}$ into the two disjoint subsets of Newtonian ($\mathcal{N}$) and non-Newtonian ($\overline{\mathcal{N}}$) trajectories. The Newtonian trajectories are the solutions of the classical canonical equations. For smooth potentials and sufficiently small $\hbar$ very good approximations to the quantum transition amplitudes can be obtained on the basis of $\mathcal{N}$ alone. The contribution of the rest of the paths is near zero because of destructive interference. In the case of non-smooth potentials particular subclasses of $\overline{\mathcal{N}}$ have to be kept besides the trajectories contained in $\mathcal{N}$ for a good representation of transition amplitudes. In other words, potentials with steps and other types of irregularities may be used as "projectors" to bring out the effects of particular classes of non-Newtonian trajectories. In the case of step potentials the importance of the non-Newtonian orbits survives the $\hbar \to 0$ limit. Thus Newtonian mechanics is not the only mechanics important in the semiclassical limit of quantum mechanics. In the case of step potentials, e.g., the underlying orbit structure in the semiclassical limit is obtained from a nondeterministic, non-Newtonian mechanics [2–6].

In order to illuminate the new concept of a non-Newtonian mechanics consider the following potential:

$$V(x,w) = \begin{cases} 0, & \text{for } x \leq 0, \\ V_0 x/w, & \text{for } 0 \leq x \leq w, \\ V_0, & \text{for } x \geq w. \end{cases} \tag{1}$$

For $w \to 0$ we obtain a step potential. We are particularly interested in the scattering of waves off the potential (1) for $E > V_0$. In the asymptotic region to the left of the potential the wave function is given by

$$\psi(x) = \mathrm{e}^{\mathrm{i}kx} + r\mathrm{e}^{-\mathrm{i}kx}, \quad x \leq 0, \quad k = \sqrt{2mE/\hbar^2}. \tag{2}$$

To the right of the potential we have

$$\psi(x) = t\mathrm{e}^{\mathrm{i}kx}, \quad x \geq w, \quad \kappa = \sqrt{2m(E-V_0)/\hbar^2}. \tag{3}$$

Since (1) is a piecewise linear potential, r can be computed with the help of Airy functions. We obtain

$$r = \frac{\mathrm{i}k\kappa C_1 + kqC_2 - \kappa q C_3 - \mathrm{i}q^2 C_4}{\mathrm{i}k\kappa C_1 + kqC_2 + \kappa q C_3 + \mathrm{i}q^2 C_4}, \tag{4}$$

where

$$q = \left(\frac{2mV_0}{\hbar^2 w}\right)^{1/3}. \tag{5}$$

The constants C are given by

$$\begin{aligned} C_1 &= \mathrm{Ai}(-\beta)\mathrm{Bi}(-\alpha) - \mathrm{Ai}(-\alpha)\mathrm{Bi}(-\beta), \\ C_2 &= \mathrm{Ai}(-\alpha)\mathrm{Bi}'(-\beta) - \mathrm{Ai}'(-\beta)\mathrm{Bi}(-\alpha), \\ C_3 &= \mathrm{Ai}(-\beta)\mathrm{Bi}'(-\alpha) - \mathrm{Ai}'(-\alpha)\mathrm{Bi}(-\beta), \\ C_4 &= \mathrm{Ai}'(-\beta)\mathrm{Bi}'(-\alpha) - \mathrm{Ai}'(-\alpha)\mathrm{Bi}'(-\beta), \end{aligned} \tag{6}$$

where

$$\alpha = qwE/V_0, \quad \beta = qw\left(\frac{E}{V_0} - 1\right). \tag{7}$$

We are mainly interested in the double limit $w \to 0$, $\hbar \to 0$. Investigation of Eq. (4) shows that the two limits do not commute. Moreover, let w and $\hbar$ approach 0, but keep their ratio $\nu = \hbar/w$ constant. Then it is easy to show that for $\hbar \to 0$ the reflection amplitude is $r \neq 0$ and depends on ν. A finite r for $\hbar \to 0$ means that in the classical limit there exist trajectories reflecting off the step although $E > V_0$. These must clearly be non-Newtonian trajectories since Newtonian trajectories transmit with probability 1 for $E > V_0$. The probability for a particle to go left is $p = |r|^2$, the probability to go right is $1 - p$. The decision about whether to reflect (go left) or to transmit (go right) is left to chance, governed by p. Thus, the non-Newtonian dynamics for a step potential is non-deterministic. If we represent the incoming path of the particle by a ray, there are two possibilities for this ray to leave the step: the particle may reflect (with probability p) or transmit (with

probability $1-p$). Thus, one incident ray creates two (or sometimes more) outgoing rays. We call this situation "ray splitting".

Ray splitting is a universal phenomenon that occurs in all wave systems with sharp interfaces in the limit of small wavelength. Examples are the splitting of light rays at the interface between two transparent dielectrics, the splitting of acoustic rays at the interface between two media of different density, the splitting of rays associated with water surface waves at the interface between two different depths, and finally the splitting of rays associated with de Broglie matter waves in quantum mechanics at the position of a potential step.

The wave implications of ray splitting were recently studied in the context of acoustic and quantum systems [2–7]. Major findings were the importance of non-Newtonian orbits for the oscillating part of the density of states [2–6], the necessity of correcting the Weyl formula [8] for the average density of states of ray-splitting systems [7] and the need to modify existing trace formulas [8] to include non-Newtonian periodic orbits [2]. Additional quantum implications are the existence of new classes of scars in the quantum wave functions [3].

The signatures of periodic non-Newtonian orbits were recently identified experimentally [5, 6] in the context of microwave resonance spectroscopy. We used thin dielectric- and metal-loaded cavities to generate ray-splitting of microwaves at sharp air/teflon and air/metal interfaces. The Fourier transform of the measured density of resonances shows peaks at the optical path lengths of non-Newtonian orbits. Since for thin microwave resonators the electromagnetic Helmholtz equation and the quantum Schrödinger equation are equivalent [9, 10], these experiments are of direct relevance for quantum ray-splitting systems.

Having established the importance of non-Newtonian orbits experiments should now aim at testing the ray-splitting correction of the Weyl formula. In order to do this the experiments have to be improved in such a way that ≈ 500 levels can be measured without missing a single one. Not missing a single level is a stringent experimental constraint which may be achieved with the help of numerical support. It was recently demonstrated [4] that a few hundred levels are indeed enough for a first qualitative test of the ray-splitting correction.

The theory of ray-splitting systems is also not complete yet. For example, the ray-splitting correction derived analytically in Ref. [7] applies only to rectilinear ray-splitting boundaries. What is missing is the computation of the correction for curved ray-splitting boundaries.

Another promising route for theoretical research is the identification of prebifurcation ghosts [11] in ray-splitting systems. As non-Newtonian orbits undergo much the same type of bifurcations as Newtonian orbits, we expect the existence of non-Newtonian ghosts in ray-splitting systems. Theoretical work on the identification of the signatures of non-Newtonian ghosts is currently in progress.

Fruitful discussion with Prof. Fritz Haake on the nature of ghost orbits are gratefully acknowledged. The author is grateful for financial support by the Deutsche Forschungsgemeinschaft.

References

[1] R.P. Feynman, *Rev. Mod. Phys.* **20,** 367 (1948).

[2] L. Couchman, E. Ott, T.M. Antonsen, Jr., *Phys. Rev. A* **46,** 6193 (1992).

[3] R. Blümel, T.M. Antonsen, B. Georgeot, E. Ott, R.E. Prange, *Phys. Rev. Lett.* **76,** 2476 (1996); *Phys. Rev. E* **53,** 3284 (1996).

[4] A. Kohler, G.H.M. Killesreiter, R. Blümel, *Phys. Rev. E*, in press.

[5] L. Sirko, P.M. Koch, R. Blümel, *Phys. Rev. Lett.* **78,** 2940 (1997).

[6] Sz. Bauch, A. Błędowski, L. Sirko, P.M. Koch, R. Blümel, submitted to *Phys. Rev. E.*

[7] R.E. Prange, E. Ott, T.M. Antonsen, Jr., B. Georgeot, R. Blümel, *Phys. Rev. E* **53,** 207 (1996).

[8] M.C. Gutzwiller, *Chaos in Classical and Quantum Mechanics*, Springer, New York 1990.

[9] J.D. Jackson, *Classical Electrodynamics*, Wiley, New York 1975.

[10] H.-J. Stöckmann, J. Stein, *Phys. Rev. Lett.* **64,** 2215 (1990).

[11] M. Kuś, F. Haake, D. Delande, *Phys. Rev. Lett.* **71,** 2167 (1993).

Vol. 93 (1998) ACTA PHYSICA POLONICA A No. 1

Proceedings of the International Conference "Quantum Optics IV", Jaszowiec, Poland, 1997

QUANTUM CONTROL OF MOTIONAL STATES OF NEUTRAL ATOMS: EXPLOITING THE EXTERNAL DEGREES OF FREEDOM

N.P. Bigelow, W. Chalupczak, R. Ejnisman, H. Pu, P. Rudy and J. Shaffer

Department of Physics and Astronomy and the Laboratory for Laser Energetics
The University of Rochester
Rochester, NY 14627, USA

As research in quantum optics has advanced, so too has our ability to precisely tailor the quantum state of a system. Indeed, techniques for quantum state preparation have become sufficiently advanced that an entire subfield has appeared which has been given the name "quantum control". Parallel to these advances have been other striking developments in quantum optics, in particular, laser cooling and trapping of neutral atoms. In this paper we describe some of the recent advancements in laser cooling, particularly in our laboratories, and point out that laser cooling and trapping is also realizing an important form of quantum control. In laser cooling, instead of exercising control over the internal quantum state of an atom or molecule or a laser field, we are instead controlling a complementary set of degrees of freedom: those of the *external* coordinates of the atom.

PACS numbers: 03.75.Fi, 32.80.Pj, 42.50.Dv

1. One atom interacting with many photons: laser cooling and trapping

1.1. Manipulating the atomic velocity: laser cooling basics

The idea that atoms could be slowed and cooled by their interaction with light was first proposed in 1975 [1] and demonstrated shortly thereafter on trapped ions in 1978 [2]. It was not, however, until 1981 that a group at the Institute of Spectroscopy in Moscow demonstrated the application of laser cooling to the slowing of a neutral atomic beam [3]. Soon afterwards, a group at the National Institute of Standards and Technology (NIST) reported the cooling of an atomic beam to temperatures of less than 100 mK [4]. This accomplishment opened the door to the realization of the three-dimensional cooling of a vapor of neutral sodium atoms to a few hundred microkelvin by a group at Bell Laboratories in 1985 and

the subsequent cooling and trapping of an atomic vapor using the now ubiquitous magneto-optical trap (MOT) in 1987 by the same group [5].

Formally, we can derive expressions for the light pressure force on an atom interacting with a laser field by starting from the Lorentz force. In practice, a detailed microscopic understanding of the light pressure force which is valid under all conditions is complex and in some cases incomplete. However, by restricting the situation to moderate atomic velocities and moderate laser field intensities, a convenient decomposition of the force can be made [6].

All of the forces involved in the optical cooling and trapping of atoms hinge on the exchange of energy and momentum between the atom, the laser field, and the vacuum; an exchange which occurs through photon absorption and emission. In this paper we consider two classes of interaction. One of these concerns processes in which the atom absorbs a photon and then reemits it spontaneously some characteristic time $\tau_{\rm sp} \equiv 1/\Gamma$ later. The other class of processes are those which involve stimulated emission. In many situations we can associate each of these two types of processes with distinct force mechanisms: the spontaneous and the dipole forces.

The first realization of an optical trap was based on the force which emphasizes stimulated emission of photons: the dipole force. In a semi-classical treatment, the dipole force arises from the interaction between the quadrature component of the dipole moment induced in the atom by the laser field and the gradient of the field itself. This interaction produces a shift in the atomic energy levels via the AC Stark shift. If there is a spatial gradient in this shift, then the atom experiences a net force. In a more quantum mechanical treatment, the dipole force is understood in terms of the momentum transfer to the atom which occurs as the atom mediates the transfer of photons from one mode of the applied laser field to another. Because this transfer occurs at constant photon energy the dipole force is a conservative force. Indeed, for a two-level atom, the dipole force can be conveniently expressed in terms of a potential $U(x) = -\hbar\Delta \ln[1 + p(x)]$ where $p(x) = [I(x)/I_{\rm sat}]\Gamma^2/(4\Delta^2 + \Gamma^2)$. Here $I_{\rm sat}$ is the two-level transition saturation intensity and $\Delta = \omega_0 - \omega_{\rm laser}$ is the laser field detuning from the atomic resonance. For moderate field intensities and/or large detunings $U(x) \propto I(x)$ and hence $\boldsymbol{F} \propto \nabla I(x)$.

Cooling of an atom arises from the dissipation of kinetic energy and hence forces which can cool an atomic vapor are intrinsically nonconservative. In laser cooling, this is generally achieved by absorbing a photon of one wavelength and emitting a photon of a different wavelength, the difference in photon energy ($\Delta E = hc/\lambda_{\rm emit} - hc/\lambda_{\rm absorb}$) being provided by the change in atomic kinetic energy. The simplest such cooling processes are referred to as the dissipative or spontaneous force and with a particular laser field configuration which has been named "optical molasses".

Consider a two-level atom, initially in its ground state $|g\rangle$ with center-of-mass momentum $\boldsymbol{P}$ interacting with an infinite plane traveling wave characterized by a wave vector $\boldsymbol{k}$. When the atom absorbs a single photon from this wave the atomic momentum changes by $\hbar\boldsymbol{k}$ and the atom emerges in the excited state $|e\rangle$. Simply put, the atom receives a momentum kick along $\boldsymbol{k}$. Some characteristic time later

(τ_{sp}) the atom spontaneously decays back to the ground state $|g\rangle$, reemitting a photon with wave vector $\boldsymbol{k}'$, receiving another momentum kick: $\hbar\boldsymbol{k} + |g, \boldsymbol{P}\rangle \rightarrow |e, \boldsymbol{P} + \hbar\boldsymbol{k}\rangle \rightarrow \hbar\boldsymbol{k}' + |g, \boldsymbol{P} + \hbar(\boldsymbol{k} - \boldsymbol{k}')\rangle$. If we consider the average over n cycles then as $n \rightarrow \infty$ the state of the atom approaches $|g, \boldsymbol{P} + n\hbar\boldsymbol{k}\rangle$: a net momentum $n\hbar\boldsymbol{k}$ has been transferred to the atom over a time scale of approximately $n\tau_{sp}$ (Fig. 1). To estimate the size of the resulting force, consider the case of a sodium atom ($M_{Na} = 23$ amu) absorbing light which is nearly resonant with the $D2$ line (589 nm). The change in momentum, $\hbar\boldsymbol{k}$, in one absorption/spontaneous emission cycle ($\tau_{sp} = 16$ ns) gives an acceleration, $\boldsymbol{a} = \hbar\boldsymbol{k}\Gamma/2M_{Na}$ of the order of 10^6 m/s^2 ($10^5 g$!).

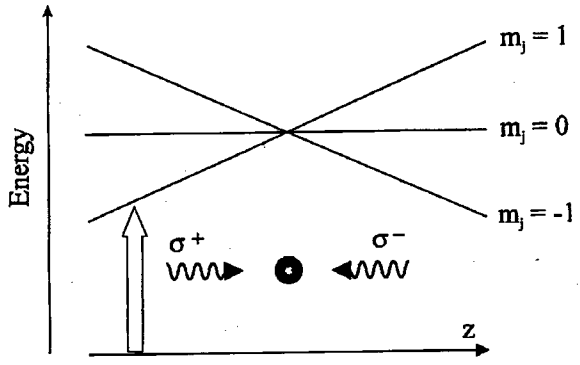

Fig. 1. The operation of a magneto-optical trap for a $J = 0 \rightarrow J = 1$ transition. As the atom propagates to either the left or the right it is Zeeman shifted into resonance with the laser beam that it is counterpropagating with respect to its displacement and it is "pushed" by the dissipative force back towards the magnetic field zero. This interaction provides the restoring or trapping force. If the laser is also detuned below the atomic resonance, the cooling effect of optical molasses (see Fig. 2) will simultaneously cool the atom.

If the light field is an optical standing wave formed from two counter-propagating infinite traveling waves, and the field frequency is tuned below (to the red of) the two-level transition frequency (i.e. $\Delta < 0$), then the spontaneous force can generate a velocity dependent force which causes a damping of the atomic velocity. The velocity damping — the cooling — arises from the fact that an atom with a finite velocity will be Doppler shifted into resonance with the traveling wave component of the standing wave which is directed opposite to the atomic motion. The atom will therefore absorb more photons per unit time from the counter propagating wave than from the copropagating wave and will experience a net force which opposes its motion. The result is a velocity dependent force which causes the atom to decelerate regardless of the direction of atomic motion. This standing wave configuration is referred to as optical molasses.

The energy flow in optical molasses can be understood semi-classically by noting that when the atom re-emits a photon spontaneously, this photon is emitted

at the atom's rest frame resonance frequency ω_0 and this photon is higher in energy than that of the absorbed photon by an amount equal to the Doppler shift $\hbar\Delta = \hbar\boldsymbol{k} \cdot \boldsymbol{v}$. To conserve energy, the kinetic energy of the atom decreases and the atom is cooled. In a more quantum mechanical picture, the cooling can be understood as the irreversible scattering of photons out of the laser field and into the empty electromagnetic field modes of the vacuum.

The steady-state temperature for a gas of atoms in equilibrium with an optical molasses is determined by the balance between the Doppler cooling and the spontaneous or diffusive heating associated with the individual random velocity recoil kicks experienced during spontaneous emission. In the limit where the atom is modeled as a simple two-level system it is predicted [6] that the vapor will equilibrate at the so-called Doppler temperature $T_{\text{Doppler}} = \hbar\Gamma/2k_{\text{B}}$ which, for sodium, is 240 μK. Clearly then optical molasses enables us to modify one important external coordinate: the atomic center-of-mass velocity.

To the surprise of many researchers, it was discovered in 1988 by the group at NIST that the atoms in optical molasses could be cooled to well below the Doppler temperature. Indeed, more recently, temperatures below 2 μK (barely a few photon recoil kicks of average momentum!) have been achieved for Cs atoms using optical molasses [6]. The microscopic explanation for this remarkable super-cooling power of optical molasses involves two facts. First, the atoms are not two-level systems; they have a complex magnetic substructure that cannot be neglected. Second, the light field of optical molasses usually involves complex spatially varying intensities and polarizations which also cannot be ignored. These two facts give rise to a new time scale: the time scale for motion of population amongst these internal states via an effect referred to as optical pumping [7]. This microscopic mechanism was described by a beautiful model introduced by the Paris group and is now referred to generally as "polarization gradient" cooling.

1.2. Manipulating the atomic position: trap basics and the MOT

Although optical molasses can be used to modify the velocity distribution of a vapor of atoms, it cannot necessarily be used to control their position and hence to confine them in space. To accomplish this task, we need to create a restoring force centered about some position in space, or, in other words, we need to create a trap. More than any other single device, the magneto-optical trap is the hallmark of laser cooling and trapping.

In the MOT, the trapping force is also produced using the scattering force. This is achieved by introducing a spatially varying Zeeman shift which acts much like the Doppler shift does, except in position space rather than velocity space [5]. Figure 1 illustrates a simple one-dimensional model of how the MOT functions for the case of a $J = 0 \rightarrow J = 1$ atomic transition. A quadrupolar field, produced by a set of magnetic field coils, creates a linear magnetic field gradient which increases from a zero located at the center of the trap. As in optical molasses, the laser light is detuned to the red of the atomic resonance but now we also require that each of the counterpropagating fields has opposite circular polarization: σ^+ traveling in the $z+$ direction and σ^- traveling in the $z-$ direction. Now, if the atom is displaced from the field zero (i.e. the trap center) the upper level ($J = 1$)

manifold will be Zeeman split into its magnetic sublevels m_J as shown in Fig. 1. Because of the careful choice of field polarizations, the sub-level which is shifted lower in energy will also be shifted into resonance with the counterpropagating laser beam and be pushed back towards trap center. The end result is a restoring force towards the magnetic field zero and hence the formation of a trap. Because the laser fields are tuned to the red of resonance $\Delta < 0$ the atoms are also cooled by the molasses and by polarization gradient effects such that the MOT both cools and traps the atoms. The temperatures in the real MOT range from a few T_{recoil} (where $T_{\text{recoil}} = \hbar^2 k^2 / 2 k_{\text{B}} M$) to a few T_{Doppler} depending on the intensities and detunings of the trapping laser beams. The record densities for the MOT are $> 10^{11}$ atoms/cm^3 and the total number of atoms held in a MOT can exceed 10^9 atoms [8].

2. Many individual atoms + many photons: optical lattices and parametric excitation of motional states

2.1. The optical lattice

When multiple laser beams overlap in space they can interfere. An atom placed in this interference pattern will experience the spatial variations of the electromagnetic field. The result is that there are forces acting upon the atoms on the scale of an optical wavelength. For a two-level atom, these forces will be exactly the dipole force described earlier. To describe the evolution of an atom moving in the interference pattern, we can think in terms of a potential surface $U(\boldsymbol{x}) \propto I(\boldsymbol{x})$ which directly reflects the one, two or three-dimensional periodicity of the optical interference pattern. So far we have stressed the way in which this potential surface contributes to cooling of atoms whose energy is large enough that they can climb the hills of $U(\boldsymbol{x})$. However, as the atoms evolve on this surface they can reach a low enough total energy that they can become localized in the periodic minima for long periods of time. When this occurs, a highly organized array of atoms is created which is referred to as an optical lattice. Optical lattices have played an important role in a variety of experiments. In one class of experiments, optical lattices have been used as a model of the familiar solid-state crystal and the correspondence between these systems has been extensively studied. In the second class of experiments, optical lattices have been used as a tool for controlling the motional state of the individual atomic de Broglie waves.

In many ways, the optical lattice is a novel model of the solid-state where the atoms play the role of a gas of electrons interacting with a periodic potential. Many exciting optical lattice experiments have been carried out which probe this analogy. Unlike a true solid, however, the lattice potential in an optical lattice is externally imposed. As a result, it is as if the periodic potential exists whether the lattice is fully occupied or not, maintaining its perfect order. For this reason optical lattices can and are used to explore another very interesting limit inaccessible in the true solid-state: the highly dilute limit where the atoms behave as isolated particles arranged randomly on the lattice grid. In this way the optical lattice still displays perfect long-range order even though most of the lattice sites may be empty! This last fact has recently been demonstrated in an elegant set of experiments in which

a probe laser beam was Bragg diffracted from an optical lattice [9] despite the fact that less than one in ten of the lattice sites was occupied by an atom.

The first experiments which showed that atoms could be localized in an 3D optical lattice were based on spectroscopy of light scattered by atoms in an optical molasses lattice [10]. In these experiments the NIST group used homodyne spectroscopy to show that a narrow peak less than 50 kHz wide was present in the spectrum even though the natural line width of the atoms was much much larger ($\approx$ 10 MHz). This peak was attributed to the motional narrowing predicted by Dicke [11] for a radiator confined within a potential well. Soon thereafter, these experiments were improved and distinct side bands were observed on this peak. The presence of these side bands proved that not only were the atoms confined in the lattice wells but that the bound states in the wells were clearly and resolvably quantized (see Fig. 2). Since that time a variety of lattice symmetries have been investigated, representing a "crystallography" of the optical lattice and well known properties such as magnetic susceptibility of the lattice have been measured optically [12].

Some of the important properties of a gas of electrons in a solid include the ideas of Bloch waves, energy band curvature and effective mass — all properties which relate to the presence of extended states. In a recent set of experiments

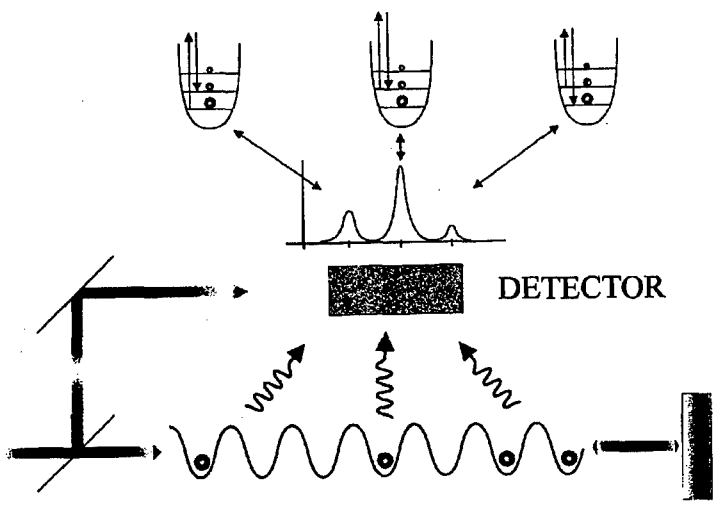

Fig. 2. In an optical lattice atoms are trapped in the interference patterns produced by overlapping multiple laser beams. The motional state of the atom localized in each lattice potential well is shown to be quantized using homodyne spectroscopy. In this experiment, a portion of the lattice light was mixed with the scattered light and the spectrum of the beat note was studied. The beat signal showed three well resolved peaks corresponding to spontaneous Raman transitions between the bound states of the lattice. The different amplitudes of the two side bands of the central peak reflects the fact that the population of the lower bound states is larger than the upper bound states. This ratio can be used to measure the temperature distribution of the localized atoms.

these effects have also been observed in optical lattices [13]. In what follows, we briefly describe the beautiful experiment carried out by Paris group in which Bloch oscillations were observed [14].

Bloch oscillations are a purely quantum mechanical effect predicted by Felix Bloch decades ago. The prediction was that an electron experiencing a constant force, and hence constant acceleration, will display oscillations in its momentum. These oscillations occur because as the electron accelerates up to the edge of the Brillouin zone its quasi-momentum will effectively fold back around the zone causing the momentum to reverse. This reversal takes place every time the particle accelerates to the zone boundary. To mimic a constant acceleration, the Paris group *accelerated the optical lattice* and simultaneously measured, as a function of time, the momentum distribution of the atoms in the lattice. Clear oscillations were observed in this momentum at exactly the Bloch period. Moreover, a detailed analysis of the data clearly revealed the signature of extended states through effects such as the curvature of the energy bands of the optical lattice. It is interesting to note that although Bloch oscillations are a fundamental idea in solid-state theory, they are essentially impossible to observe in natural crystals because of electron scattering from lattice defects. In the optical lattice, the periodicity of the lattice potential is nearly perfect, defect scattering is essentially absent, and the Bloch oscillations gracefully emerge. A series of closely related experiments were carried out by a group in Texas who have also used optical lattices as a system for studying the physics of Wannier–Stark ladders, tunneling and quantum chaos [15].

2.2. Parametric excitation of motional wave packets in an optical lattice

Groups in Japan, at NIST, in Munich and our group at Rochester [16], have also been using optical lattices to explore another interesting problem: the quantum control of center-of-mass wave packet motion in the optical lattice. In these experiments we have taken advantage of the fact that the potential wells which bind the atoms in the lattice can be manipulated rapidly and with great precision. For example, by changing the light field parameters of the lattice beams as a function of time, the atoms in the lattice can be excited into novel motional states and the evolution of these states can be carefully studied. Simply put, by dynamically controlling the spring constants and origins of the lattice wells, the atomic wave packets in the lattice can be tailored and caused to vibrate and move in a highly controlled manner.

In our experiments we achieved this effect by modulating the laser field intensity and detuning as a function of time. If we view the atom as a nearly harmonic oscillator, our technique corresponds to the familiar parametric excitation of that oscillator. In particular, consider a single atom bound in a single well. If the spring constant of the well is suddenly decreased, then a wave packet originally stationary in the center of the original well will begin to execute a breathing motion. In a quantum picture this is because when the initial wave packet state is projected onto the bound states of the final well the resulting superposition state evolves in time in a manner that produces the breathing motion. In our experiments we probe the wave packet evolution by time resolved spectroscopy of the fluorescence from the lattice atoms. This technique relies on the fact that the lattice potential

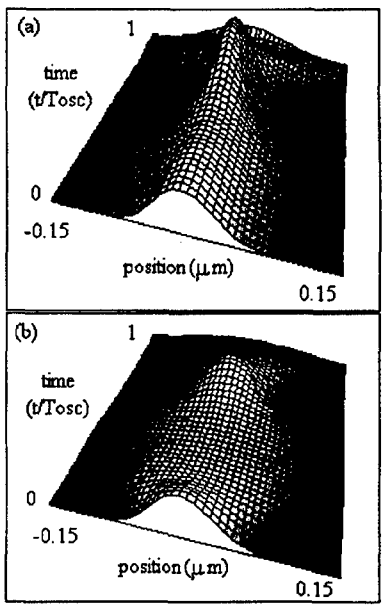

Fig. 3. The spring constant of the lattice potentials are modulated in time to induce coherent motion of the atomic wave packets bound in the lattice potentials. In these experiments the motion is detected through time resolved fluorescence measurements. This technique takes advantage of the fact that the lattice potential $U(\boldsymbol{x}) \propto I(\boldsymbol{x})$. The result is that as the atoms vibrate, they explore different laser intensities, causing their fluorescence to vary in time. From this data we can reconstruct the wave packet motion and compare the desired wave packet motion as calculated analytically. This experiment clearly demonstrates the ability to use optical lattices to execute a novel form of quantum control (from P. Rudy et al., Ref. [16]).

scales as $U(\boldsymbol{x}) \propto I(\boldsymbol{x})$. Since the fluorescence rate depends on $I(\boldsymbol{x})$, and $\boldsymbol{x} = \boldsymbol{x}(t)$, as the packet moves the fluorescence is a measure of the wave packet distribution in the well. In Fig. 3 we show the time evolution of an atomic wave packet in a driven optical lattice as reconstructed from data taken when $U(\boldsymbol{x})$ was varied linearly in time. We also show a reconstruction of the predicted and measured wave packet for this experiment. The shape and evolution of this wave packet are in good agreement with our theoretical predictions for this $U(\boldsymbol{x}, t)$ demonstrating our ability to use a pre-tailored $U(\boldsymbol{x}, t)$ to generate a desired wave packet evolution.

In our optical lattice wave packet experiments, the oscillations were observed to decay after several oscillation cycles. Typical decay data for a given set of initial conditions (laser intensity, detuning, sample temperature, etc.) is shown in Fig. 4. A fit to this data yields a decay time of ≈ 15 μs. The origin of the wave packet damping for our experiments can be understood in terms of an interplay of anharmonicity induced dephasing and irreversible damping due to spontaneous emission. To estimate the dephasing rate due to anharmonicity in the lattice potential, we consider the first order correction to the sinusoidal potential and find

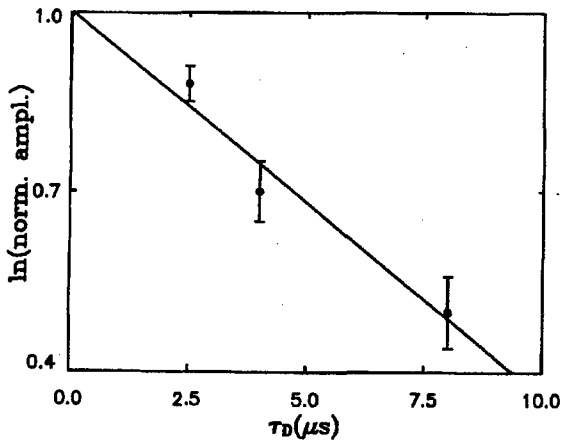

Fig. 4. Decay rates of parametrically excited optical lattice wave packets. The best-fit slope gives a decay constant of 15 μs.

$T_{\rm an} \propto 1/(j^2+j+1/2)$, where j is the mean level index for the levels used to form the wave packet. In our experiments $j \approx 1$ and we find $\tau_{\rm an} \approx 10$ μs, in reasonable agreement with the observed decay time. If, on the other hand, we estimate the decay time expected from spontaneous emission, treating spontaneous emission as a random walk in frequency space, we find $\tau_{\rm sp-decay} \propto \omega_{\rm osc}/\omega_{\rm recoil} R$, where $\omega_{\rm osc}$ is the harmonic frequency for wave packet oscillation in the well, $\omega_{\rm recoil}$ is the single photon recoil shift and R is the spontaneous emission rate. For our experimental conditions, $\tau_{\rm sp-decay} \approx 10$ μs also! In other words, in our experiment we cannot discriminate between these two decay processes. One very important conclusion is, given that spontaneous dephasing is present, there is little hope of observing quantum revivals [17] in our current experiment — irreversible decay will mask such quantum effects. If, however, we repeat our experiments for larger detunings (which reduces the spontaneous emission rates) such revivals may be observable.

Quantum revivals can be expected to occur in the optical lattice due to the fact that the lattice wells are not perfectly harmonic. For the optical lattice, the observation of revivals would provide dramatic proof of the quantum nature of the system. To investigate this possibility we have carried out a numerical study of wave packet evolution in the lattice [18]. In particular, we have solved Schrödinger's equation numerically and modeled the time evolution of a wave packet created at $t = 0$ from a superposition of the bound lattice states. For simplicity, we have neglected band structure effects. For deeper lattice wells, and for wave packets involving mostly the low lying states, band structure effects should be unimportant. However, we note that for shallow potentials, well-to-well tunneling may become important and band curvature may not be negligible. In Fig. 5 we show the autocorrelation function between the initial wave packet and the wave packet at a time t after a sudden change of the lattice well. Here $C(t) = \int \psi^*(x,0)\psi(x,t){\rm d}x$. Not only is there a clear revival seen, but there are well resolved fractional revivals. In the inset, we show the norm of the initial wave

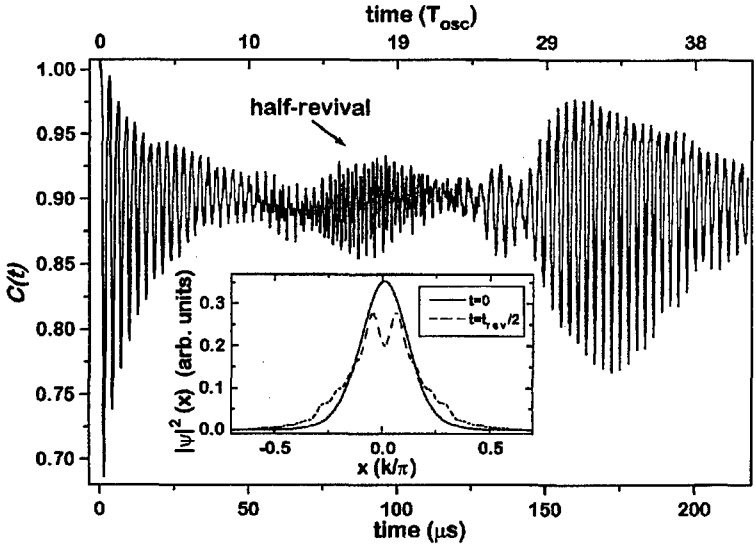

Fig. 5. Model wave packet dynamics showing a clear revival and a clear half-revival. The inset shows the wave packet shape at the half revival point (dashed line) and at the full revival. Note the characteristic double peaked structure at the half-revival signifying the presence of two wave packets which cause the oscillation frequency to be doubled at the half-revival point.

packet and the norm of the wave packet at the peak of the half revival. At the half revival time, a clear double peaked structure is seen, as expected for the spatial wave packet structure at a half revival.

3. Many pairs of atoms + many photons I: cold collisions

One very active area of research involves the study of ultra-cold collisions [19]. Experimental and theoretical studies of cold collisions in optical traps have provided a remarkably rich view of what might have appeared to be a simple reaction: the binary interaction between two identical atoms interacting with a laser field.

Many of the interesting properties of ultra-cold collisions which make them different from collisions that take place at high temperature stem from the fact that in the MOT the thermal de Broglie wavelength of the atom $\lambda_{dB} \approx 5-50$ nm. This makes λ_{dB} much larger on the scale of variation of the interatomic collision potentials and far greater than the s-wave scattering length, $a_s \approx 1-10$ nm. This hierarchy defines these vapors as "quantum gases" meaning that the atoms can exhibit highly wave-like behavior in their interactions but are clearly nondegenerate. A separate feature of ultra-cold collisions is that the scale of the interatomic potential energy is large as compared to the average kinetic energy of atoms in the trap, even at larger internuclear separations. Indeed, the collision partners in a MOT measurably experience the long-range van der Waals interactions at interatomic separations of hundreds or even thousands of angströms when dressed by a nearly resonance laser field. In recent years these features of ultra-cold collisions

have been put to excellent use and researchers have demonstrated the ability to probe long-range atom–atom interactions with exquisite resolution. Perhaps the most important point about ultra-cold collisions is that they occur on a time scale, $\tau_{\rm coll} \approx 100$ ns $\gg \tau_{\rm sp} \approx 10$ ns. This fact allows for an exciting new possibility: that both absorption *and* emission processes can modify the collision process. In an ultra-cold collision both the absorbed and emitted photons are able to change the collision, or reaction, pathway *during* the ongoing collision process. In this way the photons can play a role much more similar to that of a "reaction constituent" rather than the more familiar role as a means of state preparation or interrogation.

One particularly interesting cold collision process that has been investigated by several groups is photoassociative ionization (PAI). Photoassociative ionization is a two-step process in which two colliding atoms absorb two photons sequentially after which the colliding pair ejects an electron through an Auger-like process and produces a bound molecular ion as the final state. In essence, PAI of ultra-cold atoms represents another form of quantum control, namely, the use of laser light to activate and mediate the creation of a molecule starting from the monatomic vapor.

PAI is described schematically in Fig. 6. To date PAI has been primarily studied in ultra-cold Na collisions and in Fig. 7a we show a set of interatomic interaction potentials which can be used to describe this collision. In the MOT, the collision begins as two atoms in their ground state approach one another. At

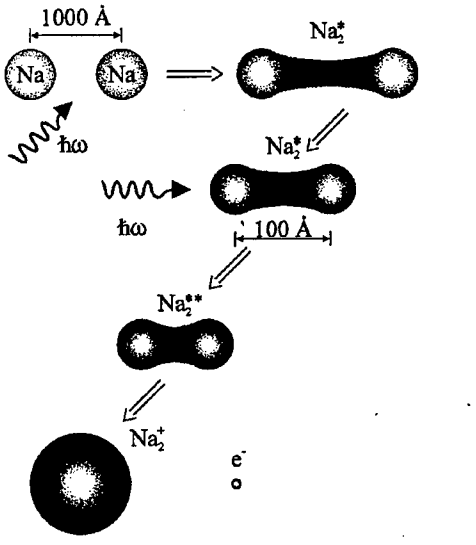

Fig. 6. Photoassociative ionization begins as two atoms approach each other and are excited into a long-range quasi-molecule. This state evolves until the atoms are at a closer range where the molecule can be further excited into a doubly excited state. This doubly excited intermediate state can then autoionize forming a molecular ion.

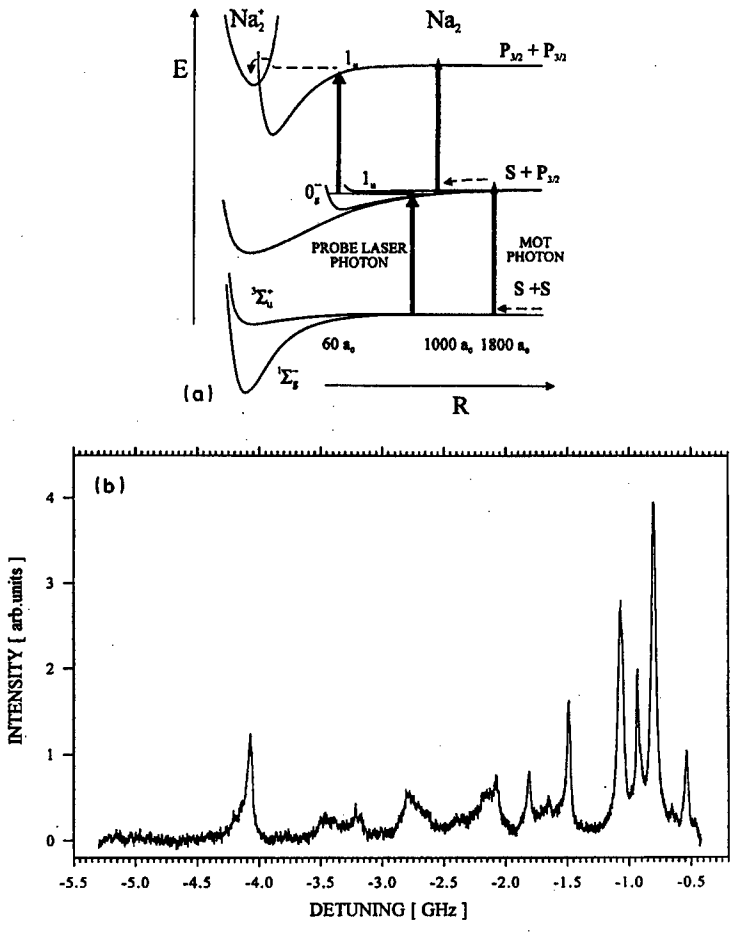

Fig. 7. (a) The intermolecular potential curves and the laser fields describing the photoassociative ionization process illustrated in Fig. 9. R is the internuclear separation. Processes involving trap photons are shown by the two rightmost upward arrows whereas those explored with the second probe laser are the leftmost two upward arrows. This second configuration was used to generate the spectrum shown in Fig. 10b. (b) A portion of the photoassociative ionization spectrum obtained from a Na trap. The zero of the spectrum is at the $F = 2$ to $F' = 3$ transition on the $D2$ line of Na. The probe laser intensity for this spectrum is 1 W/cm^2.

remarkably large internuclear spacings ($R \approx 1800a_0$) a trap photon is absorbed. The approaching pair then interacts through a very long-range resonant dipole interaction and begins to accelerate toward each other. Some time later, the pair comes back into resonance with the trap lasers and can absorb a second photon ($R \approx 1000a_0$). When this happens, the doubly excited pair can then either dissociate or autoionize leading to the final ionic molecule.

There are a wealth of exciting processes which can be investigated in just this one ultra-cold collision process alone. Let us consider only one of those here: the spectroscopy of the long-range O_g^- state. Using a second tunable laser as a probe for linear spectroscopy, both the tightly bound state structure of this novel long-range state can be probed as can the near dissociation limit levels and their coupling to the doubly excited 1_u state. Groups at NIST, Maryland, in Brazil and in Utrecht have carried out elegant spectroscopic measurements of this type as has our group at Rochester. The experimental efforts have been paralleled by extensive theoretical work and a remarkable coherence between experiment and theory has been achieved [20]. The richness of this one type of PAI spectroscopy is characterized in the spectrum shown in Fig. 7b, taken in our laboratory. This spectrum displays several striking features. For example, the narrowest peak widths are 200 μK wide and the spectrum begins 24 mK below the dissociation limit. Furthermore, the structures in this spectrum show clearly that the PAI process involves photoassociation of the atoms into well resolved intermediate molecular states which are very long-range (internuclear spacings of hundreds of Bohr!).

4. Many pairs of atoms + many photons II: heteronuclear cold collisions

PAI is only one of many sides of the cold collision problem. Most recently, a group at the University of São Paulo in Brazil and our group at Rochester have opened the door to a new class of ultra-cold collision experiments: we have realized novel *multiple species* optical traps (see Fig. 8) [21].

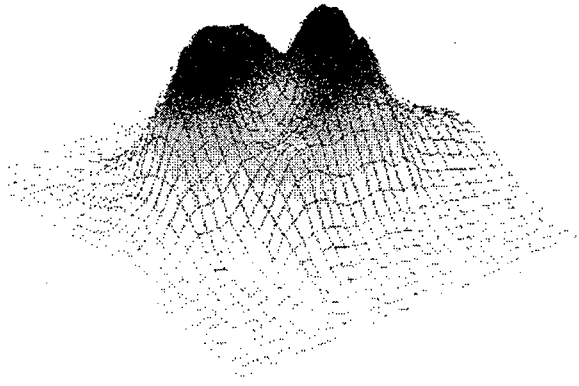

Fig. 8. An image of the trapped atom cloud in a two-species magneto-optical trap. Here the two species are cesium and sodium and the cloud centers have been intentionally displaced.

In our group in Rochester, we have investigated traps composed of different combinations of three alkalis: Na, Rb and Cs. Unfortunately, little is known about the interatomic potentials for any of these bi-alkali pairs and hence little is known about collision cross-sections, scattering lengths etc. An important starting point then is to determine the degree of coupling expected between the different

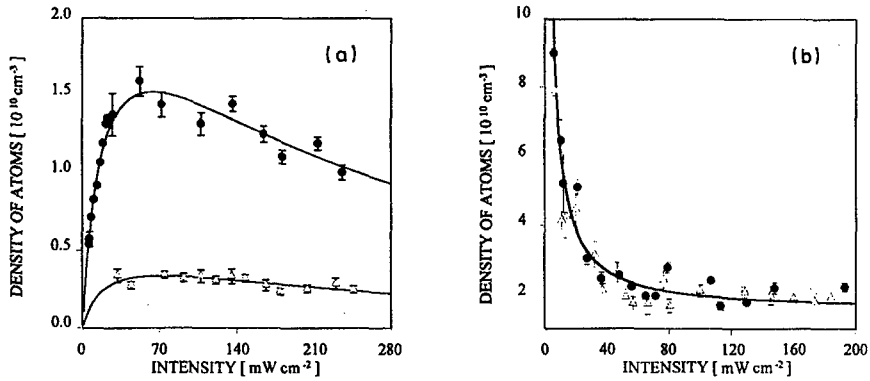

Fig. 9. Intensity dependence of trapped atom number density in two-species Na–Cs trap. The left curve is the sodium density as a function of the total intensity of the sodium trapping light while the left curve is the cesium atom density as a function of the total intensity of the cesium trapping light. The solid circles are for the single species traps (i.e. pure Na on the left and pure Cs on the right) whereas the triangles are for the two-species trap.

ultra-cold vapors in the trap. In the case of a binary mixture of sodium and cesium atoms, we have found experimentally that the coupling is strong! In Fig. 9a we show a plot of the density of sodium atoms contained within the trap as a function of sodium trap light intensity. The solid circles are for a trap containing pure sodium and the open triangles are for a trap containing a mixture of sodium and cesium atoms. In Fig. 9b we show a similar plot for the number density of trapped cesium atoms. Clearly, although the cesium vapor is almost unaffected by the presence of sodium in the trap, the sodium vapor is greatly affected by the cesium atoms. In fact, at high laser intensities, the density of sodium atoms decreases by almost an order of magnitude when cesium is introduced into the trap. We find experimentally that these effects require two ingredients: (1) that ultra-cold atoms of both species be in the trap and (2) that some of the atoms are in their excited state. We note that we have eliminated the possibility that the sodium vapor density is modified by the cesium trapping light alone.

The measurements described by this data clearly show that there is a strong coupling of the two species in this novel MOT, but they do not provide much information about what the microscopic processes are which cause the loss of sodium. One measurement which does provide more insight, as mentioned above, is photoassociative ionization. Applying the same ion detection techniques used to investigate the pure sodium trap, we have investigated the production of ions in our multi-species traps. For the case of the sodium–cesium mixtures another remarkable change was observed: despite the fact that the trapped sodium atom density is lower in the Na–Cs mixture, the flux of ions was observed to *increase*, and by almost one order of magnitude! Using a time-of-flight technique to mass analyze the ions we find that not only are we observing the production of Na_2^+ ions, but also Cs^+ ions and, most importantly, $NaCs^+$ heteronuclear ions. Simply put,

using laser cooling and trapping techniques we have demonstrated the ability to "build" heteronuclear molecules! We are currently carrying out detailed spectroscopic measurements to determine the states of the atoms and the molecules which are involved in the heteronuclear PAI process. One particularly exciting possibility is that we can use PAI spectroscopy to determine the two-species s-wave scattering length, much as has been done for sodium–sodium and for rubidium–rubidium collisions. These interaction parameters are particularly important for research on the creation and control of another interesting quantum state: the Bose–Einstein condensate.

5. Many identical atoms: Bose–Einstein condensation

In the proceedings of the 1993 meeting "Quantum Optics III" a paper by Lewenstein et al. [22] marked the emergence of a new problem in the quantum optics community: that of the Quantum Optics of a Bose–Einstein condensation (BEC) of a dilute, cooled and trapped atomic vapor [23]. In this meeting, several excellent seminars were presented on BEC and we refer the reader to these papers for some excellent and more detailed discussion.

One of earliest successes of trapped alkali BEC has been in the excellent agreement between the experimental data and the theoretical results derived using a mean-field theory. A representation of the condensate wave function in the mean field picture can be derived from the Gross–Pitaevskii (GP) equation. Essentially, this is a Schrödinger equation for the many-particle ground state (the BEC) with an additional term in the Hamiltonian which is of the form: $U_0|\Psi|^2$. Here Ψ is the BEC wave function and U_0 is the interaction potential between the atoms in the condensate. In many situations $U_0 \propto a_s$ where a_s is the s-wave scattering length of the particles. Frequently it is simplest to solve the GP equation in the so-called Thomas–Fermi approximation which essentially means that the kinetic energy term of the Hamiltonian can be neglected. At Rochester, we have developed a new numerical technique based on a variational approach for solving the GP equation without making any approximations [24]. In most situations, the modifications to the shape of Ψ due to the inclusion of the kinetic energy are small. In fact, only in regions where there is a large curvature in Ψ (and hence a large contribution from the $\nabla^2\Psi$ term in the Hamiltonian) does the Thomas–Fermi approximation cause problems. It is not surprising that these problems can become most marked near the condensate boundaries.

6. Many not completely identical atoms: two-species Bose–Einstein condensation

With the advent of multi-species traps and the recent realization of a Bose condensate comprised of two different spin-states of a vapor of rubidium atoms [25] a new and important question has arisen: what is the nature of a *two-species Bose–Einstein condensate — the 2BEC*? In approaching this question it is important to realize that we cannot expect that each condensate will simply co-exist with the other condensate. The reason for this is that, even though the alkali BECs are very dilute ($\approx 10^{13}$ atoms/cc) the role of interparticle interactions is still crucial. For a 2BEC, then, we must consider three classes of interactions:

the two self-interactions of each species and a third "cross-species" interaction. In the mean field limit, this means that the 2BEC can be characterized by two coupled GP equations and three scattering lengths a_{11}, a_{22} and a_{12} (the cross-species scattering length) [26].

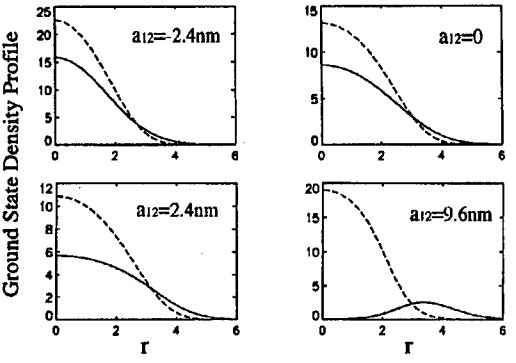

Fig. 10. The ground state density profiles of a two-species Bose–Einstein condensate (2BEC) for two different choices of cross-scattering length a_{12}. For this figure we consider a mixture of sodium (Na with $a_{11} = 3$ nm — the solid lines) and rubidium ($a_{22} = 6$ nm — the dashed lines) atoms. Here $N_1 = N_2 = 10^3$.

A rich array of new phenomena have been predicted for this system including modifications to the ground state wave function profile, the excitation spectrum and even the essential stability of the condensate itself [27]. We have been investigating the 2BEC using a modification of our variational technique [24]. In Fig. 10 we show the ground state condensate wave function for a mixture of sodium atoms and rubidium atoms contained in a spherically parabolic trap. The parameter which is varied between the different parts of this figure is the cross scattering length a_{12}. We see that for strong repulsive interactions (i.e. $a_{12} > 0$) the ground state is definitely not a mixture of two overlapping condensates, but that instead the system has phase separated into two distinct condensates. Because the ground state condensate wave function in the mean field is the state which minimizes the mean field energy we can provide a physical interpretation of the phase separation. When the system separates, the overlap between the condensates is reduced, and hence the cross-species mean field energy is decreased. Simultaneously, the outer species must be spread over a larger volume, which decreases its mean field energy. By contrast, the mean field energy of the core increases because the core atoms are now closer together (the core atoms are not "diluted" by the second species). Overall, the total system energy is determined by the interplay of these individual energies and in the phase separated state the total mean field energy is minimized. A careful analysis of the JILA two-spin state condensates has provided some evidence for the effective "condensate repulsion", however a true two-species condensate has yet to be realized. At Rochester, an experimental effort on this problem is well underway.

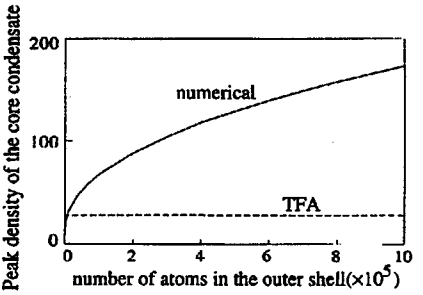

Fig. 11. The density of atoms in the core condensate as a function of the number of atoms in the outer shell condensate. Note that as the number of atoms in the shell increases, the inner condensate is compressed. The dotted line is the density of the core as calculated within the Thomas–Fermi approximation.

In Fig. 11, we show a plot of the density of the core species as a function of the number of atoms in the shell condensate. What is predicted is that as the outer condensate particle number increases, the shell will compress the core condensate. In addition to the prediction of this new phenomenon, this result highlights another point: in the 2BEC, once phase separation has occurred and boundaries have appeared, the Thomas–Fermi approximation does not give reliable results. In the figure, the dotted line is the density as calculated using the Thomas–Fermi approximation and the solid line is for the full GP equation.

7. Conclusion

Physicists from many backgrounds have become excited by the problems that laser cooling has brought into view and generations of students are emerging with Ph.D.s earned in the field. Laser coolers have refined the techniques for manipulating individual atoms, and ensembles of atom, the collisions between atoms, and in creating novel macroscopic quantum states. Overall the efforts in quantum optics to control and manipulate the external coordinates of atoms have developed into a remarkable and dynamic field and we are pleased to be part of this excitement.

The list of remarkable scientists that have contributed to our understanding is too large to list — we thank them nevertheless — and we apologize for the many omissions we have made. N.P.B. is particularly grateful to K. Rzążewski for insightful discussions and inspiration early on in our lattice wave packet work. We are grateful to the National Science Foundation, the David and Lucile Packard Foundation and the Laboratory for Laser Energetics for Financial Support. R.E. acknowledges support of the CNPq.

References

[1] D. Wineland, H. Demelt, *Bull. Am. Phys. Soc.* **20,** 637 (1975); T. Hansch, A. Schalow, *Opt. Commun.* **13,** 68 (1975).

[2] D.J. Wineland, R. Drullinger, F. Walls, *Phys. Rev. Lett.* **40,** 1639 (1978).

[3] S.V. Andreev, V.I. Balykin, V.S. Letokhov, *JETP Lett.* **34,** 442 (1978).

[4] W.D. Phillips, J.V. Prodan, in: *Coherence and Quantum Optics V*, Eds. L. Mandel, E. Wolf, Plenum, New York 1984, p. 15.

[5] E.L. Raab, M. Prentiss, A. Cable, S. Chu, D.E. Pritchard, *Phys. Rev. Lett.* **59,** 2631 (1987).

[6] C. Cohen-Tannoudji, in: *Proc. Int. School of Physics, Enrico Fermi, course CXVIII, Varenna (Italy) 1991*, Eds. E. Arimondo, W.D. Phillips, F. Strumia, North-Holland, New York 1992, p. 99.

[7] J. Dalibard, C. Cohen-Tannoudji, *J. Opt. Soc. Am. B* **6,** 2023 (1989); P. Unger, D. Weiss, E. Riis, S. Chu, *J. Opt. Soc. Am. B* **6,** 2058 (1989); J. Dalibard, C. Salomon, A. Aspect, E. Arimondo, R. Kaiser, N. Vansteenkiste, C. Cohen-Tannoudji, in: *Atomic Physics*, Vol. 11, Eds. S. Haroche, J.C. Gray, G. Grynberg, World Scientific, Singapore 1989, p. 199.

[8] C.J. Myatt, N.R. Newbury, R.W. Ghrist, S. Loutzenhiser, C.E. Wieman, *Opt. Lett.* **21,** 290 (1996).

[9] G. Brikl, M. Gatzke, I.H. Deutsch, S. Rolston, W.D. Phillips, *Phys. Rev. Lett.* **75,** 2823 (1995); M. Weidemuller, A. Hemmerich, A. Gorlitz, T. Esslinger, T.W. Hansch, *Phys. Rev. Lett.* **75,** 4583 (1995).

[10] C.I. Westbrook, R.N. Watts, C.E. Tanner, S.L. Rolston, W.D. Phillips, P.D. Lett, P.L. Gould, *Phys. Rev. Lett.* **65,** 33 (1990); N.P. Bigelow, M. Prentiss, *Phys. Rev. Lett.* **65,** 29 (1990); P.S. Jessen, C. Gerz, P.D. Lett, W.D. Phillips, S.L. Rolston, R.J.C. Spreeuw, C.I. Westbrook, *Phys. Rev. Lett.* **69,** 49 (1992).

[11] R. Dicke, *Phys. Rev.* **89,** 472 (1953).

[12] K.I. Petsas, A.B. Coates, G. Grynberg, *Phys. Rev. A* **50,** 5173 (1994).

[13] M. Raizen, C. Salomon, Q. Niu, *Phys. Today* **50,** 30 (1997).

[14] M.B. Dahan, E. Peik, J. Reichel, Y. Castin, C. Salomon, *Phys. Rev. Lett.* **76,** 4508 (1996).

[15] Q. Niu, X.-G. Zhao, G.A. Geogakis, M.G. Raizen, *Phys. Rev. Lett.* **76,** 4504 (1996); S.R. Wilkinson, C.F. Bharucha, K.W. Madison, Q. Niu, M.G. Raizen, *Phys. Rev. Lett.* **76,** 4512 (1996).

[16] M. Kozuma, N. Nakagawa, W. Jhe, M. Ohtsu, *Phys. Rev. Lett.* **76,** 2428 (1996); G. Raithel, G. Birkl, W.D. Phillips, S.L. Rolston, *Phys. Rev. Lett.* **78,** 2928 (1997); A. Gorlitz, W. Weidemuller, T.W. Hansch, A. Hemmerich, *Phys. Rev. Lett.* **78,** 2096 (1997); P. Rudy, R. Ejnisma, N.P. Bigelow, *Phys. Rev. Lett.* **78,** 4906 (1997).

[17] J.H. Eberly, N.B. Narozhny, J.J. Sanchez-Mondragon, *Phys. Rev. Lett.* **44,** 1323 (1980).

[18] R. Ejnisman, P. Rudy, H. Pu, N.P. Bigelow, *Phys. Rev. A* **56,** 4331 (1997).

[19] See for example, P. Julienne, in Ref. [6], p. 733; T. Walker, *Adv. Atom. Mol. Opt. Phys.* **34,** 125 (1994); P.S. Julienne, *J. Natl. Inst. Stand. Technol.* **101,** 487 (1996).

[20] Recent experiments include those by P.D. Lett, K. Helmerson, W.D. Phillips, L.P. Ratcliffe, S.L. Rolston, M.E. Wagshul, *Phys. Rev. Lett.* **71,** 2200 (1993); V. Bagnato, L. Marcassa, C. Tsao, Y. Wang, J. Weiner, *Phys. Rev. Lett.* **70,** 3225 (1993); J.J. Blange, J.M. Zijlstra, A. Amelink, X. Urbain, H. Rudolph, P. van der Straten, H.C. Beijerinck, H.G.M. Hiedeman, *Phys. Rev. Lett.* **78,** 3089 (1997). Many aspects of the theoretical work are summarized in R.W. Heather, P.S. Julienne, *Phys. Rev. A* **47,** 1887 (1993) and references therein.

[21] M.S. Santos, P. Nussenzweig, L.G. Marcassa, K. Helmerson, J. Flemming, S.C. Zilio, V.S. Bagnato, *Phys. Rev. A* **52,** 4340 (1995); J.P. Shaffer, N.P. Bigelow, *Opt. Photon. News* **12,** 46 (1995).

[22] M. Lewenstein, L. You, J. Cooper, *Acta Phys. Pol. A* **86,** 173 (1994).

[23] M.H. Anderson, J.R. Ensher, M.R. Mathews, C.E. Wieman, E.A. Cornell, *Science* **269,** 198 (1995); C.C. Bradley, C.A. Sackett, J.J. Tollett, R.G. Hulet, *Phys. Rev. Lett.* **75,** 1687 (1995); K.B. Davis, M.-O. Mews, M.R. Andrews, N.J. van Druten, D.S. Durfee, D.M. Kurn, W. Ketterle, *Phys. Rev. Lett.* **75,** 3969 (1995).

[24] H. Pu, N.P. Bigelow, submitted to *Phys. Rev. Lett.*

[25] C.J. Myatt, E.A. Burt, R.W. Ghrist, E.A. Cornell, C.E. Weiman, *Phys. Rev. Lett.* **78,** 586 (1997).

[26] Tin-Lun Ho, V.B. Shenoy, *Phys. Rev. Lett.* **77,** 3276 (1996); see also B.D. Esry, C.H. Green, J.P. Burke, J.L. Bohn, *Phys. Rev. Lett.* **78,** 3594 (1997) and E.V. Goldstein, P. Meystre, *Phys. Rev. A* **55,** 2935 (1997).

[27] C.K. Law, H. Pu, N.P. Bigelow, J.H. Eberly, *Phys. Rev. Lett.* **79,** 3105 (1997).

Vol. 93 (1998) *ACTA PHYSICA POLONICA A* No. 1

Proceedings of the International Conference "Quantum Optics IV", Jaszowiec, Poland, 1997

QUANTUM-CLASSICAL CORRESPONDENCE IN INTENSE LASER FIELD–ATOM INTERACTIONS

C.M. BOWDEN, S.D. PETHEL

Weapons Sciences Directorate, AMSMI-RD-WS-ST
Research, Development, and Engineering Center
U.S. Army Missile Command
Redstone Arsenal, AL 35898-5248, USA

A.T. ROSENBERGER

Department of Physics and Center for Laser and Photonics Research
Oklahoma State University, Stillwater, OK 74078-3072, USA

AND C.C. SUNG

Department of Physics, University of Alabama in Huntsville
Huntsville, AL 35899, USA

High-field ionization suppression in a classical Kepler ensemble is discussed in terms of optimization with respect to pulse turn-on rate as well as pre-pulse preparation. It is argued that high-field ionization suppression is best understood in terms of reduced probability of ionization for pulsed fields, whereas for a quasi-steady field, high-field ionization suppression implies a reduced ionization rate at higher intensities. The classical ensemble is used to calculate the high-field ionization rate of a one-dimensional atomic model using a Gaussian short-range potential and the results are compared with high-frequency Floquet theory results recently reported by other authors. Better than qualitative agreement is found and the results are compared and discussed in terms of quantum superposition and classical interference. Finally, high-field ionization suppression is discussed in relation to statistical relative stability of classical orbits of the ensemble, and classical interference for both short- and long-range potentials. Correspondence with quantum superposition is interpreted in relation to quantum-classical correspondence.

PACS numbers: 32.80.Rm, 42.50.Hz

1. Introduction

The possibility of atomic stabilization in an intense optical field has been an area of active theoretical research in recent years [1, 2]. Both quantum and classical approaches have been taken, using many different model atomic potentials. We and our collaborators have studied several classical-ensemble models for intense-field stabilization and the correspondence between their results and those of quantum treatments [3–10]. This report is a synopsis of our most recent results [7–10].

Seemingly contradictory results can be found in the literature [2], and there is not universal agreement that the phenomenon of atomic stabilization in an intense laser field even exists. Also, those who do feel that the evidence supports its existence are not always in agreement on the conditions for its manifestation. We have attempted to clarify this situation in our recent work. Part of the disagreement stems from a potential ambiguity in the meaning of "stabilization". Some authors interpret it strictly, so that it refers to an ionization probability that is less than unity or that decreases with increasing field; in this strict interpretation, it is inappropriate to describe a decreasing ionization rate as stabilization, unless the rate decreases to zero. Many other authors, however, would prefer to state that any reduction in ionization rate makes the atom more stable. To avoid this possible ambiguity, we will use the term "high-field ionization suppression" (HFIS); this term can refer to either a reduced ionization rate or a probability of ionization that is less than unity. The interpretation of HFIS as a reduced rate of ionization makes sense if the field is in a quasi-steady state (changing no faster than adiabatically); this is because the ionization rate $\Gamma(\alpha_0)$ is determined by the field strength ($\alpha_0 = A/\omega^2$, where A is the field amplitude and ω is its frequency). Only when the field has a finite duration, as in the case of a pulse ($\alpha_0(t)$), is the interpretation as a reduced ionization probability meaningful, and then the probability of ionization is given by

$$P = 1 - \exp\left\{-\int \Gamma[\alpha_0(t)]\mathrm{d}t\right\}, \tag{1}$$

where the ionization rate Γ is integrated over the pulse duration.

Most of the apparent contradictions in the literature can be resolved by taking care in making comparisons, as there are many parameters whose variation can lead to qualitatively different results. For example, in considering ionization rates, one must ask how the atom is excited to a quasi-steady state [6, 7, 11, 12]. In the case of pulsed fields, the probability of ionization depends very much on the pulse shape, particularly on how the pulse turns on (ramp-up); ionization is most likely to happen during ramp-up [7, 8]. One must also consider the range of the potential [6, 9, 10] and its dimensionality. The angular momentum of the initial state is important, as is the field frequency relative to the binding energy. One must also be careful in using a criterion to define when ionization occurs. In spite of the great diversity of results reported in the literature, quantum-classical correspondence [10] indicates that the various theoretical methods predicting HFIS [2] may actually have more in common than previously thought.

In the next section, we present a treatment of HFIS as a classical Kepler problem and emphasize how HFIS can be enhanced by proper tailoring of the field

pulse. The reduction of ionization rate in a short-range potential is presented in Sec. 3. Section 4 contains a discussion of the classical interpretation of HFIS in terms of statistical relative stability of orbits, and we conclude with a discussion of our results and quantum-classical correspondence in Sec. 5.

2. Classical Kepler ensemble

We use the Kepler model to write the classical equations of motion for atomic hydrogen in cylindrical coordinates (ρ, z) and atomic units ($e = m_e = \hbar = 1$):

$$\frac{\mathrm{d}^2\rho}{\mathrm{d}t^2} = -\frac{\partial V}{\partial \rho} + \frac{m^2}{\rho^3}, \tag{2}$$

$$\frac{\mathrm{d}^2 z}{\mathrm{d}t^2} = -\frac{\partial V}{\partial z} + \eta(t) A \sin(\omega t), \tag{3}$$

where $V(\rho, z) = -1/r = -1/(\rho^2 + z^2)^{1/2}$ is the potential function and m is the azimuthal angular momentum. The external field $\varepsilon(t) = \eta(t) A \sin(\omega t)$ is specified by the maximum amplitude A and frequency ω, and it takes the form of a trapezoidal pulse whose envelope is given by

$$\eta(t) = \begin{cases} t/T_0, & 0 \le t \le T_0, \\ 1, & T_0 \le t \le T, \\ (T + T_0 - t)/T_0, & T \le t \le T + T_0. \end{cases} \tag{4}$$

The ramp slope, R, defined by

$$R \equiv \frac{A}{T_0}, \tag{5}$$

is an important parameter. We solve Eqs. (2) and (3), using $\omega = 1$ and $m = 0.75$. The roles played by ω and m were discussed earlier [6, 7]. We fix the length of the pulse plateau, $T - T_0$, at 30 optical periods. The initial conditions determine whether or not a particle will be ionized; we take a distribution of initial conditions

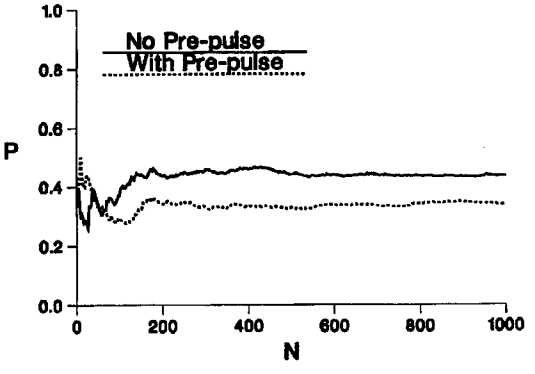

Fig. 1. Ionization probability P versus the number of particles in the ensemble N. A pre-pulse (described in the text) is seen to reduce P from 0.44 to 0.34.

consistent with $r = (z^2 + \rho^2)^{1/2} = 1$, where $\rho \leq 0.75$, and a total (ground state) energy of $E = -0.5$. A particle is considered to have ionized if it has a positive total energy at the end of the pulse.

A discussion of the process of ionization will be given in Sec. 4. Here we present some results showing how to enhance HFIS by tailoring the shape of the pulse. We use an ensemble of 200 members; Fig. 1 shows this to be sufficient. In Fig. 1, the probability of ionization (fraction of the ensemble that ionizes) is shown as a function of ensemble size for the case of $A = 8$, $R = 2$. Also shown in this figure is the enhancement of HFIS that results from preceding the main pulse with a small trapezoidal prepulse with $A = 0.5$, $T_0 = 0.25$ periods, and $T - T_0 = 1.5$ periods — the effect of the prepulse is to move the electron to a larger orbit, making it less likely for the electron to pass near the nucleus during the critical ramp-up phase of the field. We have found that most ionizations take

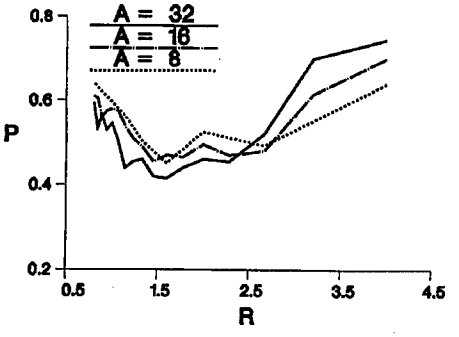

Fig. 2. Probability of ionization during ramp-up, as a function of ramp rate, for $m = 0.75$.

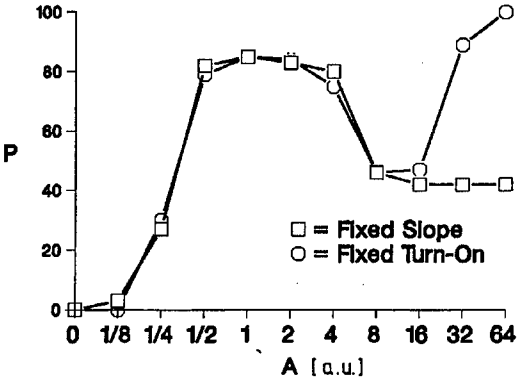

Fig. 3. Percent ionization P versus field amplitude A. Open squares represent a fixed turn-on slope $R = 2$. Open circles represent a fixed turn-on time of 4 periods. Ionization returns to 100% in the latter case because the slope R becomes very steep as A increases.

place during ramp-up, and that the ramp rate R is critical: too slow, and the electron spends too much time in the "death valley" region, of highest ionization rate, around $A = 2$ [13]; too fast, and the electron can be subject to a high field while still close to the nucleus. We have shown $R = 2$ to be the optimal value, producing the least ionization [7]. This is illustrated in Figs. 2 and 3. Shown in Fig. 2 is the probability of ionization during ramp-up vs. ramp-up rate for three values of A larger than the "death valley" value of $A = 2$, clearly demonstrating an optimum turn-on rate of $R = 2$. In Fig. 3, the percent ionization (for a pulse with no pre-pulse) is given for different values of A, both for constant $T_0 = 4$ (periods) and for constant $R = 2$. Some apparently contradictory results in the literature are probably a result of these two different choices.

3. Classical HFIS in a short-range potential

A recent paper [14] calculates high-constant-field ionization rates using the approximate solution to the Schrödinger equation given by high-frequency Floquet theory (HFFT). The (short-range) potential used is a Gaussian well with one bound state, as treated in previous quantum calculations [15, 16]. An interesting feature of the results, for sufficiently large fields, is that the ionization rate decreases non-monotonically with increasing field strength. (This behavior has also been found in a long-range potential, the one-dimensional soft Coulomb potential [17].) The same results can be obtained by a classical calculation [10], and the agreement with quantum methods is better than merely qualitative.

The results of Ref. [14] are found by an adiabatic quantum method and represent HFIS in a short-range potential. Field–atom interaction in the HFFT may be thought of as a perturbation to the steady-state Kramers–Henneberger (K–H) potential [1, 2], which is the time average, in the infinite-frequency limit, of the potential $V(u)$ given below. The ionization rate of interest is that of the K–H ground state, which has been reached from the Gaussian well's bound state by adiabatic turn-on of the field. We wish to approximate this method classically, and to do so we solve the classical equation of motion (in atomic units) for an electron in a 1D potential V and subject to a field of amplitude A and frequency ω,

$$\ddot{x} = -\frac{\partial V}{\partial x} - A\cos(\omega t), \tag{6}$$

by making the transformation

$$u = x - \frac{A}{\omega^2}\cos(\omega t), \tag{7}$$

so that the equation of motion becomes

$$\ddot{u} = -\frac{\partial V}{\partial u}. \tag{8}$$

In Eq. (8), the potential to be considered here is

$$V(u) = -0.27\exp\{-[u + \alpha_0\cos(\omega t)]^2/4\}, \tag{9}$$

where $\alpha_0 = A/\omega^2$. We take $\omega = 0.236$ a.u., as in Refs. [14–16]. We begin with a large number of particles with a random, uniform distribution of initial conditions $(u(0), \dot{u}(0))$, such that the initial energy of each is $E(0) = -0.13$, equal to that

of the bound state of V for $\alpha_0 = 0$ [14]. This ensemble is meant to approximate, in an average sense, the corresponding quantum state. The field is then ramped linearly from zero to its final value at a constant rate, chosen to be slow enough (e.g., $d\alpha_0/dt = 0.5$/optical period $= 0.019$ a.u.) that this process approximates adiabatic evolution to the perturbed ground K–H eigenstate. The members of the initial ensemble that survive the ramp-up of the field (remain unionized) then constitute an ensemble approximating the perturbed K–H ground state. Finally, while the field amplitude remains constant (hence constant α_0), the decay of the number of survivors is analyzed to find the ionization rate $\Gamma(\alpha_0)$; a particle is considered to be ionized when the absolute value of its coordinate u becomes greater than $4\alpha_0$.

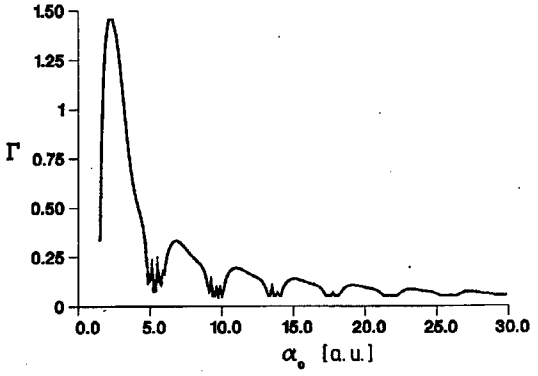

Fig. 4. Ionization rate Γ (in inverse optical periods) as a function of oscillation amplitude α_0 $(= A/\omega^2)$. A limited initial ensemble produces a very narrow distribution, around the phase-space point u, $\dot{u} = (-9, 0.39)$, among survivors of the field ramp. The field ramp-up rate is $d\alpha_0/dt = 0.5$/optical period $= 0.019$ a.u., and $\omega = 0.236$ a.u. The ionization distance is taken to be $4\alpha_0$.

Results of our classical calculation are shown in Fig. 4, where the ionization rate Γ (in inverse optical periods) is plotted as a function of α_0. Note that the decrease in Γ with increasing α_0 is not monotonic. The classical results are consistent with the quantum results [14–16], which indicate a minimum lifetime of approximately one optical period and an oscillatory decrease in rate. The precise values of Γ and shape of the Γ vs. α_0 curve depend somewhat on the choice of ramp slope and initial ensemble; these determine the ensemble that remains after the end of the ramp. We limit the ensemble that survives the ramp to a distribution localized in phase space; but, qualitatively the results do not depend upon the specific selection of members of the ensemble as long as they are sufficiently clustered in the phase space.

The oscillatory behavior of $\Gamma(\alpha_0)$ can be understood classically as resulting from the combination of the periodic field variation with the near-periodic return of the electron to the vicinity of the nucleus where large momentum transfer can take place to cause ionization [2]. The electron motion will be determined by α_0

and, because only a narrow range of initial conditions in the ensemble survives the ideal adiabatic ramp-up, certain values of α_0 will make ionization more likely than others due to the resulting coincidence between electron return and high field.

The fact that we find suppression of ionization in a short-range potential does not contradict our earlier results [6], despite our claim therein that there is no stabilization due to interference suppression (in the sense of Fedorov [18–20]) in short-range potentials. That conclusion was based on the fact that short-range potentials have only a finite number of bound states, thus limiting the number of states that can interfere effectively; the result is that the probability of ionization by a pulse goes to unity at high fields in short-range potentials. Careful distinction must be made between probability of ionization and rate of ionization; the apparent absence of stabilization (no reduced ionization probability) in short-range potentials is simply due to a quantitative difference in the integrated ionization rates (see Eq. (1)), compared to those for long-range potentials. There is no qualitative difference between long-range and short-range potentials as far as ionization suppression (reduction of ionization rates) is concerned. By comparing $\Gamma(\alpha_0)$ for a short-range and a Coulomb potential [9], we find that under identical pulsed-field conditions which result in only $\approx 63\%$ ionization for the long-range potential, there will be $> 99\%$ ionization for the short-range potential. This means that our earlier conclusion of minimal stabilization in a short-range potential is, in fact, consistent with these results showing an ionization rate that decreases with increasing field, because the decrease is significantly slower than that for a long-range potential [9, 14, 21].

4. Statistical relative stability of classical orbits

We study the stability of orbits (solutions to Eqs. (2) and (3)) within the time domain during the turn-on, $0 \leq t_0 \leq T_0$. A difficulty in analyzing stability is that the field, $\varepsilon(t_0)$, is the dominant term in Eqs. (2) and (3) for larger A; thus stability at any instant does not necessarily imply stability at later times. A point to note here is that the stability equations (10)–(14), given below, do not involve the field amplitude A explicitly. Therefore, what we find is the instantaneous stability condition of the orbits in the absence of an external field. Here, we take an approach somewhat modified from the conventional one, and define an ionization point (IP) to be that point for an orbit that ionizes within $0 \leq t_0 \leq T_0$ for which the ρ-component of the force acting on the particle is maximum. For the overwhelming majority of cases, the IP corresponds to the point of closest approach to the nucleus, after which the particle's ρ coordinate increases monotonically. An example is shown in Fig. 5.

The IP, defined this way with respect to the ρ coordinate, is an expression of the fact that for the ensemble represented here, i.e., for sufficiently large azimuthal angular momentum, the condition for ionization resides almost entirely with respect to the dynamics associated with ρ. This can be made plausible by examination of Eqs. (2) and (3). A particle of the ensemble is first accelerated along the z direction in a strong field, then accelerated back toward the nucleus after having reached the z turning point at $|z| = \alpha_0$. When the particle reaches the azimuthal plane it is experiencing an acceleration along the ρ direction at the

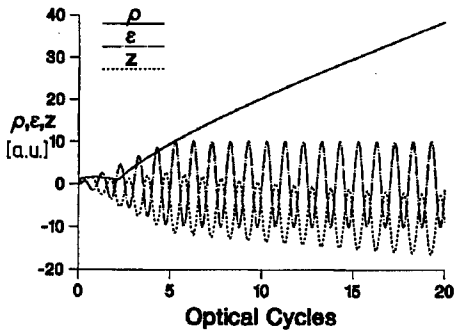

Fig. 5. Field $\epsilon(t)$ and coordinates (ρ, z) as functions of time for a member of the ensemble that does not survive ramp-up. Here $A = 10$, $m = 0.75$, and $R = 2$.

same time that the z-component of acceleration is small or zero. If the centrifugal term is larger than the Coulomb attraction, the particle will experience an acceleration along the ρ direction, away from the nucleus. This acceleration is larger, the smaller the ρ coordinate, corresponding to the closest approach to the nucleus. We find this to be overwhelmingly the case for the dynamics corresponding to our ensemble. We define a critical point (CP) for an orbit that remains bounded in $0 \leq t_0 \leq T_0$ using the identical criterion, the maximum ρ-component of the force acting on the particle. These definitions enable consistent statistical comparison of the relative stability of ionization points and critical points.

Thus we examine the behavior of $\rho = \rho(t_0) + \delta\rho$ and $z = z(t_0) + \delta z$ at an IP or CP, and analyze statistically the relative stability of the points, IP and CP, using the ansatz $\delta\rho \sim \exp(\mathrm{i}\omega_0 t)$, $\delta z \sim \exp(\mathrm{i}\omega_0 t)$. Equations (2) and (3) become

$$\frac{\mathrm{d}^2\delta\rho}{\mathrm{d}t^2} = -\left.\frac{\partial^2 V}{\partial\rho\partial z}\right|_0 \delta z - \left.\frac{\partial^2 V}{\partial\rho^2}\right|_0 \delta\rho - \left.\frac{3m^2}{\rho^4}\right|_0 \delta\rho, \tag{10}$$

$$\frac{\mathrm{d}^2\delta z}{\mathrm{d}t^2} = -\left.\frac{\partial^2 V}{\partial z^2}\right|_0 \delta z - \left.\frac{\partial^2 V}{\partial\rho\partial z}\right|_0 \delta\rho, \tag{11}$$

where $|_0$ indicates evaluation at $\rho_0 = \rho(t_0)$ and $z_0 = z(t_0)$. The stability eigenvalue, ω_0^2, is determined by

$$\omega_0^4 - B\omega_0^2 + C = 0, \tag{12}$$

where

$$B = -\frac{|V'|}{r} - |V''| + \frac{3m^2}{\rho^4}, \tag{13}$$

$$C = |V'|\frac{|V''|}{r} - \frac{3m^2}{\rho^4}\left(|V'|\frac{\rho^2}{r^3} + |V''|\frac{z^2}{r^2}\right). \tag{14}$$

An orbit is unstable at the IP if the stability eigenvalue ω_0^2 is negative or complex. In our study of many potentials with different parameters and initial conditions, all IP have values of $\omega_0^2 < 0$ (i.e., $C < 0$ when the negative sign of the solution of Eq. (12) is taken). The values of B and C are found by using the potential

$V(r) = -(1/r)\exp[-\alpha(r-1)]$. The reason for using this particular functional form is to make a fair comparison between short-range potentials ($\alpha > 0$) and the long-range Coulomb potential ($\alpha = 0$); in both cases we use the same ensemble of 200 sets of initial conditions, and at $r = 1$ the kinetic and potential energy will be the same for both types of potential.

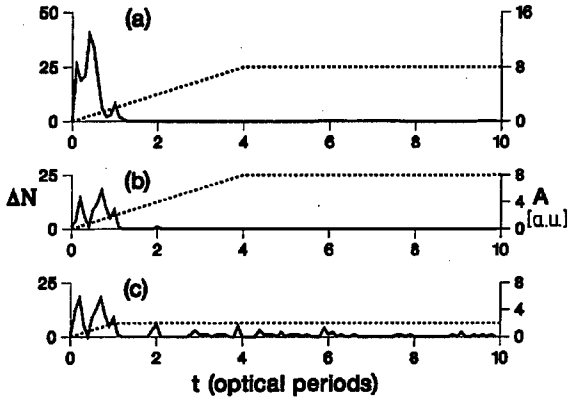

Fig. 6. Number, ΔN, of particles (out of 200) that reach ionization points per one-tenth optical period versus time (solid line); field envelope and plateau value A (dotted line). Graphs (a) and (b) are for short-range ($\alpha = 0.2$) and long-range ($\alpha = 0$) potentials, respectively, with a four-period ramp-up and $A = 8$. Graph (c) represents a one-period ramp-up with $A = 2$ for the long-range potential.

We consider the probability P of ionization by a pulse with $T - T_0 = 30$ optical periods and $R = 2$; we find that a small reduction of the range of the potential can destroy HFIS. For the long-range potential, P decreases with increasing A, even though the field amplitude ramps up through the "death valley" (where A has a value around 1 or 2) at the same rate for all A, because of the decreasing ionization rate in the plateau region of the pulse. For the short-range potential, P never decreases because there is essentially complete ionization on the ramp-up. This is illustrated in Fig. 6a, where the number of ensemble members reaching an IP in each 0.1-optical-period interval (proportional to the product of the ionization rate and the number remaining unionized) is plotted as a function of time for a fixed value of A. For the Coulomb potential, it can be seen from Figs. 6b and c that approximately the same amount of ionization (about 50% of the particles) occurs on the ramp-up, whether to $A = 2$ or to $A = 8$. At larger plateau values of A, once the particle survives passage through "death valley" we obs- ve that its orbit becomes so large that its motion is controlled by the external field, and it is virtually immune from the atomic force; ionization in the ensemble becomes negligible, as in Fig. 6b. On the other hand, $A = 2$ can produce complete ionization ($P = 1$) because the orbits remain closer to the nucleus, resulting in a larger $|\omega_0^2|$ (Eq. (12)); hence consistently unstable orbits arise and continued ionization occurs in the ensemble. Although the pulses are completed, and ionization

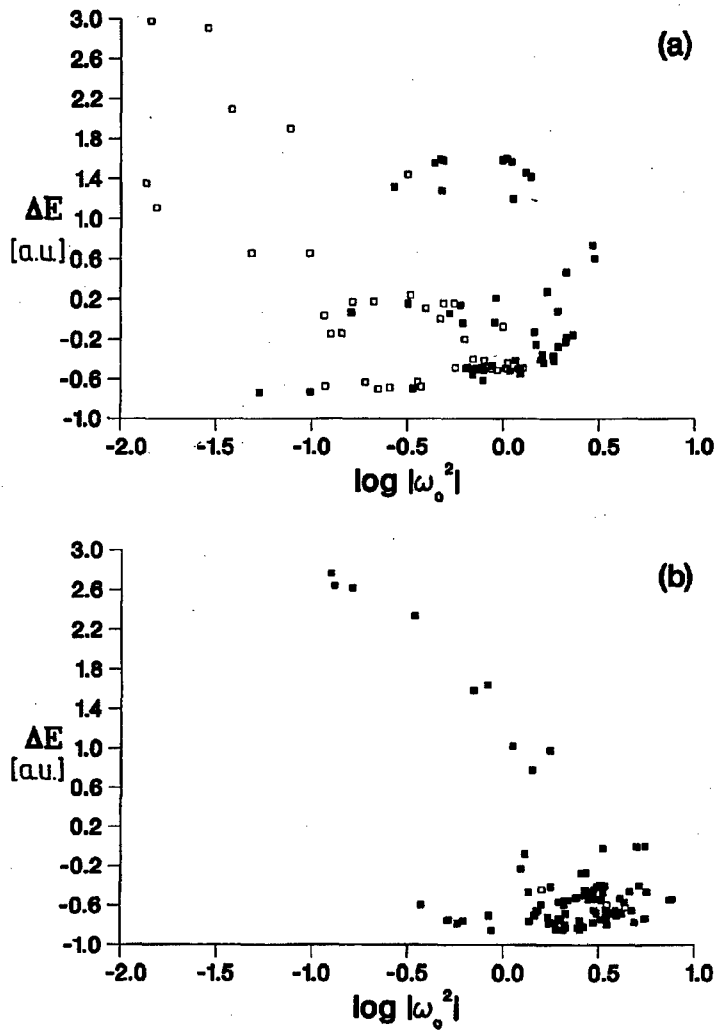

Fig. 7. Energy input ΔE, as measured at the ionization point or critical point, versus $\log_{10}(|\omega_0^2|)$ for (a) long-range ($\alpha = 0$) and (b) short-range ($\alpha = 0.3$) potentials. Solid squares (■) represent ionized particles and hollow squares (□) are survivors.

determined afterward, Fig. 6 does not show the ramp-down; as we pointed out earlier [6], ionization during pulse turn-off is negligible. We now understand this to be a result of the orbits not having time to return close to the nucleus before the field passes through the region around $A \approx 1$–2. It is evident statistically that the size of $|\omega_0^2|$ can indicate a measure of instability and likelihood of ionization, despite the obvious limitations of the method. The application of the method in the case of a short-range potential demonstrates its utility; for $A = 8$, there is complete ionization, in contrast to the Coulomb case. We can see from Fig. 6 that

the reason for this is that the ionization rate, for a given value of field amplitude on the ramp-up, is significantly larger for the short-range potential. The analysis of stability explains this, as is illustrated in Fig. 7. Each point in Figs. 7a and b reflects the state at an IP or CP. The overwhelming majority of orbits that ionize have larger $|\omega_0^2|$ at that point than orbits that do not ionize. Another minor indicator of stability is ΔE, the energy input, i.e., the difference between the particle's energy at the IP or CP and its energy at $t = 0$. A very large ΔE pumps the orbit to ionization even when the particle is located far away from the nucleus and $|\omega_0^2|$ is small. A comparison of parts (a) and (b) of Fig. 7 shows that as α increases and the range of the potential becomes shorter, both $|\omega_0^2|$ and ΔE are pushed toward larger values, enhancing the ionization.

Equations (12) and (14) explain why $|\omega_0^2|$ can serve the purpose of predicting ionization. For C to be negative at an IP, the value of the coordinate ρ_0 should be small or z_0 should be large. A small ρ_0 implies a large azimuthal angular speed $\dot{\theta}_0$ from $\dot{\theta}_0 = m/\rho_0^2$. A larger $\dot{\theta}_0$ coupled with a short-range force of diminishing influence over the orbits moving away from the nucleus, causes ionization, as expected. This same physical picture is also applicable to explain the presence of HFIS for the Coulomb potential. In this case, when the plateau amplitude of the field pulse is at $A = 2$ (near the "death valley" region of high ionization rate), those particles not ionized in their first pass at small ρ_0 can try again, whereas at $A = 8$, the orbits escape safely to a larger ρ (smaller $|\omega_0^2|$), where they stay as relatively more stable orbits. Our extensive numerical investigation, however, demonstrates that all orbits are unstable throughout most of their dynamical history. This is an important point. We have examined many pairs of orbits, originating from two very close initial conditions resulting in only slightly different $\dot{\theta}_0$ or $|\omega_0^2|$, in which one ionizes and one remains bound after reaching the IP or CP. This explains why ionized and unionized orbits cannot be clearly distinguished in a simple way based on the initial conditions, much as the initial conditions determine regular or chaotic behavior in the model of Ref. [22].

Our explanation of the importance of $|\omega_0^2|$ in producing ionization, as shown in Figs. 7a and b, is a statistical statement. There are obviously a number of exceptions because of other factors that contribute to the probability of ionization at an IP or CP: the position coordinate z_0, which determines ΔE; the time, which determines the phase of the field at the IP or CP; and the direction of the particle's velocity there. These minor factors are difficult to correlate to form a cohesive deterministic picture. We account for them through their distribution over the ensemble, giving us a statistical interpretation.

5. Conclusions

The role of the ramp-up of the external field in HFIS was analyzed. The realization of an optimum turn-on rate, R, provides an essential clue to the explanation of HFIS using the classical ensemble. The results have led to the use of a weak prepulse to enhance HFIS, and suggest the expediency to implement an optimization procedure within suitable constraints.

We point out the need to distinguish between two different interpretations of HFIS. One interpretation, applicable to the case of pulsed fields, is that HFIS

is a reduction in the probability of ionization with increasing pulse intensity. The other, for quasi-steady fields, is that HFIS is a reduction in the ionization rate with increasing field amplitude. The major features in either case are that high field amplitudes induce less ionization, and that ionization is more likely for a particle bound in a short-range potential. We show that these features may be explained in terms of a classical dynamical ensemble. We show that orbits in general are characterized by a stability eigenvalue (ω_0^2) that is a good indicator of whether ionization will occur. Our results show that there exist points (IP and CP) in configuration space at which the particle experiences an impulse; a short-range potential is more likely than a long-range potential to lose its grip on the particle at the IP or CP, meaning that ionization is more likely in the short-range case. This means that at any value of field amplitude, the ionization rate will be larger for a short-range potential than for a long-range potential; this quantitative difference in instantaneous rates, acting over the duration of a pulse, can result in a qualitative difference in the resultant ionization probabilities.

The question as to just why the classical model gives results equivalent to those of the quantum approach, even for a short-range potential, merits further investigation. In earlier work [6], we suggested that the classical-quantum equivalence for a long-range potential derived from the importance of interference and coherent superpositions of many quantum bound states out of the infinite number available [18–20]. For the short-range potential, our preliminary suspicion is that interference is again responsible, although it is less effective because the number of the bound states of the potential, and therefore the number of K–H eigenstates for finite α_0, is finite. Evidence pointing to interference can be found in Ref. [14], where the initial decline in the ground-state ionization rate begins shortly after the appearance of the first light-induced excited state. Further evidence for the role of interference between K–H eigenstates may be found in the existence (absence) of ionization suppression for a one-dimensional (three-dimensional) delta-function potential [2, 23–25]. An explanation for this behavior of delta-function potentials may be found by applying the method used in Ref. [6], for estimating the number of bound states, to the corresponding time-averaged (K–H) potentials. It is found that the number of bound states of the K–H potential derived from a one- (three-) dimensional delta function goes to infinity (zero) as α_0 increases without limit — in the three-dimensional case, there are no light-induced excited states to interfere. For the Gaussian potential treated here, agreement with the quantum results also suggests that the field-induced superposition of K–H eigenstates is not dominated by nonclassical interferences, in which the Wigner quasi-probability distribution takes on negative values [26]. Thus we suggest that these quantum-classical correspondences point to interference as the mechanism underlying HFIS even in the adiabatic limit.

References

[1] J.H. Eberly, K.C. Kulander, *Science* **262**, 1229 (1993).

[2] N.B. Delone, V.P. Krainov, *Usp. Fiz. Nauk* **165**, 1295 (1995) [*Phys. Usp.* **38**, 1247 (1995)].

[3] B. Ritchie, C.M. Bowden, C.C. Sung, Y.Q. Li, *Phys. Rev. A* **41**, 6114 (1990).

[4] C.M. Bowden, C.C. Sung, S.D. Pethel, A.B. Ritchie, *Phys. Rev. A* **46,** 592 (1992).

[5] C.M. Bowden, S.D. Pethel, C.C. Sung, J.C. Englund, *Phys. Rev. A* **46,** 597 (1992).

[6] M. Dombrowski, A.T. Rosenberger, C.C. Sung, *Phys. Lett. A* **199,** 204 (1995).

[7] C.C. Sung, A.T. Rosenberger, S.D. Pethel, C.M. Bowden, in: *Super-Intense Laser-Atom Physics IV*, Eds. H.G. Muller, M.V. Fedorov, Kluwer Academic Publishers, Dordrecht 1996, p. 73.

[8] S.D. Pethel, C.M. Bowden, C. C. Sung, *Laser Phys.* **7,** 558 (1997).

[9] A.T. Rosenberger, C.C. Sung, S.D. Pethel, C.M. Bowden, *Laser Phys.* **7,** 563 (1997).

[10] A.T. Rosenberger, C.C. Sung, S.D. Pethel, C.M. Bowden, *Phys. Rev. A*, to be published.

[11] T. Grochmalicki, M. Lewenstein, K. Rzazewski, *Phys. Rev. Lett.* **66,** 1038 (1991).

[12] K.C. Kulander, K.J. Schafer, J.L. Krause, *Phys. Rev. Lett.* **66,** 1038 (1991).

[13] F. Benvenuto, G. Casati, D.L. Shepelyansky, *Phys. Rev. A* **45,** R7670 (1992).

[14] M. Marinescu, M. Gavrila, *Phys. Rev. A* **53,** 2513 (1996).

[15] G. Yao, S.-I. Chu, *Phys. Rev. A* **45,** 6735 (1992).

[16] A. Fearnside, R.M. Potvliege, R. Shakeshaft, *Phys. Rev. A* **51,** 1471 (1995).

[17] T. Millack, *J. Phys. B* **26,** 4777 (1993).

[18] M.V. Fedorov, A.M. Movsesian, *J. Opt. Soc. Am. B* **6,** 928 (1989).

[19] M.V. Fedorov, A.M. Movsesian, *J. Opt. Soc. Am. B* **6,** 1504 (1989).

[20] M.V. Fedorov, *Comments At. Mol. Phys.* **27,** 203 (1992).

[21] M. Pont, M. Gavrila, *Phys. Rev. Lett.* **65,** 2362 (1990).

[22] F. Benvenuto, G. Casati, D.L. Shepelyansky, *Z. Phys. B* **9,** 481 (1994).

[23] S. Geltman, *Phys. Rev. A* **45,** 5293 (1992).

[24] V.P. Krainov, M.A. Preobrazhenskii, *Zh. Eksp. Teor. Fiz.* **103,** 1143 (1993) [*Sov. Phys. JETP* **76,** 559 (1993)].

[25] H.R. Reiss, *J. Opt. Soc. Am. B* **13,** 355 (1996).

[26] J.B. Watson, C.H. Keitel, P.L. Knight, K. Burnett, *Phys. Rev. A* **52,** 4023 (1995).

Proceedings of the International Conference "Quantum Optics IV", Jaszowiec, Poland, 1997

TRAPPED BOSE–EINSTEIN CONDENSATES AT FINITE TEMPERATURE: A TWO-GAS MODEL

R.J. DODD

Institute for Physical Science and Technology
University of Maryland at College Park
College Park, MD 20742, USA

K. BURNETT

Clarendon Laboratory, Department of Physics, University of Oxford
Parks Road, Oxford OX1 3PU, UK

M. EDWARDS

Department of Physics, Georgia Southern University, Statesboro, GA 30460, USA

AND CH.W. CLARK

Electron and Optical Physics Division
National Institute of Standards and Technology
Gaithersburg, MD 20899, USA

A simple picture describes the results of recent treatments of partially-condensed, dilute, trapped Bose gases at temperature $T > 0$. The condensate wave function is nearly identical to that of a $T = 0$ condensate with the same number of condensate atoms, N_0. The cloud of non-condensed atoms is described by the statistical mechanics of an ideal Bose gas in the combined potentials of the magnetic trap and the cloud–condensate interaction. We provide a physical motivation for this result, show how it emerges in the Hartree–Fock–Bogoliubov–Popov approximation, and explore some of its implications for future experiments.

PACS numbers: 03.75.Fi, 67.40.Db, 67.90.+z

1. Introduction

Most recent experiments [1–3] on dilute, magnetically-trapped, alkali-atom Bose gases have viewed phenomena which are well described by the zero-temperature ($T = 0$) mean-field theory of the Bose–Einstein condensate (BEC), in which virtually all the gas in the system resides in the condensed state. The technique of evaporative cooling [4] used in all such experiments, grows the BEC by selective

extraction of the non-condensed, "thermal" component of the gas, which is located at the outer edges of the trap [5]. The $T = 0$ mean-field theory has been found to give a good account of many BEC properties observed in these systems [6, 7]. New experiments [8, 9] have started to probe BECs at $T > 0$, and so the testing of alternative finite-temperature BEC theories has begun.

This paper draws attention to common features emerging from several independent finite-temperature theories, which suggest that a relatively simple picture, which we call the "two-gas model", describes many of the properties of a dilute Bose gas with repulsive atomic pair interactions (scattering length $a > 0$). The two gases concerned are the condensate gas, the intrinsic properties of which are essentially *independent* of temperature; and the thermal, non-condensed gas, which behaves much like an ideal Bose gas at temperature T in an effective potential created by the condensate. This model emerges naturally as a limiting case of the Hartree–Fock–Bogoliubov–Popov (HFB–Popov) [10–12] and Hartree–Fock (HF) [13] approximations, but its features seem also to be manifested in recent quantum Monte Carlo [14] and semiclassical [15] calculations. The two-gas picture offers some straightforward implications for interpretation of experiments and for further development of first-principles theories.

Our evidence for the validity of this picture first emerged from large-scale numerical calculations, but its origin can be traced back qualitatively within the structure of finite-temperature field theory. In Sec. 2, we show how such a theory can plausibly lead to a two-gas scenario. Section 3 explores some of the implications of the model.

2. Two-gas model as a limit of the HFB–Popov approximation

The HFB–Popov equations have been derived elsewhere [10] and we merely state the basic equations here. In the Heisenberg equation of motion, the Bose field operator, $\widehat{\psi}(r)$ is decomposed into a c-number wave function $\psi_0(r)$ that describes a condensate of N_0 atoms, and an operator $\widetilde{\psi}(r)$ describing the non-condensate atoms: $\widehat{\psi}(r) = \sqrt{N_0}\psi_0(r) + \widetilde{\psi}(r)$. In the HFB–Popov approximation, the wave function for a condensate of trapped atoms satisfies a generalized Gross–Pitaevskii (GP) equation

$$\left\{\widehat{H}_0 + U_0\left[N_0|\psi_0(r)|^2 + 2\widetilde{n}(r)\right]\right\}\psi_0(r) = \mu\psi_0(r), \tag{1}$$

where $\widehat{H}_0 = \frac{-\hbar^2}{2M}\nabla^2 + V_{\rm trap}(r)$ is the Hamiltonian for a single atom of mass M and position coordinate r; the trapping potential (for cylindrically symmetric systems of current interest) is given by $V_{\rm trap}(r) = M(\omega_\rho^2\rho^2 + \omega_z^2 z^2)/2$, with ω_ρ and ω_z the radial and axial angular frequencies of the trap; $U_0 = 4\pi\hbar^2 a/M$ expresses the binary interaction between atoms; the chemical potential μ, interpreted as the work required to add one more atom to the *condensate*, is treated as an eigenvalue; and $\psi_0(r)$ is normalized to unity.

The function $\widetilde{n}(r)$ is the density of the non-condensed component of the gas,

$$\widetilde{n}(r) = \sum_j \left\{\left[|u_j(r)|^2 + |v_j(r)|^2\right]N_j + |v_j(r)|^2\right\}, \tag{2}$$

where

$$N_j = [\exp(\beta E_j) - 1]^{-1} \tag{3}$$

is the Bose–Einstein factor, $\beta^{-1} = k_B T$ and k_B is the Boltzmann constant. The quasi-particle excitation energies E_j and amplitudes $u_j(r), v_j(r)$ are obtained by solution of the coupled HFB–Popov equations

$$\widehat{\mathcal{L}} u_j(r) + N_0 U_0 |\psi_0(r)|^2 v_j(r) = E_j u_j(r), \tag{4}$$

$$\widehat{\mathcal{L}} v_j(r) + N_0 U_0 |\psi_0(r)|^2 u_j(r) = -E_j v_j(r), \tag{5}$$

where $\widehat{\mathcal{L}} \equiv \widehat{H}_0 + 2U_0 n(r) - \mu$, and $n(r) = N_0 |\psi_0(r)|^2 + \widetilde{n}(r)$ is the total trapped-atom density.

In simple physical terms, Eqs. (1)–(5) describe a condensate subject to interaction with itself and a thermal cloud, with the cloud being generated by thermal excitations of condensate quasi-particles. (There is also a non-thermal contribution to this cloud, the so-called "quantum depletion" term represented by the rightmost term of Eq. (2), but it is much smaller than the thermal component except near $T = 0$.) To solve these equations for a given atomic species and trap configuration, we fix the values of T and N_0, and then determine all other quantities self-consistently, eventually obtaining the total number of trapped atoms, N, via

$$N = \int \mathrm{d}r\, n(r) = N_0 + \sum_j N_j. \tag{6}$$

By carrying out a sequence of such (laborious) calculations, we can map out the $\{N, N_0, T\}$ phase diagram of the interacting Bose gas. We present elsewhere [12] a detailed comparison of the results of this approach with experimental data for the ^{87}Rb condensate at JILA [9]; for the temperature-dependent quasiparticle excitation energies, HFB–Popov approximation agrees with experiment to within 5% for temperatures from zero up to 65% of the temperature T_0 of the phase transition for the corresponding ideal gas (corresponding to thermal fractions from less than 1% to about 50%). Although at present there are considerable discrepancies as $T \to T_0$, it seems that HFB–Popov approximation is a useful working theory over a significant temperature range.

Several calculations [11, 12] have shown that, for current experiments, the quantum depletion of a small condensate is negligible, i.e., $\int \mathrm{d}r\, \widetilde{n}(r)|_{T=0} = \sum_j \int \mathrm{d}r |v_j(r)|^2 \ll N_0$. This justifies use of the approximation

$$v_j(r) \equiv 0, \tag{7}$$

which is equivalent to the Hartree–Fock approximation used by other authors [13, 16]. If we apply this approximation to Eq. (4) (and neglect the contribution of $\widetilde{n}(r)$ to $n(r)$), we obtain an ordinary Schrödinger equation for $u_j(r)$,

$$\left[-\frac{\hbar^2}{2M} \nabla^2 + V_{\mathrm{eff}}(r) \right] u_j(r) = E_j u_j(r), \tag{8}$$

where the effective potential, given by

$$V_{\mathrm{eff}}(r) = V_{\mathrm{trap}}(r) + 2N_0 U_0 |\psi_0(r)|^2, \tag{9}$$

is that of the trap modified by the repulsive pair interaction between the thermally-excited atoms and the condensate density.

If we consider the case of a relatively small thermal fraction, then we expect to find the condensate localized near the center of the trap, so that Eq. (9) presents the thermal cloud with a trap and repulsive core. Thus, at least the low-energy quasi-particle amplitudes $u_j(r)$ will be expelled from the core, i.e., they will have little overlap with the condensate wave function. This then gives consistency of Eq. (5) with our initial approximation, Eq. (7). It also justifies the approximation that completes our portrayal of a two-gas system: because of the expulsion of quasi-particle amplitudes from the condensate, we assume that $\tilde{n}(r)$ can be neglected in Eq. (1), so that the condensate wave function is determined by solving

$$\left[-\frac{\hbar^2}{2M}\nabla^2 + V_{\text{trap}}(r) + N_0 U_0 |\psi_0(r)|^2\right] \psi_0(r) = \mu \psi_0(r), \tag{10}$$

which is just the usual GP equation for a condensate of N_0 atoms at $T = 0$.

Thus, these arguments have led us to a simple picture in which the finite--temperature Bose system appears to be composed of two distinct gases. One of these gases, the BEC, is always effectively at zero temperature, and is described by an equation which depends only on its own atomic population, N_0, and the trap parameters. The other gas, the thermal cloud, behaves as a normal Bose gas at finite temperature, sensing the presence of the condensate through an elastic interaction; it does not undergo Bose–Einstein condensation itself, but serves as an atomic reservoir for the BEC. This resembles the phenomenon of BEC of an ideal gas in an external potential, except that we account for interactions in the identification of the ground state, and in the modification by the condensate of the external potential exposed to the thermal cloud.

3. Implications of the two-gas model

The two-gas model provides us with a straightforward way of computing the phase diagram of the dilute Bose gas for $T < T_0$. If there are N_0 atoms in the BEC, we solve Eq. (10) to obtain what we will call an equivalent zero-temperature condensate (EZC), i.e. the corresponding $T = 0$ condensate that contains N_0 atoms. The EZC solution provides us an orbital $\psi_0(r; N_0)$ and chemical potential $\mu(N_0)$; with these in hand, we can construct $V_{\text{eff}}(r)$ and find the spectrum of Eq. (8). This procedure, which is independent of T, gives us the information we need to compute the equilibrium value of N for given values of N_0 and T: we evaluate Eq. (6) from Eq. (3).

In short, the EZC provides a "reference condensate" which, for a given set of trap parameters, describes all systems with the *same number of condensate atoms* N_0. As we have shown elsewhere [12], this model provides good agreement with the results of full HFB–Popov calculations of condensate and thermal densities and the critical temperature T_0; the emergence of an EZC can also be seen in the analysis by Krauth [14] of the results of his quantum Monte Carlo calculations, and in the recent quasi-classical calculations of Minguzzi et al. [15]. Comparison of the EZC condensate densities with those of HFB–Popov calculations is made in Fig. 1; this shows that even in cases where the condensate fraction $f = N_0/N$ is as small as 0.1, the condensate is relatively unperturbed by the presence of the thermal cloud.

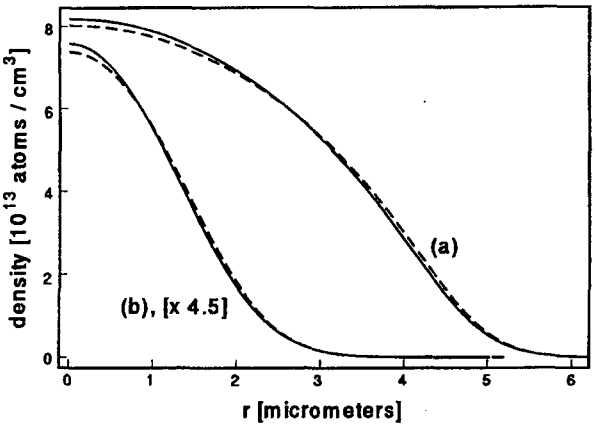

Fig. 1. Condensate densities in the $z = 0$ plane for systems of ^{87}Rb atoms in the JILA TOP trap [1] with radial frequency $\nu_\rho = 74$ Hz. The solid line shows the condensate density as computed in the HFB–Popov approximation, and the dashed line is the density of the corresponding EZC. Case (a): A system of $N = 13150$ atoms at $T = 70$ nK, corresponding to $f = 0.54$ in the HFB–Popov approximation, i.e. $N_0 = 7106$. (b) A system of $N = 2000$ atoms at $T = 51$ nK, corresponding to $f = 0.1$. The EZC densities are seen to be very close to those of the HFB–Popov approximation.

Another straightforward implication of the two-gas model concerns the density profile of the thermal cloud. If we entertain the simple hypothesis that the cloud would be described by classical statistical mechanics of an ideal gas, then its density $\widetilde{n}(r)$ would be proportional to $\exp[-\beta V_{\rm eff}(r)]$. Since $V_{\rm eff}(r)$ is repulsive at small $|r|$ and confining at large $|r|$, $\widetilde{n}(r)$ will attain its maximum away from the center of the condensate. If we consider the Thomas–Fermi limit [17] appropriate to large condensates, then for the case of a spherical condensate [$V_{\rm trap}(r) = M\omega^2 r^2/2$] we find that

$$V_{\rm eff}(r) = \begin{cases} (M\omega^2/2)\left(2r_{\rm TF}^2 - r^2\right), & r < r_{\rm TF}, \\ M\omega^2 r^2/2, & r > r_{\rm TF}, \end{cases}$$

where the Thomas–Fermi radius, $r_{\rm TF} = \left(\frac{15 N_0 U_0}{4\pi M\omega^2}\right)^{1/5}$, defines the sharp boundary of the condensate. Thus in this limit, $\widetilde{n}(r)$ is largest at the surface of the condensate, and its distribution becomes more localized as N_0 increases, albeit slowly.

The key qualitative aspects of this classical description are applicable to the quantum system, as shown in Fig. 2: this displays results of a full quantum-mechanical finite-number description, without any of the semiclassical continuous spectrum approximations made by other authors [15, 18]. This figure clearly suggests that quantitative interpretations of experimental data on finite-temperature condensates, e.g. determination of a condensate fraction from density measurements, will have to invoke some detailed model of the thermal distribution, since this distribution is neither monotonic nor close to the results obtained for a noninteracting gas. On the other hand, our current model suggests that the condensate and thermal densities are relatively distinctly segregated within the cloud,

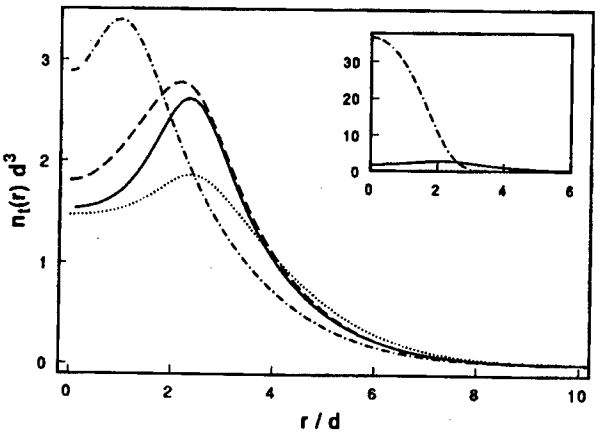

Fig. 2. Thermal density for $N \approx 2000$ ^{87}Rb atoms in a spherical trap with $\nu_r = \omega/2\pi =$ 200 Hz, $T = 75$ nK, corresponding to $f = 0.5$ in the HFB–Popov approximation. The radius r is given in units of the characteristic length of the oscillator $d = \sqrt{\hbar/M\omega}$. These parameters were previously used by Hutchinson et al. [11], whose numerical HFB–Popov results we have reproduced and use here. The main figure shows the thermal density as computed in various approximations. Chain-dashed line: the confined ideal quantum gas; dashed line: full solution of the HFB–Popov equations; solid line: full quantum-statistical distribution as computed from two-gas model, which obtains $N = 1965$ (vs. the exact value of 2000) from $N_0 = 1000$ and $T = 75$ nK; dotted line: result of classical statistical mechanics applied to the two-gas model, using a fit to force $N = 2000$. The inset compares the HFB–Popov thermal density (solid line) with that of the condensate (dashed). Thus, even when the system is only 50% condensate, the peak condensate density is clearly much higher than that of the thermal cloud.

which may considerably simplify the qualitative understanding of some properties. Since it originates in the distinction between interactions of condensate and non-condensate atoms, this spatial segregation of the two gases seems to be a fundamental aspect of the behavior of *inhomogeneous* Bose gases, such as the trapped-atom systems of current interest. This may have interesting consequences for applications: for example, it may be possible to selectively extract condensate vs. thermal atoms from a trap by appropriate positioning of a probe, thus obtaining an outcoupled matter wave with higher coherence than would be otherwise expected [19]. In homogeneous systems, on the other hand, condensate and non-condensate populations are intertwinned; this is one of the essential features of the two-fluid model of liquid helium [20].

Taking this idea further, we suggest that any property of a finite-temperature BEC should be compared in the first instance to that of the corresponding EZC. In the two-gas model, we expect most of the T-dependence of a given quantity to be reduced to N_0-dependence. For example, in Fig. 3 we show the quasiparticle excitation frequencies for the JILA TOP trap, over a range of temperatures relevant to recent experiments, as computed in the full HFB–Popov approximation and in the

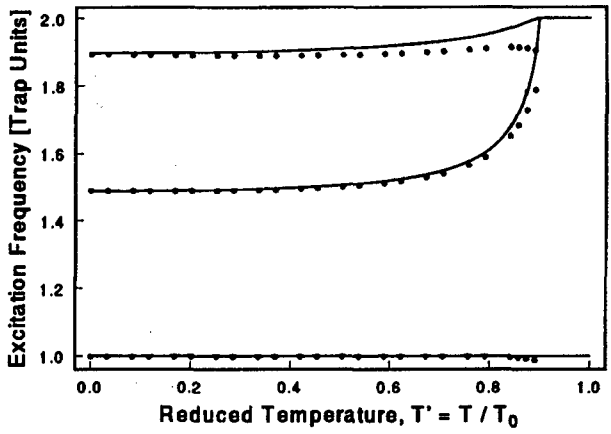

Fig. 3. HFB–Popov excitation frequencies (filled circles) for the $m = 0$ (top), $m = 2$ (middle), and the $m = 1$ modes (bottom) for the JILA TOP trap with radial frequency $\nu_r = 129$ Hz and $N = 2000$ ^{87}Rb atoms, vs. temperature in units of T_0. Overlaid (solid lines) are the frequencies for a zero-temperature system with the same number N_0 of condensate atoms as in the finite-temperature system.

two-gas model. It is seen that the two methods agree up to temperatures quite close to the phase transition, so the main effect of finite temperature is renormalization of the value of N_0. An analogous result was seen in earlier calculations [21, 22] for the *homogeneous* Bose-condensed gas of the temperature dependence of the speed of sound, which found it to be given by an equivalent $T = 0$ expression adjusted for the temperature-dependence of the condensate density.

4. Conclusions

We find that condensate and thermal populations of a partially Bose–Einstein-condensed trapped-atom system separate out to a considerable extent. Treating the condensate as uncoupled from the thermal cloud, and the thermal cloud as interacting with a static condensate potential, yields results similar to those that come from involved self-consistent field calculations. These results motivate the identification of the equivalent zero-temperature condensate as a consolidating feature of finite-temperature systems. In this model, the main effect of finite temperature on the condensate is *depletion* of the condensate number. Condensate properties that depend only weakly upon N_0, such as the quasi-particle spectrum in the large-N_0 limit (corresponding to the excitation frequencies of large condensates) [7], should exhibit only weak temperature dependence.

Acknowledgments

This work was supported in part by the U.S. National Science Foundation under grants PHY-9601261 and PHY-9612728, the U.S. Office of Naval Research, by MCS grant No. PAN/NIST-93-156, and by the U.K. Engineering and Physical Sciences Research Council.

References

[1] M.H. Anderson, J.R. Ensher, M.R. Matthews, C.E. Wieman, E.A. Cornell, *Science* **269,** 198 (1995); C.J. Myatt, E.A. Burt, R.W. Ghrist, E.A. Cornell, C.E. Wieman, *Phys. Rev. Lett.* **78,** 586 (1997).

[2] K.B. Davis, M.-O. Mewes, M.R. Andrews, N.J. van Druten, D.S. Durfee, D.M. Kurn, W. Ketterle, *Phys. Rev. Lett.* **75,** 3969 (1995); M.-O. Mewes, M.R. Andrews, N.J. van Druten, D.M. Kurn, D.S. Durfee, W. Ketterle, *Phys. Rev. Lett.* **77,** 416 (1996); M.-O. Mewes, M.R. Andrews, N.J. van Druten, D.M. Kurn, D.S. Durfee, C.G. Townsend, W. Ketterle, *Phys. Rev. Lett.* **77,** 988 (1996); M.-O. Mewes, M.R. Andrews, D.M. Kurn, D.S. Durfee, C.G. Townsend, W. Ketterle, *Phys. Rev. Lett.* **78,** 582 (1997); M.R. Andrews, M.-O. Mewes, N.J. van Druten, D.S. Durfee, D.M. Kurn, W. Ketterle, *Science* **273,** 84 (1996); M.R. Andrews, C.G. Townsend, H.-J. Miesner, D.S. Durfee, D.M. Kurn, W. Ketterle, *Science* **275,** 637 (1997).

[3] C.C. Bradley, C.A. Sackett, J.J. Tollet, R.G. Hulet, *Phys. Rev. Lett.* **75,** 1687 (1995); C.C. Bradley, C.A. Sackett, R.G. Hulet, *Phys. Rev. Lett.* **79,** E1170 (1997); C.C. Bradley, C.A. Sackett, R.G. Hulet, *Phys. Rev. Lett.* **78,** 985 (1997).

[4] W. Ketterle, N.J. van Druten, in: *Advances in Atomic, Molecular, and Optical Physics*, Vol. 37, Eds. B. Bederson, H. Walther, Academic, New York 1997.

[5] E. Cornell, *J. Res. Nat. Inst. Stand. Technol.* **101,** 419 (1996).

[6] M. Holland, J. Cooper, *Phys. Rev. A* **53,** R1954 (1996); M. Edwards, R.J. Dodd, C.W. Clark, P.A. Ruprecht, K. Burnett, *Phys. Rev. A* **53,** R1950 (1996); M. Edwards, P.A. Ruprecht, K. Burnett, R.J. Dodd, C.W. Clark, *Phys. Rev. Lett.* **77,** 1671 (1996); M. Edwards, R.J. Dodd, C.W. Clark, K. Burnett, *J. Res. Natl. Inst. Stand. Technol.* **101,** 553 (1996); R.J. Dodd, M. Edwards, C.J. Williams, C.W. Clark, M. Holland, P.A. Ruprecht, K. Burnett, *Phys. Rev. A* **54,** 661 (1996); Y. Castin, R. Dum, *Phys. Rev. Lett.* **77,** 5315 (1996); V.M. Perez-Garcia, H. Michinel, J.I. Cirac, M. Lewenstein, P. Zoller, *Phys. Rev. Lett.* **77,** 5320 (1996); B.D. Esry, *Phys. Rev. A* **55,** 1147 (1997); M.J. Holland, D.S. Jin, M.L. Ciofalo, J. Cooper, *Phys. Rev. Lett.* **78,** 3801 (1997).

[7] S. Stringari, *Phys. Rev. Lett.* **77,** 2360 (1996).

[8] J.R. Ensher, D.S. Jin, M.R. Andrews, C.E. Weiman, E.A. Cornell, *Phys. Rev. Lett.* **77,** 4984 (1996).

[9] D.S. Jin, M.R. Matthews, J.R. Ensher, C.E. Wieman, E.A. Cornell, *Phys. Rev. Lett.* **78,** 764 (1997).

[10] A. Griffin, *Phys. Rev. B* **53,** 9341 (1996).

[11] D.A.W. Hutchinson, E. Zaremba, A. Griffin, *Phys. Rev. Lett.* **78,** 1842 (1997).

[12] R.J. Dodd, M. Edwards, C.W. Clark, K. Burnett, *Phys. Rev. A*, in press; R.J. Dodd, K. Burnett, M. Edwards, C.W. Clark, submitted to *Phys. Rev. A*.

[13] T. Bergeman, *Phys. Rev. A* **55,** 3658 (1997).

[14] W. Krauth, *Phys. Rev. Lett.* **77,** 3695 (1996).

[15] A. Minguzzi, S. Conti, M.P. Tosi, *J. Phys., Condens. Matter* **9,** L33 (1997).

[16] M. Houbiers, H.T.C. Stoof, *Phys. Rev. A* **55,** 5055 (1996).

[17] G. Baym, C. Pethick, *Phys. Rev. Lett.* **76,** 6 (1996).

[18] S. Giorgini, L.P. Pitaevskii, S. Stringari, *Phys. Rev. Lett.* **78,** 3987 (1997).

[19] R.J. Dodd, C.W. Clark, M. Edwards, K. Burnett, *Optics Express* **1,** 284 (1997).

[20] As reviewed, for example, by R.P. Feynman, *Statistical Mechanics,* Addison Wesley, Reading, Massachusetts 1972, Ch. 11; A. Griffin, *Excitations in a Bose-Condensed Liquid,* Cambridge University Press, Cambridge 1993.

[21] P. Szépfalusy, I. Kondor, *Ann. Phys. (N.Y.)* **82,** 1 (1974).

[22] S.H. Payne, A. Griffin, *Phys. Rev. B* **32,** 7199 (1985).

Vol. 93 (1998) *ACTA PHYSICA POLONICA A* No. 1

Proceedings of the International Conference "Quantum Optics IV", Jaszowiec, Poland, 1997

CLASSICAL CONTROL OF QUANTIZED FIELDS: CAVITY QED AND THE PHOTON PISTOL

J.H. EBERLY AND C.K. LAW

Department of Physics and Astronomy
and
Rochester Theory Center for Optical Science and Engineering
University of Rochester
Rochester, NY 14627, USA

By using the double-lambda configuration of energy levels and three classical fields, an atom or ion in a high-Q resonant cavity can be manipulated to create a single-mode quantum state in the cavity that is an arbitrary combination of Fock states for that mode. The same principles of operation can be applied to a cavity with much lower Q in order to produce a "photon pistol", a device that "shoots" one and only one photon when a trigger is pulled, and emits no photons at other times.

PACS numbers: 42.50.Dv, 42.50.Ct, 32.80.Qk

Cavity QED now provides a realistic framework for experimental study of strongly interacting quantum systems, and for the production of interesting varieties of non-classical states of atoms and photons. It is almost too easy in the context of cavity QED to produce hyper-quantum states, states that are extremely tangled combinations of mixed numbers of atoms and photons. It is not usually realized that in 1958 Jaynes already predicted [1] that cavity QED would provide an attractive way to study entanglement.

Here we address a related question that has captured some attention in the past few years but has proved difficult to answer with complete satisfaction. This is the question how best to produce arbitrary, pre-specified, quantized cavity-mode states *without* entanglement with atomic states, even without entanglement of the atom used to generate the photons, and to do so using classically controllable inputs.

What classical device or collection of classical devices would be suitable to generate an arbitrary non-entangled quantum state with sufficient reliability that it could serve as the heart of a photon factory? Such a factory could, for example, act as supplier for a shop such as the one shown in Fig. 1. Or, if the engine were compact and reliable enough, perhaps Fock & Associates could install one in the cellar of their shop and run their own factory. At the present time there are three

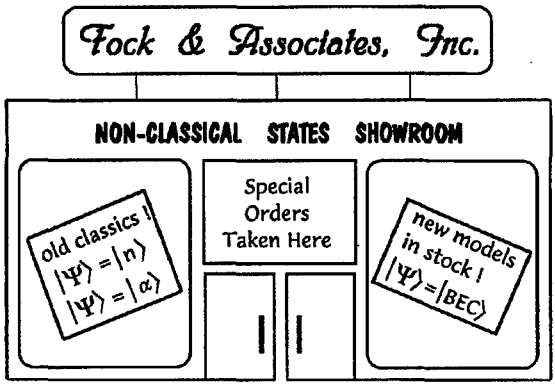

Fig. 1. A retail showroom where quantum states are available.

models for a photon engine capable, in principle, of generating an arbitrary state of the cavity mode, say

$$|\Psi\rangle = \sum_{n=0}^{N} c_n |n\rangle, \tag{1}$$

where the coefficients c_n are to be specified by the customer and must satisfy probability conservation, $\sum |c_n|^2 = 1$, but are otherwise arbitrary, and where N is the highest occupation number desired.

These model engines are sketched in Fig. 2. Model 1 is an "exit control" model [2]. It uses extremely low-cost raw materials, just a stream of identically prepared two-level atoms, but it requires a rigorous quality control stage, because the action of the atoms inside the cavity is fully quantum mechanical and the cavity builds up to its desired state only after the passage of at least N atoms, and typically many more than that. The state of each atom must be monitored when it leaves the cavity to determine if the cavity state is on the right path to the desired result. Because of the statistical rarity of achieving the desired output and the overtime wages of the quality control inspector, this is a low-profit model.

Model 2 is an "input control" model [3]. It can produce a desired output with commendable reliability, but it consumes very expensive raw materials. The raw materials required are carefully tailored quantum systems with imprinted coherence properties, for example a distribution of properly sequenced probability amplitudes in a Zeeman multiplet. Under the right conditions in the cavity, this coherence can be transformed into a coherence property of the cavity mode, yielding the desired cavity state directly, with only a cursory inspection of the output to make sure the transformation has occurred. Because of the expense of producing the carefully tailored raw materials (and drastically different tailoring for every customer must be anticipated), this is also a low-profit model.

Model 3 is a "process control" model [4]. It uses even less expensive raw materials than model 1 because it needs only a single atom, and it requires minimal quality control. However, it uses a carefully programmed interaction sequence during the time the atom is in the cavity. This means that external classical fields

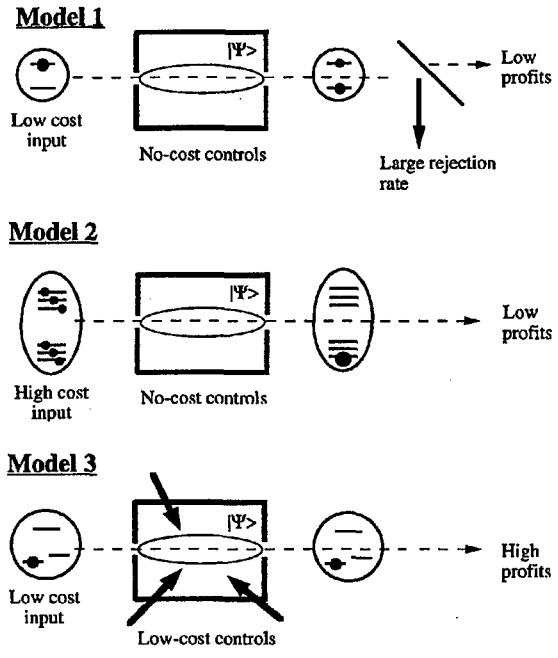

Fig. 2. Sketches of three models that have been proposed for a photon engine that will generate photon states according to a customer's prescription.

are used to excite and de-excite the atom in a predetermined sequence of steps. The major cost is not in supplying such external fields but in building a cavity that permits these fields to enter and leave without seriously affecting the Q value of the quantized cavity mode of interest. This is a capital cost that needs to be undertaken only once, independent of the state that is to be produced. Thus a factory using model 3 needs sufficient business volume to recover the capital cost of the unusual cavity, but is otherwise a low-cost and high-profit model.

The odds appear to be in favor of model 3, so we will now explain its advantages more carefully. One important difference that was not mentioned explicitly, although it is implied by the sketch in Fig. 2, is that the atom is used in a stimulated Raman mode, which means that the two-level atom is really a three-level atom being excited and de-excited very far off resonance in a lambda configuration. Moreover, the lambda interaction is employed twice, so the atom is actually a "double-lambda" atom, as shown in Fig. 3.

The absorption-emission events are those of two Raman-type processes acting between the same two levels of an atom at the same time: absorption of a pump photon and the accompanying emission of a Stokes photon, followed by the absorption of another pump photon and then the emission of an anti-Stokes photon, and in the figure R and L denote the "right" and "left" pump modes, while S and A label the usual Stokes and anti-Stokes modes. In an alternating-pair sequence these fields can take the atom from state $|-\rangle$ to state $|+\rangle$ and around to $|-\rangle$ again.

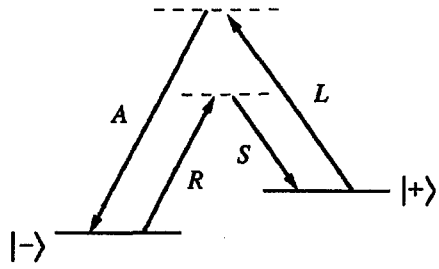

Fig. 3. Sketch of double-lambda atom. Dipole transition matrix elements connect the two "ground" states with an upper opposite-parity state that is not shown.

In this way, the atom ends where it began, but the field inventory of photons is different. In the end there are two fewer pump photons and one additional photon in each of the Stokes and anti-Stokes modes. The atom has acted as a wave-mixing catalyst, and is ready to be used again. The Jaynes–Cummings system has only a single channel connecting its two states, so cyclic operation of this kind is not possible.

The double-lambda atom has not received a lot of attention in the literature, but there are applications for which its advantages have already been recognized. Some of the previous works can be identified with the following themes and names:

(i) amplification without inversion, Kocharovskaya and Mandel [5];

(ii) excitation via a classical and a quantum channel simultaneously, Law and Eberly [6];

(iii) exact quantum solutions for 3 modes, Wang et al. [7];

(iv) boson spin algebra for 4 modes, Wang and Eberly [8];

(v) two mechanisms for inversionless amplification, Keitel et al. [9];

(vi) perfect Greenberger–Horne–Zeilinger (GHZ) correlator, Wodkiewicz et al. [10];

(vii) two-mode squeezing and phase correlation, Law and Eberly [11];

(viii) lasing without inversion and phaseonium, Scully et al. [12];

(ix) transparency and dressing in a double-lambda medium, Cerboneschi and Arimondo [13];

(x) photon engine, Law and Eberly [4];

(xi) quantum image storage, Kneer and Law [14];

(xii) photon pistol, Law and Kimble [15].

The double-lambda is obviously a two-channel extension of the well-known Jaynes–Cummings (JC) model [1]. One knows that the JC model is essentially a handy toy in which to examine fundamental aspects of both optical spectroscopy and laser action, with the major advantage that strong-field cavity interactions of current experimental interest can be treated in detail. However, many effects and processes familiar in optical physics do not fit into the Jaynes–Cummings framework at all. These include:

(a) pump-probe effects,

(b) nonlinear wave mixing, including down conversion,

(c) three-mode correlations of the GHZ type,

(d) two-photon lasing, and

(e) optical pumping of laser action.

Because of its two channels, the double-lambda model is able to treat some or all of these effects. The main important difference to the JC model is the ability to manipulate the atom by connecting the states $|+\rangle$ and $|-\rangle$ in two independent ways. This has been shown [4] to be the key to avoid entanglement. Although a 3-mode quantum model of the two-channel process also exists [7], we are concerned here only with a 4-mode model [8]. In any case a single atom (or ion) is either laser-cooled and allowed to drift very slowly through the cavity or it is permanently trapped in the cavity. Figure 4 sketches the three (classical) light beams incident from outside the cavity that are imposed to control atomic excitation in either case.

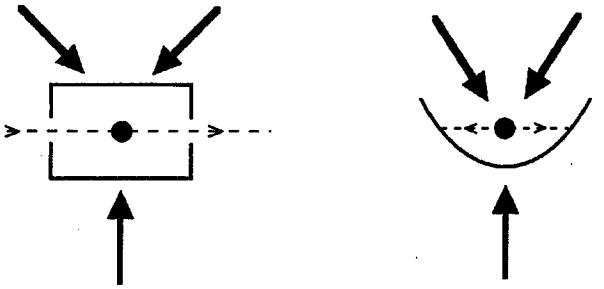

Fig. 4. Arrows designate three classical external radiation fields (laser beams) that are directed at a double-lambda atom that drifts through a cavity or is held in a trap, which is located in a cavity too. The cavity supports excitation of a fourth mode, which is excited one photon at a time and is treated as quantized.

It is remarkable that the much more complex quantum double-lambda is "solvable" in the same sense as the JC model — the eigenvalues and eigenfunctions of its Hamiltonian can be found exactly. For comparison, the two models' interaction Hamiltonians are

$$V_{\rm JC} = g\hat{a}\hat{\sigma}_{+-}\text{h.c.},$$

$$V_{\Lambda-\Lambda} = g(\hat{a}_R\hat{a}_S^\dagger + \hat{a}_L^\dagger\hat{a}_A)\hat{\sigma}_{+-} + \text{h.c.} \qquad (2)$$

It is well known that the raising and lowering operators for the JC model atom have an angular momentum interpretation. In the 3-mode case Schwinger's procedure extends an angular momentum property to the radiation mode operators. For example, we define L_1 operators using bilinear combinations of the R and S modes: $L_{1+} \equiv a_R^\dagger a_S$ and $L_{1-} \equiv a_R a_S^\dagger$, and $L_{1z} \equiv \frac{1}{2}[L_{1+}, L_{1-}]$. Then L_2 operators are formed from the A and L mode operators in the same way. The

connections between angular momentum quantum numbers and photon numbers are given by

$$l_1 = \frac{1}{2}(n_R + n_S), \qquad m_1 = \frac{1}{2}(n_R - n_S), \tag{3}$$

and

$$l_2 = \frac{1}{2}(n_A + n_L), \qquad m_2 = \frac{1}{2}(n_A - n_L). \tag{4}$$

These angular momenta, plus the atom's two-level pseudo-spin $\boldsymbol{S}$, are used to define a new "total" angular momentum $\boldsymbol{J} = \boldsymbol{L}_1 + \boldsymbol{L}_2 + \boldsymbol{S}$. It has been shown [8] that the eigenvalues and eigenfunctions can be found for this Hamiltonian exactly and analytically in closed form. (The same is true for the 3-mode double-lambda systems [7], but angular momentum algebra is not helpful there and the results are strikingly different.) In the 4-mode case of interest here we only quote the eigenvalue formula, which is given by a Clebsch–Gordan coefficient

$$\lambda = \sqrt{(l-m)(l+m+1)}, \tag{5}$$

where l and m belong to the "mode angular momentum" $\boldsymbol{L} = \boldsymbol{L}_1 + \boldsymbol{L}_2$.

Surprisingly, the most interesting applications of the double-lambda model are not even on our list of effects lying outside the reach of the JC model. These are the consequences of understanding the working of a photon "engine", and one of these is the invention of a "photon pistol."

Only the design for the photon engine [4] has been published so far. In the case of the photon pistol, the same combination of external and cavity modes is used as for the engine, but the cavity Q is drastically lowered so that as soon as a cavity photon is generated in the cycling of the "engine", it is transmitted through one of the cavity mirrors ("shot") out of the cavity. A second photon will not be emitted until the engine is run through another cycle. Since the principle of the pistol is clear, the remaining issue is only one of practicality. Surprisingly, the device is not impractical and a photon pistol can probably be made in the laboratory in the near future.

Here we list the results of a study of a photon pistol in the context of the $D1$ line of Cs. This turns out to provide a particularly attractive context for pistol operation. The relevant Cs transitions for this are shown in Fig. 5. The $F = 4 \rightarrow F = 4$ transition in Fig. 5 is the one we have labelled R above, and r_0 is its peak Rabi frequency. The $F = 4 \rightarrow F = 3$ transition is the one labeled S above, and g is its one-photon Rabi frequency. The "recycling" transitions involving the external fields labeled L and A above, that make up the other half of the double lambda are omitted from the figure for simplicity.

Some of the key operating points are these. Once an atom is chosen, the value of g is fixed according to the relevant dipole moment, the size of the cavity, and the position of the atom in it. The other transitions in the atom determine how strong r_0 can be made before higher excitations need to be considered. In the Cs case this means the critical parameter, the effective two-photon Rabi frequency Ω_{RS} given by

$$\Omega_{RS} = \frac{1}{2}\frac{g r_0}{\Delta}, \tag{6}$$

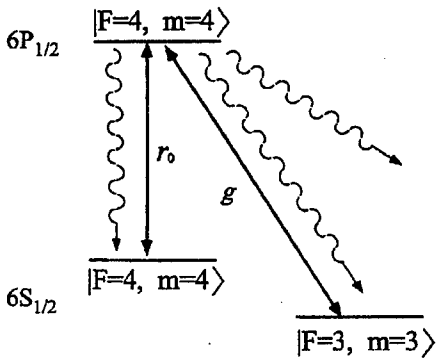

Fig. 5. The basis for operation of the photon pistol is the induced appearance of a photon in the cavity (channel "g" here). The relevant energy levels of the experimental atom (Cs operating on the $D1$ line) are shown, along with the principle atomic relaxation channels. The cavity relaxation is much more rapid, allowing the photon "bullet" to emerge from the pistol with less than 0.1 μs delay.

is too weak to be effective unless Δ, the one-photon detuning, is nearly resonant. This has no effect on the pistol concept, but does allow the upper state ($m = 4$ in the figure) to become populated, thus opening an extra relaxation channel (spontaneous emission from $m = 4$) disregarded up to now. Both quantum trajectory calculations and also more elaborate master equation calculations [15] show that this effect can be tolerated.

At resonance, the following parameter values are currently realizable in the laboratory for the Cs transitions shown: (r_0, g, the cavity loss rate κ and the atomic decay rate γ) = (22.5, 45, 45, 4.5), where all values are in MHz. To be specific, $\kappa = 2\pi \cdot 45$ MHz, etc. Given a temporal halfwidth $T_0 = 3\gamma^{-1} = 105$ ns for the external field R, calculations that take full account of hyperfine structure, atomic decay channels, and operating cavity conditions lead to the following conclusions [15]. The one-photon emission probability rises more than 95% within less than 0.1 μs, just two atomic lifetimes ($\gamma t = 2$). An even higher emission probability (99.5%) can be reached when $g = 2\pi \cdot 120$ MHz. In the absence of another R pulse there will be no second photon. This is an operational reliability that is probably acceptable to most customers (quantum optics Mafia, etc.). An important selling point is that the fall-off in performance is not great even for a significant decrease in reliability of input. For example, if g fluctuates by a factor of 2 it is predicted that the firing probability still remains near to, or well above, 90%.

In summary, we have discussed progress toward classical control of quantum processes. The two-channel double-lambda system has been exploited here to provide two examples of classical control, the photon state engine and the photon pistol. Both rely on very highly lossless operation of an optical cavity of very small dimension. Until recently these requirements would have been unrealistic, and at this time they remain just beyond realization for the photon engine. However, the photon pistol requires a much lower storage time for the cavity mode, and we have reported the results of a recent calculation [15] to show that a pistol is prob-

ably feasible at the present time. Just as interesting are the items in the second listing above. They represent targets for future application of the double-lambda principle.

Acknowledgment

The research reported here was supported by the US National Science Foundation through grants PHY94-08733 and PHY94-15583.

References

[1] E.T. Jaynes, Microwave Lab Report 502, Stanford Univ., 1958; see also E.T. Jaynes, F.W. Cummings, *Proc. IEEE* **51**, 89 (1963).

[2] K. Vogel, V.M. Akulin, W.P. Schleich, *Phys. Rev. Lett.* **71**, 1816 (1993); B.M. Garraway, B. Sherman, H. Moya-Cessa, P.L. Knight, G. Kurizki, *Phys. Rev. A* **49**, 535 (1994); for a model using a single conditional measurement, see A. Kozhekin, G. Kurizki, B. Sherman, *Phys. Rev. A* **54**, 3535 (1996).

[3] A.S. Parkins, P. Marte, P. Zoller, H.J. Kimble, *Phys. Rev. Lett.* **71**, 3095 (1993); A.S. Parkins, P. Marte, P. Zoller, O. Carnal, H.J. Kimble, *Phys. Rev. A* **51**, 1578 (1995).

[4] C.K. Law, J.H. Eberly, *Phys. Rev. Lett.* **76**, 1055 (1996).

[5] O. Kocharovskaya, P. Mandel, *Phys. Rev. A* **42**, 523 (1990).

[6] C.K. Law, J.H. Eberly, *Phys. Rev. A* **43**, 6337 (1991).

[7] L. Wang, R.R. Puri, J.H. Eberly, *Phys. Rev. A* **46**, 7192 (1992).

[8] L. Wang, J.H. Eberly, *Phys. Rev. A* **47**, 4248 (1993).

[9] C.H. Keitel, O.A. Kocharovskaya, L.M. Narducci, M.O. Scully, S.-Y. Zhu, H.M. Doss, *Phys. Rev. A* **48**, 3196 (1993).

[10] K. Wodkiewicz, L. Wang, J.H. Eberly, *Phys. Rev. A* **47**, 3280 (1993).

[11] C.K. Law, J.H. Eberly, *Phys. Rev. A* **47**, 3195 (1993).

[12] M. Fleischhauer, M.D. Lukin, D.E. Nikonov, M.O. Scully, *Opt. Commun.* **110**, 351 (1994).

[13] E. Cerboneschi, E. Arimondo, *Phys. Rev. A* **52**, R1823 (1995).

[14] B. Kneer, C.K. Law, Paper MEE7, Annual Meeting, Optical Society of America, Rochester, NY, October 20–24, 1996.

[15] C.K. Law, H.J. Kimble, *J. Mod. Opt.*, special issue on *Quantum States Preparation and Measurement*, Eds. W.P. Schleich, M.G. Raymer, in press.

Vol. 93 (1998) ACTA PHYSICA POLONICA A No. 1

Proceedings of the International Conference "Quantum Optics IV", Jaszowiec, Poland, 1997

AGAINST QUANTUM NOISE

A. EKERT* AND CH. MACCHIAVELLO†

Clarendon Laboratory, University of Oxford, Oxford OX1 3PU, U.K.

This is a brief description of how to protect quantum states from dissipation and decoherence that arise due to uncontrolled interactions with the environment. We discuss recoherence and stabilization of quantum states based on two techniques known as "symmetrization" and "quantum error correction". We illustrate our considerations with the most popular quantum-optical model of the system–environment interaction, commonly used to describe spontaneous emission, and show the benefits of quantum error correction in this case.

PACS numbers: 89.70.+c, 03.65.Bz

1. Introduction

Suppose we want to transmit or store a block of l qubits (i.e. two-state quantum systems) in a noisy environment. Here "noisy" means that each qubit may become entangled with the environment. Thus due to spurious interactions with the environment the actual state of the l qubits, described by a density operator $\rho(t)$, will differ from the original state $|\Psi\rangle$. This deviation can be quantified by the fidelity

$$F(t) = \langle\Psi|\rho(t)|\Psi\rangle = 1 - \epsilon(t). \tag{1}$$

In order to maximize this fidelity we may try all sorts of tricks ranging from the most obvious one, i.e. isolating the qubits from the environment to more sophisticated methods such as "symmetrization" [1, 2], "purification" [3, 4], and "quantum error correction" [5]. The last method seems to be the most popular one at the moment and relies on encoding the state of l qubits into a set of n qubits and trying to disentangle a certain number of qubits from the environment after some period of time. In the following we describe, very briefly, how some of these techniques work.

We will assume that in the block of l qubits each qubit is coupled to a different environment. This is a perfectly reasonable assumption, which is valid if the coherence length of the environment/reservoir is less than the spatial separation between the qubits [6], and introduces a great deal of simplifications to the

*ekert@physics.ox.ac.uk.

†chiara@mildred.physics.ox.ac.uk. Also at: Dipartimento di Fisica Generale "A. Volta", Via Bassi 6, 27100 Pavia, Italy.

calculations. Basically it allows us to view any dissipation of l qubits as a set of independent dissipations of l single qubits (i.e. we ignore collective phenomena such as superradiance etc.).

The qubit–environment interaction leads to the qubit–environment entanglement, which in its most general form is given by

$$|0\rangle|R\rangle \longrightarrow |0\rangle|R_{00}(t)\rangle + |1\rangle|R_{01}(t)\rangle, \tag{2}$$

$$|1\rangle|R\rangle \longrightarrow |0\rangle|R_{10}(t)\rangle + |1\rangle|R_{11}(t)\rangle, \tag{3}$$

where states of the environment $|R\rangle$ and $|R_{ij}\rangle$ are neither normalised nor orthogonal to each other (thus we have to take additional care at the end of our calculations and normalise the final states). The r.h.s. of the formulae above can also be written in a matrix form as

$$\begin{pmatrix} |R_{00}\rangle & |R_{01}\rangle \\ |R_{10}\rangle & |R_{11}\rangle \end{pmatrix} \begin{pmatrix} |0\rangle \\ |1\rangle \end{pmatrix}, \tag{4}$$

and the 2×2 matrix can be subsequently decomposed into some basis matrices e.g. into the unity and the Pauli matrices

$$|R_0\rangle 1 + |R_1\rangle\sigma_x + \mathrm{i}|R_2\rangle\sigma_y + |R_3\rangle\sigma_z, \tag{5}$$

where $|R_0\rangle = (|R_{00}\rangle + |R_{11}\rangle)/2$, $|R_3\rangle = (|R_{00}\rangle - |R_{11}\rangle)/2$, $|R_1\rangle = (|R_{01}\rangle + |R_{10}\rangle)/2$, and $|R_2\rangle = (|R_{01}\rangle - |R_{10}\rangle)/2$. Thus the qubit initially in state $|\Psi\rangle$ will evolve as

$$|\Psi\rangle|R\rangle \longrightarrow \sum_{i=0}^{3} \sigma_i|\Psi\rangle|R_i\rangle \tag{6}$$

becoming entangled with the environment (we have relabelled the unity operator and the Pauli matrices $\{1, \sigma_x, \sigma_y, \sigma_z\}$ respectively as $\{\sigma_0, \sigma_1, \sigma_2, \sigma_3\}$). Its fidelity with respect to the initial state $|\Psi\rangle$ evolves as

$$F(t) = \sum_{i,j} \langle\Psi|\sigma_i|\Psi\rangle\langle\Psi|\sigma_j|\Psi\rangle\langle R_j(t)|R_i(t)\rangle. \tag{7}$$

The formula (6) describes how the environment affects any quantum state of a qubit and shows that a general qubit–environment interaction can be expressed as a superposition of unity and Pauli operators acting on the qubit. As we will see in the following, in the language of error correcting codes this means that the qubit state is evolved into a superposition of an error-free component and three erroneous components, with errors of the σ_x, σ_y and σ_z type.

We can carry on this description even if the qubit itself is not in a pure state $|\Psi\rangle$ but is entangled with some other qubits. For example, if in a three qubit register initially in state $\left|\widetilde{\Psi}\right\rangle = |0\rangle|0\rangle|0\rangle - |1\rangle|1\rangle|1\rangle$ the second qubit interacted with its environment then the state of the register at some time t is given by

$$\sum_{i=0}^{3} \sigma_i^{(2)} \left|\widetilde{\Psi}\right\rangle |R_i(t)\rangle = \sum_{i=0}^{3} [|0\rangle(\sigma_i|0\rangle)|0\rangle - (|1\rangle(\sigma_i|1\rangle)|1\rangle]|R_i(t)\rangle, \tag{8}$$

where the superscript (2) reminds us that the Pauli operators act only on the second qubit. We can then say that the second qubit was affected by quantum errors which are represented by the Pauli operators σ_i. Errors affecting classical

bits can only change their binary values ($0 \leftrightarrow 1$), in contrast quantum errors operators σ_i acting on qubits can change their binary values (σ_x), their phases (σ_z) or both (σ_y).

In general, a batch of n qubits initially in some state $\left|\widetilde{\Psi}\right\rangle$, each of them interacting with different environments, will evolve as

$$\prod_{k=1}^{n}\sum_{i=0}^{3}\sigma_i^{(k)}\left|\widetilde{\Psi}\right\rangle\left|R_i^{(k)}(t)\right\rangle, \tag{9}$$

namely multiple errors of the form $\sigma_i \otimes \sigma_j \cdots \otimes \sigma_k$ may occur, affecting several qubits at the same time.

So much about unwelcome dissipation, what about remedies?

2. Stabilization via symmetrization

The first proposed remedy was based on a symmetrization procedure [1]. The basic idea is as follows. Suppose you have a quantum system, you prepare it in some initial state $|\Psi_i\rangle$ and you want to implement a prescribed unitary evolution $|\Psi(t)\rangle$ or simply you want to preserve $|\Psi_i\rangle$ for some period of time t. Now, suppose that instead of a single system you can prepare R copies of $|\Psi_i\rangle$ and subsequently you can project the state of the combined system on the symmetric subspace, i.e. the subspace containing all states which are invariant under any permutation of the subsystems. The claim is that frequent projections on the symmetric subspace will reduce errors induced by the environment. The intuition behind this concept is based on the observation that a prescribed error-free storage or evolution of the R independent copies starts in the symmetric subspace and should remain in that subspace. Therefore, since the error-free component of any state always lies in the symmetric subspace, upon successful projection it will be unchanged and part of the error will have been removed. Note however that the projected state is generally not error-free since the symmetric subspace contains states which are not of the simple product form $|\psi\rangle|\psi\rangle\ldots|\psi\rangle$. Nevertheless it has been shown that the error probability will be suppressed by a factor of $1/R$ [2].

We illustrate here this effect in the simplest case of two qubits. The projection into the symmetric subspace is performed in this case by introducing the symmetrization operator

$$S = \frac{1}{2}(P_{12} + P_{21}), \tag{10}$$

where P_{12} represents the identity and P_{21} the permutation operator which exchanges the states of the two qubits. The symmetric-projection of a pure state $|\Psi\rangle$ of two qubits is just $S|\Psi\rangle$, which is then renormalised to unity. It follows that the induced map on mixed states of two qubits (including renormalization) is

$$\rho_1 \otimes \rho_2 \longrightarrow \frac{S(\rho_1 \otimes \rho_2)S^\dagger}{\mathrm{Tr}S(\rho_1 \otimes \rho_2)S^\dagger}. \tag{11}$$

The state of either qubit separately is then obtained by partial trace over the other qubit.

Consider for example the symmetric projection of $\rho \otimes \rho$ followed by renormalization and partial trace (over either qubit) to obtain the final state ρ_s of one

qubit, given that the symmetric-projection was successful. A direct calculation based on (11) yields

$$\rho \mapsto \rho_s = \frac{\rho + \rho^2}{\mathrm{Tr}(\rho + \rho^2)}. \tag{12}$$

For any mixed state ξ of a qubit the expression $\mathrm{Tr}\xi^2$ provides a measure of the purity of the state, ranging from $\frac{1}{4}$ for the completely mixed state $I/2$ (where I is the unit operator) to 1 for any pure state. From (12) we get

$$\mathrm{Tr}\rho_s^2 > \mathrm{Tr}\rho^2 \tag{13}$$

so that ρ_s is *purer* than ρ. This illustrates that successful projection of a mixed state into the symmetric subspace tends to enhance the purity of the individual systems.

To be more specific, let us assume now that the two copies are initially prepared in pure state $\rho_0 = |\Psi\rangle\langle\Psi|$ and that they interact with independent environments. After some short period of time δt the state of the two copies $\rho^{(2)}$ will have undergone an evolution

$$\rho^{(2)}(0) = \rho_0 \otimes \rho_0 \longrightarrow \rho^{(2)}(\delta t) = \rho_1 \otimes \rho_2, \tag{14}$$

where $\rho_i = \rho_0 + \varrho_i$ for some Hermitian traceless ϱ_i. We will retain only terms of first order in the perturbations ϱ_i so that the overall state at time δt is

$$\rho^{(2)} = \rho_0 \otimes \rho_0 + \varrho_1 \otimes \rho_0 + \rho_0 \otimes \varrho_2 + \mathrm{O}(\varrho_1 \varrho_2). \tag{15}$$

We can calculate the average purity of the two copies before symmetrization by calculating the average trace of the squared states

$$\frac{1}{2}\sum_{i=1}^{2} \mathrm{Tr}[(\rho_0 + \varrho_i)^2] = 1 + 2\mathrm{Tr}(\rho_0 \tilde{\varrho}), \tag{16}$$

where $\tilde{\varrho} = \frac{1}{2}(\varrho_1 + \varrho_2)$. Note that $\mathrm{Tr}(\rho_0 \tilde{\varrho})$ is negative, so that the expression above does not exceed 1. After symmetrization each qubit is in state

$$\rho_s = [1 - \mathrm{Tr}(\rho_0 \tilde{\varrho})]\rho_0 + \frac{1}{2}\tilde{\varrho} + \frac{1}{2}(\rho_0 \tilde{\varrho} + \tilde{\varrho}\rho_0) \tag{17}$$

and has purity

$$\mathrm{Tr}(\rho_s^2) = 1 + \mathrm{Tr}(\rho_0 \tilde{\varrho}). \tag{18}$$

Since $\mathrm{Tr}\rho_s^2$ is closer to 1 than (16), the resulting symmetrised system ρ_s is left in a purer state.

Let us now see how the fidelity changes by applying the symmetrization procedure. The average fidelity before symmetrization is

$$F_{bs} = \frac{1}{2}\sum_i \langle\Psi|\rho_0 + \varrho_i|\Psi\rangle = 1 + \langle\Psi|\tilde{\varrho}|\Psi\rangle, \tag{19}$$

while after successful symmetrization it takes the form

$$F_{as} = \langle\Psi|\rho_s|\Psi\rangle = 1 + \frac{1}{2}\langle\Psi|\tilde{\varrho}|\Psi\rangle. \tag{20}$$

The state after symmetrization is therefore closer to the initial state ρ_0.

For the generic case of R copies the purity of each qubit after symmetrization is given by [2]

$$\mathrm{Tr}(\rho_s^2) = 1 + 2\frac{1}{R}\mathrm{Tr}(\rho_0\tilde{\varrho}), \tag{21}$$

where now $\tilde{\varrho} = \frac{1}{R}\sum_{i=1}^{R}\varrho_i$, and the fidelity takes the form

$$\langle\Psi|\rho_s|\Psi\rangle = 1 + \frac{1}{R}\mathrm{Tr}(\rho_0\tilde{\varrho}). \tag{22}$$

Formulae (21) and (22) must be compared with the corresponding ones before symmetrization, i.e. (16) and (19). As we can see, ρ_s approaches the unperturbed state ρ_0 as R tends to infinity. Thus by choosing R sufficiently large and the rate of symmetric projection sufficiently high, the residual error at the end of a computation can, in principle, be controlled to lie within any desired small tolerance.

The efficiency of the symmetrization procedure depends critically on the probability that the state of the R qubits is successfully projected into the symmetric subspace. It has been shown that if the projections are done frequently enough, then the cumulative probability that they all succeed can be made as close as desired to unity. This is a consequence of the fact that the fidelity of the state of the R computers with respect to the corresponding error-free state for small times δt has a parabolic behaviour (see Sec. 5). Therefore the probability of successful projection, which is unity at the initial time, begins to change only to second order in time. If we project n times per unit time interval, i.e. we choose the time interval between two subsequent projections $\delta t = 1/n$, then the cumulative probability that all projections in one unit time interval succeed is given by

$$[1 - k(\delta t)^2]^n = \left(1 - \frac{k}{n^2}\right)^n \to 1 \quad \text{as} \quad n \to \infty. \tag{23}$$

Here k is a constant depending on the rate of rotation of the state out of the symmetric subspace. This effect is known as the "quantum watch-dog effect" or the "quantum Zeno effect".

3. Quantum encoding and decoding

The idea of protecting information via encoding and decoding lies at the foundations of the classical information theory. It is based on a clever use of redundancy during the data storage or transmission. For example, if the probability of error (bit flip) during a single bit transmission via a noisy channel is p and each time we want to send bit value 0 or 1 we can encode it by a triple repetition i.e. by sending 000 or 111. At the receiving end each triplet is decoded as either zero or one following the majority rule — more zeros means 0, more ones means 1. This is the simplest error correcting protocol which allows to correct up to one error.

In the triple repetition code the signalled bit value is recovered correctly both when there was no error during the transmission of the three bits, which happens with probability $(1-p)^3$, and when there was one error at any of the three locations, which happens with probability $3p(1-p)^2$. Thus the probability of the correct transmission (up to the second order in p) is $1-3p^2$ i.e. the probab-

ility of error is now $3p^2$, which is much smaller when compared with the probability of error without encoding and decoding p ($p \ll 1$). This way we can trade the probability of error in the signalled message for a number of transmissions via the channel. In our example the reduction of the error rate from p to $3p^2$ required to send three times more bits. If sending each bit via the channel costs us money we have to decide what we treasure more, our bank account or our infallibility. The triple repetition code encodes one bit into three bits and protects against one error, in general we can construct codes that encode l bits into n bits and protect against t errors. The best codes, of course, are those which for a fixed value l minimize n and maximize t.

Quantum error correction which protects quantum states is a little bit more sophisticated simply because the bit flip is not the only "quantum error" which may occur, as we have seen in the previous sections. Moreover, the decoding via the majority rule does not usually work because it may involve measurements which destroy quantum superpositions. Still, the triple repetition code is a good starting point to investigate quantum codes and even to construct the simplest ones.

The simplest interesting case of the most general qubit–environment evolution (3) is the case of decoherence [7] where the environment effectively acts as a measuring apparatus

$$|0\rangle|R\rangle \longrightarrow |0\rangle|R_{00}(t)\rangle, \tag{24}$$

$$|1\rangle|R\rangle \longrightarrow |1\rangle|R_{11}(t)\rangle. \tag{25}$$

Following our discussion in Sec. 1 we can see that this model leads only to dephasing errors of the σ_z type. It turns out that a phase flip can be handled almost in the same way as a classical bit flip. Again, consider the following scenario: we want to store, in a computer memory, one qubit in an *unknown* quantum state of the form $\alpha|0\rangle + \beta|1\rangle$ and we know that any single qubit which is stored in a register may, with a small probability p, undergo a decoherence type entanglement with an environment (Eq. (25)); in particular

$$(\alpha|0\rangle + \beta|1\rangle)|R\rangle \longrightarrow \alpha|0\rangle|R_{00}\rangle + \beta|1\rangle|R_{11}\rangle. \tag{26}$$

Let us now show how to reduce the probability of decoherence to be of the order p^2.

Before we place the qubit in the memory register we *encode* it: we can add two qubits, initially both in state $|0\rangle$, to the original qubit and then perform an encoding unitary transformation

$$|000\rangle \longrightarrow |C_0\rangle = (|0\rangle + |1\rangle)(|0\rangle + |1\rangle)(|0\rangle + |1\rangle), \tag{27}$$

$$|100\rangle \longrightarrow |C_1\rangle = (|0\rangle - |1\rangle)(|0\rangle - |1\rangle)(|0\rangle - |1\rangle), \tag{28}$$

generating state $\alpha|C_0\rangle + \beta|C_1\rangle$. Now, suppose that only the second stored qubit was affected by decoherence and became entangled with the environment

$$\alpha(|0\rangle + |1\rangle)(|0\rangle|R_{00}\rangle + |1\rangle|R_{11}\rangle)(|0\rangle + |1\rangle)$$

$$+\beta(|0\rangle - |1\rangle)(|0\rangle|R_{00}\rangle - |1\rangle|R_{11}\rangle)(|0\rangle - |1\rangle), \tag{29}$$

which, following Eq. (8), can be written as

$$(\alpha|C_0\rangle + \beta|C_1\rangle)|R_0\rangle + \sigma_z^{(2)}(\alpha|C_0\rangle + \beta|C_1\rangle)|R_3\rangle. \tag{30}$$

If vectors $|C_0\rangle$, $|C_1\rangle$, $\sigma_z^{(k)}|C_0\rangle$, and $\sigma_z^{(k)}|C_1\rangle$ are orthogonal to each other we can try to perform a measurement on the qubits and project their state either on the state $\alpha|C_0\rangle + \beta|C_1\rangle$ or on the orthogonal one $\sigma_z^{(2)}(\alpha|C_0\rangle + \beta|C_1\rangle)$. The first case yields the proper state right away, the second one requires one application of σ_z to compensate for the error. In this simple case one can even find a direct unitary operation which can fix all one qubit phase flips regardless their location. For example the transformation

$$\begin{aligned} |000\rangle &\to |000\rangle \qquad |100\rangle \to |011\rangle \\ |001\rangle &\to |001\rangle \qquad |101\rangle \to |110\rangle \\ |010\rangle &\to |010\rangle \qquad |110\rangle \to |101\rangle \\ |011\rangle &\to |111\rangle \qquad |111\rangle \to |100\rangle \end{aligned} \tag{31}$$

corrects any single bit flip $0 \leftrightarrow 1$ and when applied in the conjugate basis ($|0'\rangle = |0\rangle + |1\rangle$, $|1'\rangle = |0\rangle - |1\rangle$) it corrects any single phase flip (the bit flips become phase flips in the new basis). The snag is that using the scheme above we can correct up to one phase error σ_z or we can go to a conjugate basis and the same scheme will correct up to one amplitude error σ_x but it cannot correct up to one general error, be it amplitude or phase.

To fix this problem Peter Shor in 1995 combined the phase and the amplitude correction schemes into one constructing the following nine qubit code [5]:

$$|0\rangle \to \frac{1}{2\sqrt{2}}(|000\rangle + |111\rangle)(|000\rangle + |111\rangle)(|000\rangle + |111\rangle) \tag{32}$$

$$|1\rangle \to \frac{1}{2\sqrt{2}}(|000\rangle - |111\rangle)(|000\rangle - |111\rangle)(|000\rangle - |111\rangle). \tag{33}$$

This code involves double encoding, first in base $|0\rangle$ and $|1\rangle$ and then in base $|0'\rangle$ and $|1'\rangle$, and it allows to correct up to one either bit or phase flip. It turns out that the ability to correct both amplitude and phase errors suffices to correct any error due to entanglement with the environment. In other words the action of the environment on qubits can be viewed in terms of bit and phase flips.

4. Quantum error-correcting codes

The original nine qubit code of Shor can be further simplified. It has been shown that a five qubit code suffices to correct a single error of any type. Let us now specify the conditions for the existence of quantum error-correcting codes.

We say we can correct a single error $\sigma_i^{(k)}$ (where $i = 0 \ldots 3$ refers to the type of error) if we can find a transformation such that it maps all states with a single error $\sigma_i^{(k)} \left|\widetilde{\Psi}\right\rangle$ into the proper error-free state $\left|\widetilde{\Psi}\right\rangle$:

$$\sigma_i^{(k)} \left|\widetilde{\Psi}\right\rangle \longrightarrow \left|\widetilde{\Psi}\right\rangle. \tag{34}$$

To make it unitary we may need an ancilla

$$\sigma_i^{(k)} \left|\widetilde{\Psi}\right\rangle |0\rangle \longrightarrow \left|\widetilde{\Psi}\right\rangle |a_i^k\rangle. \tag{35}$$

For encoded basis states of a single qubit $|C_0\rangle$ and $|C_1\rangle$ this implies [8]

$$A_k|C_0\rangle|0\rangle \longrightarrow |C_0\rangle|a_k\rangle \tag{36}$$

$$A_k|C_1\rangle|0\rangle \longrightarrow |C_1\rangle|a_k\rangle, \tag{37}$$

where A_k denotes all the possible types of independent errors affecting at most one of the qubits. The above requirement leads to the following unitarity conditions:

$$\langle C_0|A_k^\dagger A_l|C_0\rangle = \langle C_1|A_k^\dagger A_l|C_1\rangle = \langle a_k|a_l\rangle, \tag{38}$$

$$\langle C_0|A_k^\dagger A_l|C_1\rangle = 0. \tag{39}$$

The above conditions are straightforwardly generalised to an arbitrary t error correcting code, which corrects any kind of transformations affecting up to t qubits in the encoded state. In this case the operators A_k are all the possible independent errors affecting up to t qubits, namely operators of the form $\Pi_{i=1}^t \sigma_i$ acting on t different qubits. In the case of the so-called "nondegenerate codes" Eq. (38) takes the simple form [9]

$$\langle C_0|A_k^\dagger A_l|C_0\rangle = \langle C_1|A_k^\dagger A_l|C_1\rangle = 0. \tag{40}$$

This condition requires that all states which are obtained by affecting up to t qubits in the encoded states are all orthogonal to each other, and therefore distinguishable. This ensures that by performing suitable projections of the encoded state we are able to detect the kind of error which occurred and "undo" it to recover the desired error-free state. Condition (40), even if more restrictive than (38), is particularly useful because it allows to establish bounds on the resources needed in order to have efficient nondegenerate codes. Let us assume that the initial state of l qubits is encoded in a redundant Hilbert space of n qubits. If we want to encode 2^l input basis states and correct up to t errors we must choose the dimension of the encoding Hilbert space 2^n such that all the necessary orthogonal states can be accomodated. According to Eq. (40), the total number of orthogonal states that we need in order to be able to correct i errors of the three types σ_x, σ_y and σ_z in an n-qubit state is $3^i \begin{pmatrix} n \\ i \end{pmatrix}$ (this is the number of different ways in which the errors can occur). The argument based on counting orthogonal states then leads to the following condition:

$$2^l \sum_{i=0}^{t} 3^i \begin{pmatrix} n \\ i \end{pmatrix} \leq 2^n. \tag{41}$$

Equation (41) is the quantum version of the Hamming bound for classical error-correcting codes [10]; given l and t it provides a lower bound on the dimension of the encoding Hilbert space for nondegenerate codes. Let us mention that an explicit construction for quantum codes for some values (l, n, t) which saturate the quantum Hamming bound has been provided [11]. It is interesting that this bound has not been beaten so far by degenerate codes[‡].

[‡]In fact, during the "Workshop in Quantum Computation" in Torino in summer 1996 the authors offered a good bottle of Barolo wine to the first person who can construct quantum error correction codes which encode l qubits into n qubits, correct perfectly up to t errors, and which violate the quantum Hamming bound (41).

The quantum version of the classical Gilbert–Varshamov bound [10] can be also obtained, which gives an upper bound on the dimension of the encoding Hilbert space for optimal non degenerate codes

$$2^l \sum_{i=0}^{2t} 3^i \begin{pmatrix} n \\ i \end{pmatrix} \geq 2^n. \tag{42}$$

This expression can be proved from the observation that in the 2^n dimensional Hilbert space with a maximum number of encoded basis vectors (or code-vectors) $|C^k\rangle$ any vector which is orthogonal to $|C^k\rangle$ (for any k) can be reached by applying up to $2t$ error operations of σ_x, σ_y, and σ_z type to any of the 2^l encoded basis vectors. Clearly all vectors which cannot be reached in the $2t$ operations can be added to the encoded basis states $|C^k\rangle$ as all the vectors into which they can be transformed by applying up to t amplitude and/or phase transformations are orthogonal to all the others. This situation cannot happen because we have assumed that the number of code-vectors is maximal. Thus the number of orthogonal vectors that can be obtained by performing up to $2t$ transformations on the code-vectors must be at least equal to the dimension of the encoding Hilbert space.

It follows from Eq. (41) that a one-bit quantum error correcting code to protect a single qubit ($l = 1$, $t = 1$) requires at least 5 encoding qubits and, according to Eq. (42), this can be achieved with less than 10 qubits. Indeed, Shor's nine qubit code can be simplified to the seven qubit code [12], and ultimately to the quantum Hamming bound [8, 13]. We will consider explicitly one form of the five qubit code in Sec. 6.

The asymptotic form of the quantum Hamming bound (41) in the limit of large n is given by

$$\frac{l}{n} \leq 1 - \frac{t}{n} \log_2 3 - H\left(\frac{t}{n}\right), \tag{43}$$

where H is the entropy function $H(x) = -x \log_2 x - (1-x)\log_2(1-x)$. The corresponding asymptotic form for the quantum Gilbert–Varshamov bound (42) is

$$\frac{l}{n} \geq 1 - \frac{2t}{n} \log_2 3 - H\left(\frac{2t}{n}\right). \tag{44}$$

As we can see from Eq. (43), in quantum error correction there is an upper bound on the error rate t/n which a code can tolerate. In fact, differently from the classical case, where any arbitrary error rate can be corrected by a suitable code, in the quantum world the ratio t/n cannot be larger than 0.18929 for nondegenerate codes.

5. System–environment dynamics

In order to provide a tangible illustration of some abstract ideas discussed in the text we have picked up the most popular quantum-optical model of dissipation commonly used to describe spontaneous emission. A two-level atom, with two energy eigenstates $|0\rangle$ and $|1\rangle$ separated by $\hbar\omega_0$, interacting with an environment modelled as a set of quantised harmonic oscillators, e.g. a set of quantised modes of radiation with frequencies ω_m. The Hamiltonian of the combined system

$H = H_0 + V$ includes both the free evolution of the qubit and the environment. The free evolution Hamiltonian is given by

$$H_0 = \hbar\omega_0|1\rangle\langle 1| + \sum_m \hbar\omega_m a_m^\dagger a_m, \tag{45}$$

where a_m and $a_m^\dagger$ represent the annihilation and creation operators of the radiation mode of frequency ω_m. The interaction (in the rotating wave approximation) is described by

$$V = \sum_m \lambda_m|0\rangle\langle 1|a_m^\dagger + \lambda_m^*|1\rangle\langle 0|a_m, \tag{46}$$

where λ_m is the coupling constant between the qubit and the mode of frequency ω_m.

In order to find the time evolution of the relative states of the environment $|R_i(t)\rangle$ we need some knowledge about the qubit–environment interaction. Let us then have a closer look at a dissipative dynamics in our model of a qubit coupled to a continuum of field modes or harmonic oscillators. If all the oscillators in the environment are in their ground states and the qubit is initially prepared in state $|\Psi\rangle = \alpha|0\rangle + \beta|1\rangle$ then the dynamics described by the Hamiltonian $H = H_0 + V$ does not affect state $|0\rangle$. It is state $|1\rangle$ which undergoes a decay. Let us then consider a case when the initial state of the combined system (qubit+environment) is

$$|\phi_i\rangle = |1\rangle(|0\rangle_1|0_2\rangle \ldots |0\rangle_f \ldots |0\rangle_{\max}), \tag{47}$$

meaning the qubit is in state $|1\rangle$ and all the harmonic oscillators in their ground states $|0\rangle$ (we will denote the state where all harmonic oscillators are in the ground state as the vacuum $|\mathbf{0}\rangle$). Possible final states of the combined system are

$$|\phi_f\rangle = |0\rangle(|0\rangle_1|0\rangle_2 \ldots |1\rangle_f \ldots |0\rangle_{\max}), \tag{48}$$

where the qubit decayed to state $|0\rangle$ and one of the harmonic oscillators got excited. Let us note that

$$H_0|\phi_i\rangle = \hbar\omega_0|\phi_i\rangle,\ H_0|\phi_f\rangle = \hbar\omega_f|\phi_f\rangle,\ \langle\phi_f|H_0|\phi_i\rangle = 0,\ \langle\phi_f|V|\phi_i\rangle = \lambda_f. \tag{49}$$

Let us write $|\phi(t)\rangle$ as

$$|\phi(t)\rangle = c_i(t)\mathrm{e}^{-\mathrm{i}\omega_0 t}|\phi_i\rangle + \sum_f c_f(t)\mathrm{e}^{-\mathrm{i}\omega_f t}|\phi_f\rangle \tag{50}$$

which, using our notation from the previous section, implies $|R_{00}\rangle = |\mathbf{0}\rangle$, $|R_{01}\rangle = 0$, $|R_{10}(t)\rangle = \sum_f c_f(t)\mathrm{e}^{-\mathrm{i}\omega_f t}|1_f\rangle$ and $|R_{11}(t)\rangle = c_i(t)\mathrm{e}^{-\mathrm{i}\omega_0 t}|\mathbf{0}\rangle$.

In order to find the relevant time dependence we have to solve the Schrödinger equation

$$\mathrm{i}\hbar\dot{c}_i(t) = \sum_f \lambda_f^*\mathrm{e}^{-\mathrm{i}(\omega_f-\omega_0)t}c_f(t), \tag{51}$$

$$\mathrm{i}\hbar\dot{c}_f(t) = \lambda_f\mathrm{e}^{\mathrm{i}(\omega_f-\omega_0)t}c_i(t). \tag{52}$$

The second equation can be solved formally for $c_f(t)$

$$c_f(t) = -\frac{\mathrm{i}}{\hbar}\int_0^t \mathrm{d}t'\lambda_f\mathrm{e}^{\mathrm{i}(\omega_f-\omega_0)t'}c_i(t') \tag{53}$$

and after substituting this expression for $c_f(t)$ in Eq. (51) we obtain

$$\dot{c}_i(t) = -\int_0^t \mathrm{d}t' K(t-t') c_i(t'), \qquad K(\tau) = \frac{1}{\hbar^2}\sum_f |\lambda_f|^2 \mathrm{e}^{-\mathrm{i}(\omega_f-\omega_0)\tau}. \tag{54}$$

It is the function $\lambda_f = \lambda(\omega_f)$ which determines the character of the evolution.

• Parabolic decay

At short times, the exponential in $\mathrm{e}^{-\mathrm{i}(\omega_f-\omega_0)(t-t')}$ in $K(t-t')$ can be replaced by 1. This is justified when $t \ll 1/\Delta$, where Δ is a typical width of the $\lambda(\omega_f)$ curve. Usually, for a bell-shaped $\lambda(\omega_f)$ curve the order of Δ is pretty well approximated by ω_0. For example if we analyse spontaneous emission in the optical domain then $\omega_0 = \Delta = 10^{15}$ Hz thus the short time means here much less than 10^{-15} s. The integration in Eq. (53) together with the initial condition $c_i(t=0) = 1$ gives

$$|c_i(t)|^2 = |\langle\phi_i|\phi(t)\rangle|^2 = 1 - 2\frac{t^2}{\hbar^2}\sum_f \lambda_f^2. \tag{55}$$

The same result can be obtained directly by writing

$$|\phi(t)\rangle = \mathrm{e}^{-\mathrm{i}Ht/\hbar}|\phi_i\rangle = \left(1 - \frac{\mathrm{i}}{\hbar}Ht - \frac{1}{\hbar^2}H^2t^2 + \ldots\right)|\phi_i\rangle \tag{56}$$

which, together with Eq. (49) gives

$$|\langle\phi_i|\phi(t)\rangle|^2 = 1 - 2\frac{t^2}{\hbar^2}(\langle H^2\rangle - \langle H\rangle^2)\ldots = 1 - 2\frac{t^2}{\hbar^2}\sum_f \lambda_f^2 + \ldots \tag{57}$$

Thus for short times the decay is always parabolic. Let us mention in passing that from a purely mathematical point of view we have assumed here that expression $(\langle H^2\rangle - \langle H\rangle^2) = \sum_f \lambda_f^2$, i.e. the variance of the energy in the initial state $|\phi_i\rangle$ is finite. Needless to say in reality it is always finite but there are mathematical models in which, due to various approximations, this may not be the case (e.g. the Lorentzian distribution which has no finite moments).

• Exponential decay

Expression $|\lambda_f|^2\mathrm{e}^{-\mathrm{i}(\omega-\omega_0)\tau}$ viewed as a function of $\omega_f - \omega_0$ oscillates with frequency $1/\tau$ whereas $\lambda_f = \lambda(\omega_f)$ varies smoothly in the frequency domain. Again taking Δ as the typical width of the $\lambda(\omega_f)$ curve for $\tau \gg 1/\Delta$ the sum in $K(\tau)$ averages out to zero. This allows to substitute $c_i(t)$ for $c_i(t')$ in Eq. (51) which gives

$$\dot{c}_i(t) \approx -c_i(t)\int_0^t \mathrm{d}\tau K(\tau) \approx -c_i(t)\int_0^\infty \mathrm{d}\tau K(\tau). \tag{58}$$

Now we can calculate $\int_0^\infty \mathrm{d}\tau K(\tau)$ using the identity

$$\int_0^\infty \mathrm{d}\tau \mathrm{e}^{\mathrm{i}\omega\tau} = \lim_{\epsilon\to 0+}\int_0^\infty \mathrm{d}\tau \mathrm{e}^{\mathrm{i}(\omega+\mathrm{i}\epsilon)\tau} = \lim_{\epsilon\to 0+}\frac{\mathrm{i}}{\omega+\mathrm{i}\epsilon} = \mathrm{i}\mathrm{P}\frac{1}{\omega} + \pi\delta(\omega). \tag{59}$$

It gives

$$\int_0^\infty \mathrm{d}\tau K(\tau) = \frac{\gamma}{2} + \mathrm{i}\delta, \quad \frac{\gamma}{2} = \frac{\pi}{\hbar^2}|\lambda(\omega_f=\omega_0)|^2, \quad \delta = \mathrm{P}\sum_f \frac{|\lambda_f|^2}{\omega_0-\omega_f}. \tag{60}$$

Incorporating the energy shift $\hbar\delta$ into the modified energy separation $\hbar(\omega_0+\delta)$ we finally obtain

$$\dot{c}_i(t) = -\frac{\gamma}{2}c_i(t) \qquad \text{that is} \qquad c_i(t) = \mathrm{e}^{-\gamma t/2} \tag{61}$$

and consequently

$$c_f(t) = \frac{\lambda_f}{\hbar} \frac{1 - e^{i(\omega_f - \omega_0' + i\gamma/2)t}}{\omega_f - \omega_0' + i\gamma/2}. \tag{62}$$

Let us now go back to the language introduced in Sec. 1. The states of the environment $|R_0(t)\rangle$, $|R_1(t)\rangle$, $|R_2(t)\rangle$ and $|R_3(t)\rangle$ in the present context take the explicit form

$$|R_0(t)\rangle = \frac{1}{2}\left[1 + c_i(t)e^{-i\omega_0 t}\right]|0\rangle, \tag{63}$$

$$|R_1(t)\rangle = \frac{1}{2}\sum_f c_f(t)e^{-i\omega_f t}|1\rangle_f, \tag{64}$$

$$|R_2(t)\rangle = -\frac{1}{2}\sum_f c_f(t)e^{-i\omega_f t}|1\rangle_f, \tag{65}$$

$$|R_3(t)\rangle = \frac{1}{2}\left[1 - c_i(t)e^{-i\omega_0 t}\right]|0\rangle. \tag{66}$$

By formula (7), the fidelity of this process is given by

$$F(t) = \langle R_0(t)|R_0(t)\rangle + \langle R_3(t)|R_3(t)\rangle - 2\mathrm{Re}\langle R_0(t)|R_3(t)\rangle$$

$$= |c_i(t)|^2. \tag{67}$$

Therefore, the fidelity in the case of a parabolic decay takes the form

$$F_{\mathrm{par}}(t) = 1 - 2\frac{t^2}{\hbar^2}\sum_f \lambda_f^2, \tag{68}$$

while in the case of an exponential decay it has the exponential form

$$F_{\mathrm{exp}}(t) = e^{-\gamma t}. \tag{69}$$

6. Benefits of quantum error correction

In order to get an idea about the efficiency of quantum error correction, we will now discuss an explicit construction of the single error-correcting five qubit code. The initial state of the qubit $\alpha|0\rangle + \beta|1\rangle$ is encoded in state $\alpha|C_0\rangle + \beta|C_1\rangle$, where [13]

$$|C_0\rangle = |00010\rangle + |00101\rangle - |01011\rangle + |01100\rangle + |10001\rangle$$

$$-|10110\rangle - |11000\rangle - |11111\rangle, \tag{70}$$

$$|C_1\rangle = |00000\rangle - |00111\rangle + |01001\rangle + |01110\rangle + |10011\rangle$$

$$-|10100\rangle + |11010\rangle - |11101\rangle. \tag{71}$$

(To see the benefits of quantum error correction we do not need to use the explicit form of the code, we wrote it down here for those curious readers who may want to play with quantum error correcting codes.) These encoded states are chosen in such a way that conditions (40) are satisfied. Since this code can correct any type of error

affecting one qubit, it is suitable for protecting quantum states against spontaneous emission. We notice that the spontaneous emission process described in Sec. 5, unlike decoherence, involves both phase and amplitude errors and therefore it cannot be successfully defeated with less than five bit codes.

The probability that the state undergoes exponential decay in the presence of spontaneous emission is approximately given by

$$P_{\rm dec}(t) = 1 - F_{\rm exp}(t) = 1 - {\rm e}^{-\gamma t}. \tag{72}$$

If we assume that the five qubits decay independently from each other, the probability that none of them decays is given by

$$P_{\rm no\ dec}(t) = {\rm e}^{-5\gamma t}, \tag{73}$$

while the probability that only one of them decays is

$$P_{1\ \rm dec}(t) = {\rm e}^{-4\gamma t}(1 - {\rm e}^{-\gamma t}). \tag{74}$$

Since by construction the above error correction scheme corrects perfectly the encoded state when only one of the qubits is affected, the fidelity of reconstruction of the state after the error correction is at least as high as the probability of having at most one qubit decay during the process, that is

$$F_{\rm ec}(t) \geq P_{\rm no\ dec}(t) + 5P_{1\ \rm dec}(t) == {\rm e}^{-4\gamma t}(5 - 4{\rm e}^{-\gamma t}). \tag{75}$$

In order to have a successful error correction the such fidelity must be greater than the fidelity $F_{\rm exp}(t)$ corresponding to a single qubit in the absence of error correction. This is true when the decay probability $P_{\rm dec}(t)$ is much smaller than one, namely when the correction procedure is applied at times $t \ll 1/\gamma$. Actually, for $t \ll 1/\gamma$ the fidelity of reconstruction after error correction is bounded by

$$F_{\rm ec}(t) \geq 1 - 10\gamma^2 t^2 + {\rm O}(t^3), \tag{76}$$

namely it has parabolic form, while the single qubit decay probability is

$$P_{\rm dec}(t) \approx 1 - \gamma t. \tag{77}$$

7. Concluding remarks

Research in quantum error correction in its all possible variations has become vigorously active and any comprehensive review of the field must be obsolete as soon as it is written. Here we have decided to provide only some very basic knowledge, hoping that this will serve as a good starting point to enter the field. The reader should be warned that we have barely scratched the surface of the current activities in quantum error correction neglecting topics such as group theoretical ways of constructing good quantum codes [14], concatenated codes [15], quantum fault tolerant computation [16] and many others. Many interesting papers in these and many related areas can be found at the Los Alamos National Laboratory e-print archive (http:/xxx.lanl.gov/archive/quant-ph).

This work was supported in part by the European TMR Research Network ERP-4061PL95-1412, the TMR Marie Curie Fellowship Programme, Hewlett–Packard, The Royal Society London and Elsag-Bailey, a Finmeccanica Company.

References

[1] D. Deutsch, talk presented at the Rank Prize Funds Mini-Symposium on Quantum Communication and Cryptography, Broadway, England 1993; A. Berthiaume, D. Deutsch, R. Jozsa, in: *Proc. Workshop on Physics and Computation — PhysComp94*, IEEE Computer Society Press, Dallas, Texas, 1994.

[2] A. Barenco, A. Berthiaume, D. Deutsch, A. Ekert, R. Jozsa, C. Macchiavello, *SIAM J. Comput.* **26**, in press.

[3] C.H. Bennett, G. Brassard, S. Popescu, B. Schumacher, J.A. Smolin, W.K. Wootters, *Phys. Rev. Lett.* **76**, 722 (1996).

[4] D. Deutsch, A. Ekert, R. Jozsa, C. Macchiavello, S. Popescu, A. Sanpera, *Phys. Rev. Lett.* **77**, 2818 (1996).

[5] P. Shor, *Phys. Rev. A* **52**, R2493 (1995).

[6] G.M. Palma, K.-A. Suominen, A. Ekert, *Proc. R. Soc. Lond. A* **452**, 567 (1996).

[7] W.H. Zurek, *Phys. Today*, Vol. 44, October, p. 36 (1991).

[8] C.H. Bennett, D.P. DiVincenzo, J.A. Smolin, W.K. Wootters, *Phys. Rev. A* **54**, 3824 (1996).

[9] A. Ekert, C. Macchiavello, *Phys. Rev. Lett.* **77**, 2585 (1996).

[10] F.J. MacWilliams, N.J.A. Sloane, *The Theory of Error Correcting Codes*, North-Holland, Amsterdam 1977.

[11] D. Gottesman, *Phys. Rev. A* **54**, 1862 (1996).

[12] A. Steane, *Phys. Rev. Lett.* **77**, 793 (1996); A. Steane, *Proc. R. Soc. Lond. A* **452**, 2551 (1996).

[13] R. Laflamme, C. Miquel, J.P. Paz, W.H. Zurek, *Phys. Rev. Lett.* **77**, 198 (1996).

[14] A.R. Calderbank, E.M. Rains, P.W. Shor, N.J.A. Sloane, *Phys. Rev. Lett.* **78**, 405 (1997).

[15] E. Knill, R. Laflamme, e-print quant-ph/9608012.

[16] P.W. Shor, e-print quant-ph/9605011; D.P. DiVincenzo, P.W. Shor, *Phys. Rev. Lett.* **77**, 3260 (1996).

Proceedings of the International Conference "Quantum Optics IV", Jaszowiec, Poland, 1997

THE INITIAL-VALUE PROBLEM IN THE QUASI-CLASSICAL THEORY OF STRONG-FIELD PHOTOIONIZATION OF RYDBERG ATOMS

O.V. TIKHONOVA

Institute of Nuclear Physics, Moscow State University
119899, Moscow, Russia

AND M.V. FEDOROV

General Physics Institute, Russian Academy of Sciences
38 Vavilov St., 117942 Moscow, Russia

Photoionization of Rydberg atoms is considered in the quasi-classical (WKB) approach. The total nonlinear strong-field ionization rate is found and investigated. The time of ionization, as a function of a growing field--strength amplitude, is shown to approach asymptotically the Kepler period t_K. Interference stabilization of Rydberg atoms is confirmed to exist in the case of short pulses (shorter than the Kepler period).

PACS numbers: 32.80.Fb, 32.80.Rm

1. Introduction

Interference stabilization (IS) of Rydberg atoms is known [1, 2] to arise due to Rydberg-continuum Λ-type field-induced transitions between neighboring Rydberg levels. In such a case, the time of ionization $t_i(\varepsilon_0)$ of a Rydberg atom in its dependence on the light field strength amplitude ε_0 was predicted [1, 2] to have the "death-valley" form, i.e., the form of a curve with the minimum at some critical field ε_c. The quasi-classical (WKB) estimate of ε_c and $t_{\min} = t_i(\varepsilon_c)$ are very simple: $\varepsilon_c \sim \omega^{5/3}$, where ω is the frequency of light (in atomic units) and $t_{\min} \approx t_K = 2\pi n^3$, where n is the principal quantum number of the originally populated Rydberg level and t_K is the classical Kepler period.

The results of the first works on IS were generalized later [3, 4] to take into account a possibility of excitation of Rydberg levels with higher values of the electron angular momentum ℓ via the Λ-type Raman transitions. The main result of such a generalization is the prediction that the "death-valley" behavior of the function $t_i(\varepsilon_0)$ can be replaced by the "death-plateau" behavior which means that at $\varepsilon_0 < \varepsilon_c$ the function $t_i(\varepsilon_0)$ falls, then at $\varepsilon_0 \sim \varepsilon_c$ achieves the level $\sim t_K$, and

remains at this level more or less constant at a rather large interval of ε_0 (such that $\varepsilon_0 \geq \varepsilon_c$).

All the above-mentioned theories of IS [1–4] were based on a series of approximations [such as the rotating wave approximation (RWA) and the "pole" approximation (PA)] validity of which is sometimes far from being evident. An alternative approach to the theory of strong-field photoionization of Rydberg atoms, free from these approximations, can be based on an attempt to apply the quasi-classical approach directly to the Schrödinger equation for a Rydberg electron in a light field [5, 6]. In the framework of such an approach, in Ref. [5] the complex quasienergies of the system were found. However, the consideration of Ref. [5] failed to describe in a satisfactory way time evolution of the ionization probability as well as many other important characteristics of the strong-field photoionization process. For this reason, one of the conclusions of Ref. [5] consisted of the suggestion to consider in future, in the framework of the same general quasi-classical approach as in Ref. [5], the initial-value rather than the eigenvalue problem. The first attempt to realize such a program was made in our recent paper [6]. In this talk we report about our newest findings in this direction.

2. Strong-field quasi-classical solutions of the Schrödinger equation

The main idea of the quasi-classical approach [5–7] can be formulated as an assumption that the field-induced Rydberg-continuum transitions occur mainly in the region of electron–nucleus distances r of the order of the so-called quasi-classical length r_q, where [7]

$$r_q = \omega^{-2/3}. \tag{1}$$

Though, typically, much larger than one ($r_q \gg 1$ at $\omega \ll 1$), the quasi-classical length is usually much shorter than the size of the Rydberg orbit $r_{max} = 2n^2$, $r_q \ll r_{max}$. Under these conditions, the centrifugal energy in the Schrödinger energy, estimated at $r \sim r_q$, appears to be much smaller than the Coulomb potential energy $1/r$, if only average angular momentum is smaller than $\omega^{-1/3} \gg 1$ [7, 8]. This observation gives rise to the approximation of slow angular motion [5, 6], under which the centrifugal energy is dropped at all from the atomic Hamiltonian. As the result, the original three-dimensional Schrödinger equation can be reduced to the one-dimensional radial equation

$$\mathrm{i}\frac{\partial\chi(r,t;\theta)}{\partial t} = \left[-\frac{1}{2}\frac{\partial^2}{\partial r^2} - \frac{1}{r} + \cos(\theta)\varepsilon_0(t) r \sin(\omega t)\right]\chi(r,t;\theta), \tag{2}$$

where $\chi = rR$ and R is the radial wave function of an electron; in a light field, both χ and R depend parametrically on the angle θ between the field-strength vector ε_0 and the electron position vector; $\varepsilon_0(t)$ is a slow field-strength amplitude describing how a light pulse is switched on and off. Following to the ideas of Refs. [5, 6], let us solve first the Schrödinger equation (2) at a frozen angle θ (θ = const) and, then, average the results over θ. At the first stage, to simplify notations, let us drop $\cos\theta$ in Eq. (1) and further formulas keeping in mind that in the final results $\cos\theta$ has to reappear in front of $\varepsilon_0(t)$.

Our goal consists of solving the initial-value problem, i.e., of finding non-perturbative solution of Eq. (2) $\chi(r,t)$ obeying the initial condition

$$\chi(r,t)|_{t\to-\infty} = \chi_n^{(0)}(r,t) \equiv \sqrt{\frac{2}{\pi n^3 p_n(r)}} \sin\left\{\int_0^r p_n(r')\mathrm{d}r'\right\} \exp\{-\mathrm{i}E_n t\}, \quad (3)$$

where $\chi_n^{(0)}(r,t)$, $E_n = -1/2n^2$, and $p_n(r)$ are the wave function, energy and quasi-classical momentum of the initially populated field-free Rydberg state,

$$p_n(r) = \sqrt{2\left(E_n + \frac{1}{r}\right)}. \quad (4)$$

By using the Euler formula for the sine on the right hand side of Eq. (3), let us present both $\chi_n^{(0)}(r,t)$ and $\chi(r,t)$ in the form of sums of diverging and converging waves, $\chi_{n,\pm}^{(0)}(r,t)$ and $\chi_\pm(r,t)$, respectively. The initial conditions for $\chi_\pm(r,t)$ have the form

$$\chi_\pm(r,t)|_{t\to-\infty} = \frac{\mp\mathrm{i}}{\sqrt{2\pi n^3 p_n(r)}} \exp\left\{\pm\mathrm{i}\int_0^r p_n(r')\mathrm{d}r' - \mathrm{i}E_n t\right\}. \quad (5)$$

Let us search for the solutions of the Schrödinger equation in the form

$$\chi_\pm(r,t) = \frac{\mp\mathrm{i}}{\sqrt{2\pi n^3 p_n(r)}} \exp\left\{\pm\mathrm{i}\int_0^r p_n(r')\mathrm{d}r' - \mathrm{i}E_n t - \mathrm{i}\sigma_\pm(r,t)\right\} \quad (6)$$

with the new unknown functions $\sigma_\pm(r,t)$ obeying the zero initial conditions

$$\sigma_\pm(r,t)|_{t\to-\infty} = 0. \quad (7)$$

In accordance with the above-discussed role of relatively small electron–nucleus distances $r \sim r_q \ll r_{max}$, we can expand the quasi-classical momentum $p_n(r)$ (4) in powers of $r|E_n| = r/r_{max} \ll 1$:

$$p_n(r) \approx \sqrt{\frac{2}{r}} + E_n\sqrt{\frac{r}{2}}. \quad (8)$$

Under this approximation and with $\chi_\pm(r,t)$ (6) substituted into Eq. (2), by dropping the second-order derivative of $\sigma_\pm(r,t)$ over r, let us reduce the arising equation for $\sigma_\pm(r,t)$ to the following simplest form:

$$\frac{\partial\sigma_\pm(r,t)}{\partial t} \pm \sqrt{\frac{2}{r}}\frac{\partial\sigma_\pm(r,t)}{\partial r} = \varepsilon_0(t) r \sin(\omega t). \quad (9)$$

The solution of this equation is easily found to be given by

$$\begin{aligned}\sigma_\pm(r,t) &= \int_{-\infty}^{t} \mathrm{d}t'\varepsilon_0(t')\sin(\omega t')r_{cl}[\pm t' \mp t + \tau(r)] \\ &\equiv \int_0^\infty \mathrm{d}t''\varepsilon_0(t-t'')\sin[\omega(t-t'')]r_{cl}[t'' \mp \tau(r)], \end{aligned} \quad (10)$$

where $t'' = t - t'$ and $\tau(r)$ is the time of motion from 0 to r of a classical particle with zero total energy in the Coulomb field

$$\tau(r) = \int_0^r \frac{\mathrm{d}r'}{p_n(r')} \approx \frac{\sqrt{2}}{3} r^{3/2}; \quad (11)$$

$r_{\rm cl}(t)$ is the corresponding classical trajectory, or the solution of the Newton equation, or the solution of the equation $\tau(r_{\rm cl}) = t$:

$$r_{\rm cl}(t) \approx \frac{3^{2/3}}{2^{1/3}} t^{2/3} \tag{12}$$

and $r_{\rm cl}(-t) = r_{\rm cl}(t)$.

By substituting $\sigma_{\pm}(r,t)$ (10) into Eq. (6), we find the searched for solution of the Schrödinger equation (2) obeying the appropriate initial conditions (5) and (7). In its dependence on t, the functions $\exp[-{\rm i}\sigma(r,t)]$ contain a periodical part [via $\sin[\omega(t-t'')]$ in the last expression on the right hand side of Eq. (10)]. By expanding these periodical functions in the Fourier series, we get

$$\chi(r,t) = \sum_k \chi_k(r,t) \equiv \sum_k \left[\chi_k^+(r,t) + \chi_k^-(r,t)\right], \tag{13}$$

where $k = 0, \pm 1, \pm 2, \ldots$ and the functions $\chi_k^{\pm}(r,t)$ are given by

$$\chi_k^{\pm}(r,t) = \frac{\mp {\rm i} r^{1/4}}{2^{3/4}\sqrt{\pi n^2}} J_k[\zeta_{\pm}(r,t)]$$

$$\times \exp\left\{\pm {\rm i}[2^{3/2}\sqrt{r} + E_n \tau(r)] - {\rm i}(E_n + k\omega)t - {\rm i}k\phi_{\pm}\right\}. \tag{14}$$

Here J_k are the Bessel functions, $\phi_{\pm}$ are some phases, and $\zeta_{\pm}(r,t)$ are the functions very similar to $\sigma_{\pm}(r,t)$ (10):

$$\zeta_{\pm}(r,t) = \left| \int_0^{\infty} {\rm d}t'' \varepsilon_0(t-t'') \exp({\rm i}\omega t'') r_{\rm cl}[t'' \mp \tau(r)] \right|$$

$$\equiv \left| \int_{-\infty}^{t} {\rm d}t' \varepsilon_0(t') \exp(-{\rm i}\omega t') r_{\rm cl}[t - t' \mp \tau(r)] \right|. \tag{15}$$

In a general form, Eqs. (13)–(15) solve the problem formulated in the beginning of this section: they determine the solution of the Schrödinger equation obeying the initial condition (3).

3. Above-threshold and total ionization

The quickest variations of the functions $\chi_k^{\pm}(r,t)$ (13) in time t are determined by the factors $\exp[-{\rm i}(E_n + k\omega)t]$. For this reason, the functions $\chi_k(r,t)$ can be interpreted as the wave functions of the above-threshold wave packets with mean energies equal to $E_n + k\omega$. The t- and r-dependent electron density in the k-th above-threshold wave packet is given by

$$\rho_k(r,t) = |\chi_k(r,t)|^2 = |\chi_k^+(r,t) + \chi_k^-(r,t)|^2. \tag{16}$$

The total probability of ionization to the time t can be determined as

$$w_i(t) = \sum_{k=1}^{\infty} \int_0^{\infty} {\rm d}r \rho_k(r,t) = \sum_{k=1}^{\infty} \int_0^{\infty} {\rm d}r |\chi_k^+(r,t) + \chi_k^-(r,t)|^2. \tag{17}$$

Let us discuss now the r-dependence of the functions $\chi_k^{\pm}(r,t)$ (14). The quickest part of this dependence is determined by the factor $\exp(\pm {\rm i}2^{3/2}\sqrt{r})$. This dependence disappears in the squared absolute values of the functions $\chi_k^{\pm}(r,t)$. But

in their cross-product, $2\mathrm{Re}\{[\chi_k^+(r,t)]^*\chi_k^-(r,t)\} \propto \cos(2^{5/2}\sqrt{r})$, this dependence gives rise to very fast oscillations with a period of the order of one in atomic units. Being averaged over these fast oscillations, Eq. (17) gives

$$w_i(t) = \sum_{k=1}^{\infty} \int_0^{\infty} \mathrm{d}r \left(|\chi_k^+(r,t)|^2 + |\chi_k^-(r,t)|^2\right)$$

$$= \int_0^{\infty} \frac{\mathrm{d}r\sqrt{r}}{4\sqrt{2}\pi n^3} \left\{2 - J_0^2[\zeta_+(r,t)] - J_0^2[\zeta_-(r,t)]\right\}. \tag{18}$$

Let us discuss now the structure of the functions $\zeta_\pm(r,t)$ (15) determining the arguments of the Bessel functions in Eqs. (14) and (18). In accordance with the definition (15), these functions are given by the integrals of products of the fast oscillating $[\exp(-\mathrm{i}\omega t')]$ and slow $(\varepsilon_0(t')r_{\mathrm{cl}}[t - t' \mp \tau(r)])$ functions. Such integrals are known to be determined mainly by the ends of the integration regions, if only the slow part of the integrand is everywhere smooth. An important part of these slow function is the function $r_{\mathrm{cl}}[t - t' \mp \tau(r)]$ in which $t' \leq t$ and $\tau(r) \geq 0$. For the lower sign the argument of r_{cl} is always positive, whereas for the upper sign it changes sign at $t' = t - \tau(r)$. In terms of the corresponding classical trajectories this means that in the first case the classical particle comes monotonously from infinity to the point r, whereas in the second case (the upper sign in the argument of r_{cl}) it comes from infinity, reaches the origin $r = 0$, experiences reflection, and then returns to the point r (see Fig. 1). In fact it appears that just this reflection from the origin is responsible for irreversible ionization. Mathematically, the reflection of the classical trajectory from the origin means that, in the case of ζ_+, the slow part of the integrand has a cusp at the point $t' = t - \tau(r)$. Hence, in this case

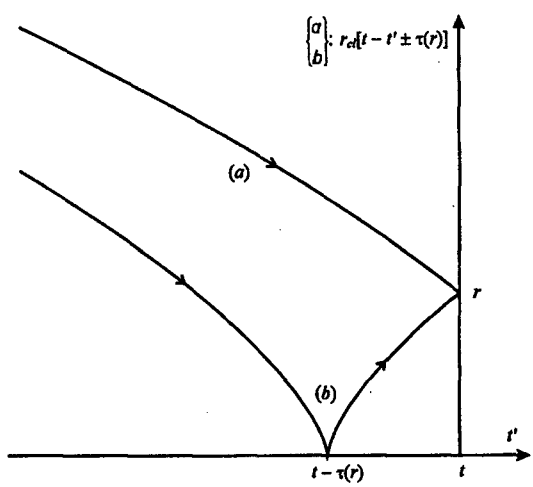

Fig. 1. The classical trajectories $r_{\mathrm{cl}}[t-t'+\tau(r)]$ (a) and $r_{\mathrm{cl}}[t-t'-\tau(r)]$ (b) determining the functions $\zeta_-(r,t)$ and $\zeta_+(r,t)$ (15), respectively. The arrows indicate the direction of motion over the classical trajectories.

the integral over dt' from $-\infty$ to t turns in fact in the sum of two integrals with different integrands, from $-\infty$ to $t-\tau(r)$ and from $t-\tau(r)$ to t. This is the limit $t'=t-\tau(r)$ in both of these two integrals that gives the main contribution to the irreversible ionization. Not dwelling upon any further details of calculations, let us reproduce the result of integration in (15) for the case of large t, $t \gg T$, where T is the pulse duration, i.e., for the case when the light pulse has gone

$$\zeta_+(r,t)=\frac{2^{2/3}3^{1/6}\Gamma(\frac{2}{2})\varepsilon_0[t-\tau(r)]}{\omega^{5/3}}, \qquad \zeta_-(r,t)=0, \tag{19}$$

where $\Gamma(x)$ denotes the gamma-function.

Equation (19) describes the wave packet that moves away from the nucleus. The shape of this packet coincides with that of the pulse envelope. With the help of Eq. (19) the general expression (18) for the probability of ionization per pulse w_i can be further simplified. The substitution of the integration variable r by $\tau(r)$ and, then, by t gives

$$w_\mathrm{i}=\int_{-\infty}^{\infty}\frac{dt}{2t_\mathrm{K}}\left\{1-J_0^2\left[\frac{2^{2/3}3^{1/6}\Gamma\left(\frac{2}{3}\right)\varepsilon_0[t-\tau(r)]}{\omega^{5/3}}\right]\right\}, \tag{20}$$

where $t_\mathrm{K}=2\pi n^3$ is the Kepler period.

Finally, for a square pulse of a duration T Eq. (20) yields

$$w_\mathrm{i}=\Gamma T, \tag{21}$$

where Γ is the nonlinear rate of transitions

$$\Gamma=\frac{1}{2t_\mathrm{K}}\left[1-J_0^2(\zeta)\right], \tag{22}$$

where

$$\zeta=\frac{2^{2/3}3^{1/6}\Gamma\left(\frac{2}{3}\right)\varepsilon_0}{\omega^{5/3}}, \tag{23}$$

and now $\varepsilon_0=\mathrm{const}$. In the weak-field limit ($\varepsilon_0 \ll \omega^{5/3}$), Eq. (22) yields the Fermi-golden-rule rate of ionization

$$\Gamma_\mathrm{FGR}=\frac{3^{1/3}\Gamma\left(\frac{2}{3}\right)\varepsilon_0^2}{2^{5/3}\pi n^3\omega^{10/3}}\left|\langle Y_{l',m}\left|\cos\theta\right|Y_{l,m}\rangle\right|^2, \tag{24}$$

where $Y_{l,m}$ are spherical functions, l and l' denote the electron angular momentum in the initial and final states, m is z-projection of the angular momentum, and the factor $\left|\langle Y_{l',m}\left|\cos\theta\right|Y_{l,m}\rangle\right|^2$ is added to the expression following from Eqs. (22) and (23) to take into account the electron angular motion. In the case of a strong field, $\varepsilon_0 \geq \omega^{5/3}$, the angular motion of a Rydberg electron can hardly be taken into account rigorously in such a simple way. However, in the approximation of a slow angular motion discussed in the beginning of Sec. 2 we can use the procedure of Ref. [5]. In the framework of this procedure, in the expressions (22) and (23) for the strong-field rate of ionization, the field strength amplitude ε_0 has to be substituted by $\varepsilon_0\cos\theta$ and the result has to be averaged over $x\equiv\cos\theta$ to give

$$\overline{\Gamma}=\frac{1}{2t_\mathrm{K}}\left[1-\int_0^1 dx J_0^2(\zeta x)\right]. \tag{25}$$

The characteristic time of ionization can be determined as the inverse double rate of ionization

$$t_i = 1/2\Gamma \qquad \text{and} \qquad \bar{t}_i = 1/2\overline{\Gamma} \tag{26}$$

for the case $\theta = 0$ and for the rate $\overline{\Gamma}$ (25) averaged over θ, respectively.

3. Discussion

The dependence of the ionization rates and time of ionization on the field--strength parameter ζ (23) is shown in Figs. 2 and 3 for the two above-discussed cases: for $\theta = 0$ (Fig. 2) and for $\overline{\Gamma}$ (25) averaged over θ (Fig. 3), the rates of ionization and the time of ionization are measured in units of the inverse double Kepler period and Kepler period, respectively. The pictures of Fig. 2 show that for a given θ, both the rate and time of ionization are oscillating functions of the field-strength amplitude ε_0. This result agrees with and specifies the qualitative prediction of Ref. [5]. By comparing the results of the present theory with those of Refs. [1–4], we can make an assumption that, possibly, the oscillating dependencies $t_i(\varepsilon_0)$ and $\Gamma(\varepsilon_0)$ arise when and because one does not use the rotating-wave and pole approximations inherently present in the earlier theories [1–4]. The minima of the oscillating curve $t_i(\zeta)$ and the maxima of the curve $\Gamma(\zeta)$ correspond to the

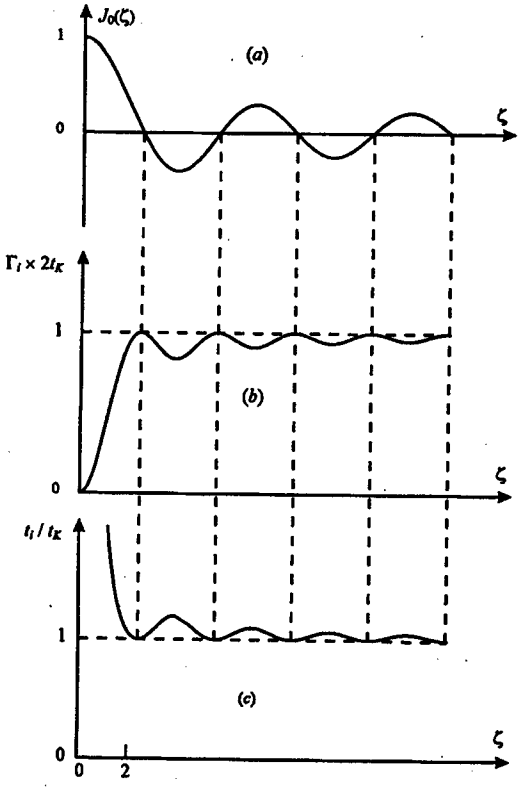

Fig. 2. The zero-order Bessel function (a), the rate of ionization Γ (b), and the time of ionization t_i (c) vs. the field-strength parameter ζ (23).

positions of zeros of the zero-order Bessel function $J_0(\zeta)$ shown for comparison in Fig. 2a. The minimal time of ionization achieved at these points is equal to one Kepler period t_K and the corresponding maximal rate of ionization is equal to $1/(2t_K)$. This means that the strong-field stabilization in Rydberg atoms has to occur if the pulse duration is less or of the order of the Kepler period, in accordance with the main ideas of Refs. [3, 4]. In agreement with Refs. [3, 4], the "death-plateau" rather than the "death-valley" behavior of the curve $t_i(\varepsilon_0)$ is confirmed: in the strong-field limit the function $t_i(\varepsilon_0)$ saturates at the level t_K rather than grows unlimitedly.

The curves of Fig. 3 show that the above-discussed oscillations appear to be smoothed out when the electron angular motion is taken into account, though in the framework of a very rough and approximate procedure of averaging over θ. This result can be interpreted as an indication that the 3D structure of an atom can result in a well pronounced "death-plateau" structure of the dependence $t_i(\varepsilon_0)$: saturation in a strong field at the level t_K without any oscillations or growth. This conclusion agrees with that of Refs. [3, 4] though the methods of analysis in these papers were absolutely different from that of the present one.

At last, it should be mentioned that, in the case of rectangular pulses, the derived probability of ionization per pulse (21) depends linearly on the pulse duration T, though this is not the lowest order perturbation theory and the rate of ioniza-

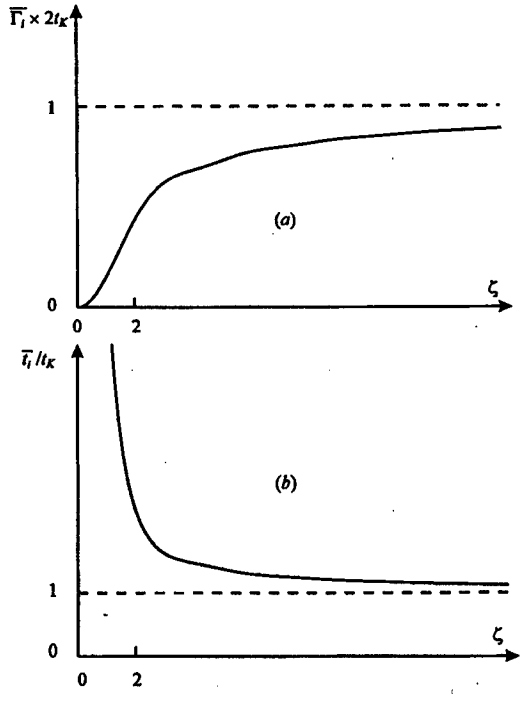

Fig. 3. The rate of ionization averaged over θ, $\overline{\Gamma}_i$ (a) and the corresponding "average" time of ionization $\overline{t}_i = 1/(2\overline{\Gamma}_i)$ (b) vs. ζ (23).

tion Γ (22) is not a linear function of ε_0^2. The linear dependence of the ionization probability $w_{\rm i}$ on the pulse duration T means that the suggested theory cannot describe the regime of depletion of the initially populated Rydberg state. Equation (21) assumes that the results derived are valid only if $\Gamma T < 1$, i.e., only for short pulses. In the strong-field case, when $\Gamma \sim 1/t_{\rm K}$, this limitation yields $t < t_{\rm K}$, i.e., the pulse duration has to be shorter than the Kepler period. These restrictions are explained by the used approximations in which the quasi-classical momentum $p_n(r)$ (4) was expanded in powers of $r|E_n| \ll 1$ (8) and the squared derivative of the functions $\sigma_\pm(r,t)$ was dropped in Eq. (9). Unfortunately, these approximations are crucially important for the found above rather simple solutions of the Schrödinger equation (13)–(15) to be valid. Construction of a theory free from the discussed approximations can be very interesting but also much more complicated than in the case considered here. Another equally important but, probably, equally difficult direction of future investigations has to include attempts to consider more rigorously the electron angular motion. We hope to return to these problems later.

Acknowledgment

The work is supported partly by the Russian Fund of Basic Research (the grants ## 96-02-19286 and 96-02-17649), and by the Civilian Research and Development Fund (USA) jointly with the Russian State Committee on Science and Technologies (the grant # RP1-244).

References

[1] M.V. Fedorov, A.M. Movsesian, *J. Phys. B* **21,** L155 (1988).

[2] M.V. Fedorov, *Laser Phys.* **3,** 219 (1993).

[3] M.V. Fedorov, M.-M. Tegranchi, S.M. Fedorov, *J. Phys. B* **29,** 2907 (1996).

[4] A. Woiczik, R. Parzynski, *Laser Phys.* **7,** 574 (1997).

[5] M.V. Fedorov, *J. Phys. B* **27,** 4145 (1994).

[6] O.V. Tikhonova, M.V. Fedorov, *Laser Phys.* **7,** 574 (1997).

[7] M. Adams, M.V. Fedorov, V.P. Krainov, D.D. Meyerhofer, *Phys. Rev. A* **52,** 125 (1995).

[8] N.B. Delone, S.P. Goreslavsky, V.P. Krainov, *J. Phys. B* **16,** 2369 (1983); **22,** 2941 (1989).

Vol. 93 (1998) *ACTA PHYSICA POLONICA A* No. 1

Proceedings of the International Conference "Quantum Optics IV", Jaszowiec, Poland, 1997

ADIABATIC DYNAMICAL CONTROL PHYSICS OF DIELECTRIC MEDIA

R. GROBE

Intense Laser Physics Theory Unit, Department of Physics
Illinois State University, Normal, IL 61790-4560, USA

We summarize recent developments in the area of the coherent propagation of laser pulses through dielectric media. We will show that the principle of dynamical adiabaticity opens new avenues to control the non-perturbative and resonant interaction between two laser pulses and a three-level medium. Examples include the formation of stable wave forms that can travel through optical dielectric media in a loss-free manner with arbitrary pulse shapes, novel possibilities to store optical information in dielectric media in the form of spatially dependent excitations and techniques to exploit this information to control laser pulse envelopes.

PACS numbers: 42.65.Hw, 42.65.Re

1. Nonlinear optics and adiabatic dynamical control physics

In order to describe the spatial and temporal evolution of electromagnetic radiation pulses in dielectric media, the Maxwell equations have to be solved together with the quantum Liouville or Schrödinger equation. The Maxwell equations determine how the electric field (of the laser pulse) evolves as a function of time and space. Its behavior is controlled by the macroscopic polarization of the dielectric medium, which serves as the "source term" in the Maxwell equations. The macroscopic polarization is proportional to the product of the dipole moment and the number density N of the atoms in the medium. The temporal evolution of the polarization is determined by the Liouville equation of the atoms that are driven by the external field. This itself would not be a major complication for the theoretical analysis. If there was just a single differential equation for the polarization, one could use this equation to eliminate the polarization from the Maxwell equations and one would not need to solve for the entire complicated atomic dynamics.

The key problem is that in general there is not just one single differential equation for the polarization but a coupled set of equations that contain several (auxiliary) quantities, such as the inversion or the population of the electronic states that need to be solved simultaneously. A non-perturbative solution of the combined Maxwell and Schrödinger equations is therefore in most cases analytically inaccessible and even numerically it is a demanding computational task. To master this challenge in a computationally more feasible way, it would be helpful to have a more direct relation between the electric field and the polarization.

As is well known, such a direct relation can be found if the laser field is sufficiently weak and/or its frequency is not near any of the atoms' resonance frequencies. In this case the polarization P can be expanded perturbatively as a standard power series in the electric field amplitude $\mathcal{E}$

$$P(z,t) = \sum a_n \mathcal{E}^n. \tag{1.1}$$

In this domain the medium plays a relatively passive role as the atoms get only very weakly excited. This regime is, of course, the realm of nonlinear optics. The optical properties of the medium are modeled by the expansion coefficients a_n, such as (possibly nonlinear) indices of refraction and higher-order nonlinear susceptibilities. Especially in strongly dissipative atomic systems, the quantum state of the medium can reach quickly its steady state during the duration of the laser pulse and the perturbative expansion above is typically well justified. Using relation (1.1) the polarization as a function of the electric field strength can be inserted back into the Maxwell equations and the problem of solving the atomic equations is elegantly avoided. The resulting set of equations for the electric field can then be solved under various additional approximate assumptions leading, e.g., to nonlinear Schrödinger equations for the field, as shown in many textbooks on linear and nonlinear optics.

The theme of the present work is to describe a different regime in the interaction of laser fields with dielectric media in which another relation between the polarization and the electric field vector can be found. In this regime adiabaticity is the key characteristic to provide this relation. We will describe some recent predictions for this dynamical regime in which the laser field is either relatively strong and/or in resonance with an atomic transition, such that the standard perturbative relation of nonlinear optics between the polarization and the electric field is not valid. We illustrate this regime for the special case of the resonant interaction of a pair of laser pulses with a medium of three-level lambda atoms. This system has recently found some revived interest in the context of electromagnetically-induced transparency [1, 2] and also lasing without inversion [3].

For this system it is possible to find a direct relation between the polarization and the electric fields that leads to a fully analytical theory. We assume here that the two laser frequencies are sufficiently different such that each laser pulse excites only one atomic transition. To keep the formalism as transparent as possible and to focus on the essential elements of this approach, we also neglect all dissipative influences. Subsequent work will be devoted to explore how the basic theory needs to be modified to account for relaxation effects.

Under these simplifying assumptions the temporal response of each lambda-atom to the two laser pulses is given by the well-known Schrödinger equation for the state amplitudes C_i of the three levels

$$\mathrm{i}\frac{\partial}{\partial\tau}C_1(z,\tau) = -\frac{1}{2}\Omega_a^* C_2(z,\tau), \tag{1.2a}$$

$$\mathrm{i}\frac{\partial}{\partial\tau}C_2(z,\tau) = -\frac{1}{2}\Omega_a C_1(z,\tau) - \frac{1}{2}\Omega_b C_3(z,\tau), \tag{1.2b}$$

$$\mathrm{i}\frac{\partial}{\partial\tau}C_3(z,\tau) = -\frac{1}{2}\Omega_b^* C_2(z,\tau), \tag{1.2c}$$

where we have used the rotating wave approximation. With respect to the spatial evolution we have replaced the laboratory time t by a retarded time variable $\tau = t - z/c$. The time and space dependent parameters Ω_a and Ω_b are the Rabi frequencies of the two fields.

One eigenvector of the system of Eqs. (1.2) is the well-known dark or trapped state [4, 5] of the form $(C_1, C_2, C_3) \approx (\Omega_b/\Omega, 0, -\Omega_a/\Omega)$, where $\Omega^2 \equiv \Omega_a^2 + \Omega_b^2$ is the so-called two-photon Rabi frequency. In the following we will assume that this trapped state condition approximates the response of the atoms to the fields sufficiently well. In practice, this can be achieved via an appropriate sequencing of the turn-on times of the two laser pulses [6]. If we insert this eigenvector back into the right hand side of equations (1.2a) and (1.2c) and solve for the amplitude of the upper state $C_2(z,\tau)$, we obtain $C_2 \approx -2\mathrm{i}/\Omega_a^*(\partial/\partial\tau)(\Omega_b/\Omega) = 2\mathrm{i}/\Omega_b^*(\partial/\partial\tau)(\Omega_a/\Omega)$. This approximation leads then to a direct relation between the effective polarizations (for the reduced wave equation of the Rabi frequencies) and the electric field vector (represented by the Rabi frequencies)

$$P_a(z,\tau) = \mathrm{i}\mu_a C_1^* C_2 = -(2\mu/\Omega)\frac{\partial}{\partial\tau}(\Omega_a/\Omega), \tag{1.3a}$$

$$P_b(z,\tau) = \mathrm{i}\mu_b C_3^* C_2 = -(2\mu/\Omega)\frac{\partial}{\partial\tau}(\Omega_b/\Omega). \tag{1.3b}$$

The coupling coefficients $\mu_{a,b}$ are related to the number density of atoms N via $\mu_{a,b} \equiv N d_{a,b}^2 \omega_{a,b}/(\varepsilon_0 \hbar c)$, where the dipole moment matrix elements for the transitions 1–2 and 2–3 are denoted by d_a and d_b, respectively.

These relations are in striking contrast to the perturbative relation (1.1) of nonlinear optics. In this case the polarization increases with decreasing electric field strength (which is proportional to Ω) and a perturbative expansion would not be valid. Another difference lies in the fact that the size of the polarization depends also on the time derivative of the field. Rapidly changing envelopes in Ω_a and Ω_b induce an enhanced polarization. The polarization for the 1–2 transition depends on both fields Ω_a and Ω_b.

Both polarizations vanish completely if the two pulses have identical envelopes and differ only by their amplitudes. In this case the source term Eq. (1.3) for the Maxwell equations is zero and one could conjecture that any two input pulses with matching envelopes evolve in a fully transparent manner with the velocity c. However, the corresponding trapped state for matched pulses $(1/\sqrt{2}, 0, -1/\sqrt{2})$ does not agree with the state of a medium initially in the ground level $(1, 0, 0)$. We will see in Sec. 2 that the relations (1.3) force the fields to evolve into "antimatched" pulse shapes to become transparent. This kind of transparency is fully dynamical, that means the polarization is not zero and a significant amount of population gets transferred between the levels as the pulses propagate.

A new exciting research area is based on these relations (1.3). This is an example of what one could call "adiabatic dynamical control physics". As we will argue below, these relations predict the control of nearly arbitrary pulse envelopes and quantum states of the medium. One has to be careful not to confuse the term adiabatic with weak or off-resonant fields. One can show that the inverse of the upper state amplitude C_2 can serve as a measure for the degree of adiabaticity [7].

From the scaling of C_2 as a function of Ω, it is clear that a stronger Rabi frequency Ω favors a more adiabatic response. When we use the term adiabatic, from now on we mean "temporally" adiabatic. Its relation to "spatial" adiabaticity in three-level pulse propagation has been discussed in Ref. [8].

In the following sections we will briefly summarize the basic ideas for three interesting phenomena that can be derived analytically from the relations (1.3). These phenomena are exploited in new forms of optical transparency, novel possibilities to control laser pulse shapes and to store optical information in dielectric media in the form of spatially dependent excitations.

2. Loss-free pulse forms

The reduced wave equations for the fields in the slowly varying envelope approximation and in one spatial dimension take the well-known form: $(\partial/\partial\tau)\Omega_a(z,\tau) = P_a(z,\tau)$ and $(\partial/\partial\tau)\Omega_b(z,\tau) = P_b(z,\tau)$. To keep here the theoretical description analytically feasible, we assume that both atomic transitions have identical oscillator strengths $\mu_a = \mu_b \equiv \mu$.

Analogous to non-linear optics we can insert the relation between the effective polarization and the electric field into the reduced Maxwell equations, which take the following form [9]:

$$\frac{\partial}{\partial\tau}\Omega_a = -\frac{2\mu_a}{\Omega}\frac{\partial}{\partial\tau}\frac{\Omega_a}{\Omega}, \tag{2.1a}$$

$$\frac{\partial}{\partial\tau}\Omega_b = -\frac{2\mu_b}{\Omega}\frac{\partial}{\partial\tau}\frac{\Omega_b}{\Omega}. \tag{2.1b}$$

Reduced wave equations in general neglect internal reflections of the medium and often also transverse propagation effects. In our case the two equations are non-linearly coupled via the Rabi frequency Ω. By multiplying the first of the two equations with Ω_a and the second with Ω_b and adding both equations, one can find that the total Rabi frequency is not a function of the position z, $\Omega(z,\tau) = \Omega(z,\tau=0) \equiv \Omega(\tau)$, and it is therefore determined once and forever by the two pulses at the entry surface of the medium at $z = 0$. If we choose appropriate initial pulse pairs such that $\Omega(\tau)$ becomes time independent after a characteristic time T^*, $\Omega(\tau) = \Omega$ for $\tau > T^*$, then it is clear that the wave equations are decoupled and describe the shape invariant propagation of two laser pulses after this time T^*. In other words, each layer of the medium is passed by the same pulse pair. Measured in the (z,τ) space-time frame, the velocity of the pulses is $2\mu/\Omega^2$, corresponding to a laboratory velocity v as given by $1/v = 1/c + 2\mu/\Omega^2$. These pulse pairs do not travel with the (vacuum) speed of light c, but with velocities that can be several orders of magnitudes smaller than c.

Quite remarkably, the two non-linearly coupled partial differential Eqs. (2.1) can be solved fully analytically and require only the inversion of an integral

$$\Omega_{a,b}(z,\tau) = \frac{\Omega_{a,b}[z=0, X^{-1}(X(\tau)-z)]}{\Omega[z=0, X^{-1}(X(\tau)-z)]}\Omega(z=0,\tau), \tag{2.2}$$

where X^{-1} denotes the inverse function of the integral $X(\tau) \equiv (1/2\mu)\int^\tau \mathrm{d}\tau' |\Omega(\tau')|^2$.

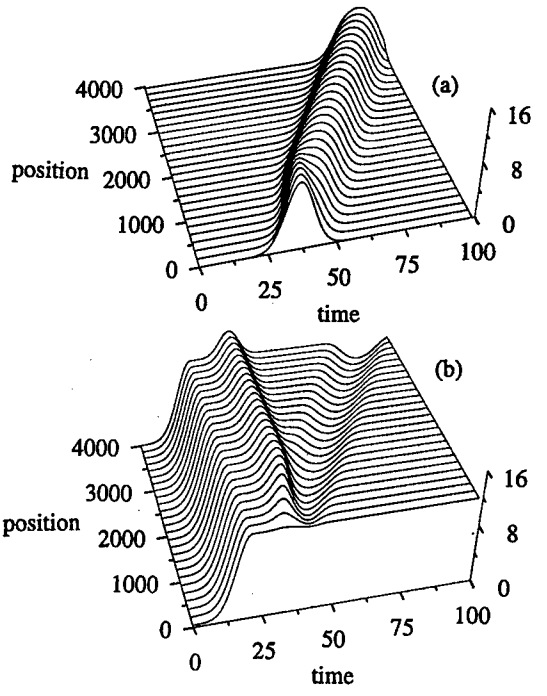

Fig. 1. The formation of loss-free pulses. (a) $\Omega_a(z,\tau)$ and (b) $\Omega_b(z,\tau)$ as predicted by Eq. (2.2). The parameters are: $\mu = 1$, $\Omega_a(z=0,\tau) = A\exp[-0.5((\tau-35)/7)^2]$, $\Omega_b(z=0,\tau) = B\exp(-0.5[(\tau-4\tau_p)/\tau_p]^2)$ for $\tau < 4\tau_p$ and $\Omega_b(z=0,\tau) = B$ for $\tau_p < \tau$, $A = 10$, $B = 12$, $\tau_p = 5$.

In Fig. 1 we display the evolution of the two pulses as a function of the position z and position τ. The pulses were chosen such that Ω is constant for $\tau > T^*$. Both pulses reshape until after a characteristic propagation distance a shape-invariant and nearly loss-free propagating pulse-pair is formed. The energy of each pulse is conserved during the propagation. The final two "antimatched" pulses are called adiabatons [9]. First experimental evidence of these pulse forms has been reported by the Stanford group of S.E. Harris [10]. We should note here that adiabatons are intrinsically different than solitons, which are exact solutions and take typically specific functional forms [11, 12]. The difference between adiabatons and electromagnetically induced transparency is discussed in Ref. [13]. In contrast, adiabatons can take arbitrary forms and are characterized by "antimatched" amplitudes such that $\Omega_a^2(z,\tau) + \Omega_b^2(z,\tau)$ is independent of time.

3. Control of the excitation state of three-level media

There has been a growing interest in studying the optical properties of media that are in a coherent superposition of two states [2, 14–18]. In this section we will address the question whether it is possible to bring the medium into a prescribed excited state with a given spatial dependence. Can one use lasers to

control the final state of excitation of the medium after interaction with the two pulses? The surprising answer is yes [19, 20]. As the state of the medium is coupled to the instantaneous amplitudes of the fields via the trapped state relation, we can therefore obtain analytically the temporal and spatial evolution of the medium. The population in the third state $|C_3|^2 = \rho_{33}$ is given by $\rho_{33} = |\Omega_a(z,\tau)/\Omega(\tau)|^2$, whose evolution is known from the solution (2.2). The final state of the medium after both laser pulses have propagated through it takes the following form:

$$\rho_{33}(z,\tau=T) = \left|\frac{\Omega_a[z=0,X^{-1}(Z-z)]}{\Omega[z=0,X^{-1}(Z-z)]}\right|^2 \equiv |G(z)|^2, \tag{3.1}$$

where T is the pulse duration for Ω and $Z \equiv X(T)$ is the corresponding integral which is proportional to the total energy contained in the input pulses. This result shows that any desired spatially dependent profile $G(z)$ can be obtained with an appropriate choice of two control laser pulses at input. From a mathematical standpoint, however, it is non-trivial to invert Eq. (3.1), that is to solve this equation for Ω_a and Ω_b as a function of a given excitation function $G(z)$.

To illustrate Eq. (3.1) let us present here an illustrative example for which such a mathematical inversion is formally possible by restricting the input pulses shapes to have "antimatched" envelopes such that $\Omega_a(z=0,\tau)^2+\Omega_b(z=0,\tau)^2 \equiv B^2$ is a square pulse for $0<\tau<T_b$ and zero otherwise. This, of course, does not necessarily imply that Ω_a and Ω_b are constant. In this case the integral can be solved easily $X(\tau) = (B^2/2\mu)[\tau-(\tau-T_b)\vartheta(\tau-T_b)]$, where ϑ is the Heaviside unit step function. Its inverse function is $X^{-1}(x) = (2\mu/B^2)x$ for $0 \le x < Z$ and it has a singularity at $x = Z = (B^2/2\mu)T_b$. If we insert this into Eq. (3.1) and solve for $\Omega_a(z=0,\tau)$, we obtain the pulse shape of the input pulses as a function of the given excitation profile $G(z)$

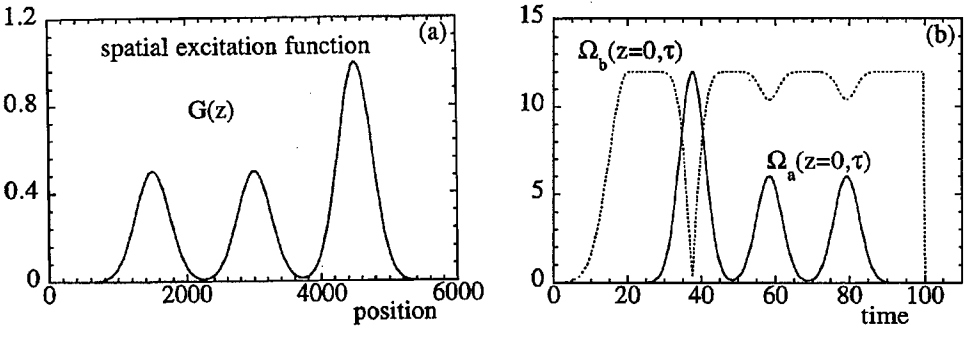

Fig. 2. Generation of spatially dependent excitations. (a) An example for a three--peaked excitation distribution function $G(z), G(z) = 0.5\{\exp[-((z-z_1)/w)^2] + \exp[-((z-z_2)/w)^2]\} + \exp[-((z-z_3)/w)^2]$, where $z_1 = 1500$, $z_2 = 3000$, $z_3 = 4500$ and $w = 350$. (b) Temporal profiles of the two input laser pulses Ω_a and Ω_b (dashed line) that generate the distribution $G(z)$ for a medium that is initially entirely in the ground state. The pulse shapes are described in Eq. (3.2) with $T_b = 100$, $B = 12$ and $\mu = 1$.

$$\Omega_a(z=0,\tau) = BG(z=\frac{B^2}{2\mu}(T_b-\tau)), \tag{3.2a}$$

$$\Omega_b(z=0,\tau) = B\sqrt{1-[G(z=\frac{B^2}{2\mu}(T_b-\tau))]^2}. \tag{3.2b}$$

In this case the required input pulse shape $\Omega_a(z=0,\tau)$ is just a mirror symmetric replica of the desired spatial excitation profile $G(z)$. In Fig. 2 we give an example of how one can convert a ground state medium into a state characterized by a three-peaked excitation function $G(z)$. In the second figure we show the temporal profiles of the corresponding two control pulses at input, which, after having propagated through the ground state medium, leave behind the medium's excitation in exactly the desired form $G(z)$. The pulse shape of the field $\Omega_b(z=0,\tau)$ at early times before the second field $\Omega_a(z=0,\tau)$ is turned on does not influence the final excitation function. The relative abrupt turn-off at $\tau = T_b$ is required by our condition $\Omega(z=0,\tau) = \text{const}$ for $0 < \tau < T_b$. This condition, however, was only imposed by us to invert relation (3.1) so as to obtain the fully analytical solutions (3.2).

4. Optical properties of media with space-dependent excitations

Let us now assume we have a medium which has been successfully brought into the space dependent state given by $G(z)$. Let us take the three-peaked distribution shown in Fig. 2a as our working case here. How can one verify whether the medium is really precise in this state? Is there a method which allows us to retrieve the information stored in the spatially excited medium? It turns out that this can be done [19] if we inject a laser pulse with a constant amplitude field through the medium. As we will see below, a second laser field will be created inside the medium and its temporal profile at output reflects the original medium's quantum mechanical state as described by $G(z)$.

We denote the Rabi frequency of the input field by $R(\tau)$ and refer to it as the "recall" field. Its frequency is assumed to be close to the 2–3 transition frequency of the medium. A pulse of this type would have been called Ω_b in the previous section. Again the polarization–electric field relations of Eq. (1.3) are the key to understanding how this recall can happen. If we insert the relation $\rho_{33} = |\Omega_a(z,\tau)/\Omega(\tau)|^2$ into the nonlinear wave equation, we obtain the temporal and spatial evolution of $\rho_{33}(z,\tau)$

$$\frac{\partial}{\partial z}\rho_{33}(z,\tau) = -(2\mu/\Omega^2)\frac{\partial}{\partial\tau}\rho_{33}(z,\tau). \tag{4.1}$$

Here it is important to note that $\Omega(\tau)$ has been replaced with $R(\tau)$, as in this case there is only one field injected into the medium. In other words, the space-time evolution of $\rho_{33}(z,\tau)$ is entirely determined by $R(\tau)$ and $\rho_{33}(z,\tau=0) = |G(z)|^2$. Under these boundary and initial conditions the solution for $\rho_{33}(z,\tau)$ is straightforward $\rho_{33}(z,\tau) = |G(z-X(\tau))|^2$. As $R(\tau)$ is turned on after time $\tau = 0$, we have assumed $X(0) = 0$. Returning to the trapped state relation $\rho_{33} = |\Omega_a/R|^2$, we can solve this relation for Ω_a which we call the signal field $S(z,\tau) \equiv \Omega_a(z,\tau)$. We obtain the following solution for the signal field: $S(z,t) = -G(z-X(\tau))R(\tau)$.

During those times for which $R(\tau)$ is constant for $0 < \tau < T_R$, $R(\tau) = R$, the integral $X(\tau)$ can be simplified to $X(\tau) = R^2[\tau - (\tau - T_R)\vartheta(\tau - T_R)]/2\mu$. In other words our solution simplifies for this time interval and we obtain

$$S(z,\tau) = -G(z - R^2\tau/2\mu)R. \tag{4.2}$$

This shows that a second field has been created inside the medium whose temporal envelope reflects the spatial distribution of the medium $G(z)$. This, of course, opens the possibility to control laser pulse shapes using spatially prepared dielectric media.

In Fig. 3 we have injected a recall field into the medium prepared according to the three-peaked distribution $G(z)$. We show the recall and signal field as a function of z and τ. At the three positions where the function $G(z)$ is peaked, the signal field $S(z,\tau)$ is generated. After a characteristic propagation distance when the information transfer is complete, the signal carries all the information of $G(z)$ and travels shape invariant. Figure 3b displays the recall field. The three "holes" in $R(z,\tau)$ indicate that the recall field looses some of its energy to form the signal field. After both fields have left the medium, the final state is the ground state for each atom and the memory of the original excitation function $G(z)$ is lost.

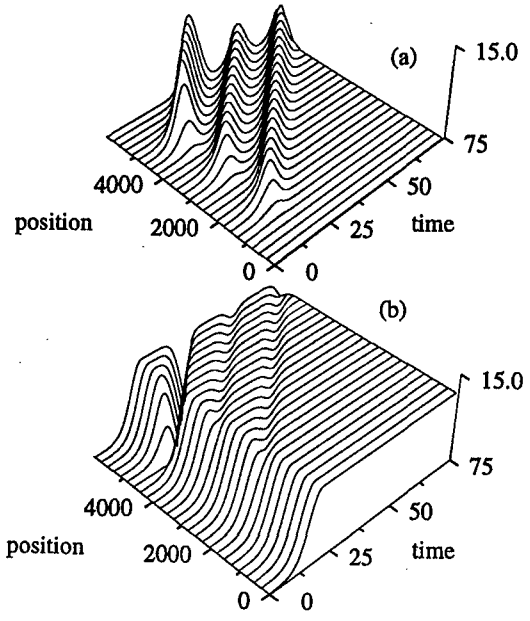

Fig. 3. Recall of spatially dependent excitations. (a) Temporal and spatial profile of the signal field $S(z,\tau)$ that is generated by the three-peaked spatial distribution $G(z)$ of Fig. 2a. (b) Temporal and spatial evolution of the recall field $R(z,\tau)$. The parameters were: $\mu = 1$ and $R(z=0,\tau) = R\exp(-0.5[(\tau - 4\tau_p)/\tau_p]^2)$ for $\tau < 4\tau_p$; $\Omega_b(z=0,\tau) = R$ for $4 < \tau/\tau_p$, $R = 12$, $\tau_p = 5$.

5. Discussion and conclusion

In this review we have given an example of adiabatic control theory for a medium consisting of three-level lambda systems and driven by a pair of resonant laser pulses. This research area is just in its cradle, and many important questions need to be addressed in the future. A direct relation between the polarization and the electric field vector is the key to investigating this regime fully analytically. This direct relation is completely different to the standard perturbative expansion of nonlinear optics.

We have restricted our discussion to a very simplified model of a three-level atom. An important question of course concerns the range of applicability of the adiabaticity relation and the corresponding validity of the trapped state assumption. The validity of the adiabaticity relation (see, e.g. Ref. [6]) requires basically that the (dimensionless) product $\Omega\tau \gg 1$. This condition can be quite easily satisfied for optical transitions in dielectric media if the lasers have intensities in the range of a few MW/cm^2 and have pulse durations in the nanosecond range. This is also confirmed by the experimental observation of adiabatons in the study by Kasapi et al. [10]. In a previous work [9] we compared the predictions of the approximate analytical solutions based on adiabaticity with those obtained from direct numerical simulations of the fully-coupled Maxwell–Schrödinger equation and we found that the agreement is excellent.

Another equally important question concerns the applicability of the theory to dissipative systems. The trapped state condition relies on the coherence between the two lowest levels 1 and 3. Any dissipative influence that destroys this coherence changes the dynamics sufficiently. On the other hand, any relaxation process which is associated with the upper level 2 has only a small influence on the dynamics if the Rabi frequencies are chosen larger than the relaxation rates. This is due to the fact that the population in the upper state is very small during the entire evolution, and the exchange of population happens to be restricted to levels 1 and 3.

We finish this report with a comment about possible applications. The nearly loss-free propagation properties of adiabatons could be exploited in the long-distance transmission of optical signals. Because of the fact that the temporal features of one of the input pulses (Ω_a) are imprinted on the other pulse duration, the formation of adiabatons could also be advantageous in a signal replicator.

The function $G(z)$ determines obviously the optical properties for a weak optical probe field. The optical index of refraction can be directly proportional to the degree of excitation as described by $G(z)$. We have shown above that practically arbitrary excitation functions can be generated by an appropriate choice of input fields. In other words, the index of refraction in its spatial dependence can be controlled. The state 3 is typically metastable and its lifetime determines how long a medium can maintain the spatially dependent index of refraction until it relaxes back into its ground state and its normal space-independent index. The faster time scale on which the two-photon coherence decays due to energy conserving collisions, e.g., is not expected to affect the index. The combination of the recall and excitation mechanism could be exploited in the intermediate storage of optical data.

Acknowledgment

We would like to acknowledge our collaborators J.H. Eberly, F.T. Hioe and A. Rahman in Rochester, and B.K. Clark, J.R. Csesznegi and Q. Su in Normal. We acknowledge the receipt of a travel grant under NSF grant INT 9722745 to participate at the wonderful Quantum Optics IV conference in Jaszowiec, Poland. This work has been supported by the NSF under grant #PHY-9631245. This research was also supported in parts by a Cottrell College Science Award from Research Corporation and by Illinois State University.

References

[1] K.-J. Boller, A. Imamoglu, S.E. Harris, *Phys. Rev. Lett.* **66,** 2593 (1991); J.E. Field, K.H. Hahn, S.E. Harris, *Phys. Rev. Lett.* **67,** 3062 (1991).

[2] For a review on electromagnetically induced transparency, see S.E. Harris, *Phys. Today* **50**, No. 7, 36 (July 1997).

[3] For a review, see O. Kocharovskaya, *Phys. Rep.* **219,** 175 (1992) and articles in the special issue of *Quantym Opt.* **6,** No. 4 (1994). For some early work on LWI, see, e.g, M.O. Scully, S.Y. Zhu, *Phys. Rev. Lett.* **62,** 2812 (1989); S.E. Harris, *Phys. Rev. Lett.* **66,** 1033 (1989); O. Kocharovskaya, P. Mandel, *Phys. Rev. A* **42,** 523 (1989); A. Imamoglu, J.E. Field, S.E. Harris, *Phys. Rev. Lett.* **66,** 1154 (1991).

[4] G. Alzetta, A. Gozzini, L. Moi, G. Orriols, *Nuovo Cimento B* **36,** 5 (1976).

[5] R.M. Whitley, C.R. Stroud, Jr., *Phys. Rev A* **14,** 1498 (1976).

[6] J.R. Kuklinski, U. Gaubatz, F.T. Hioe, K. Bergmann, *Phys. Rev. A* **40,** R6749 (1989).

[7] M. Fleischhauer, A. Manka, *Phys. Rev. A* **54,** 794 (1996).

[8] K.M. Paul, J.R. Csesznegi, R. Grobe, *Laser Phys.* **7,** 884 (1997).

[9] R. Grobe, F.T. Hioe, J.H. Eberly, *Phys. Rev. Lett.* **73,** 3183 (1994).

[10] A. Kasapi, M. Jain, G.Y. Yin, S.E. Harris, *Phys. Rev. Lett.* **74,** 2447 (1995).

[11] F.T. Hioe, R. Grobe, *Phys. Rev. Lett.* **73,** 2559 (1994).

[12] J.H. Eberly, *Quantum Semiclas. Opt.* **7,** 373 (1995).

[13] R. Grobe, J.H. Eberly, *Laser Phys.* **5,** 542 (1995).

[14] M.O. Scully, *Phys. Rev. Lett.* **55,** 2802 (1985) and *Phys. Rev. Lett.* **67,** 1855 (1991).

[15] For a review on phaseonium, see, e.g., M.O. Scully, *Phys. Rep.* **219,** 191 (1992) and *Quantum Opt.* **6,** 201 (1994).

[16] J.H. Eberly, A. Rahman, R. Grobe, *Phys. Rev. Lett.* **76,** 3687 (1996).

[17] G. Vemuri, K.V. Vasada, G.S. Agarwal, *Phys. Rev. A* **54,** 3394 (1996).

[18] J.H. Eberly, A. Rahman, R. Grobe, *Laser Phys.* **6,** 69 (1996).

[19] J.R. Csesznegi, R. Grobe, *Phys. Rev. Lett.* **79,** 3162 (1997).

[20] J.R. Csesznegi, B.K. Clark, R. Grobe, *Phys. Rev. A*, to be published.

Vol. 93 (1998) *ACTA PHYSICA POLONICA A* No. 1

Proceedings of the International Conference "Quantum Optics IV", Jaszowiec, Poland, 1997

QUANTUM INSTABILITIES AND DECOHERENCE PROBLEM

S.Ya. Kilin, D.B. Horoshko and V.N. Shatokhin

Institute of Physics, Belarus Academy of Sciences
F. Skarina Avenue 70, Minsk 220072, Belarus

A decoherence problem is discussed by means of quantum continuous measurement theory. It is shown that the conditional state of quantum system interacting with a bath preserves its initial purity. In this presentation decoherence arises as a result of averaging over the stochastic times of reduction moments ("clicks"). A method based on external phase feedback is proposed to slow down the decoherence of field superposition state in an open optical cavity. It is also shown that an atom placed inside the optical cavity plays a role of internal self-organized positive feedback between field and atom, which leads to an exponential increase in the mean dipole moment of the atom for the field initially prepared in a superposition of coherent states, i.e. to quantum instability.

PACS numbers: 42.50.Lc, 03.65.Bz

1. Introduction

A decoherence problem is one of the fundamental problems of quantum theory. The problem has been formulated by E. Schrödinger in his famous "cat-state" paper [1] published in 1935. The problem was presented in a grotesque form which is perturbing our perception of the world. E. Schrödinger asked about possibility of observing macroscopic superposition of two states of a cat: alive $|\overset{0}{Q}\rangle$ and dead $|0Q\rangle$. Why has such kind of macroscopic superposition never been registered in the real world? A reasonable answer for the question has been done by Zurek et al. in a series of papers [2–5]. Using the density matrix approach they argued about a rather common statement: the larger the cat size the faster the interference part of density matrix $\left(|\overset{0}{Q}\rangle\langle 0Q| + |0Q\rangle\langle\overset{0}{Q}|\right)$ disappears, and the superposition evolves into a classical mixture. Decoherence being a very fundamental problem obtained recently a practical meaning because of limits put by it on the practical realization of quantum computers [6]. In this paper we discuss some new methods to influence fast decoherence and to slow it down.

2. External feedback and the decoherence problem

There have been several proposals for slowing down the fast decoherence process in quantum systems [7–11]. Most of them are connected with Zurek's idea [2] that in the course of relaxation the quantum system is projected into a preferable basis ("pointer basis") formed via "quantum system – environment" interactions. Let us choose a harmonic oscillator as a quantum system interacting with the environment formed by a set of reservoir harmonic oscillators via an interaction Hamiltonian

$$H_{\rm int} = A(a, a^+)\Gamma^+ + A^+(a, a^+)\Gamma, \tag{1}$$

with $\Gamma = \hbar \sum_i g_i b_i$, where $A(a, a^+)$ is a function of annihilation and creation operators of the selected oscillator, g_i are coupling constants and b_i, b_i^+ are annihilation and creation operators of the reservoir oscillators. In this case it becomes evident that for $A = A^+ = R$ the eigenstates of R form the pointer basis and they are not changed via interaction with environment. Therefore there is a possibility to select a different pointer basis by constructing a different form of coupling operator $A(a, a^+)$ (the so-called "quantum reservoir engineering"). Some known examples are summarized in Table.

TABLE

Overview of different forms of system–reservoir coupling.

Form of coupling	Zurek's "pointer basis"	Steady state	References
$A = a + a^+ \sim x$	position eigenstates	vacuum	Zurek et al. (1981,82,89,91) Caldeira, Leggett(1985) Walls, Milburn (1985)
$A = a^2$	even, odd coherent states	vacuum	Gerry, Hach (1993)
$A = (a + \alpha)(a - \alpha)$	even, odd coherent states (CS)	even, odd CS	Garraway, Knight (1994) Filho, W. Vogel (1996) Poyatos, Zoller, Cirac (1996)
$A = a^+ a$	Fock states	vacuum	Poyatos, Zoller, Cirac (1996)
$A = a(a^+ a - n)$	Fock states	Fock state	Poyatos, Zoller, Cirac (1996)
$A = \mathrm{e}^{\mathrm{i}\pi a^+ a} a$	Yurke–Stoler CS	vacuum	Horoshko, Kilin (1997)

In the present paper we discuss the decoherence problem for a specific initial state of the harmonic oscillator: a superposition of two coherent states with

opposite phases

$$|\psi_+\rangle = N\left(|\alpha\rangle + \mathrm{e}^{\mathrm{i}\theta}|-\alpha\rangle\right), \quad N^{-2} = 2\left(1+\cos\theta\exp(-2|\alpha|^2)\right). \tag{2}$$

This state exhibits remarkable quantum features [12]. For instance, the Wigner function $W(\beta)$ of this state besides two positive peaks centered at $\beta = \pm\alpha$ has the interference part at $\beta = 0$ which can take negative values. This nonpositive interference structure is a manifestation of quantum nature of the superposition (2). In the case of linear system–reservoir interaction ($A = a$), the decoherence process consists in the fast disappearance of this interference part with the speed, which is $|\alpha|^2$ times higher than the speed of the peaks decay. The evolution of the density matrix averaged over the vacuum states of the reservoir in the Born–Markov approximation is described by the standard master equation

$$\dot{\varrho} = \frac{\gamma}{2}\left(2a\varrho a^+ - a^+a\varrho - \varrho a^+a\right), \tag{3}$$

where $\gamma = \pi\varrho(\omega)|g(\omega)|^2$ is the energy decay rate of the selected oscillator, $\varrho(\omega)$ is the density of reservoir states at the oscillator frequency ω. The exact solution of Eq. (3) with the initial condition $\varrho(0) = |\psi_+\rangle\langle\psi_+|$ has the following form:

$$\varrho(t) = \frac{1}{2}\left(|\alpha_t\rangle\langle\alpha_t| + |-\alpha_t\rangle\langle-\alpha_t|\right)$$
$$+\frac{1}{2}\mathrm{e}^{-2|\alpha|^2(1-\exp(-\gamma t))}\left(\mathrm{e}^{\mathrm{i}\theta}|-\alpha_t\rangle\langle\alpha_t| + \mathrm{e}^{-\mathrm{i}\theta}|\alpha_t\rangle\langle-\alpha_t|\right), \tag{4}$$

where $\alpha_t = \alpha\mathrm{e}^{-\gamma t/2}$. Expression (4) clearly shows the fast disappearance of the quantum interference terms with the rate of $t_{\mathrm{decoh}}^{-1} = 2\gamma|\alpha|^2$. However, it does not allow us to understand all the details of the decoherence process. The most convenient and furthermore productive way for that is to use the continuous measurement theory [13]. Using this theory one can calculate the conditional state of the harmonic oscillator after emitting exactly n quanta into the reservoir at stochastic times $t_1, t_2, \ldots, t_n$ in the time interval $[0, t)$

$$|\psi_{\mathrm{cond}}(t)\rangle = \gamma^n S(t, t_n)aS(t_n, t_{n-1})a\ldots aS(t_1, 0)|\psi_+\rangle, \tag{5}$$

where $S(t_i, t_{i-1}) = \exp\left(-\gamma a^+a(t_i - t_{i-1})/2\right)$ is a nonunitary operator of evolution between two emission times t_{i-1} and t_i The emission of quanta at times $\{t_i\}$ makes a reduction of the system state according to action of the annihilation operator a. So, according to Eq. (5) and the relation

$$a\left(|\alpha\rangle \pm \mathrm{e}^{\mathrm{i}\theta}|-\alpha\rangle\right) = \alpha\left(|\alpha\rangle \mp \mathrm{e}^{\mathrm{i}\theta}|-\alpha\rangle\right), \tag{6}$$

the system changes the relative phase θ on π at the moments of clicks but the state of the system remains a pure superposition state. Between the clicks the amplitude of the state diminishes according to non-unitary evolution operator action

$$\exp\left(-\gamma a^+a(t_i - t_{i-1})/2\right)\left(|\alpha\rangle \pm \mathrm{e}^{\mathrm{i}\theta}|-\alpha\rangle\right)$$
$$= \left(|\alpha\mathrm{e}^{-\gamma(t_i - t_{i-1})/2}\rangle \pm \mathrm{e}^{\mathrm{i}\theta}|-\alpha\mathrm{e}^{-\gamma(t_i - t_{i-1})/2}\rangle\right). \tag{7}$$

Therefore, the stochastic history of the selected harmonic oscillator tells us that its state during all period of evolution is a superposition state with preserved coherence

$$|\psi_{\mathrm{cond}}(t)\rangle = N(\gamma\alpha)^n\left(|\alpha\mathrm{e}^{-\gamma t/2}\rangle + (-1)^n\mathrm{e}^{\mathrm{i}\theta}|-\alpha\mathrm{e}^{-\gamma t/2}\rangle\right). \tag{8}$$

However if we want to discuss the unconditional state which suits for ensemble measurements, we should average the conditional density matrix $|\psi_{\rm cond}(t)\rangle\langle\psi_{\rm cond}(t)|$ over the stochastic times of clicks $\{t_i\}$. This averaging gives exactly the density matrix (4) which describes the loss of coherence which can be understood as the loss of information about the system state. From the continuous measurement theory representation it becomes evident that to erase the quantum interference terms it is enough to average over the first click time. And because the mean time of waiting for the first click is of the order of $1/\left(\gamma|\alpha|^2\right)$, one can immediately obtain the decoherence time value $t_{\rm decoh} = 1/\left(\gamma|\alpha|^2\right)$. Another lesson which follows from the consideration is that there is a way for slowing down the decoherence: after each click it is necessary to change back the relative phase in the superposition of coherent states.

We can also come to the same conclusion using the quantum engineering approach [11]. As is shown in this paper, the generalized annihilation and creation operators

$$A_\varphi = \mathrm{e}^{\mathrm{i}\varphi a^+ a}a, \quad A_\varphi^+ = a^+\mathrm{e}^{-\mathrm{i}\varphi a^+ a} \tag{9}$$

obey boson commutation relations

$$[A_\varphi, A_\varphi^+] = 1 \tag{10}$$

and, what is more useful, the eigenstates of the operator A_φ

$$A_\varphi|\mathcal{A}_\varphi\rangle = \mathcal{A}_\varphi|\mathcal{A}_\varphi\rangle \tag{11}$$

are the states with Poissonian distribution of photons, but with quadratic dependence of amplitude phase

$$|\mathcal{A}_\varphi\rangle = \mathrm{e}^{-|\mathcal{A}_\varphi|^2/2}\sum_n \frac{\mathcal{A}_\varphi^n}{\sqrt{n!}}\mathrm{e}^{\mathrm{i}\varphi n(n-1)/2}|n\rangle. \tag{12}$$

These states belong to the class of states, firstly introduced by Glauber and Titulaer in Ref. [14], where they discussed the states with all degrees of coherence equal to unity. Note that the class of states (9) has a number of unusual quantum properties. As an example we demonstrate the Q-function of $|\mathcal{A}_{2\pi/7}\rangle$-state in Fig. 1. The $|\mathcal{A}_\pi\rangle$-state coincides with the Yurke–Stoler state given by Eq. (2) with $\theta = \pi/2$, $\mathcal{A}_\pi = \mathrm{i}\alpha$. Taking into account this fact, we use A_π as a nonlinear coupling operator in interaction Hamiltonian (1) and obtain the following master equation:

$$\dot{\varrho} = \frac{\gamma}{2}\left([A_\pi, \varrho A_\pi^+] + [A_\pi\varrho, A_\pi^+]\right). \tag{13}$$

Being rewritten in a different form

$$\dot{\varrho} = \frac{\gamma}{2}\left(2\mathrm{e}^{\mathrm{i}\pi a^+ a}a\varrho a^+\mathrm{e}^{-\mathrm{i}\pi a^+ a} - a^+ a\varrho - \varrho a^+ a\right) \tag{14}$$

this master equation is exactly the one for system under measurement mediated feedback. The evolution introduced by the first right-hand term is the state reduction (due to emission of quantum) followed by feedback action corresponding to interactive field phase changing on π. And now the conditional state evolution is described by the following equation:

$$|\psi_{\rm cond}(t)\rangle = \gamma^n S(t,t_n)\mathrm{e}^{\mathrm{i}\pi a^+ a}aS(t_n,t_{n-1})\mathrm{e}^{\mathrm{i}\pi a^+ a}a\ldots\mathrm{e}^{\mathrm{i}\pi a^+ a}aS(t_1,0)|\psi_+\rangle, \tag{15}$$

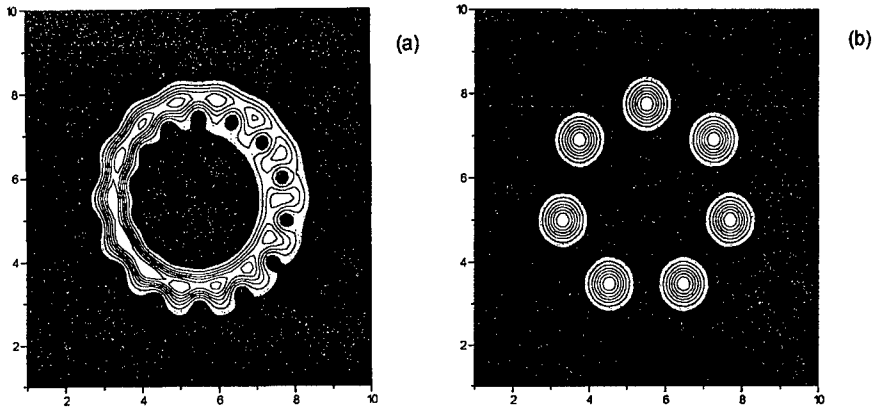

Fig. 1. Q-function (view from above) of the generalized coherent state given by Eq. (12) for $\alpha = 5$ and (a) $\varphi = \pi/7$, (b) $\varphi = 2\pi/7$.

rather than Eq. (5). From this equation we easily find that this conditional state

$$|\psi_{\rm cond}(t)\rangle = \frac{1}{\sqrt{2}}(\gamma\alpha)^n \left(|\alpha e^{-\gamma t/2}\rangle + {\rm i}|-\alpha e^{-\gamma t/2}\rangle\right), \tag{16}$$

remains a superposition with a fixed relative phase. So, averaging over the stochastic times $\{t_i\}$ does not influence this statement, and the *unconditional* state in this case will be a pure superposition

$$|\psi(t)\rangle = \frac{1}{\sqrt{2}} \left(|\alpha e^{-\gamma t/2}\rangle + {\rm i}|-\alpha e^{-\gamma t/2}\rangle\right). \tag{17}$$

Therefore a simple experimental scheme for slowing down the decoherence or for improving error introduced by decay processes could be proposed [11] as follows: after each successful click of the photon detector collecting all the light escaping the optical cavity one should use this information and change the intracavity field phase by π. Repeating this procedure we will allow the cat state $|\psi_+\rangle$ for $\theta = \pi/2$ to be a superposition as long as there are photons in the cavity*.

3. Quantum instabilities, entanglement and feedback action of an atom in a high Q cavity

As is seen from the previous consideration, the intracavity field initially prepared in a superposition (2) will evolve to a mixture in a fast mode. So, in an empty cavity after a time larger than $t_{\rm decoh}$ the state of the field will be described by density matrix

$$\varrho_{\rm mix} = \frac{1}{2}\left(|\alpha\rangle\langle\alpha| + |-\alpha\rangle\langle-\alpha|\right) \tag{18}$$

without any quantum features. From the first sight the time $t_{\rm decoh} = 1/(\gamma|\alpha|^2)$ will limit all possible manifestations of quantum peculiarities of superposition state (2).

*A technical aspect of the proposed scheme should be noted: the feedback loop action time $\tau_{\rm FB}$ should be less than the average time between two successive clicks, which is of order $t_{\rm decoh} = 1/\left(\gamma|\alpha|^2\right)$. Therefore this fast switching of the intracavity field phase can put some problems with the single mode operation of the cavity.

Below we show that a two-level atom placed inside cavity acts as internal positive feedback and this action leads to a quantum instability [15, 16] as well as to more prolonged period for field coherence manifestation.

As was shown in Ref. [15] the Glauber P-function of state (2) has four terms

$$P(\beta) = N_+ \left\{ \delta^{(2)}(\alpha - \beta) + \delta^{(2)}(\alpha + \beta) + \left[\mathrm{e}^{-2|\alpha|^2}/|\beta| \right] \delta\left(\varphi_\alpha - \varphi_\beta + \pi/2\right) \right.$$
$$\left. \times \left[\mathrm{e}^{\mathrm{i}\theta} \delta_{\mathrm{AC}}\left(|\beta| - \mathrm{i}|\alpha|\right) + \mathrm{e}^{-\mathrm{i}\theta} \delta_{\mathrm{AC}}\left(|\beta| + \mathrm{i}|\alpha|\right) \right] \right\}. \tag{19}$$

The first two terms correspond to a classical part. The latter terms describing the quantum interference part of this state are proportional to the so-called delta-functions of analytic continuation $\delta_{\mathrm{AC}}\left(|\beta| \pm \mathrm{i}|\alpha|\right)$. The δ-function of analytic continuation may be defined by its action on a probe function $F(x)$

$$\int_{-\infty}^{\infty} \mathrm{d}x \delta_{\mathrm{AC}}(x - z) F(x) = F(z), \; x \in R^1, \; z \in C^1. \tag{20}$$

The well-known solution for a mean dipole moment of a two-level atom in a free space immediately leads to an exponentially divergent solution when averaged with this function. We call this effect quantum instability [15] because of the reason of the effect: the quantum interference part of the density matrix of state (2).

The effect of the quantum instability may be observable in a high-Q cavity at the initial part of evolution. If we use the Jaynes–Cummings (J–C) model the mean dipole moment of a two-level atom is (for an atom initially prepared in the ground state and the field in a state $|\psi\rangle$)

$$\langle \sigma_-(t) \rangle = -\mathrm{i} \langle \psi | \cos\left(gt\sqrt{\widehat{n}}\right) \frac{\sin\left(gt\sqrt{\widehat{n}+1}\right)}{\sqrt{\widehat{n}+1}} a |\psi\rangle, \tag{21}$$

where $\widehat{n} = a^+ a$, g is the atom-field coupling constant. For initial coherent field state $|\psi\rangle = |\alpha\rangle$ Eq. (21) gives

$$\langle \sigma_-(t) \rangle_{\mathrm{coh}} = -\mathrm{i}\alpha \mathrm{e}^{-|\alpha|^2} \sum_k \frac{|\alpha|^{2k}}{k!\sqrt{k+1}} \cos\left(gt\sqrt{k}\right) \sin\left(gt\sqrt{k+1}\right), \tag{22}$$

while for the Yurke–Stoler superposition state ($\theta = \pi/2$)

$$\langle \sigma_-(t) \rangle_{\mathrm{YS}} = \alpha \mathrm{e}^{-2|\alpha|^2} \sum_k \frac{\left(-|\alpha|^2\right)^k}{k!\sqrt{k+1}} \cos\left(gt\sqrt{k}\right) \sin\left(gt\sqrt{k+1}\right). \tag{23}$$

For the mixture (18) of coherent states $\langle \sigma_-(t) \rangle_{\mathrm{mix}} = 0$ for all moments of time. The main difference between Eq. (22) and Eq. (23) is that the Fourier components of the sum (23) have alternating sign in contrast to that of the sum (22). For large values of coherent amplitude $|\alpha|$ when the spacing $g\left(\sqrt{k+1} - \sqrt{k}\right) \approx g/(2\sqrt{k}) \approx g/(2|\alpha|)$ between significant components of the sum much less than the width $2|\alpha|g$ of the components distribution, the asymptotic of Eq. (23) is

$$\langle \sigma_-(t) \rangle \approx \frac{1}{4\sqrt{1 - gt/(2|\alpha|)}} \mathrm{e}^{-2|\alpha|^2 + 2|\alpha|gt - (gt/2)^2} \tag{24}$$

instead of Rabi oscillation for Eq. (22). So, the exponential growth of the mean dipole moment for times $t \ll 2\alpha/g$, which are smaller than revivals time $T_{\mathrm{R}} = 2\pi\alpha/g$ is also observable for the J–C model.

A physical reason for this instability is entanglement between atomic and field states [15, 17]. As it has been shown in Ref. [15] the phase of interference part of the conditional Wigner function of the field follows the atomic state: the phase changes by π when atom makes a transition from the ground state $|g\rangle$ to excited $|e\rangle$ and vice versa. It can be easily seen from the time-evolved atom-field state for initial state $|\psi(0)\rangle = |g\rangle|\psi_+\rangle$

$$|\psi(t)\rangle = \cos\left(gt\sqrt{n}\right)|\psi_+\rangle|g\rangle - \mathrm{i}\frac{\sin\left(gt\sqrt{n+1}\right)}{\sqrt{n+1}}|\psi_-\rangle|e\rangle. \tag{25}$$

So we can conclude that the quantum positive feedback (entanglement) between the phase of interference part of field Wigner function and state of two-level atom is the factor which leads to the quantum instability of the mean dipole moment.

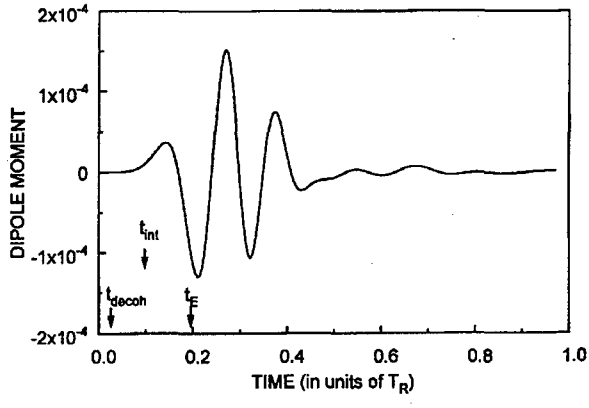

Fig. 2. Temporal dependence of the mean dipole moment in the optical resonator with the parameters $g = 2\pi \times 2.7$ MHz, $k = 2\pi \times 0.7$ MHz, $\gamma = 2\pi \times 2.5$ MHz for the initial superposition state $|\alpha\rangle + \mathrm{i}|-\alpha\rangle$ with $\alpha = 3$. Arrows mark the decoherence time $t_{\mathrm{decoh}} = 1/(k\alpha^2)$, the interaction time t_{int} and the time of the field energy decay $t_{\mathrm{E}} = 1/k$.

When a cavity damping is included into consideration, the fast decoherence processes should diminish all manifestations of coherent interactions. However atom seating in cavity sees *continuously* the state of the field, and as we demonstrated in Sec. 2, the continuous state of the field is nothing more than a pure superposition state with a changing relative phase at the moments when a photon escapes the cavity. That is why one could observe the effect of quantum instability at the initial stage of a two-level atom interaction with damping cavity mode prepared in the superposition state (2). The solution of master equation for the Jaynes–Cummings model with cavity decay [16, 18] supports this statement (see Fig. 2).

4. Conclusions

On the basis of quantum continuous measurement theory we demonstrated that the decoherence arises as a result of *combination* of averaging over stochastic

times of the clicks due to the quanta *passing* into a bath, and reduction of the system state which occurs at these times. Without averaging the single-run-state of the decaying system is a pure quantum state. We showed that because of this purity the decoherence processes can be slowed down by adding corrections after reduction which each click makes. We proposed the concrete scheme for slowing down the decoherence of the Yurke–Stoler state on the basis of phase feedback which introduces a π phase shift after detecting each photon escaping the cavity.

We also showed that a two-level atom placed inside a cavity plays a role of an internal positive feedback (in other words, entanglement) which leads to the effect of the quantum instability of the mean dipole moment of an atom. The exponential growth of the dipole moment can be observed at the initial stage of evolution of an atom in a cavity containing field prepared in a superposition state.

The authors gratefully acknowledge financial support by INTAS under grant RFBR 95-0656 and Belarus Foundation for Basic Researches under grants F205 and MP 96-38.

References

[1] E. Schrödinger, *Naturwissenschaften* **23,** 807 (1935).

[2] W.H. Zurek, *Phys. Today* **44,** 36 (1991).

[3] W.H. Zurek, *Phys. Rev. D* **24,** 1516 (1981).

[4] W.H. Zurek, *Phys. Rev. D* **26,** 1862 (1982).

[5] W.G. Unruh, W.H. Zurek, *Phys. Rev. D* **40,** 1071 (1989).

[6] D.P. DiVincenzo, *Science* **270,** 255 (1995).

[7] C. Gerry, E.E. Hach, *Phys. Lett. A* **174,** 185 (1993).

[8] B.R. Garraway, P.L. Knight, *Phys. Rev. A* **49,** 1266 (1994); *ibid.* **50,** 2548 (1994).

[9] M.R.L. Filho, W. Vogel, *Phys. Rev. Lett.* **76,** 608 (1996).

[10] J.F. Poyatos, J.I. Cirac, P. Zoller, *Phys. Rev. Lett.* **77,** 4728 (1996).

[11] D.B. Horoshko, S.Ya. Kilin, *Phys. Rev. Lett.* **78,** 840 (1997).

[12] W. Schleich, M. Pernigo, Fam Le Kien, *Phys. Rev. A* **44,** 2172 (1991).

[13] E.B. Davies, *Quantum Theory of Open Systems*, Academic Press, New York 1976; S.Ya. Kilin, *Quantum Optics: Fields and Detection of them*, Nauka i Tekhnika, Minsk 1990 (in Russian).

[14] V.M. Titulaer, R.J. Glauber, *Phys. Rev. A* **145,** 1046 (1986).

[15] S.Ya. Kilin, V.N. Shatokhin, *Phys. Rev. Lett.* **76,** 1051 (1996).

[16] S.Ya. Kilin, V.N. Shatokhin, *Opt. Spectrosc.* **82,** 972 (1997).

[17] S.J.D. Phoenix, P.L. Knight, *Phys. Rev. A* **44,** 6023 (1991).

[18] J.H. Kimble, in: *Advances in Atomic, Molecular and Optical Physics*, Ed. P. Berman, Suppl. 2. Academic Press, New York 1994, p. 203.

Vol. 93 (1998) *ACTA PHYSICA POLONICA A* No. 1

Proceedings of the International Conference "Quantum Optics IV", Jaszowiec, Poland, 1997

POLARIZATION DEPENDENCE OF MICROWAVE "IONIZATION" OF EXCITED HYDROGEN ATOMS

P.M. Koch*

Department of Physics and Astronomy, State University of New York
Stony Brook, NY 11794-3800, USA

After a brief review of the ionization of excited hydrogen atoms by a linearly polarized field, we discuss experimental results for the polarization dependence of this process. Experiments at $\omega/2\pi = 9.904$ GHz used two different ranges of principal quantum number n_0 between 29 and 98. At low scaled frequencies, $\Omega_0 \lesssim 0.1$, ionization data for certain narrow ranges of n_0 exhibit striking sensitivity to fields with elliptical polarization not too far from circular polarization. Classical calculations reproduce this behavior and show it to be the result of 2ω driving terms that appear when the Hamiltonian is transformed to a frame rotating at ω. It shows how higher-dimensional dynamics can influence the ionization and be used to control it when the polarization departs from linear or circular polarization. At higher scaled frequencies, $0.6 \lesssim \Omega_0 \lesssim 1.4$, near the onset of ionization circularly and elliptically polarized data show surprising similarities with linearly polarized data in a parameter regime where the ionization dynamics is dominated by the influence of the pendulumlike resonance zone centered at scaled frequency $n_0^3\omega \equiv \Omega_0 = 1$. The stabilizing influence of this zone can be understood classically, but nonclassical stability associated with quantal separatrix states at its edge is a semiclassical effect.

PACS numbers: 32.80.Rm, 05.45.+b, 42.50.Hz

1. Introduction

Experiments on the ionization of hydrogen atoms with principal quantum number n_0 by a linearly polarized (LP) microwave electric field $F\sin(\omega t)$ have been a cornucopia of data. For recent reviews and commentary that emphasize experimental data obtained at Stony Brook and compare them to other experimental data and classical, semiclassical, and quantal calculations, see [1, 2]; for ones appearing earlier in the 1990s, see [3–8]. Reviews or extended articles in the 1990s that emphasize theoretical calculations, but contain comparisons with or commentary on LP ionization data, include [9–29].

*Internet: Peter.Koch@sunysb.edu.

From the vantage point of semiclassical theory, the experiments attract attention because for a wide range of parameters the onset of ionization coincides classically with the onset of irregular (chaotic) trajectories. This system is the paradigm for the experimental/theoretical/numerical study of non-perturbative quantal dynamics in a time-dependent, low-dimensional, classically chaotic system. All previous LP experiments, as well as those in this paper for varying polarization, required the (net) absorption of many photons to reach the ionization continuum. This, and so many quantal states being coupled by the strong driving field, renders quantal perturbation theory questionable, if not useless, as a calculational method for simulating the experiments. Brute-force numerical integrations of the Schrödinger equation on large, fast computers are used, but often the crucial insights into the complexities of the ionization dynamics have come from semiclassical or even fully classical theory and calculations.

Dynamics is about time scales, which means comparing frequencies. Because of its special dynamical symmetries, the classical bound orbits of the unperturbed, non-relativistic 3d hydrogen atom at total energy $E < 0$ depend only upon the principal action I_0. In atomic units (a.u.)[†] classically $E = -(2I_0^2)^{-1}$; quantally, replace I_0 with n_0. Therefore, at $E < 0$ there is only the Kepler frequency $\omega_K = \partial E/\partial I_0 = I_0^{-3}$. Exemplifying Bohr's correspondence principle, in the limit of $n_0 \to \infty$, ω_K is the frequency splitting between adjacent n-states, $|\Delta n| = 1$. For large but finite n_0, ω_K is close to the average of the $\Delta n = \pm 1$ splittings.

When the excited hydrogen atom is driven at frequency ω, the important frequency ratio is the *scaled frequency* $\omega/\omega_K = n_0^3\omega \equiv \Omega_0$. Similarly, the *scaled amplitude* $n_0^4 F \equiv F_0$ is the ratio of the peak amplitude of the driving field to the Coulomb field at the Bohr (circular) orbit $r_n = n^2$ a.u. As was first shown in [31] the resultant classical dynamics does not depend independently on ω, F, and I_0; it depends on the ratios Ω_0 and F_0. However, a non-zero Planck's constant $\hbar$ spoils the classical scaling invariance in the quantal dynamics. Varying n_0, ω, and F in such a way as to keep Ω_0 and F_0 constant changes the size of the effective $\hbar$, $\widetilde{\hbar} = \hbar/n_0$. However, Refs. [1, 2, 32, 33], as well as the discussion in Sec. 5 below, show that the experimental, i.e., quantal, ionization data can follow classical scaling for at least up to 50% changes in $\widetilde{\hbar}$.

All results mentioned above were obtained for the case of an LP driving field.

It is well known from pulsed laser experiments with tightly bound atoms that the polarization of an intense electromagnetic field can strongly influence atomic ionization when many photons must be absorbed. In a perturbation expansion polarization-dependent electric dipole selection rules determine pathways through unperturbed states, so small changes in polarization may dramatically vary the ionization rate for fixed peak field amplitude. Except for the case [34] of few-photon ($\lesssim 3$) ionization dominated by a resonance between intermediate bound states, early optical [35] and microwave [36] experiments, using atoms in initial states

[†]Atomic units (a.u.) are defined by setting $(2\pi)^{-1}$·Planck's constant, $\hbar$, the electron mass, m_e, the antielectron charge, e, and the electrostatic constant, $4\pi\epsilon_0$, all equal to one. Definitions and numerical values for a.u. are listed in Ref. [30]. When confronting experimental data obtained with real hydrogen atoms or its isotopes, one should use *physical* a.u. that result from substituting for m_e the reduced electron mass μ_e.

$|n_0, \ell, m\rangle$ with low values of the angular momentum ($\ell \leq 2$) and a driving frequency $\omega \ll (E_{n_0+1} - E_{n_0})/\hbar$, showed that many-photon ($\gtrsim 11$) ionization in a circularly polarized (CP) field required significantly larger field intensities than in an LP field. A smaller effective quantal density of participating, unperturbed states in CP fields was used to explain [37] these many-photon results. The monotonic change of the azimuthal quantum number m with each absorbed photon forces an eventual monotonic increase in ℓ, whereas in LP the $\Delta m = 0$ selection rule does not seriously constrain the upward and downward movement in ℓ permitted by the $\Delta \ell = \pm 1$ selection rule. Classically, quasistatic pictures including effects of frame rotation and an angular momentum barrier were used [38, 39] to explain the microwave ionization results. Nevertheless, these explanations are all "rules of thumb", applicable only to particular cases. They have no universal validity. In a succinct description of our limited knowledge a recent review [40] stated, "the matter of polarization ... is more complicated than previously realized".

CP ionization experiments with pulsed lasers (for references, see above) and tightly bound atoms or with microwave fields and alkali Rydberg atoms [36, 38, 41, 42], as well as most theories to date, have focused on fields with $\Omega_0 < 1$. When $\Omega_0 \ll 1$, a quasistatic view should be applicable if narrow quantal resonances [43] are avoided, while at higher frequencies dynamics should play an important role.

Early work on the non-LP ionization of excited hydrogen atoms was theoretical [44, 45], using classical analysis and numerical simulations to follow trajectories near $\Omega_0 = 1$ for the case of a CP field. The approximate classical resonance analysis presented in Sec. 6.F of [46] led to a conclusion that the onset of ionization for hydrogen atoms driven by a CP field near $\Omega_0 = 1$ would occur at a peak amplitude estimated to be 1.5–2 times below that for an LP field. This estimate correctly anticipated the trend found experimentally; see Sec. 5 below.

The recent flurry of theoretical activity on the ionization of Rydberg atoms by a CP field was stimulated by the first CP experiment with alkali atoms [36]. Since then several theoretical groups have published growing series of papers on excited hydrogen atoms driven by a strong CP field. These include [13, 39, 47–79]. Several contain the lively give-and-take of theoretical controversies not yet completely resolved, both about the ionization mechanism in a CP field and the existence and nature of nonspreading wave-packet states of hydrogen atoms in a strong CP field.

Unlike the LP and CP cases, the elliptically polarized (EP) case has no integrals of the motion: it has three degrees of freedom and is not conservative. Moreover, the case that interests us here, that of many unperturbed states being strongly coupled, is unlikely to be amenable to any simple selection rule analysis for LP vs. CP vs. EP driving.

Intended to be a reasonably self-contained, mid-length review that emphasizes experimental and theoretical work on hydrogen atoms, this paper is organized as follows. Section 2 describes the experimental method. Section 3 reviews what has been learned from previous LP experiments and theory. It describes six regimes of strong-field dynamical behavior, each lying within a certain range of the scaled frequency Ω_0, though the dividing lines are fuzzy. Section 4 presents experimen-

tal and classical theoretical results for the polarization dependence of ionization at low scaled frequencies, $\Omega_0 \lesssim 0.1$. For certain, narrow ranges of n_0, striking EP-induced resonances dominate the ionization dynamics. Section 5 presents experimental and classical theoretical results for the polarization dependence of ionization for $0.6 \lesssim \Omega_0 \lesssim 1.4$. This includes a range where the ionization dynamics is dominated by the influence of the main, pendulumlike resonance zone centered at $\Omega_0 = 1$. Section 6 presents some conclusions and directions for future work.

2. Experimental method

2.1. Apparatus

Because the details of the experimental method are given in [1, 2, 80–83], this discussion is brief. Ions extracted from a hydrogen ion source were accelerated, focused, and deflected in a mass-analyzer magnet tuned to transmit protons. 14.6 keV H^+–Xe electron-transfer collisions produced fast hydrogen atoms with an approximately n^{-3}-weighted distribution of states. A static electric field $\gtrsim$ 100 kV/cm ionized all $H(n > 9)$ atoms, while those with $n \lesssim 6$ radiatively decayed in flight. With parabolic quantum numbers $(n, n_1, |m|)$ labeling Stark substates, in a 29.2 kV/cm static field half of the $(7, 0, 0)$ population was driven into $(10, 0, 0)$ by a CO_2 laser. Another CO_2 laser drove the transition $(10, 0, 0) \rightarrow (n_0, 0, 0)$ in a static field whose strength was between a few to a few hundred V/cm. This created a beam of $H(n_0)$ atoms that was collimated by a 0.21 cm diameter aperture before it traversed the 9.904 GHz cavity described in Sec. 2.2. This paper involves $H(n_0)$ atoms with individual n_0-values between 29 and 98. A surviving atom signal I_{surv} consisting of energy-labeled protons was produced by ionization of excited atoms in a voltage-labeled, rectilinear, 9.8 GHz cavity, followed by electrostatic deflection, transmission through an electrostatic filter lens, and detection in a particle multiplier; see Sec. 13.3c of [80]. A uniform, longitudinal 3.8 V/cm field before the 9.8 GHz cavity caused only atoms with n-values below the n cutoff $n_c^q \approx 110$ to contribute to I_{surv}; see Sec. 2.3.3 of [1].

Reduction of the signal I_{surv} was caused by $H(n_0)$ in the 9.904 GHz cavity being either truly ionized or excited to final n-values $n > n_c^q$. Calling these two contributions to the reduction in I_{surv} an "ionization" signal [1], the "ionization" and survival probabilities are related as $P_{\text{"ion"}} = 1 - P_{\text{surv}}$. Experimentally, we measured P_{surv}, but we interpret this in terms of $P_{\text{"ion"}}$; see Sec. 2.3.4 of [1]. Energetically, "ionization" required the net absorption of at least $\mathcal{N} = 1 + \left[\left((2n_0^2)^{-1} - (2n_c^{q\,2})^{-1}\right)/\omega\right]$ photons, where $[\ldots]$ means "the integer part of". At $\omega/2\pi = 9.904$ GHz, and taking $n_c^q = 110$, $\mathcal{N} = 396$ at $n_0 = 29$, dropping to $\mathcal{N} = 8$ at $n_0 = 98$.

For clarity in the remainder of this paper, we no longer write "ionization" and "ion", but the presence of quotation marks will be understood.

2.2. Microwave cavity

The cylindrical brass cavity had inner dimensions length $L = 2.57$ cm and diameter $D = 6.350$ cm. The beam traversed 0.26 cm diameter holes in the

0.159 cm thick entrance and 0.476 cm thick exit endcaps, respectively. Exciting the cavity via two spatially orthogonal coupling slots in the entrance endcap to resonate degenerate TE_{121} modes, one could vary at will the polarization of the 9.904 GHz cavity field. The on-axis field was

$$\boldsymbol{F}(t) = \lambda(t)\mathcal{F}[\widehat{\boldsymbol{X}}\alpha\sin(\omega t) + \widehat{\boldsymbol{Y}}\sin(\omega t + \delta)], \tag{1}$$

with $0 \leq \alpha \leq 1$ and $0 \leq \delta \leq \frac{\pi}{2}$; $0 \leq \lambda(t) \leq 1$ is the 152 cycle, half-sine pulse envelope seen by the atoms in their rest frame, and (X, Y, Z) are spatial coordinates in the laboratory frame. The ratio $F/\mathcal{F}$ of the peak amplitude F to the amplitude $\mathcal{F}$ of the $\widehat{\boldsymbol{Y}}$-component depends on the polarization. With an attenuator in one arm, to control α, and a phase shifter in the other, to control δ, we used the atoms to fine-tune the polarization. Extinguishing the power in one arm ($\alpha \leq 0.0002$) created LP. To create EP one could either (i) keep $\alpha = 1$ and vary δ or (ii) make $\alpha < 1$ and keep $\delta = \pi/2$ or (iii) vary both α and δ. Experimentally it was more precise to use scheme (ii), but for comparisons with theory to be made below, it will be easier to characterize the EP via scheme (i), for which $F/\mathcal{F} = \sqrt{2}\cos(\delta/2)$ varies from 1, at CP, to $\sqrt{2}$, at LP.

For converting scalar microwave power measurements to F (or $\mathcal{F}$) with an estimated 5% accuracy for the case of arbitrary polarization, we adapted the method presented for LP cavity fields in [84]. S. Zelazny [85] kindly checked this method for determining the power-to-amplitude calibration for our CP microwave ionization data for hydrogen. He used the same apparatus to take CP Stueckelberg oscillation data (for the case of LP fields, see [86]) for $(1sn_0s)^3S_1$ He Rydberg atoms with n_0 near 30. He calculated Floquet eigenvalues for He triplet Rydberg atoms in the CP field to provide quasienergy potential curves for modeling the experimental data and determining the absolute field amplitude to 5%.

2.3. Ionization curves

Taken for LP, CP, and two values of EP, Fig. 1 shows representative ionization curves, P_{ion} vs. the scaled peak field amplitude F_0, for two different, nearby n_0 values. For both the scaled frequency Ω_0 is low enough to be in regime-II, as is described for LP in the next section. Little change occurs near the onset of ionization as the polarization is varied. However, this is not the case well past the onset of ionization: the CP curves "stretch out", reaching $P_{\text{ion}} = 1$ only at a significantly larger value of F_0 than do the other curves. Why this happens, as well as what produces the structure evident in the $\delta = 0.45\pi$ EP curve for $n_0 = 42$, will be explained in Sec. 4. For now we emphasize the usefulness of the stretching out for experimentally setting CP precisely. In fact, for large P_{ion}, say $P_{\text{ion}} = 0.8$, the measured CP peak field thresholds were systematically larger than those for LP driving for $n_0 = 30, \ldots, 78$. (No similar, simple statement applies to smaller values of P_{ion} and/or $75 < n_0 \leq 98$.) Because, for these parameters, small departures from CP to EP lowered the large-P_{ion} threshold, we used this dependence, usually for $n_0 = 58$, to fine-tune the polarization to CP [36, 82, 83] giving $\alpha = 1.00 \pm 0.05$ and $\delta = 90° \pm 1°$.

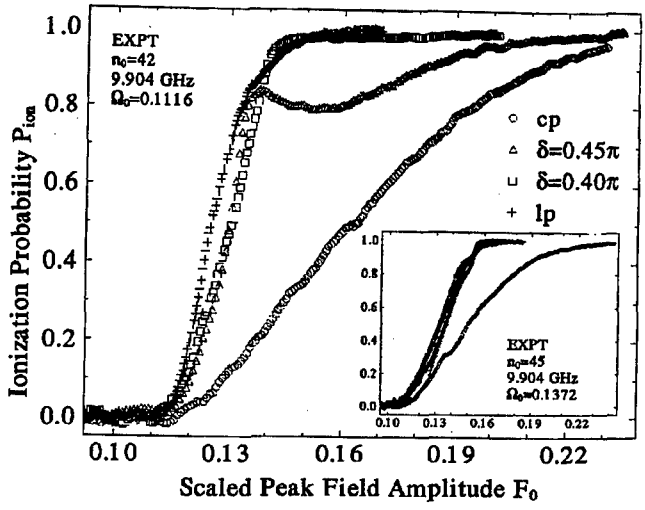

Fig. 1. A survey of the polarization dependence for experimental ionization curves for $n_0 = 42$ and $n_0 = 45$ (inset).

3. Ionization by a linearly polarized field

3.1. Regimes of behavior

In LP experiments at Stony Brook we have thus far varied Ω_0 in a stepwise manner between 0.021–2.8 with use of cavities between 7.6 and 36 GHz and various ranges of n_0-values between 24 and 98; for reviews, see [1, 2, 6, 81]. We have also used a broadband, waveguide interaction region for a smaller number of LP studies between 26–40 GHz; see, e.g., [87–89] and see the early 9.6–11.4 GHz LP waveguide data in [90], reconsidered in Appendix B of [1]. The combined experimental-theoretical investigation of this wide dynamic range of Ω_0 led to classifying six different regimes of dynamical behavior, the first five of which we have studied experimentally. References [1, 2] discuss them in some detail. The dividing lines between these regimes are fuzzy.

Figure 2 is helpful for a brief description of regimes I through V. It compares two sets of our experimental data with the results of 3d classical Monte Carlo calculations (3dCL) [91–93] that closely modeled the experimental situation: for each initial classical principal action I_0 a microcanonical distribution of orbits, which corresponds to the uniform distribution of quantal substates of fixed n_0 that entered the microwave cavity in the experiment [1]; the pulse envelope $\lambda(t)$; and the n cutoff n_c^q. Plotted are scaled 10%-thresholds, i.e., the scaled amplitude $n_0^4 F(0.1) = F_0(0.1)$ at which $P_{\rm ion}$ reaches 0.1, vs. Ω_0.

Regime-I: the quasistatic tunneling regime. When Ω_0 gets low enough, one expects quantal penetration of the slowly oscillating Coulomb–Stark potential barrier to become the dominant ionization mechanism. Comparisons of 9.91 GHz data for $n_0 = 24$–32 with 3d quantal and theoretical calculations [94], reviewed in [1], show this behavior: as n_0 decreases with fixed ω, the experimental onset of ionization falls systematically *below* the classical onset. A 1d theoretical

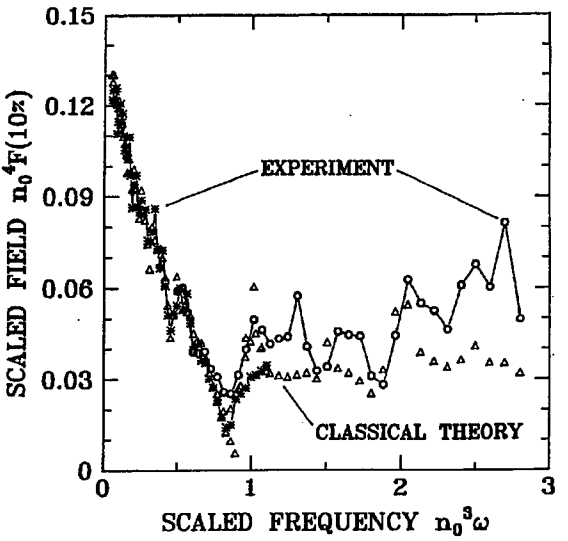

Fig. 2. Scaled amplitudes for 10% ionization probability for 3d hydrogen atoms in an LP field. (∗): 9.92 GHz experiments with a flat-top pulse envelope with each $n_0 = 32, \ldots, 90$ and an n-cutoff $n_c \approx 92$; (○): 36.02 GHz experiment with a flat-top pulse envelope with each $n_0 = 45, \ldots, 80$ and an n-cutoff $n_0 \approx 89$; (△): 3d classical Monte-Carlo simulations of the experiments.

model [43, 95, 96] reproduces and explains this behavior when the coupling constant $C_{n_0} = 1.5 n_0 (n_0^3\omega)(n_0^4 F)$ between adjacent quantal adiabatic basis states is sufficiently small. At 9.91 GHz, this occurs for $n_0 \lesssim 28$, or $\Omega_0 \lesssim 0.03$; see Fig. 16 of [1]. Reference [43] predicts that the quantal resonances between adiabatic states, which are the distinctive feature of regime-II discussed next, will also be present in regime-I, but that as a function of frequency the resonances get exponentially narrow as Ω_0 decreases.

Regime-II: the low frequency regime. For $0.05 \lesssim \Omega_0 \lesssim 0.3$, some experimental microwave ionization and quench curves have shown structures such as non-monotonic bumps, steps, or changes in slope; see ionization curves in [1, 96] for examples. These structures can be understood as the consequence of amplitude-tuned resonances between the adiabatic basis states mentioned above. Other 1d quantal theoretical treatments [10, 97, 98] based in part on Floquet theory have given good numerical estimates for the onset of experimental ionization. In these treatments the experimental structures are caused by interactions at avoided crossings of quasienergy (Floquet) states.

Regime-III: the near-classical regime. For Ω_0 between about 0.1–1.2, the general agreement in Fig. 2 between experimental 10%-thresholds and those obtained from 3dCL must mean that the strong driving field is coupling not a small number of quantal states: the density of participating quantal states must be high enough for near-classical behavior. The onset of classical ionization coincides with the onset of unstable (chaotic) classical trajectories; see [1, 2] for lists of references. The

classical dynamics in regime-III and neighboring regimes is strongly influenced by nonlinear (trapping) resonances, wherein the local motion is pendulumlike; see previously cited references and [1, 2, 19, 28, 99–105]. They give enhanced stability, i.e., higher ionization thresholds, when Ω_0 is near simple rational fractions and give a semiclassical explanation for the bumps in the experimental data in Fig. 2 for Ω_0 near, e.g., 1/3, 1/2, 1, and 2. Nevertheless, localized disagreement in Fig. 2 shows that quantal effects are still important in regime-III.

Notice in Fig. 2 the good agreement for Ω_0 between about 0.5–0.8 for the experimental data sets taken at two different frequencies, 9.9 and 36 GHz, for two different ranges of n_0. This is an example of classical scaling in the quantal dynamics. As is explained in [1, 2], that the 9.9 GHz data lie systematically below the 36 GHz data for Ω_0 between 0.8–1.1 is an n-cutoff effect. This occurs when initial n_0 values in one data set are much closer to the n cutoff than in the other data set. See also Sec. 3.3 and Fig. 4, below.

Regime-IV: the transition regime. In the range $1 \lesssim \Omega_0 \lesssim 2$, Fig. 2 shows that the experimental data begin to deviate in a systematic way from 3dCL, although similarities remain near resonances, e.g., near $\Omega_0 = 1$ and 2. But notice, in particular, that the large measured [1, 2, 33, 87, 89, 106, 107] peak near $\Omega_0 = 1.3$ is absent classically; we shall return to this in Sec. 5.

The first data [106] displaying this striking example of nonclassical local stability with 3d atoms stimulated 1d quantal calculations [108] that confirmed the effect via numerical integrations of the time-dependent Schrödinger equation and gave a clear semiclassical physical picture [19, 109] for it. Via projections of the Husimi (coherent-state-smoothed Wigner function) wave function distribution onto phase portraits of the periodically driven 1d classical hydrogen atom, the stability was shown to be associated with a wave packet localized in the chaotic part of the phase space just outside the main pendulumlike resonance zone, i.e., the one centered at $\Omega_0 = 1$. The preparation of this wave packet was found numerically [108–110] to be associated with the slow turn-on of the driving field amplitude by the pulse envelope $\lambda(t)$. Moreover, subsequent 1d theoretical work [22, 111] associated this nonclassical, local stability specifically with wave packet states living near the *separatrix* of the pendulumlike classical motion. For earlier work on separatrix states in the kicked rotor model, see [112–114].

Following earlier quantal theoretical work carried out in (2 or 3)d + time [115–118], recent quantal calculations using the complex-coordinate-rotated Floquet method [11–13, 17, 49, 119–122] have extended to 3d the treatment of hydrogen in LP microwaves. However, the 3d Floquet calculations still have to address the important role of the slow experimental turn-on $\lambda(t)$ in the 3d experiments.

References [33, 107] used a powerful experimental technique to demonstrate the classical "origin" of the nonclassical local stability peak at $\Omega_0 \approx 1.3$, viz., that it scaled classically; see also [1, 2, 32]. When n_0, ω, and the microwave amplitude F were all varied, the nonclassical local stability remained near $\Omega_0 = 1.3$ and for a nearly constant value of the scaled 10%-threshold $F_0(0.1)$. This was shown for three ranges of n_0 at the driving frequencies 26.4, 30.36, and 36.0 GHz.

Moreover, Refs. [2, 87, 89] showed experimentally and theoretically that broad-band noise added to the coherent driving field had a strong effect on the

nonclassical peaks. Indeed, *the addition of noise was used as an experimental tool* for finding the influence of separatrix states both below and above the resonance zone centered at $\Omega_0 = 1$. Reference [89] demonstrated a strong frequency dependence near these nonclassical peaks that was also strongly affected by broad-band noise. Remarkably, both the frequency dependence and the influence of added noise observed experimentally with 3d hydrogen atoms near the onset of ionization was reproduced with 1d quantal numerical simulations based on an integration of the time-dependent Schrödinger equation.

Section 5 presents experimental evidence for the persistence with varying polarization of the observed nonclassical local stability associated with separatrix states.

Regime-V: the high-frequency regime. When $\Omega_0 > 2$, observed threshold amplitudes in Fig. 2 rise systematically above classical thresholds. The LP experiments in [106] were stimulated by and provided the first experimental confirmation of the earlier prediction of this quantal effect for periodically driven hydrogen atoms [115, 116, 123, 124]; see also [11, 19, 97, 119] and the reviews [117, 125–128]. Subsequent microwave ionization experiments with hydrogen [129] and rubidium [130] Rydberg atoms confirmed the rise of the thresholds.

The theoretical prediction of the quantal stabilizing effect of *dynamical localization* followed from the hydrogen atom periodically driven by a high frequency, LP field being modeled by the periodically delta-kicked rotor. The kicked rotor is a theoretical model much used in quantum chaos studies, and it is known to be a close analog [114, 131, 132] to the tight-binding model in solid state physics for a periodic 1d lattice perturbed by disorder that causes Anderson (exponential) localization of the electronic wave function. Another experimental realization of quantal kicked-rotor dynamics uses laser cooled sodium atoms [133–135].

Other theoretical explanations for enhanced high-frequency stability of the quantal driven atom vs. its classical counterpart have been based on uncertainty principle violation [136]; dynamics in a severely truncated, quasiresonant state basis [19, 137–139]; and quantal vs. classical transport through cantori [140, 141], but see Secs. 7.4 and 9.4 of [127] for critical comments.

Regime-VI: the photoelectric effect. When the photon energy rises above the threshold for one-photon ionization, $\hbar\omega > (2n_0^2)^{-1}$, all vestiges of classical behavior are gone, at least for weak field intensities. Theoretically, this is predicted not to be so for intensities high enough for so-called *stabilization* phenomena to come into play; see papers in [142] and references therein.

The first experimental evidence for adiabatic stabilization of Ne Rydberg atoms in the $5g$ circular state in a 623 nm pulsed laser field was recently published [143, 144].

3.2. Classical phase-space portraits

Phase portraits of the driven classical motion of a 1d hydrogen atom are a useful aid for interpreting the LP experimental results. Figure 3 shows one made for amplitude $F = 3.14$ V/cm and $\omega/2\pi = 9.923$ GHz with use of a computationally efficient, area-preserving, implicit, iterated mapping that is an excellent

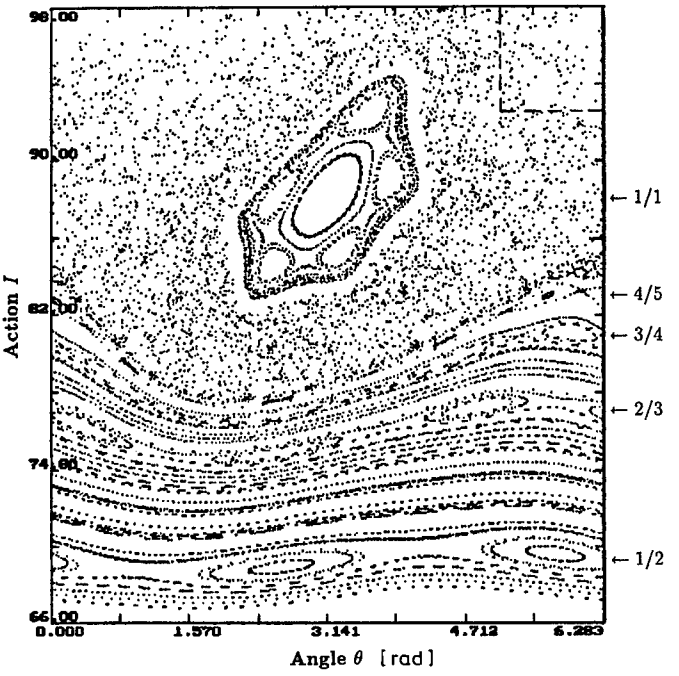

Fig. 3. Phase portrait (Poincaré surface-of-section) for the periodically driven 1d classical hydrogen atom obtained with use of an area-preserving, iterated mapping; see the text. It is an excellent approximation to the continuous dynamics for the scaled frequency $\Omega_0 = I^3\omega$ above about 0.4, here being used to record the evolution of 105 orbits having initial actions between 67.9 and 95.7 (in $\hbar$), for $F = 3.14$ V/cm and $\omega/2\pi = 9.903$ GHz. The number of orbits and range of Ω_0 sampled is enough to show several resonance zones for $\Omega_0 = j/k$ from 1/2 to 1/1. Arrows along the right-hand vertical axis label them. Within each resonance zone, the local motion is pendulumlike and nearly regular, the more so far lower values of I. A region of irregular motion (sea of chaos) encircles the 1/1 zone, which is also surrounded by a five-island-chain, secondary resonance zone that is born from an orbit bifurcation found numerically to occur near 2.96 V/cm. The dashed box in the upper right-hand corner shows size of Planck's quantum of action h.

approximation to the continuous dynamics[‡] for Ω_0 above about 0.4. Note that classical scaling of the dynamics [1] means that if classical dynamical evolution were calculated for different values of I_0, ω, and F that give the same ranges of $\Omega_0 = I_0^3\omega$ and $F_0 = I_0^4 F$ used to make Fig. 3, the classical phase portrait would be identical. However, the area of Planck's constant at fixed Ω_0 and F_0 would change, becoming larger as (I_0 decreases, ω increases, F increases) and becoming smaller

[‡]The mapping used is equivalent to Eqs. (14)–(19) in Ref. [145a], except for adding a missing factor $\sin(\theta_k)$ that was inadvertently omitted from the right-hand side of Eq. (15) and for changing from positive to negative the signs in the right-hand-most terms of its Eqs. (14), i.e., the ones containing the symbol Φ_0; this serves only to move the stable, elliptic fixed points of the primary resonance islands to $\theta = \pi$, in accord with the mapping Eqs. (15) in Ref. [145b].

as (I_0 increases, ω decreases, F decreases). As is reviewed in [1, 2], the effective Planck's constant is $\tilde{h} = h/n_0$; see also Secs. 1 and 5.

Five different resonance zones are labeled by their respective rational values of the scaled frequency $I_r^3\omega = j/k$ associated with a resonant action I_r. (In a 9.923 GHz field, $I_r = 87.2$ gives $I_r^3\omega = 1$.) In a rotating frame the local motion within and near each zone is pendulumlike: librational motion around an elliptic fixed point (corresponding to a stable periodic orbit of the full motion) inside the zone and rotational motion outside the zone on either side of a separatrix (broken by the chaos-producing, higher-order terms beyond the pendulum approximation to the Hamiltonian) that connects to a hyperbolic fixed point (corresponding to an unstable periodic orbit of the full motion). The formula (see [87])

$$I_s^{\pm} = (1 \pm 0.419\sqrt{F_r} + 0.144F_r + \ldots)I_r, \tag{2}$$

where $F_r = I_r^4 F$, gives estimates for the maximal upward I_s^+ and downward I_s^- excursions in action of the separatrix of the 1/1 resonance zone. For the parameters used to make Fig. 3, $I_s^+ = 94.5$ and $I_s^- = 80.8$, so in the pendulum approximation the separatrix contains $(I_s^+ - I_s^-) = 13.7$ units of area measured in Planck's constant h. This gives a semiclassical estimate for the number of quantal states influenced by the main resonance zone at $\omega/2\pi = 9.923$ GHz and $F = 3.14$ V/cm.

One may see by eye that far smaller area and, therefore, far fewer quantal states are associated with the 1/2, 2/3, 3/4, and 4/5 resonance zones. For formulae used to estimate their areas, see [146].

The full, driven classical motion is nonintegrable but only partly so when parameter values are chosen to give a phase portrait of coexisting regular and irregular (chaotic) regions, i.e., a mixed phase space. Each separatrix becomes, in fact, a chaotic layer whose thickness grows with increasing F and within which are other fixed points with small resonance zones and chaotic layers, ad infinitum; see, e.g., p. 810 and Fig. 21 of [104]. Moreover, orbit bifurcations at certain values of the driving field amplitude produce new fixed points, resonance zones, and chaotic layers. Several such bifurcations occur for the main resonance zone at values of F below that used to make Fig. 3. (See also [28] and [147].) Surrounding the 1/1 resonance zone is a chaotic sea produced by higher-order terms beyond the pendulum approximation to the Hamiltonian. These terms mutate the separatrix into stable and unstable manifolds, converting its environs to a "sea of chaos". In this chaotic sea irregular orbits can diffuse to arbitrarily high action if the interaction time is sufficiently long. Indeed, the onset of global chaos is a classical mechanism for ionization.

One also sees in the phase portrait rotational Kolmogorov–Arnold–Moser (KAM) curves (tori) [100, 103, 104, 148, 149] that are impenetrable barriers to transport in a periodically driven, one degree of freedom system; many such tori separate the 1/2 and 2/3 resonance zones.

Above it was remarked that the mapping used to make Fig. 3 is an excellent approximation to the continuous, periodically forced dynamics in 1d for Ω_0 above about 0.4. At lower Ω_0 the approximations used to derive the mapping break down, but there is a deeper reason why not only it but phase portraits in general cease to be very useful at low Ω_0. As Ω_0 decreases, the time during which the electron

can be accelerated in a given direction by the external LP field increases. This means that the momentum impulses given to the electron by the external field get larger, so large that the notion of ionization occurring classically by a diffusive wandering (net) upward in the phase space no longer makes sense. Moreover, as Ω_0 decreases, the separation in action of the $1/k$ (subharmonic for $k > 1$) resonance zones decreases, but with increasing F, their widths explode as $F^{k/2}$ [43, 146, 150].

At low Ω_0 it makes more sense to think of the ionization as taking place by escape over a slowly oscillating barrier in coordinate space.

3.3. LP results: old vs. new

Figure 4 compares the scaled 10%- and 90%-thresholds $F_0(0.1)$ and $F_0(0.9)$, respectively, for the 9.923 GHz LP data set from [1] with those from the present 9.904 GHz LP data set [81, 82] obtained with the cavity described in Sec. 2.2. The

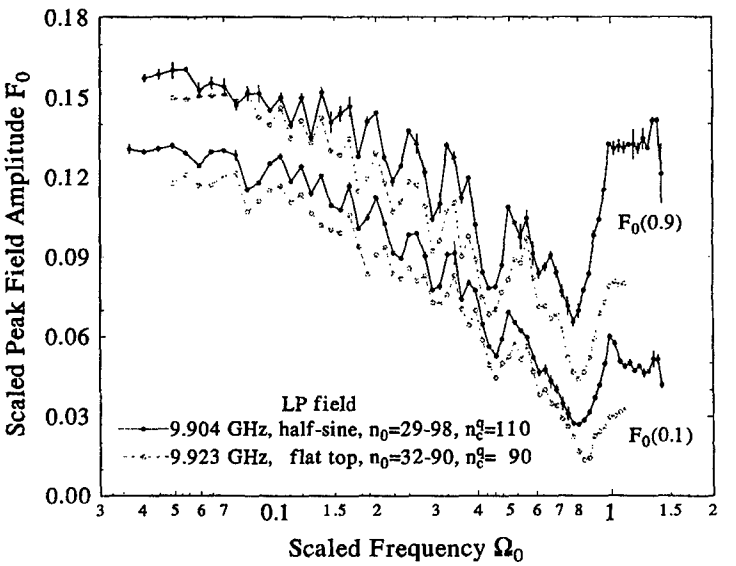

Fig. 4. A comparison of two different sets of LP microwave ionization data; see the text.

gross behavior of the two data sets is similar, but one notable, global difference is the latter data being systematically higher than the former data. The two most important contributions to this are undoubtedly

(i) the significantly shorter peak-field interaction time in the half-sine pulse envelope used to obtain the latter data, viz., above 95% peak value for only 31 field oscillations, compared to 230 oscillations for the flat-top envelope used to obtain the former data;

(ii) the significantly higher n cutoff $n_c^q \approx 110$ used for the latter data, compared to $n_c^q \approx 90$ used for the former data. One expects that this effect would be greatest as n_0 for the former data set approaches $n_c^q \approx 90$; this is just what

one sees in Fig. 4. (See the similar discussion in Sec. 3.5 of [1] about its Fig. 15.)

Because the 59 oscillation turn-on and turn-off (5% to 95% of maximum) used for the 9.904 GHz data was comparable to the 80 oscillation turn-on and 95 oscillation turn-off used for the 9.923 GHz data, i.e., both were "slow", it is less likely that they contributed to the differences in the data sets.

Notice the similar, local, undulatory structure in both data sets. As was explained above, the maxima are caused by the stabilizing influence of resonance zones centered at $\Omega_0 = j/k$. In the 9.904 GHz $F_0(0.1)$ and $F_0(0.9)$ data, there are clear peaks near $\Omega_0 = j/k$ for $k = 1, 2, 3, 4, 5, 6$ with $j = 1$, as well as peaks near 2/5 and 2/3.

Using Eq. (14) of Ref. [1] to estimate the area in units of h inside each $\Omega_0 = 1/k$ resonance zone, we obtain a semiclassical estimate of the number N of quantal states inside. Taking experimental values $F_0(0.1)$ from the 9.904 GHz LP data, the formula gives $(N; 1/k) = (18.6; 1/1)$, $(7.1; 1/2)$, $(4.5; 1/3)$, $(2.6; 1/4)$, $(2.0; 1/5)$, and $(1.4; 1/6)$. This gives a neat quantal/classical correspondence: local maxima in experimental ionization thresholds occur close to $\Omega_0 = 1/k$ when the classical resonance zones centered at these values contain at least one quantal state, i.e., when $N \gtrsim 1$.

Note that local maxima in $F_0(0.1)$ and $F_0(0.9)$ persist to lower values of Ω_0, but these no longer line up with $\Omega_0 = 1/k$ for $k \geq 7$. This could be explained, experimentally, by the discrete sampling of Ω_0 with fixed ω and integer values of n_0 and, theoretically, by the classical resonances getting ever closer as k increases and by N dropping below one for $k \geq 7$. For $F_0 \approx 0.12$, the formula gives, e.g., $(0.7; 1/7)$ and $(0.6; 1/8)$.

Why are the local maxima in the 9.904 GHz data more pronounced than in the 9.923 GHz data? Reason (i) above likely contributes because the shorter the interaction time, the larger the peak field amplitude can be before raising $P_{\rm ion}$ to a given level. Because N for classical $\Omega_0 = 1/k$ resonances grows roughly as $F_0^{k/2}$, see, e.g., Eq. (14) of [1], one expects their stabilizing influence to grow as F_0 grows, as long as the resultant increase in $P_{\rm ion}$ is offset by the shorter interaction time. One expects reason (ii) above to contribute strongly as n_0 approaches n_c^q. This likely explains why the $\Omega_0 = 1$ resonance zone centered near $n_0 = 87$ is less prominent in the 9.923 GHz data, for which $n_c^q \approx 90$ is only slightly higher. See also the discussion for regime-III in Sec. 3.1.

In both data sets, there are local maxima at other values of Ω_0. In Sec. 5 we shall explicitly comment on the peak near $\Omega_0 = 1.3$. As may be seen by comparing experimental data and 3dCL in Fig. 2, the LP peak near $\Omega_0 = 1.3$ is *not* due to a classical 4/3 resonance zone. Rather, as was discussed for regime-IV in Sec. 3.1, this nonclassical peak is associated with a quantal *separatrix state*.

4. Polarization dependence at low scaled frequencies

As was noted in Sec. 2.3, the CP ionization curves in Fig. 1 stretch out compared to those for other polarizations. We now explain why this happens when Ω_0 is low [29, 83]. First we need to recall well-known features of ionization of excited hydrogen atoms by a static, an LP, and a CP field. Hereafter using

a.u. unless explicitly noted, the Hamiltonian in the laboratory coordinate frame (X, Y, Z) is $\mathcal{H}(t) = p^2/2 - 1/R + \boldsymbol{R} \cdot \boldsymbol{F}(t)$. For a static field, $\boldsymbol{R} \cdot \boldsymbol{F}(t) = ZF$, the system is separable in parabolic coordinates (ξ, η, ϕ) [151]. Below the onset of ionization, all three classical actions $\boldsymbol{I} \equiv (I_\xi, I_\eta, I_m)$ [quantum numbers (n_1, n_2, m)] are conserved. Classically, there is a sharp threshold field $F_{\rm crit}(\boldsymbol{I})$ below which the motion with these actions remains bound; from the least robust orbit [quantally, $m = n_1 = 0$, $n_2 = (n-1)$] to the most robust orbit [$n_1 = (n-1)$, $n_2 = m = 0$], $n_0^4 F_{\rm crit}$ varies between about 0.13–0.38. Tunneling through the η-barrier allows ionization for $F < F_{\rm crit}$; for interaction times near 10^{-8} s and $n_0 \approx 40$, it lowers thresholds by 10–15% [1, 152].

For an LP field, $\boldsymbol{R} \cdot \boldsymbol{F}(t) = \lambda(t) ZF \sin(\omega t + \psi)$, with ψ an initial phase; again, separability leads to conservation of m. The dynamics is quasistatic [1, 94] if Ω_0 is sufficiently small and away from exponentially sharp resonances discussed theoretically for 1d in [43]. The spatial reversal of F on each half-cycle interchanges n_1 and n_2; therefore, as Fig. 1 of [94] shows, for a uniform mixture of substates of a given n_0, classically a microcanonical ensemble, the ionization probability $P_{\rm ion}$ rises from 0 to 1 as the scaled amplitude F_0 varies between about 0.115–0.17. This is just the beginning of the wider classical range, $F_0 = 0.13$–0.38, lowered 10–15% by tunneling, discussed above for the static field case.

In a frame (x, y, z) rotating at frequency ω, the Hamiltonian is given by

$$K(t) = p^2/2 - 1/r + \lambda(t)\mathcal{F}y + \omega L_z$$

$$+0.5\lambda(t)\mathcal{F}[y \sin 2\omega t - x(1 - \cos 2\omega t)] \sin \delta_1$$

$$+0.5\lambda(t)\mathcal{F}[x \sin 2\omega t - y(1 + \cos 2\omega t)] \sin^2(\delta_1/2), \qquad (3)$$

where $\delta_1 = \pi/2 - \delta$ measures the deviation from CP.

For CP the Hamiltonian in the rotating frame consists of the first line in Eq. (3), which represents the free hydrogen atom perturbed by a static field term and the Coriolis term ωL_z. (This CP Hamiltonian is close to one giving integrable motion [70–72].) For ω low enough one expects that the Coriolis term should have little effect on the ionization dynamics. References [29, 83] confirmed that it affected $P_{\rm ion}$ very little for $\Omega_0 \lesssim 0.1$ by finding close similarity between classical trajectory ionization curves calculated with (the CP case) and without (the static field case) the ωL_z term. Therefore, at low Ω_0 the lack of interchange of n_1 and n_2 (see above) should cause quantal CP ionization curves to stretch out and approach $P_{\rm ion} = 1$ at a higher value of F_0 than for the LP case.

Though this explains the behavior of the CP curves in Fig. 1, this is not the only polarization-dependent difference. Note the different shape of the $n_0 = 42$ EP curve for $\delta = 0.45\pi$. Figure 5 shows the EP dependence for $n_0 = 42$ over a much finer range, from $\delta = 0.42\pi$ to 0.5π, with an experimental uncertainty $\Delta\delta = 0.01\pi$. Here there is a remarkable local variation of $P_{\rm ion}$ with δ at fixed F_0. Over about the same range of δ, similar EP dependence was observed for $n_0 = 41$ and 43 (data not shown here), but *not* for $n_0 \gtrsim 44$ nor, with exceptions discussed below, for $n_0 \lesssim 40$.

We now extend the discussion above for the CP case to give a classical explanation for the physical origin of the sensitivity of $n_0 = 41, 42, 43$ at 9.904 GHz to

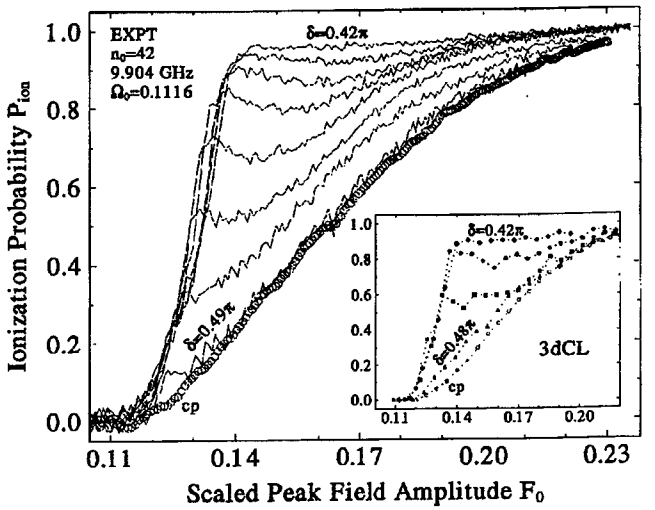

Fig. 5. The detailed elliptical-polarization dependence for $n_0 = 42$ in steps of $\delta/\pi = 0.01$ [$\delta/\pi = 0.02$] for experimental data [for 3dCL calculations (inset)].

EP for values of δ close to CP; mathematical details of the theory are given in [29]. A full understanding of the polarization-dependent dynamics will require 3d quantal calculations, but state-of-the-art 3d quantal (Floquet) calculations have been reported, so far, only for LP and CP and for $n_0 \lesssim 23$ [153]. Until improvements in computers and algorithms enable 3d quantal calculations for 3d hydrogen atoms in an EP field, with the atomic and field parameters used for the present experiments, we must use insights gleaned from comparisons of experimental data with classical calculations and theory.

We begin with 3d classical Monte Carlo calculations (3dCL), the results of which [29, 83] are shown in the inset to Fig. 5. Allowing for the $\pm 0.01\pi$ experimental uncertainty in δ, there is remarkable, quantitative agreement between the experimental data and 3dCL; similar agreement was obtained for $n_0 = 41$ and 43, not shown here.

This agreement validates the use of classical theory to understand the extreme local sensitivity of the ionization dynamics to polarization. But we need to understand what produces the local maximum in $P_{\rm ion}$ at, e.g., $F_0 \approx 0.13$ for $\delta \approx 0.45\pi$ and why it has this effect. Because it involves the complexities of multidimensional dynamics, the discussion here can only be brief; for the details see [29]. The key point is that all perturbations vary little during an unperturbed Kepler period, so one can average over this fast motion, reducing the number of degrees of freedom, and then write the resulting equations for the mean motion in terms of the vectors $\boldsymbol{X} = \boldsymbol{L} - \boldsymbol{A}$ and $\boldsymbol{Y} = \boldsymbol{L} + \boldsymbol{A}$ where $\boldsymbol{L}$ is the orbital angular momentum and $\boldsymbol{A} = (\boldsymbol{p} \times \boldsymbol{L} - r/r)/\sqrt{-2E}$ is the Runge–Lenz vector. For a CP field ($\delta_1 = 0$), both $\boldsymbol{X}$ and $\boldsymbol{Y}$ rotate uniformly about the field direction with the scaled frequency $\overline{\omega} = \sqrt{\omega_{\rm S}^2 + \Omega_0^2}$, where $\omega_{\rm S} = 3\mathcal{F}_0/2$ is a classical Stark frequency associated with the scaled amplitude $\mathcal{F}_0$. For the ranges of F_0 and Ω_0 considered here, $\overline{\omega} < \frac{1}{3}$.

Perturbations of frequency $2\Omega_0$ and strength proportional to δ_1, which appear for an EP field, can resonate with the mean motion when $\overline{\omega} = 2\Omega_0$, i.e., when $\mathcal{F}_0 \approx \mathcal{F}_{0_r} \equiv 2\Omega_0/\sqrt{3}$. For $\Omega_0 = 0.1116$ this gives $\mathcal{F}_{0_r} = 0.13$; equivalently, this is F_{0_r} varying from 0.145 to 0.13 as δ/π varies from 0.42 to 0.5, in agreement with the local maxima in Fig. 5. We use "$2\Omega_0$ resonance" to label this dynamics.

The averaged equations of motion give a model for understanding how the $2\Omega_0$ resonance affects the bound-state dynamics. With the full richness of the details being given in [29], ionization is added post hoc to the model via the time dependence of $\mathcal{F}_{\rm crit}(t) = \mathcal{F}_{\rm crit}(\boldsymbol{I}(t))$, which can be used to mimic the classical escape over the barrier when $\mathcal{F}_{\rm crit}(t) < \lambda(t)\mathcal{F}$. (Recall that $0 \leq \lambda(t) \leq 1$ is the pulse envelope.) This model, compared with exact calculations in [29], shifts one's attention to understanding the temporal evolution of the classical actions $\boldsymbol{I}(t)$ and critical fields $\mathcal{F}_{\rm crit}(\boldsymbol{I}(t))$. Though the details are complicated, the analysis shows that if $I_m > 0$ [< 0] then $\mathcal{F}_{\rm crit}(t)$ decreases [increases] as $\lambda(t)\mathcal{F}$ increases through the resonance by an amount which increases as $\mathrm{d}\lambda/\mathrm{d}t$ decreases. Numerical calculations show that the mean over $I_m > 0$ and $I_m < 0$ is dominated by the behavior of the former, thereby producing the observed local maximum in the ionization probability [29, 83].

Data for $n_0 = 31, 32, 33$ also exhibited extreme sensitivity to EP, but for lower values of δ than for the $2\Omega_0$ resonance. Figure 6 shows results for $n_0 = 31$ for eight values of δ between 0.28π–0.45π ($F/\mathcal{F}$ between 1.28–1.08). Observe the clear similarity between Figs. 6 and 5. The inset shows that the 3dCL results, obtained for the same eight values of δ, again reproduce the experimental polarization dependence.

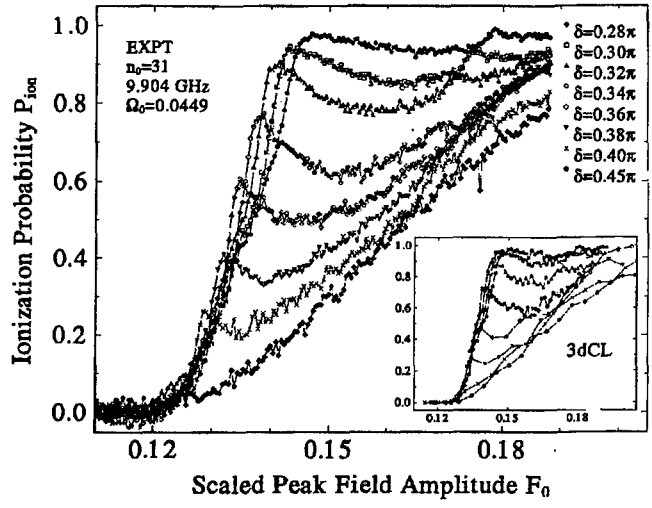

Fig. 6. The detailed elliptical-polarization dependence for $n_0 = 31$ for experimental data [for 3dCL calculations (inset)].

Though $K(t)$, Eq. (3), has harmonic terms only at $2\Omega_0$, let us, nevertheless, extrapolate the frequency-matching condition to a "$4\Omega_0$ resonance": $4\Omega_0 = \bar{\omega} = \sqrt{(3\mathcal{F}_0/2)^2 + \Omega_0^2}$, giving $\Omega_0 = 0.39\mathcal{F}_0$. The classical static field ionization threshold, $\mathcal{F}_0 = 0.13$, gives $\Omega_0 = 0.05$; at 9.904 GHz this gives $n_0 = 32$, the middle of the three n_0-values where extreme sensitivity to EP was observed [81, 83]. This result cannot be accidental. It predicts that successive application in the rotating frame of perturbation theory, classical or quantal, will lead to resonances at even powers of Ω_0. The detailed derivation has been accomplished, so far, only classically and only for the $2\Omega_0$ resonance [29].

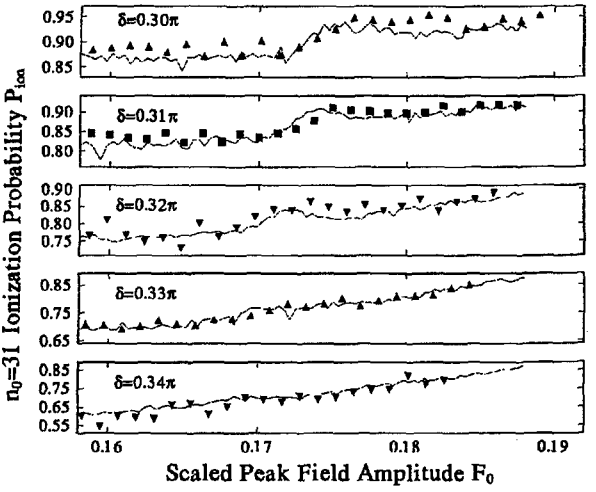

Fig. 7. The detailed elliptical-polarization dependence for $n_0 = 31$ for experimental data (solid curves) and for 3dCL calculations (inverted filled triangle: 422 orbits; upright filled triangle: 864 orbits; filled square: 1728 orbits).

The top three curves in Fig. 6 show another rise in P_{ion} near $F_0 = 0.17$ and a subsequent plateau. For five values of δ/π in steps of 0.01, Fig. 7 compares experimental data in this region with the results of 3dCL. The rise and subsequent plateau in the data for $\delta/\pi = 0.30, 0.31, 0.32$, as well as its disappearance for higher values of δ/π, is quantitatively reproduced by 3dCL. Arguments were given in [83] that this behavior is caused by the "$6\Omega_0$ resonance".

Therefore, these low frequency experiments, supported by 3dCL, establish a series of EP-induced resonances that occur when even integer powers of the scaled driving frequency Ω_0 match the frequency of the mean classical Stark motion in the rotating frame. Such resonances are a striking example of the kind of the richness that can occur in the higher-dimensional dynamics (3d + time) of a driven quantal system. In this case, even classical theory quantitatively reproduces the behavior *and* provides a clear physical picture for what causes it. As was emphasized in [83], this EP-induced resonant dynamics provides a mechanism for controlling the ionization.

5. Polarization dependence near the main resonance zone

In the preceding section we saw that the polarization dependence of the microwave ionization of excited hydrogen atoms can be dramatic at low scaled frequencies. We now examine the polarization dependence for hydrogen atoms with $n_0 = 70, \ldots, 98$ at 9.904 GHz, which corresponds the range of scaled frequency $\Omega_0 = 0.517$–1.417. This includes the main resonance zone centered at $\Omega_0 = 1$, which, we shall see, exerts a controlling influence that makes the ionization dynamics near the onset of ionization independent of polarization when a certain classically derived, amplitude-scaling of the field is used.

The experimental techniques described in Sec. 2 were used to measure [81, 82] 9.904 GHz ionization curves for LP, CP, and a number of different values of EP. From these curves were obtained the 10% and 50% ionization thresholds plotted in Fig. 8 with use of scaled parameters. (Please note the suppressed zeros on the vertical axes of panels (a) and (b).) Focusing on Fig. 8a, note that the dependence of $F_0(0.1)$ on Ω_0 has the same shape for all three polarizations. Also note that the onset of ionization for CP in this range of Ω_0 occurs at lower peak field amplitude F_0 than it does for LP. This behavior is *opposite* to the rule of thumb mentioned in Sec. 1 that emerged from laser multiphoton ionization experiments with tightly-bound atoms.

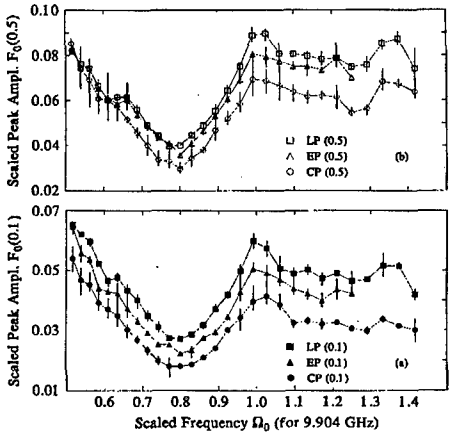

Fig. 8. Frequency- and polarization-dependence of experimental ionization *peak-field* thresholds (filled symbols, $P_{\rm ion} = 0.1$; open symbols, $P_{\rm ion} = 0.5$) for H($n_0 = 70, \ldots, 98$) atoms.

As was explained in Sec. 3, because the local maximum near $\Omega_0 = 1$ is known for the LP case to be due to the stabilizing effect of the main resonance zone, the experimental results show *this effect is independent of polarization.*

This is an important result for the following reason. Using lower case d (upper case D) to represent spatial (phase-space) dimension, the phase portrait in Fig. 3 is a result of following 1d dynamics that is periodically forced in time, visualized stroboscopically in a 2D plot. Colloquially, such dynamics is said to

have $1\frac{1}{2}$ degrees of freedom. For a 3d atom in the time-dependent driving field, the dimensionality depends on the polarization. For LP, the conservation of the projection of the orbital angular momentum on the field polarization axis reduces the dimensionality to 2d + time, or 5D, or $2\frac{1}{2}$ degrees of freedom. Because of a separation of time scales [117], the LP dynamics is well approximated near the onset of ionization by the (1d + time) model ($1\frac{1}{2}$ degrees of freedom). This explains why the surface-state-electron (SSE) model, reviewed in [19], has been able to provide good estimates for onsets of ionization measured with 3d hydrogen atoms in an LP field, at least for Ω_0 up to 2.8 or so [154]. But note that it has been predicted [24, 27] that the SSE model may not provide quantitatively useful 1d estimates for the LP ionization thresholds for 3d hydrogen atoms at much higher scaled frequencies.

The EP dynamics is 3d + time, or 7D, or $3\frac{1}{2}$ degrees of freedom.

Let us look back to Eq. (3), the Hamiltonian $K(t)$ in the frame (x, y, z) rotating at frequency ω. For CP, $\delta_1 = 0$, and ignoring the slow pulse envelope $\lambda(t)$, the time dependence is removed, but there remains the static Stark term $\mathcal{F}y$ and the Coriolis term $\omega L_z = \omega(xp_y - yp_x)$. In contrast to the discussion in Sec. 4, because we are now considering scaled frequencies that are not low, we cannot ignore the Coriolis term. That it mixes coordinates and momenta means that the concept of potential energy surface no longer applies, though one can use so-called zero-velocity curves as an effective potential [53, 63].

Figure 9 compares the experimental data shown in Fig. 8 with the results of 3dCL [82] that modeled all important features of the experiment, including the uniform distribution of initial substates, the pulse envelope $\lambda(t)$, and the n cutoff n_c^q. (See also Fig. 2.) The accord between experiment and 3dCL is equally good for CP, EP, and LP, with wide regions of striking agreement and those of disagreement being similarly localized for all polarizations. Systematically, the 3dCL lie below experimental data (a) for $\Omega_0 \gtrsim 1.15$ and (b) for $0.8 \lesssim \Omega_0 \lesssim 0.9$. Using in Eq. (2) the coordinates for the local maximum in the LP data at $(\Omega_0, F_0(0.1)) \approx (1.33, 0.052)$ gives $I_s^+ = 95$ for the location of the upper separatrix of the pendulum, in good agreement with the local maximum in the LP data at $n_0 = 96, 97$. Similarly, on the lower side of the $\Omega_0 = 1$ resonance bump, using the coordinates in the LP data at $(\Omega_0, F_0(0.1)) \approx (0.083, 0.028)$ gives $I_s^- = 81$ for the location of the lower separatrix of the pendulum; this is in good agreement with the largest local excursion at $n_0 = 82, 83$ of the LP data *above* the 3dCL results, which is matched by excursions in the EP and CP data, too.

We interpret these results as demonstrating the *polarization independence* of the nonclassical, stabilizing influence of quantal separatrix states prepared in the experiment from both above *and* below the pendulumlike resonance zone, i.e., associated with both the upper and lower branches of the separatrix.

Note that the nonclassical stability near the upper branch of the separatrix occurs at $(n_0; \omega/2\pi) = (96, 97; 9.904 \text{ GHz})$. This may be compared to previous LP data [33, 87], where it occurred for (62;36.0 GHz), (66;30.36 GHz), and (69;26.4 GHz). That enhanced, nonclassical stability associated with quantal separatrix states persists from 36.0 GHz to 9.904 GHz shows that this semiclassical

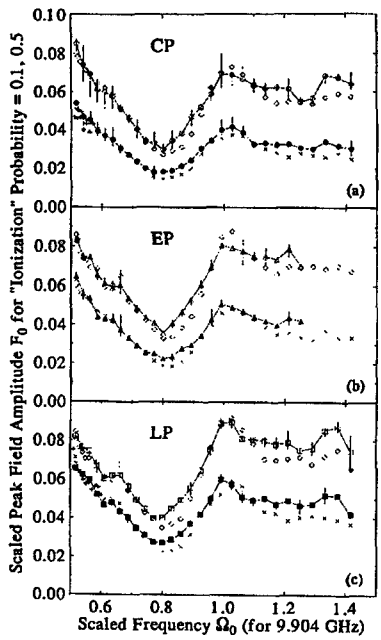

Fig. 9. The same data shown in Fig. 8 compared with the results of 3d classical Monte Carlo simulations (X) for (a): CP; (b): EP; (c): LP; and with the results of 2d classical Monte Carlo calculations (cross) for (a): CP and (c): LP. See the text.

effect [33] is insensitive to at least a 50% variation in the effective Planck's constant $\tilde{\hbar}$; see Secs. 1 and 3.2.

Other disagreements between experiment and 3dCL in Fig. 9 are localized near the top of the $\Omega_0 = 1$ resonance bump, but they are not systematic.

Also shown in Fig. 9 are the results for CP, frame (a), and LP, frame (c), of classical calculations [39] used to predict 10%-ionization thresholds for LP and CP fields over the scaled frequency range $0.01 \leq \Omega_0 \leq 0.6$; these were carried out before the present experiments on the polarization dependence of the microwave ionization of 3d hydrogen atoms were done [81–83]. Let us refer to these calculations as 2dCL because they used only ensembles of orbits whose plane of motion included the microwave electric field vector. In these 2dCL, unlike the subsequent experiments, the initial principal action was held fixed, and the frequency ω was changed to vary Ω_0. The pulse envelope used in the 2dCL rose over 200 initial Kepler periods T_K, remained flat for $40T_K$, and fell over $200T_K$. This is not too different from the experimental, half-sine pulse shape, see Sec. 2.2, whose 152 field oscillation duration corresponds to $294T_K$ at $n_0 = 70$, dropping to $107T_K$ at $n_0 = 98$. The reasonable agreement among the 2dCL, the experimental data, and the 3dCL in Fig. 9, where they overlap, bears out our expectation that modest changes in the pulse shape will exert only a small influence on the ionization thresholds when Ω_0 is not "too high". For additional 2dCL and a discussion of classical time scales for hydrogen atoms driven by a strong CP field at values of Ω_0 below the main resonance zone, see [39].

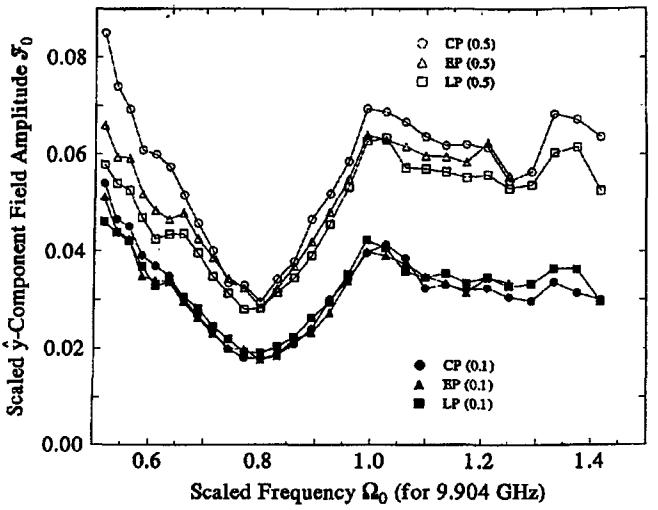

Fig. 10. Frequency- and polarization-dependence of the measured ionization thresholds expressed in terms of the scaled $\widehat{\mathbf{Y}}$-component field amplitude $\mathcal{F}_0 = n_0^4 \mathcal{F}$ defined in the text.

Figure 10 replots the experimental data in Figs. 8 and 9 using a field parameterized with the scaled $\widehat{\mathbf{Y}}$-component amplitude $\mathcal{F}$ for $\alpha = 1$ and variable δ; see Eq. (1) in Sec. 2.2. For our [LP] $\{EP\}$ (CP) data, this $\mathcal{F}$ is $[1/\sqrt{2}]$ $\{1/1.26\}$ (1.00) times the peak amplitude F. Plotted this way the classically scaled thresholds $\mathcal{F}_0 \equiv n_0^4 \mathcal{F}(X)$ vs. Ω_0 *are insensitive to polarization near the main resonance for low* X; e.g., for $\Omega_0 > 0.63$ the $\mathcal{F}_0(0.1)$ thresholds are nearly identical for LP, EP and CP. *However, this agreement persists only up to* $X = 0.3$*; at* $X \gtrsim 0.5$ *the CP thresholds are systematically higher.*

Encouraged by the agreement of the data with classical simulations, and realizing that the high values of n_0 and inherent 3d nature of this problem strain the most advanced quantal computations [11, 76, 153], a classical theory was used [82] to understand these results; Ref. [155] gives details. Here we provide only a very brief qualitative explanation of why classical dynamics leads to the invariance of $\mathcal{F}_0(X)$ with respect to polarization, observed for $X \leq 0.3$, and how the main resonance causes it. The dynamics of the 3d hydrogen atom is determined by the Hamiltonian $H = p^2/2 - 1/r + r \cdot \boldsymbol{F}(t)$, where $\boldsymbol{F}(t)$ was given in Eq. (1). Using the unperturbed, $\boldsymbol{F} = 0$, angle-action variables $(\theta_n, \theta_l, \theta_m, I_n, I_l, I_m)$ [156], one can show that near the principal resonance, where $\omega = \omega_{\rm K}(I_n)$, because $\dot{\theta}_n \approx \omega_{\rm K}$ the system has three distinctly different dynamical time scales: fastest is the field variation, slowest is the changing orientation of the Kepler ellipse, and intermediate is the change in θ_n. It follows, see [155], that for $\omega \approx \omega_{\rm K}$ there is a canonical representation in which the Hamiltonian has the form $K = K_{\rm p} + K_{\rm f}$, where $K_{\rm f}$ is a rapidly varying part that causes the escape from the regular, slow motion due to $K_{\rm p}$.

The slow Hamiltonian, $K_{\rm p}$, may be approximated by one similar to that of a plane vertical pendulum subject to gravity, with a "gravitational" coefficient that

is a function of the slowly varying angle-action variables

$$K_{\rm p} = -\frac{3p^2}{2I_{\rm R}^2} + \lambda(t)\mathcal{F}_0 H_{\rm r}(\boldsymbol{\Theta};\delta)\cos q,$$

where $\boldsymbol{\Theta} = (\theta_l, \theta_m, I_l, I_m)$, $I_{\rm R}$ is the value of the principle action satisfying $\omega = \omega_{\rm K}(I_{\rm R})$, and (q,p) are simply related to the variables describing the motion around the Kepler ellipse. Reference [45] analyzes motion produced by a Hamiltonian similar to $K_{\rm p}$, and Ref. [156] shows that $H_{\rm r}$ is an approximate adiabatic invariant and that the angles $\boldsymbol{\Theta}$ vary more slowly than (q,p) which, in turn, vary more slowly than $K_{\rm f}$. Moreover, $H_{\rm r}$ is relatively weakly dependent upon δ, the field ellipticity; the mean of $H_{\rm r}^2$ over a microcanonical distribution is independent of δ.

The slowly varying field envelope adds the final, and slowest, time scale that is important to the ionization dynamics [157]. Including its effect one can, e.g., estimate the ionization threshold at the minimum of $\mathcal{F}_0(X)$ near $\Omega_0 = 0.8$. For $\Omega_0 < 1$ the first orbits to ionize as $\mathcal{F}_0$ increases satisfy two conditions [22]: (i) they adiabatically switch onto the separatrix of $K_{\rm p}$ as $\lambda(t)$ slowly increases from 0 to 1. (ii) The amplitude $\mathcal{F}_0$ must be large enough for the first ($\Omega_0 = 1$) and second ($\Omega_0 = 2$) resonance island to touch: this is the Chirikov overlap criterion [100]. (For recent classical theoretical work applying the resonance overlap criterion to the CP and EP cases, see [74] and [158], respectively.) When (i) is satisfied, the initial phase points gradually move onto the separatrix of $K_{\rm p}$ and then wind around the edge of the resonance island. The presence of $K_{\rm f}$ converts separatrices into stable and unstable manifolds. When (ii) is satisfied, a proportion of orbits transfers to the unstable manifold of the $\Omega_0 = 2$ island and subsequently to higher actions that easily ionize.

These two conditions provide estimates for the frequency of the minimum threshold, near $\Omega_0 = 0.8$, and also the critical values of $\mathcal{F}_0$ at which ionization first occurs, $\mathcal{F}_0^c(\boldsymbol{\Theta},\delta)$; Ref. [155] gives details. Since the angles $\boldsymbol{\Theta}$ are slowly varying functions of time, the minimum of this function gives an estimate of the critical field. This minimum turns out to be only weakly dependent upon δ. As δ increases from 0 to $\pi/2$, $\min(\mathcal{F}_0^c(\boldsymbol{\Theta},\delta))$ decreases monotonically from about 0.014 to 0.011 and Ω_0^c from 0.78 to 0.77. In the 3dCL simulations the minimum of $\mathcal{F}_0(0.1)$ decreases from 0.016 to 0.014, a statistically insignificant change, and $\Omega_0^c \approx 0.8$, for all δ.

The analysis sketched above uses the approximate Hamiltonian $K_{\rm p}$ to give a theoretical explanation for the insensitivity to polarization of the ionization thresholds $\mathcal{F}_0(X = 0.1)$ plotted in Fig. 10. Therefore, it seems clear that the pendulumlike resonance dominates the strong-field dynamics in the neighborhood of Ω_0. Because such resonances are generic features of mixed-phase-space classical systems and have a clear quantal analog [22, 99, 105, 159], this result should not be regarded as a special case.

It is interesting to ask what determines the boundaries of the influence of the main resonance zone. We tentatively conclude that the marked divergence of the thresholds for different polarizations in Fig. 10 at $\Omega_0 \approx 0.63$ is the signature of its lower boundary, but analysis to demonstrate this theoretically must be left for future work. It is tantalizing that this divergence might supply a sort of crude

spectroscopy for experimentally determining where the boundaries of pendulumlike resonance zones occur in a quantal dynamical system. Because one expects the effect of quantal tunneling — now in phase space [160], not configuration space — to blur whatever sharpness there is to classical barriers to transport, even a crude spectroscopic tool homes in on some very interesting physics.

6. Conclusions

The results of our first experimental forays [81–83] into the *terra incognita* of the polarization dependence of the microwave ionization of excited hydrogen atoms has presented some surprising similarities with the extensive body of previous LP results as well as a new discovery. The surprising similarities occur in the data presented in Sec. 5 for $0.6 \lesssim \Omega_0 \lesssim 1.4$, a range that overlaps the near-classical regime-III and the transition regime-IV. When an amplitude scaling relation given by classical theory is used, the experimental data here show that, near onset, i.e., for $P_{\text{ion}} \lesssim 0.3$, the scaled ionization thresholds are approximately independent of polarization. The similarity of the EP and CP behavior with the LP behavior was an unanticipated surprise. Classical theory shows that it is a result of separation of time scales in a regime where the dynamics is influenced by the main resonance zone. For field amplitudes $\mathcal{F}$ raising P_{ion} significantly above 0.3, however, the simple similarity expressed by the theoretical amplitude scaling relation goes away. Perhaps the nature of the dynamics or its effective dimensionality change as $\mathcal{F}$ increases. We need to understand how the most easily ionized orbits (classically) or wave packets (quantally) differ from those that do not ionize until much higher values of $\mathcal{F}$. However, though the theoretical amplitude scaling relation breaks down for higher values of $\mathcal{F}$ and P_{ion}, the stabilizing influence of quantal separatrix state(s) above and below the main resonance zone does not. It will be fascinating to study and understand the detailed reasons for this behavior.

The new discovery is found in the data presented in Sec. 4 for $\Omega_0 \lesssim 0.1$. For LP driving this range overlaps the low-frequency regime-II, which is defined by resonances between quantal adiabatic states of the (atom + field) system, and the quasistatic tunneling regime-I. For certain narrow ranges of n_0 at fixed driving frequency ω, we find extreme sensitivity of the ionization dynamics to the ellipticity of an EP field near CP. Surprisingly, this behavior is reproduced quantitatively by completely classical calculations that, moreover, reveal its cause. In a frame rotating at ω, a CP field at low Ω_0 produces a new, slow motion (classically) or a Stark splitting of energy levels (quantally). In the rotating frame an EP field provides 2ω driving terms that can resonate with this new frequency (splitting). This dramatically influences the ionization dynamics and can be used to control it. It is an excellent example of the kind of manifestly higher-dimensional dynamics that occurs when the polarization of the driving field is no longer restricted to the quasi-1d, LP case.

What about the other dynamical regimes? Will the ionization of excited hydrogen atoms by CP and EP fields be similar to that for the LP field, or will there be new discoveries? Probably yes and yes. As is now being prepared for publication, we have observed [81, 161] that at very low Ω_0 the quasistatic tunneling of regime-I

becomes the dominant ionization mechanism even more dramatically for CP than it does for LP. The LP case was studied earlier [1, 94].

What about much higher Ω_0? Will the *dynamical localization* effect that produces what has been called the *quantal suppression of classical chaos* cause quantal CP and EP ionization threshold amplitudes to rise systematically above their classical values? The previously predicted [123,124], systematic rise of quantal over classical ionization thresholds was first observed in 1988 for LP driving when $\Omega_0 \gtrsim 2$ [106]. Another LP hydrogen experiment [129] confirmed this behavior.

Theoretically there is a prediction "that the same phenomenon occurs in the case of elliptically polarized fields" (which includes the CP case); see Sec. VIII of [117] and its bibliography for earlier references on dynamical localization. Coming from authors who helped to initiate the theoretical and numerical study of dynamical localization as an essential phenomenon in physics, this prediction must be tested experimentally. This is a goal for future work in our laboratory.

If the past is any guide, much remains to be discovered, studied, and understood about the polarization dependence of the microwave ionization of excited hydrogen atoms.

Acknowledgments

The Atomic, Molecular, and Plasma Physics Program of the US National Science Foundation has furnished ongoing support of this research, most recently through grant number PHY-9423001. Michael Nauenberg's persistent but friendly urging to do CP ionization experiments and early financial support by Schlumberger–Doll Research helped the polarization-dependence experiments get underway at Stony Brook. The data reported here were produced as part of the Ph.D. dissertation work of Mark Bellermann at Stony Brook. We mourn the death of our Schlumberger–Doll Research collaborator, colleague, and friend, David Mariani. Derek Richards furnished crucial theoretical support. Steve Zelazny made important recent experimental contributions.

References

[1] P.M. Koch, K.A.H. van Leeuwen, *Phys. Rep.* **255,** 289 (1995).

[2] P.M. Koch, *Physica D* **83,** 178 (1995).

[3] P.M. Koch, in *Chaos/XAOC, Proc. of a Soviet-American Conf.*, Ed. D.K. Campbell, American Institute of Physics, New York 1990, p. 441.

[4] P.M. Koch, L. Moorman, B.E. Sauer, *Comments At. Mol. Phys.* **25,** 165 (1990).

[5] P.M. Koch, in: *Multiphoton Processes*, Eds. G. Mainfray, P. Agostini, CEN-CEA Saclay, Gif-sur-Yvette (France) 1990, p. 305.

[6] P.M. Koch, in: *Chaos and Quantum Chaos*, Ed. W. Dieter Heiss, *Lecture Notes in Physics*, Vol. 411, Springer-Verlag, Berlin 1992, p. 167.

[7] L. Moorman, in: *The Electron*, Eds. D. Hestenes, A. Weingartshofer, Kluwer, Dordrecht 1991, p. 353.

[8] L. Moorman, P.M. Koch, in: *Quantum Nonintegrability*, Eds. D.H. Feng, J.-M. Yuan, World Scientific, Singapore 1992, p. 142.

[9] J.E. Bayfield, S.-Y. Luie, L.C. Perotti, M.P. Skrzypkowski, *Physica D* **83,** 46 (1995).

[10] R. Blümel, U. Smilansky, *J. Opt. Soc. Am. B* **7**, 664 (1990).

[11] A. Buchleitner, D. Delande, J.-C. Gay, *J. Opt. Soc. Am. B* **12**, 505 (1995).

[12] A. Buchleitner, D. Delande, *Chaos Solitons Fractals* **5**, 1125 (1995).

[13] A. Buchleitner, D. Delande, J. Zakrzewski, in: *Multiphoton Processes*, Eds. P. Lambropoulos, H. Walther, Institute of Physics, Bristol 1997, p. 19.

[14] G. Casati, I. Guarneri, *Comments At. Mol. Phys.* **25**, 185 (1991).

[15] G. Casati, B.V. Chirikov, *Physica D* **86**, 220 (1995).

[16] G. Casati, B. Chirikov, *Quantum Chaos: Between Order and Disorder*, Cambridge University Press, Cambridge 1995.

[17] D. Delande, A. Buchleitner, *Adv. At. Mol. Opt. Phys.* **34**, 85 (1994).

[18] R.V. Jensen, *Comments At. Mol. Phys.* **25**, 119 (1990).

[19] R.V. Jensen, S.M. Susskind, M.M. Sanders, *Phys. Rep.* **201**, 1 (1991).

[20] R.V. Jensen, *Nature* **355**, 311 (1992).

[21] J.G. Leopold, D. Richards, *J. Phys. B* **24**, 1209 (1991).

[22] J.G. Leopold, D. Richards, *J. Phys. B* **27**, 2169 (1994).

[23] P.W. Milonni, B. Sundaram, in: *Progress in Optics*, Vol. XXXI, Ed. E. Wolf, Elsevier, Amsterdam 1993, p. 1.

[24] D. Richards, in: *Aspects of Electron-Molecule Scattering and Photoionization*, Ed. A. Herzenberg, American Institute of Physics, New York 1990, p. 55.

[25] D. Richards, J.G. Leopold, in: *The Physics of Electronic and Atomic Collisions XVI*, Eds. A. Dalgarno, R.S. Freund, P.M. Koch, M.S. Lubell, T.B. Lucatorto, American Institute of Physics, New York 1990, p. 492.

[26] D. Richards, *Comments At. Mol. Phys.* **25**, 195 (1991).

[27] D. Richards, *J. Phys. B* **25**, 1347 (1992).

[28] D. Richards, *J. Phys. B* **29**, 5237 (1996).

[29] D. Richards, *J. Phys. B* **30**, 4019 (1997).

[30] W.E. Baylis, G.W.F. Drake, in: *Atomic, Molecular, & Optical Physics Handbook*, Ed. G.W.F. Drake, American Institute of Physics, Woodbury 1996, Ch. 1, p. 1.

[31] J.G. Leopold, I.C. Percival, *J. Phys. B* **12**, 709 (1979).

[32] P.M. Koch, L. Moorman, B.E. Sauer, E.J. Galvez, K.A.H. van Leeuwen, D. Richards, *Phys. Scr. Vol. T* **26**, 51 (1989).

[33] B.E. Sauer, M.R.W. Bellermann, P.M. Koch, *Phys. Rev. Lett.* **68**, 1633 (1992).

[34] Experiment: R.A. Fox, R.M. Kogan, E.J. Robinson, *Phys. Rev. Lett.* **26**, 1416 (1971); theory: P. Lambropoulos, *Phys. Rev. Lett.* **28**, 585 (1972).

[35] L.A. Lompré, G. Mainfray, C. Manus, J. Thébault, *Phys. Rev. A* **15**, 1604 (1977).

[36] Panming Fu, T.J. Scholz, J.M. Hettema, T.F. Gallagher, *Phys. Rev. Lett.* **64**, 511 (1990).

[37] H.R. Reiss, *Phys. Rev. Lett.* **29**, 1129 (1972).

[38] T.F. Gallagher, *Mod. Phys. Lett. B* **5**, 259 (1991).

[39] P. Kappertz, M. Nauenberg, *Phys. Rev. A* **47**, 4749 (1993).

[40] H.R. Reiss, *Prog. Quantum Electron.* **16**, 1 (1992).

[41] C.H. Cheng, C.Y. Lee, T.F. Gallagher, *Phys. Rev. A* **54**, 3303 (1996).

[42] C.Y. Lee, J.M. Hettema, C.H. Cheng, C.W.S. Conover, T.F. Gallagher, *J. Phys. B* **29**, 3401 (1996).

[43] P.A. Dando, D. Richards, *J. Phys. B* **26**, 3001 (1993).

[44] J. Mostowski, J.J. Sanchez-Mondragon, *Opt. Commun.* **29**, 293 (1979).

[45] B.I. Meerson, *Opt. Spektrosk.* **51**, 582 (1981) [*Opt. Spectrosc. (USSR)* **51**, 322 (1981)].

[46] N.B. Delone, B.P. Krainov, D.L. Shepelyansky, *Usp. Fiz. Nauk* **140**, 355 (1983) [*Sov. Phys. Usp.* **26**, 551 (1983)].

[47] I. Białynicki-Birula, M. Kaliński, J.H. Eberly, *Phys. Rev. Lett.* **73**, 1777 (1994). See Comment by D. Farrelly, E. Lee, T. Uzer, *Phys. Rev. Lett.* **75**, 972 (1995) and Reply, loc. cit., p. 973.

[48] I. Białynicki-Birula, M. Kaliński, J.H. Eberly, *Phys. Rev. Lett.* **75**, 973 (1995).

[49] A. Buchleitner, D. Delande, *Phys. Rev. Lett.* **75**, 1487 (1995).

[50] A.F. Brunello, T. Uzer, D. Farrelly, *Phys. Rev. Lett.* **76**, 2874 (1996).

[51] A.F. Brunello, T. Uzer, D. Farrelly, *Phys. Rev. A* **55**, 3730 (1997).

[52] D. Delande, R. Gębarowski, M. Kuklińska, B. Piraux, K. Rzążewski, J. Zakrzewski, in: *Super-Intense Laser-Atom Physics*, Eds. B. Piraux, A. L'Huillier, K. Rzążewski, Plenum Press, New York 1993, p. 317.

[53] D. Farrelly, T. Uzer, *Phys. Rev. Lett.* **74**, 1720 (1995).

[54] D. Farrelly, E. Lee, T. Uzer, *Phys. Lett. A* **204**, 359 (1995).

[55] D. Farrelly, E. Lee, T. Uzer, *Phys. Rev. Lett.* **75**, 972 (1995), a Comment, for which the Reply is *Phys. Rev. Lett.* **75**, 973 (1995).

[56] D. Farrelly, *Phys. Rev. A* **55**, 1550 (1997).

[57] M. Gajda, B. Piraux, K. Rzążewski, *Phys. Rev. A* **50**, 2528 (1994).

[58] K. Ganesan, R. Gębarowski, *Pramana* **48**, 379 (1997).

[59] R. Gębarowski, J. Zakrzewski, *Phys. Rev. A* **51**, 1508 (1995).

[60] J.A. Griffiths, D. Farrelly, *Phys. Rev. A* **45**, R2678 (1992).

[61] T.P. Grozdanov, M.J. Raković, E.A. Solov'ev, *J. Phys. B* **25**, 4455 (1992).

[62] J.E. Howard, *Phys. Rev. A* **46**, 364 (1992).

[63] J.E. Howard, *Phys. Rev. A* **51**, 3934 (1995). See Comment on this article by D. Farrelly, *Phys. Rev. A* **55**, 1550 (1997) and the Reply by J. Howard, *ibid.* **55**, 1552 (1997).

[64] M. Kalinski, J.H. Eberly, I. Bialynicki-Birula, *Phys. Rev. A* **52**, 2460 (1995).

[65] M. Kalinski, J.H. Eberly, *Phys. Rev. A* **53**, 1715 (1996).

[66] M. Kalinski, J.H. Eberly, *Phys. Rev. Lett.* **77**, 2420 (1996).

[67] H. Klar, *Z. Phys. D* **11**, 45 (1989).

[68] M. Nauenberg, *Phys. Rev. Lett.* **64**, 2731 (1990).

[69] A. Peregrine-Smew, D. Farrelly, T. Uzer, *Phys. Rev. A* **51**, 4293 (1995).

[70] M.J. Raković, S.-I. Chu, *Phys. Rev. A* **50**, 5077 (1994).

[71] M.J. Raković, S.-I. Chu, *Physica D* **81**, 271 (1995).

[72] M.J. Raković, S.-I. Chu, *Phys. Rev. A* **75**, 1358 (1995).

[73] K. Rzążewski, B. Piraux, *Phys. Rev. A* **47**, R1612 (1993).

[74] K. Sacha, J. Zakrzewski, *Phys. Rev. A* **55**, 568 (1997).

[75] D. Wintgen, *Z. Phys. D* **18**, 125 (1991).

[76] J. Zakrzewski, D. Delande, J.-C. Gay, K. Rzążewski, *Phys. Rev. A* **47**, R2468 (1993).

[77] J. Zakrzewski, D. Delande, *J. Phys. B* **28**, L667 (1995).

[78] J. Zakrzewski, R. Gębarowski, D. Delande, *Phys. Rev. A* **54**, 691 (1996).

[79] J. Zakrzewski, D. Delande, *J. Phys. B* **30**, L87 (1997).

[80] P.M. Koch, in: *Rydberg States of Atoms and Molecules*, Eds. R.F. Stebbings, F.B. Dunning, Cambridge University Press, London 1983, p. 473.

[81] M.R.W. Bellermann, Ph.D. thesis, State University of New York at Stony Brook, Physics Department, 1995.

[82] M.R.W. Bellermann, P.M. Koch, D.R. Mariani, D. Richards, *Phys. Rev. Lett.* **76**, 892 (1996).

[83] M.R.W. Bellermann, P.M. Koch, D. Richards, *Phys. Rev. Lett.* **78**, 3840 (1997).

[84] B. Sauer, K.A.H. van Leeuwen, A. Mortazawi-M., P.M. Koch, *Rev. Sci. Instrum.* **62**, 189 (1991).

[85] S.A. Zelazny, P.M. Koch, *Bull. Am. Phys. Soc.* **42**, 932 (1997).

[86] S. Yoakum, L. Sirko, P.M. Koch, *Phys. Rev. Lett.* **69**, 1919 (1992).

[87] L. Sirko, M.R.W. Bellermann, A. Haffmans, P.M. Koch, D. Richards, *Phys. Rev. Lett.* **71**, 2895 (1993).

[88] A. Haffmans, R. Blümel, P.M. Koch, L. Sirko, *Phys. Rev. Lett.* **73**, 248 (1994).

[89] L. Sirko, A. Haffmans, M.R.W. Bellermann, P.M. Koch, *Europhys. Lett.* **33**, 181 (1996).

[90] J.E. Bayfield, L.D. Gardner, P.M. Koch, *Phys. Rev. Lett.* **39**, 76 (1977).

[91] O. Rath, Ph.D. thesis, The Open University, Mathematics Faculty, 1990.

[92] O. Rath, D. Richards, 1997, to be submitted to *J. Phys. B.*

[93] D. Richards, in: *Classical, Semiclassical, and Quantum Dynamics in Atoms*, Eds. H. Friedrich, B. Eckhardt, Springer, Berlin 1997.

[94] B.E. Sauer, S. Yoakum, L. Moorman, P.M. Koch, D. Richards, P.A. Dando, *Phys. Rev. Lett.* **68**, 468 (1992).

[95] D. Richards, *J. Phys. B* **20**, 2171 (1987).

[96] D. Richards, J.G. Leopold, P.M. Koch, E.J. Galvez, K.A.H. van Leeuwen, L. Moorman, B.E. Sauer, R.V. Jensen, *J. Phys. B* **22**, 1307 (1989).

[97] R. Blümel, U. Smilansky, *Phys. Rev. Lett.* **58**, 2531 (1987).

[98] H.P. Breuer, M. Holthaus, *Z. Phys. D* **11**, 1 (1989).

[99] G.P. Berman, G.M. Zaslavsky, *Phys. Lett. A* **61**, 295 (1977).

[100] B.V. Chirikov, *Phys. Rep.* **52**, 263 (1979).

[101] B.I. Meerson, E.A. Oks, P.V. Sasorov, *Pis'ma Zh. Eksp. Teor. Fiz.* **29**, 79 (1979) [*Sov. Phys.-JETP Lett.* **29**, 72 (1979)].

[102] G.M. Zaslavsky, *Phys. Rep.* **80**, 157 (1981).

[103] A.J. Lichtenberg, M.A. Lieberman, *Regular and Stochastic Motion*, Springer, New York 1983.

[104] J.D. Meiss, *Rev. Mod. Phys.* **64**, 795 (1992).

[105] L. Sirko, P.M. Koch, *Appl. Phys. B* **60**, S195 (1995).

[106] E.J. Galvez, B.E. Sauer, L. Moorman, P.M. Koch, D. Richards, *Phys. Rev. Lett.* **61**, 2011 (1988).

[107] P.M. Koch, *Chaos* 2: 131 (1992).

[108] R.V. Jensen, S.M. Susskind, M.M. Sanders, *Phys. Rev. Lett.* **62**, 1476 (1989).

[109] R.V. Jensen, M.M. Sanders, M. Saraceno, B. Sundaram, *Phys. Rev. Lett.* **63**, 2771 (1989).

[110] H.P. Breuer, K. Dietz, M. Holthaus, *Z. Phys. D* **18**, 239 (1991).

[111] R.V. Jensen, in: *Quantum Dynamics of Chaotic Systems*, Eds. J.-M. Yuan, D.H. Feng, G.M. Zaslavsky, Gordon and Breach, Langhorne (PA) 1993, p. 113.

[112] G. Radons, R.E. Prange, *Phys. Rev. Lett.* **61**, 1691 (1988).

[113] G. Radons, R.E. Prange, in: *Quantum Chaos, Proc. Adriatico Research Conf. and Miniworkshop, 1990*, Eds. H.A. Cerdeira, R. Ramaswamy, M.C. Gutzwiller, World Scientific, Singapore 1991, p. 333.

[114] R.E. Prange, in: *Chaos and Quantum Chaos*, Ed. W. Dieter Heiss, *Lecture Notes in Physics*, Vol. 411, Springer-Verlag, Berlin 1992, p. 225.

[115] G. Casati, B.V. Chirikov, I. Guarneri, D.L. Shepelyansky, *Phys. Rev. Lett.* **59**, 2927 (1987).

[116] G. Casati, I. Guarneri, D.L. Shepelyansky, *Phys. Rev. A* **36**, 3701 (1987).

[117] G. Casati, I. Guarneri, D.L. Shepelyansky, *IEEE J. Quantum Electron.* **24**, 1420 (1988).

[118] K. Wang, S.-I. Chu, *Phys. Rev. A* **39**, 1800 (1989).

[119] A. Buchleitner, D. Delande, *Phys. Rev. Lett.* **70**, 33 (1993).

[120] A. Buchleitner, D. Delande, *Phys. Rev. Lett.* **71**, 3633 (1993).

[121] A. Buchleitner, B. Grémaud, D. Delande, *J. Phys. B* **27**, 2663 (1994).

[122] A. Buchleitner, D. Delande, *Phys. Rev. A* **55**, R1585 (1997).

[123] D.L. Shepelyansky, *Physica D* **8**, 208 (1983).

[124] G. Casati, B.V. Chirikov, D.L. Shepelyansky, *Phys. Rev. Lett.* **53**, 2525 (1984).

[125] G. Casati, B.V. Chirikov, D.L. Shepelyansky, I. Guarneri, *Phys. Rep.* **154**, 77 (1987).

[126] G. Casati, L. Molinari, *Prog. Theor. Phys. Suppl.* **98**, 287 (1989).

[127] B.V. Chirikov, in: *Chaos and Quantum Physics*, Eds. M.-J. Giannoni, A. Voros, J. Zinn-Justin, Elsevier, Amsterdam 1991, p. 444.

[128] G. Casati, B. Chirikov, *Quantum Chaos: Between Order and Disorder*, Cambridge University Press, Cambridge 1995, p. 3.

[129] J.E. Bayfield, G. Casati, I. Guarneri, D.W. Sokol, *Phys. Rev. Lett.* **63**, 364 (1989).

[130] M. Arndt, A. Buchleitner, R.N. Mantegna, H. Walther, *Phys. Rev. Lett.* **67**, 2435 (1991).

[131] S. Fishman, D.R. Grempel, R.E. Prange, *Phys. Rev. Lett.* **49**, 509 (1982).

[132] D.R. Grempel, R.E. Prange, S. Fishman, *Phys. Rev. A* **29**, 1639 (1984).

[133] F.L. Moore, J.C. Robinson, C. Bharucha, P.E. Williams, M.G. Raizen, *Phys. Rev. Lett.* **73**, 2974 (1994).

[134] F.L. Moore, J.C. Robinson, C.F. Bharucha, B. Sundaram, M.G. Raizen, *Phys. Rev. Lett.* **75,** 4598 (1995).

[135] J.C. Robinson, C. Bharucha, F.L. Moore, R. Jahnke, G.A. Georgakis, Q. Niu, M.G. Raizen, B. Sundaram, *Phys. Rev. Lett.* **74,** 3963 (1995).

[136] J.G. Leopold, D. Richards, *Phys. Rev. A* **38,** 2660 (1988).

[137] R.V. Jensen, J.G. Leopold, D. Richards, *J. Phys. B* **21,** L527 (1988).

[138] D. Richards, J.G. Leopold, R.V. Jensen, *J. Phys. B* **22,** 417 (1988).

[139] J.G. Leopold, D. Richards, *J. Phys. B* **22,** 1931 (1989).

[140] R.S. MacKay, J.D. Meiss, *Phys. Rev. A* **37,** 4702 (1988).

[141] J.D. Meiss, *Phys. Rev. Lett.* **62,** 1576 (1989).

[142] See the papers in *Atoms in Intense Laser Fields*, Ed. M. Gavrila, *Adv. Atom. Mol. Opt. Phys. Supplement 1*, Academic, San Diego 1992 and in the different proceedings whose titles follow that of the conference series *Super-Intense Laser-Atom Physics*, Eds. B. Piraux, A. L'Huillier, K. Rzążewski, Plenum Press, New York 1993; Eds. H.G. Muller, M.V. Fedorov, Kluwer, Dordrecht 1996.

[143] M.P. de Boer, J.H. Hoogenraad, R.B. Vrijen, L.D. Noordham, H.G. Muller, *Phys. Rev. Lett.* **71,** 3263 (1993).

[144] M.P. de Boer, J.H. Hoogenraad, R.B. Vrijen, R.C. Constantinescu, L.D. Noordham, H.G. Muller, *Phys. Rev. A* **50,** 4085 (1994).

[145] (a) V. Gontis, B. Kaulakys, *J. Phys. B* **20,** 5051 (1987); (b) G. Casati, I. Guarneri, D.L. Shepelyansky, *IEEE J. Quantum Electron.* **24,** 1420 (1988).

[146] R. Blümel, *Phys. Rev. A* **49,** 4787 (1994).

[147] J.E. Bayfield, S.Y. Luie, L.C. Perotti, M.P. Skrzypkowski, *Phys. Rev. A* **53,** R12 (1996).

[148] V.I. Arnold, *Mathematical Methods of Classical Mechanics*, Springer-Verlag, New York 1978.

[149] L.E. Reichl, *The Transition to Chaos: In Conservative Classical Systems: Quantum Manifestations*, Springer, New York 1992.

[150] B. Sundaram, R.V. Jensen, *Phys. Rev. A* **51,** 4018 (1995).

[151] D. Banks, J.G. Leopold, *J. Phys. B* **11,** 2833 (1978).

[152] P.M. Koch, D.R. Mariani, *Phys. Rev. Lett.* **46,** 1275 (1981).

[153] LP: A. Buchleitner, D. Delande, *Phys. Rev. Lett.* **75,** 1487 (1995); CP: D. Delande, J. Zakrzewski, A. Buchleitner, *Europhys. Lett.* **32,** 107 (1995).

[154] G.P. Brivio, G. Casati, L. Perotti, I. Guarneri, *Physica D* **33,** 51 (1988).

[155] D. Richards, in preparation.

[156] J.G. Leopold, D. Richards, *J. Phys. B* **19,** 1125 (1986).

[157] R.V. Jensen, *Phys. Scr.* **35,** 668 (1987).

[158] K. Sacha, J. Zakrzewski, *Phys. Rev. A* **56,** 719 (1997).

[159] J. Henkel, M. Holthaus, *Phys. Rev. A* **45,** 1978 (1992).

[160] M.J. Davis, E.J. Heller, *J. Chem. Phys.* **75,** 246 (1981).

[161] M.R.W. Bellermann, P.M. Koch, D. Richards, *Bull. Am. Phys. Soc.* **41,** 1092 (1996).

Proceedings of the International Conference "Quantum Optics IV", Jaszowiec, Poland, 1997

CONTROL OF OPEN QUANTUM SYSTEMS

Y. JAPHA, A.G. KOFMAN AND G. KURIZKI

Department of Chemical Physics, The Weizmann Institute of Science
Rehovot, 76100, Israel

Spontaneous decay of excited cold atoms into a cavity can drastically affect their translational dynamics, namely, atomic reflection, transmission and localization at the interface. We show that the quantum Zeno effect on excitation decay of an atom is observable in open cavities and waveguides, using a sequence of evolution-interrupting pulses on a nanosecond scale.

PACS numbers: 42.50.Lc, 03.65.Bz, 03.75.Be, 42.50.–p

1. Transmission of emitting tunneling atoms in cavities

Spontaneous emission in atomic tunneling has been virtually unexplored before our recent work [1]. Since tunneling is a distinct manifestation of wave-like properties, it is important to raise the basic questions: can spontaneous decay of internal excitations in tunneling atoms be viewed as a decoherence process that is analogous to its counterpart in diffracted atoms? and if so, how would such decoherence manifest itself?

We have put forward a theory of spontaneous emission from a two-level atom as it tunnels through a square potential barrier [1]. Our theory demonstrates that the emission process is describable as *loss of coherence between interfering classical trajectories in space-time*, which constitute the atom tunneling motion. The emitted photon at each frequency is correlated to particular atomic classical trajectories, in a way which makes them measurably distinguishable. This distinguishability destroys their interference [2], as does "which-way" ("Welcher-Weg") information, which is obtainable from spontaneous emission in diffracted atoms [3, 4].

The ensuing analysis rests on two observations. (i) The overall duration of the decay process is much longer than the inverse transition frequency ω_{eg}^{-1} (see below). This allows us to resort to the rotating wave approximation (RWA), which is used in the Wigner–Weisskopf (WW) treatment of spontaneous emission [5]. (ii) Nearly all of the cavity-enhanced spontaneous emission is funneled into the continuum of nearly resonant modes with wave-vectors $\boldsymbol{q} \approx (\omega/c)\widehat{z}$, which are aligned with the cavity axis z, perpendicular to the atomic incidence axis x. This allows us to use the dipole approximation, since $\boldsymbol{q} \cdot \boldsymbol{x} \approx 0$, and neglect off-axis photon recoil effects on the atomic wave packet. Hence, the RWA interaction Hamiltonian of the atom with the cavity-mode continuum becomes effectively one-dimensional,

$H_{\rm int} = -\zeta(x)\int d\omega\rho(\omega)[g_\omega a_\omega|e\rangle\langle g| + \text{h.c.}]$. Here $\zeta(x) = 1$ for $0 \le x \le L$ and 0 elsewhere, i.e., the interaction is confined to the cavity, whose x-axis extent coincides with that of the barrier; $\rho(\omega)$ is a Lorentzian mode-density distribution associated with the cavity-mode line width η [6]; g_ω is the coupling of the atom to the cavity mode at ω and a_ω is the corresponding annihilation operator. The transition frequency ω_{eg} is shifted (renormalized) by the difference between the AC Stark shifts of $|e\rangle$ and $|g\rangle$, $\Delta_{\rm AC} = \Omega_e^2/\delta_e - \Omega_g^2/\delta_g$).

In order to analyze the entanglement of emitted photon states with the translational degrees of freedom of the tunneling atom, we have developed a theoretical approach which combines the WW treatment [5], resulting in exponential decay of the excited state, with the Feynman path-integral method, which yields a coherent sum over the atomic classical trajectories contributing to tunneling [7].

The above analysis yields the probability for an atom incident as a nearly monochromatic wave packet to be transmitted in the excited state

$$P_e^{\rm tr} = |\sigma(E_k, V - i\hbar\Gamma)|^2, \tag{1}$$

where $\sigma(E_k, V)$ is the transmission amplitude for a structureless particle of kinetic energy E_k through a square potential barrier of height V and length L,

$$\sigma(E_k, V) = \left[\cos(pL) - i\frac{k^2+p^2}{2kp}\sin(pL)\right]^{-1}, \tag{2}$$

$k = \sqrt{2mE_k}/\hbar$ and $p = \sqrt{2m(E_k - V)}/\hbar$ being the corresponding wave vectors outside and inside the barrier, respectively. The effect of spontaneous emission is to shift the effective potential V by $-i\hbar\Gamma$.

Plots of Eq. (1) reveal the overall diminishing of $P_e^{\rm tr}$ with γ in both the tunneling (below-barrier) and allowed (above-barrier) regimes of E_k. The corresponding probability $P_g^{\rm tr}$ of the transmitted ground state wave-packet is an incoherent sum (integral) of partial wave-packet transmission probabilities P_ω associated with photon emission at ω

$$P_g^{\rm tr} = \int_0^{E_k} d\omega P_\omega,$$

$$P_\omega = \mathcal{F}(\omega)\sqrt{1 - \frac{\hbar\Delta}{E_k}}|\sigma_\omega(E_k, V)|^2, \tag{3}$$

where $\mathcal{F}(\omega) = \rho(\omega)|g_\omega|^2/(\Delta^2 + \gamma^2)$ and $\sigma_\omega(E_k, V)$ is a complicated function of E_k, V and ω. The most salient effect of spontaneous emission is seen to be (Fig. 1a) the huge enhancement of $P_g^{\rm tr}$ as a function of γ for atoms initially in the deep tunneling regime $pL = \sqrt{2m(V - E_k)}L/\hbar > 1$.

In order to gain more insight into the above general results, we shall henceforth assume that the cavity line width η and E_k satisfy the following inequalities:

$$|E_k - V| \ll \hbar\eta < E_k < \hbar\omega_{eg},\ \gamma \ll \eta. \tag{4}$$

The spectrum of spontaneous emission is then limited to $|\Delta| \ll E_k$ and becomes Lorentzian in this range, $\mathcal{F}(\omega) \approx \mathcal{L}_\gamma(\Delta)$, since the spectral variation of $\rho(\omega)$ and $|g_\omega|^2$ is slow, $\rho(\omega)|g_\omega|^2 \approx 2\pi\gamma$, in accordance with the WW approximation. The equation for σ_ω can now be simplified to

$$\sigma_\omega(E_k, V) \approx \sigma(E_k - \hbar\Delta, V) - \sigma(E_k, V - i\hbar\Gamma). \tag{5}$$

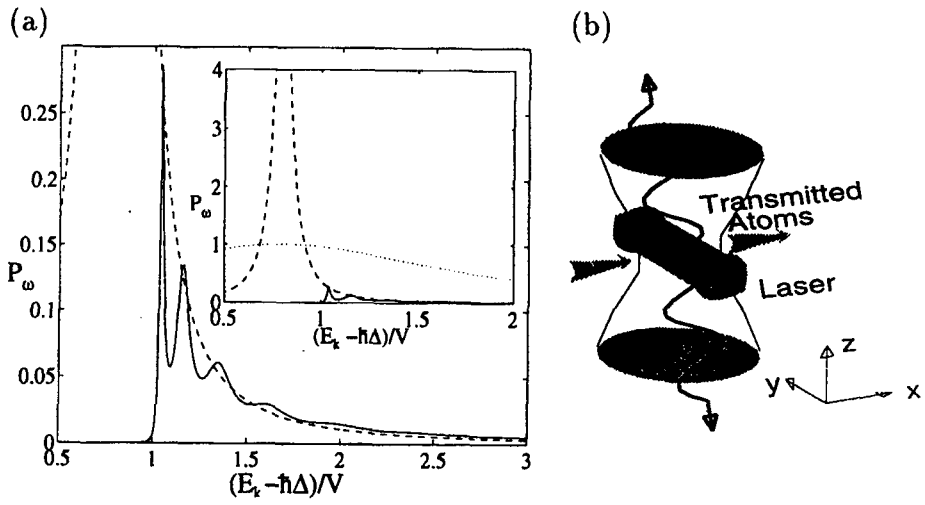

Fig. 1. (a) The energy spectrum of transmitted ground state atoms. Solid curve — transmission probability P_ω [Eq. (3)] (in units of $\hbar/V$) for $E_k/V = 0.8$, $L = 2.5\lambda_{\rm DB}$ $(E_k/V = 1)$, $\gamma = 0.05V/\hbar, \omega_{eg} = 100V/\hbar$ as a function of kinetic energy following emission. Dashed curve — spontaneous line shape. Inset: idem, on a small scale. Dotted curve — cavity line shape. (b) Schematic description of the experiment.

It is seen from Eqs. (3) and (5) that the dramatic enhancement effects in the tunneling regime are due to the first term in (5), corresponding to atoms that have decayed to the ground state shortly after entering the barrier and are subsequently transmitted through the barrier as unexcited atoms with kinetic energy $E_k - \hbar\Delta$, *which can be above the barrier* if $\Delta < 0$. By contrast, the second term in (5) corresponds to atoms that have decayed shortly before exiting the barrier after having effectively been transmitted as excited atoms with the *initial* kinetic energy E_k, whence this term is exponentially small in the tunneling regime. The use of Eq. (5) in Eq. (3) therefore leads to the enhancement of P_ω (Fig. 1a) and $P_g^{\rm tr}$ due to the possibility to gain kinetic energy from the broad vacuum field reservoir by emitting a photon detuned below the resonance $\hbar\omega_{eg}$. In the deep tunneling regime, assuming that $\gamma \ll (V - E_k)$, Eqs. (3)–(5) allow us to roughly estimate that the atoms have probability of order

$$P_g^{\rm tr} \sim \int_V^{E_k+\hbar\omega_{eg}} {\rm d}E\mathcal{L}_\gamma[(E - E_k)/\hbar] \approx \frac{\gamma}{V - E_k} \tag{6}$$

to jump over the barrier into the allowed energy regime by emitting a photon with $\Delta < E_k - V < 0$ (Fig. 1).

Under the assumptions leading to Eq. (5), along with $\hbar\Delta \ll E_k$, we can obtain a simplified expression for the total transmission probability

$$P_{\rm tot}^{\rm tr} = P_g^{\rm tr} + P_e^{\rm tr} \approx \int_0^\infty {\rm d}\tau \int_0^\infty {\rm d}\tau' {\rm e}^{-\gamma|\tau-\tau'|} \widehat{\sigma}^*(\tau, V)\widehat{\sigma}(\tau', V), \tag{7}$$

where $\widehat{\sigma}(t, V)$, the Fourier transform of $\sigma(E, V)$, is the impulse response (to a temporal δ-function) for transmission of a structureless particle. We thus obtain

the following important result: the total transmission probability $P_{\rm tot}^{\rm tr}$ coincides, in the limit of narrow spontaneous line width γ [Eq. (4)], with the transmission probability of a partially incoherent wave packet of a structureless particle with coherence time γ^{-1} (see Ref. [8]).

The following conclusions can be inferred from the above analysis. (a) The probability distribution of the transmitted atoms is approximately Lorentzian for final kinetic energies $E_k - \hbar\Delta$ above the barrier, whereas their counterparts below the barrier only contribute an exponentially small tail to this distribution. (b) The fact that fast atoms emerging from the barrier are almost always unexcited means that the barrier acts as a "filter" that transmits almost only atoms that have already decayed.

These results open a new vista into the transition from quantum dynamics to classicality via decoherence by focusing on the effects of excitation decay on atomic tunneling. In the limit of negligible decay $\gamma \to 0$, which is realizable by detuning the cavity off resonance with ω_{eg}, the excited atomic wave packet with $E_k < V$ exhibits tunneling, which is a result of interference between many classical trajectories, and is characterized by exponentially low transmission $P_e^{\rm tr}$ [Eq. (1)]. When γ is appreciable, the wave packet is dominated by the portion that has decohered by decay into the field-mode continuum and has thereby lost its tunneling properties: its energy spread becomes classical (statistical), giving rise to a Lorentzian tail into the above-barrier energy range, thereby allowing for enhancement of the transmission [Eqs. (3),(7)]. The effects of this decoherence on barrier traversal times will be discussed elsewhere.

The results predicted here can be experimentally realized by a variety of cold atoms. In accord with Eq. (4), the lifetime of the $|e\rangle \to |g\rangle$ transition should preferably be long, above 10^{-6} s. A confocal cavity whose finesse is $\approx 10^5$ and subtends a solid angle of ≈ 0.1 steradians can enhance spontaneous emission rate γ by a factor of ≈ 30. The cavity line width η should be much larger than γ, i.e., preferably above 10 MHz. Correspondingly, the potential energy V and the kinetic energy E_k must be above 0.1 GHz, which requires the laser Rabi frequency $\Omega_{e(g)}$ and detuning $\delta_{e(g)}$ to be well within the GHz range. This implies that the transition frequency ω_{eg} can lie anywhere between the GHz and the optical ranges.

2. Atomic reflection and localization at cavity interfaces

We have recently considered an excited atomic wave packet or an atomic beam propagating from a region where spontaneous emission is negligible ($x < 0$) to a region where spontaneous emission is strongly enhanced ($x > 0$), due to the high density of the electromagnetic field modes. The wave function of the total system (atom plus field) can be written in the following general form in the rotating wave approximation:

$$|\psi(r,t)\rangle = \widetilde{\psi}_e(r,t)|e,\{0\}\rangle + \sum_{q} \widetilde{\psi}_{q}(r,t)|g,\{q\}\rangle, \tag{8}$$

where the ket-vector $|e,\{0\}\rangle$ denotes the atom in the excited state with no photons in the field, whereas $|g,\{q\}\rangle$ corresponds to the ground state of the atom with a photon emitted at a mode q, and $\widetilde{\psi}_{e(q)}$ are the corresponding amplitudes.

One obtains coupled Schrödinger equations for the envelopes of these states given an atom with initial energy E and transition frequency ω_0, $\psi_e(r)$ and $\psi_{\boldsymbol{q}}(r)$ by assuming $\overline{\psi}_{e,\boldsymbol{q}}(r,t) = \psi_{e,\boldsymbol{q}}(r)\mathrm{e}^{-\mathrm{i}(E+\hbar\omega_0/2)t}$. Far from the interaction region the solution describes propagation of the atomic wave packet. The total energy of the incident excited atom $E + \hbar\omega_0$ is then equal to the kinetic energy of the ground state atom plus the emitted photon energy $\hbar\omega_{\boldsymbol{q}}$.

The coupled equations for ψ_e and $\psi_{\boldsymbol{q}}$ yield a complicated integro-differential wave equation for $\psi_e(r_e)$, with $\Gamma(r,r')$ acting as a non-local complex potential whose shape and strength are determined by the confined mode eigenfunctions $\mathcal{E}_{\boldsymbol{q}}(r)$. If the line width of the spatially confined modes $\hbar\eta_c$ is much larger than the atomic energy E, the recoil energy $E_{\mathrm{rec}} \equiv \hbar^2\omega_0^2/2mc^2$ and the spontaneous line width in the confined reservoir, $\hbar\gamma_c$, then the correlation length of the interaction of the emitted photon with the atom is much shorter than the spontaneous decay length and the de Broglie wavelength λ_{DB}. Such an atom effectively moves in a *local* complex potential

$$\Gamma(r) = \int \mathrm{d}^3r'\Gamma(r,r') = |\mu|^2\frac{\sum_{\boldsymbol{q}}|\mathcal{E}_{\boldsymbol{q}}(r)|^2\delta(\omega_{\boldsymbol{q}}-\omega_0)}{\Delta_c - \mathrm{i}\eta_c},$$

where μ is the atomic dipole matrix element, $\mathcal{E}_{\boldsymbol{q}}(r)$ are the field mode amplitudes and Δ_c is the detuning of the atomic transition frequency ω_0 from the center of the spectral line of the reservoir.

In order to concentrate on the atomic motion along the axis of incidence x and avoid diffraction effects caused by the local potential in the directions perpendicular to x, we consider a multimode confocal cavity where the many degenerate modes contributing to $\Gamma(r)$ render it approximately uniform in the directions perpendicular to x. We assume that the transition frequency ω_0 is resonant with the Lorentzian center of the degenerate modes. Then the real part of $\Gamma(x)$ is much less than the imaginary part $\gamma_c(x) = \mathrm{Im}\{\Gamma(x)\}$. We then obtain

$$\frac{\partial^2}{\partial x^2}\psi_e(x) + \frac{2m}{\hbar^2}[E + \mathrm{i}\hbar\gamma_c(x)]\psi_e(x) = 0.$$

For a step-like interaction profile $\gamma_c(x) = \gamma_c\Theta(x)$, where $\Theta(x)$ is the Heaviside step function, the probability to detect an excited atom decreases as $\mathrm{e}^{\mathrm{i}k_\gamma x}$, where $k_\gamma = \sqrt{2m(E+\mathrm{i}\hbar\gamma_c)}/\hbar$, so that only the fraction $|r|^2$ of excited atoms remains at large negative x (to the left of the interface). This reflection increases with the spontaneous emission rate γ_c. The atomic interaction with the confined vacuum reservoir for $\hbar\gamma > E$ is thus analogous to the *skin effect* of light reflection from metals. If the energy of the incident atom is comparable to E_{rec}, the width Δx of the interface should satisfy $\Delta x \approx \lambda_{\mathrm{DB}}(E) \sim \lambda_{\mathrm{opt}}$. A realistic description of the atomic entry into a confocal cavity shows a much lower reflection probability, even for subrecoil energies. However, when the real part of $\Gamma(x)$ contributes too, for ω_0 well off the center of the Lorentzian spectrum (large Δ_c), the cavity can be strongly reflective. This spectral dependence of the reflectivity on the detuning is characteristic of the atomic skin effect.

The spatial variation of the $\boldsymbol{q}$-mode amplitude in Eq. (8) can be estimated for a strong decay $\hbar\gamma_c \gg E$ and incidence energy well above the recoil limit. Then

$\psi_q \propto \exp(+ik_q x)$, where $\hbar k_q = \sqrt{2m(E - \hbar\Delta_q)}$ and $\Delta_q = \omega_q - \omega_0$. Whenever $E > \hbar\Delta_q$, k_q becomes imaginary and $\psi_q(r)$ is exponentially localized at the interface between free space and the confined-field region. A solution with imaginary k_q^x represents a transient atomic wave packet which *disappears* after the incident atomic wave packet decays or leaves the interface, and is accompanied by a *transient bound photon*, which eventually disappears with it, after the time $\sim \hbar/\Delta E$, the inverse of the energy bandwidth ΔE of the incident atom. If such a photon is detected, then a localized atomic state is formed. The subsequent evolution of the atomic wave packet is governed by the free-space Schrödinger equations with the localized atomic distribution serving as the initial condition.

To conclude, we have found that excited-atom reflection from the interface between two spatial regions with different spontaneous emission rates is appreciable for cold atoms and enhanced coupling to the mode continuum, when the effective width of the interface is smaller than the atomic de Broglie wavelength. This reflection is analogous to the optical skin effect of metal surfaces. Transient localized atomic state appear at the interface while an excited two-level atom is crossing it, due to detection of spontaneously emitted "bound photons" at "forbidden" energies, having short lifetime and range of propagation. The regime considered here is essentially different from Ref. [9], where the correlation time of the atom with the emitted photon is large, thereby responsible for the oscillation of the atomic population.

3. Quantum Zeno effect on atomic excitation decay in resonators

The "watchdog" or quantum Zeno effect (QZE) is a spectacular manifestation of the influence of continuous measurements on the evolution of a quantum system. The original QZE prediction has been the inhibition of exponential decay of an excited state into a reservoir, by repeated interruption of the system-reservoir coupling by measurements [10–12].

We have recently demonstrated [13] that the inhibition of *nearly-exponential* excited-state decay by the QZE in two-level atoms, in the spirit of the original suggestion [10], is amenable to experimental verification in resonators. Although this task is widely believed to be very difficult, we have shown, by means of our unified theory of spontaneous emission into reservoirs with arbitrary mode-density spectra [11], that several realizable configurations based on two-level emitters in cavities or in waveguides are in fact adequate for QZE observation. The possibilities for such observation have been examined in various regimes that can arise in resonators.

We start with a general analysis of the evolution of an initially excited two-level atom coupled to an *arbitrary* density-of-modes (DOM) spectrum $\rho(\omega)$ of the electromagnetic field in the vacuum state. At time τ this evolution is interrupted by a short optical pulse, which serves as a quantum measuring device [14–17]. Its role is *to break the evolution coherence*, by transferring the populations of the excited state $|e\rangle$ to an auxiliary state which then decays back to $|e\rangle$ *incoherently* [15].

As in our previous treatment [18], the atomic response, i.e., the emission rate into this reservoir at frequency ω, which is $|g(\omega)|^2\rho(\omega)$, $\hbar g(\omega)$ being the field-atom

coupling energy, is divided into two parts,

$$G(\omega) = G_{\rm s}(\omega) + G_{\rm b}(\omega). \tag{9}$$

Here $G_{\rm s}(\omega)$ stands for the sharply-varying (nearly-singular) part of the DOM distribution, associated with narrow cavity-mode lines, the frequency cut-off in waveguides, or photonic band edges. The complementary part $G_{\rm b}(\omega)$ stands for the broad portion of the DOM distribution (the "background" modes), which always coincides with the free-space DOM $\rho(\omega) \sim \omega^2$ at frequencies well above the sharp spectral features. In an open structure (see below), $G_{\rm b}(\omega)$ represents the atom coupling to the unconfined free-space modes.

We cast the excited-state amplitude in the form $\alpha_e(\tau)e^{-i\omega_a\tau}$, where $\omega_{\rm a}$ is the atomic resonance frequency. Then, for arbitrary DOM spectra and coupling strengths, one can reduce the equations for spontaneous decay [19] to the following evolution equation, up to the interruption time τ:

$$\dot{\alpha}_e(\tau) = -\int_0^\tau {\rm d}t[\Phi_{\rm s}(t) + \Phi_{\rm b}(t)]e^{i\Delta t}\alpha_e(\tau - t). \tag{10}$$

Here $\Delta = \omega_{\rm a} - \omega_{\rm s}$, $\omega_{\rm s}$ is a characteristic frequency corresponding to the maximum or the singularity of the sharp spectral feature, whereas $\Phi_{\rm s}(t)$ and $\Phi_{\rm b}(t)$ are the time-domain Fourier-transforms of $G_{\rm s}(\omega)$ and $G_{\rm b}(\omega)$, respectively,

$$\Phi_{\rm s(b)}(t) = \int_0^\infty {\rm d}\omega G_{\rm s(b)}(\omega)e^{-i(\omega-\omega_{\rm s})t}. \tag{11}$$

Restricting ourselves to sufficiently short interruption intervals τ such that $\alpha_e(\tau) \approx 1$, yet long enough to allow the rotating wave approximation (RWA), Eqs. (10),(11) yield

$$\alpha_e(\tau) \approx 1 - \int_0^\tau {\rm d}t(\tau - t)\Phi_{\rm s}(t)e^{i\Delta t} - \gamma_{\rm b}\tau/2. \tag{12}$$

The terms within the parentheses in Eq. (12) are the contribution of the background DOM, simplified according to the Weisskopf–Wigner approximation [19]. Here $\gamma_{\rm b} = 2\pi G_{\rm b}(\omega_{\rm a})$ is the effective rate of spontaneous emission into the background modes.

Equation (12) is obtained to first order in the atom–field interaction. To the same accuracy, the excited state probability after n interruptions (measurements), $W(t = n\tau) = |\alpha_e(\tau)|^{2n}$, can be written as

$$W(t = n\tau) \approx [2{\rm Re}\alpha_e(\tau) - 1]^n \approx e^{-\kappa t}, \tag{13}$$

where

$$\kappa = 2{\rm Re}[1 - \alpha_e(\tau)]/\tau. \tag{14}$$

In most structures $\gamma_{\rm b}$ is comparable to γ_f and gives rise to an *exponential* decay factor in the excited state probability regardless of how short τ is, i.e., $\kappa = \kappa_{\rm s} + \gamma_{\rm b}$, where $\kappa_{\rm s}$ is the contribution to κ from the sharply-varying modes.

Thus the background-DOM effect cannot be modified by QZE. Only the sharply-varying DOM portion allows for QZE, provided that

$$\kappa_{\rm s} = (2/\tau){\rm Re}\int_0^\tau {\rm d}t(\tau - t)\Phi_{\rm s}(t)e^{i\Delta t} \tag{15}$$

rises with τ for sufficiently short τ. This is essentially a condition on the correlation (or memory) time of the field reservoir.

First and foremost, we wish to apply the above analysis to the case of a two-level atom coupled to a near-resonant Lorentzian line centered at ω_s, characterizing a high-Q cavity mode or a "defect" mode in a photonic band structure [19]. In this case, $G_s(\omega) = g_s^2\Gamma_s/\{\pi[\Gamma_s^2 + (\omega - \omega_s)^2]\}$, where g_s is the resonant coupling strength and Γ_s is the line width (Fig. 2 — inset). In the short-time approximation, taking into account that the Fourier transform of the Lorentzian $G_s(\omega)$ is $\Phi_s(t) = g_s^2 e^{-\Gamma_s t}$, Eq. (12) yields (neglecting the background modes)

$$\alpha_e(\tau) \approx 1 - \frac{{g_s}^2}{\Gamma_s - i\Delta}\left[\tau + \frac{e^{(i\Delta - \Gamma_s)\tau} - 1}{\Gamma_s - i\Delta}\right]. \tag{16}$$

The QZE condition is $\tau \ll (\Gamma_s + |\Delta|)^{-1}, g_s^{-1}$: obviously, it is easiest to satisfy this inequality *on resonance*, when $\Delta = 0$. Then Eq. (16) yields

$$\kappa = \kappa_s + \gamma_b, \qquad \kappa_s = g_s^2\tau. \tag{17}$$

Only the κ_s term decreases with τ, indicating the QZE inhibition of the smooth nearly-exponential decay into the field reservoir as $\tau \to 0$. Since Γ_s and Δ have dropped out of Eq. (17), the decay inhibition is the *same* for both strong- and weak-coupling regimes (Fig. 2). Physically, this comes about since for $\tau \ll g_s^{-1}$ the energy uncertainty of the emitted photon is too large to distinguish between reversible and irreversible evolutions.

The experimental scheme we envisage for observing the above effects is as follows. A fraction of an atomic beam oriented perpendicular to the axis of a confocal cavity is excited to state $|e\rangle$ by a laser outside the cavity. Within the cavity the atoms repeatedly interact with a pump laser, which is resonant with the $|e\rangle \to |u\rangle$ transition frequency. The resulting $|e\rangle \to |g\rangle$ fluorescence rate is collected as in

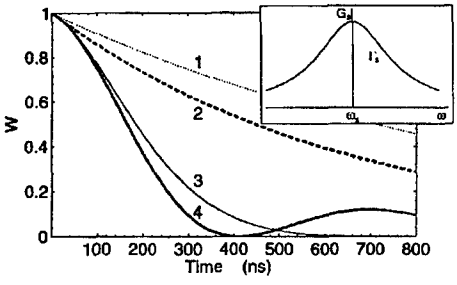

Fig. 2. Evolution of excited-state population W in two-level atom coupled to cavity mode with Lorentzian line shape (inset) in case (i) (on resonance, $\Delta = 0$): curve 1 — decay to background-mode continuum at rate $\gamma_b \approx \gamma_f = 10^6$ s^{-1}; curve 3 — uninterrupted decay in cavity with $F \equiv (1 - R)^{-2} = 10^5$, $L = 15$ cm, and $f = 0.02$; curve 4 — idem, but with $F = 10^6$ (damped Rabi oscillations); curve 2 — interrupted evolution along *both* curves 3 and 4, at intervals $\tau = 3 \times 10^{-8}$ s.

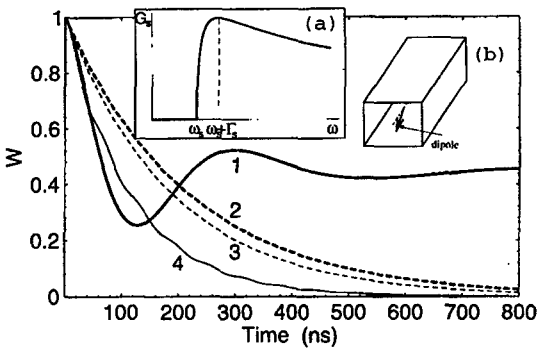

Fig. 3. Idem, for two-level atom ($\gamma_f = 10^6$ s^{-1}) coupled to waveguide field, with coupling $C^{2/3} = 1.2 \times 10^7$ s^{-1} and width $\Gamma_s = 0$: curve 1 — uninterrupted evolution at cut-off frequency ($\Delta = 0$); curve 4 — idem, $\Delta = 10^8$ s^{-1}; curve 2 — interrupted evolution at intervals $\tau = 10^{-8}$ s for $\Delta = 0$; curve 3 — idem, for $\Delta = 10^8$ s^{-1}. Insets — (a) DOM with cut-off [Eq. (17)]; (b) dipole in a waveguide.

Ref. [6] and monitored as a function of the pulse repetition rate. Each short, intense pump pulse of duration t_p and Rabi frequency Ω_p is followed by spontaneous decay (via fluorescence) from $|u\rangle$ back to $|e\rangle$, at a rate γ_u. The "measuring" pulse has to satisfy $t_p{}^{-1} \ll \gamma_u \ll \Omega_p$, so as to *destroy the coherence* of the system evolution, on the one hand, and *reshuffle the entire population* from $|e\rangle$ to $|u\rangle$ and back, on the other hand (Fig. 3 — inset). By combining these requirements with the demand that the interval between measurements significantly exceed the measurement time, we infer the inequality $\tau \gg t_p$. The above inequality can be relaxed to require $\tau \gg \gamma_u^{-1}$ if the "measurements" are performed with π pulses: $\Omega_p t_p = \pi$, $t_p \ll \gamma_u^{-1}$. The only real constraint is that $(\Gamma_s + |\Delta|)^{-1} \gg \tau \gg \gamma_u^{-1}$. This calls for choosing a $|u\rangle \rightarrow |e\rangle$ transition with a much shorter radiation lifetime than that of $|e\rangle \rightarrow |g\rangle$. The curves in Figs. 2 and 3 are calculated for such a choice, and for feasible cavity parameters: $\Gamma_s = (1 - R)c/L$, $g_s = \sqrt{cf\gamma_f/(2L)}$, $\gamma_b = (1 - f)\gamma_f$, where R is the geometric-mean reflectivity of the two mirrors, f is the fractional solid angle (normalized to 4π) subtended by the confocal cavity, and L is the cavity length.

We now extend the above analysis to any DOM distributions characterized by *a cut-off frequency*, as in a waveguide, a photonic band edge or *a phonon reservoir* (with Debye cut-off). A specific model for the spectral response of a DOM distribution with a cut-off is represented by [19] (Fig. 3 — inset (a)).

$$G_s(\omega) = [C\sqrt{\omega - \omega_s}/(\omega - \omega_s + \Gamma_s)]\Theta(\omega - \omega_s), \tag{18}$$

where ω_s is the cut-off (or band-edge) frequency, Γ_s is the cut-off smoothing parameter, C is the strength of the coupling of the atomic dipole to this reservoir, and $\Theta(\cdot)$ is the Heaviside step function. Upon computing the Fourier transform of Eq. (18), we find from Eqs. (10),(11) that the QZE condition is

$$\tau \ll \min\{\Gamma_s{}^{-1}, |\Delta|^{-1}, C^{-2/3}\}. \tag{19}$$

Under this condition, Eqs. (10) and (15) yield $\alpha_e(\tau)$ of the form

$$\kappa_s = (2^{5/2}\pi^{1/2}/3)C\tau^{1/2}. \tag{20}$$

As mentioned above, the QZE is now *less pronounced* (see Fig. 3, where we used the exact solution to compute $\alpha_e(\tau)$). This case is realizable for an active dipole layer embedded in a dielectric waveguide, using a level scheme similar to that of Fig. 2.

Instead of disrupting the coherence of the evolution by a sequence of "impulsive" measurements, i.e., short π-pulses, we can achieve this goal by *noisy-field dephasing* of $\alpha_e(t)$. Random ac-Stark shift by an intensity-fluctuating field results in

$$\kappa_s = \int G_s(\Delta + \omega_a) F(\Delta) \mathrm{d}\Delta, \tag{21}$$

where $F(\Delta)$ is a Lorentzian spectrum whose width is $\langle \Delta\omega^2 \rangle \tau_c$, the product of the mean-square Stark shift and the noisy-field correlation time.

Our unified analysis of two-level system coupling to field reservoirs has revealed the general optimal conditions for observing the QZE in various structures (cavities, waveguides, phonon reservoirs, and photonic band structures). We note that the wave function collapse notion is not involved here, since the measurement is explicitly described as an act of coherence-breaking [15]. This analysis also clarifies that QZE cannot combat the background-modes contribution to exponential decay, and is therefore inadequate for decoherence error prevention [20]. The best way to achieve such prevention is by switching-off the entire density of modes, i.e., *placing the resonance well within an ideal band gap.*

References

[1] Y. Japha, G. Kurizki, *Phys. Rev. Lett.* **77,** 2909 (1996).

[2] D. Sokolovski, J.N.L. Connor, *Phys. Rev. A* **47,** 4677 (1993) noted the connection between traversal-time measurement in tunneling and path information.

[3] T. Pfau, S. Spälter, Ch. Kurtsiefer, C.R. Ekstrom, J. Mlynek, *Phys. Rev. Lett.* **73,** 1223 (1994); P.L. Gould, P.J. Martin, G.A. Ruff, R.E. Stoner, J.-L. Picque, D.E. Pritchard, *Phys. Rev. A* **43,** 585 (1991).

[4] A. Stern, Y. Aharonov, Y. Imry, *Phys. Rev. A* **41,** 3436 (1990).

[5] C. Cohen-Tannoudji, J. Dupont-Roc, G. Grynberg, *Atom-Field Interactions,* Wiley, New York 1992; G.S. Agarwal, *Quantum Statistical Theories of Spontaneous Emission,* Springer, Berlin 1974.

[6] D.J. Heinzen, J.J. Childs, J.E. Thomas, M.S. Feld, *Phys. Rev. Lett.* **58,** 1320 (1987).

[7] R.P. Feynman, A.R. Hibbs, *Quantum Mechanics and Path Integrals,* McGraw-Hill, New York 1965.

[8] Y. Japha, V.M. Akulin, G. Kurizki, submitted to *Phys. Rev. Lett.*

[9] B.G. Englert, J. Schwinger, A.O. Barut, M.O. Scully, *Europhys. Lett.* **14,** 25 (1991); M.O. Scully, G.M. Meyer, H. Walther, *Phys. Rev. Lett.* **76,** 4144 (1996).

[10] B. Misra, E.C.G. Sudarshan, *J. Math. Phys.* **18,** 756 (1977).

[11] J. Maddox, *Nature* **306,** 111 (1983).

[12] A. Peres, *Phys. Rev. D* **39,** 2943 (1989).

[13] A.G. Kofman, G. Kurizki, *Phys. Rev. A* **54,** R3750 (1996).

[14] W.M. Itano, D.J. Heinzen, J.J. Bollinger, D.J. Wineland, *Phys. Rev. A* **41,** 2295 (1990); R. Cook, *Phys. Scr. Vol. T* **21,** 49 (1988).

[15] P.L. Knight, *Nature* **344,** 493 (1990); T. Petrosky, S. Tasaki, I. Prigogine, *Phys. Lett. A* **151,** 109 (1990); E. Block, P.R. Berman, *Phys. Rev. A* **44,** 1466 (1991); L.E. Ballentine, *ibid.* **43,** 5165 (1991); V. Frerichs, A. Schenzle, *ibid.* **44,** 1962 (1991).

[16] M.B. Plenio, P.L. Knight, R.C. Thompson, *Opt. Commun.* **123,** 278 (1996).

[17] A. Luis, J. Peřina, *Phys. Rev. Lett.* **76,** 4340 (1996).

[18] G. Kurizki, A.G. Kofman, V. Yudson, *Phys. Rev. A* **53,** R35 (1996).

[19] A.G. Kofman, G. Kurizki, B. Sherman, *J. Mod. Opt.* **41,** 353 (1994).

[20] L. Vaidman, L. Goldenberg, S. Wiesner, preprint quant-ph/9603031 (1996); S.L. Braunstein, preprint quant-ph/9604036 (1996).

Proceedings of the International Conference "Quantum Optics IV", Jaszowiec, Poland, 1997

DARK STATES AND DE BROGLIE WAVE OPTICS

H. METCALF

Physics Department, State University of New York
Stony Brook NY 11794-3800, USA

The techniques of laser cooling have now become sufficiently developed that the focus has shifted toward interesting applications such as the quantum domain of atomic motion. This topic is characterized by the failure of the classical description in which atoms move as point particles whose trajectories can be known: instead, atomic motion must be described as the optics of de Broglie waves. For example, when the de Broglie wavelength λ_{dB} exceeds $\lambda_{optical}$, then a classical description is insufficient (Bose condensation is done in the dark, and the quantum condition becomes $\lambda_{dB} >$ nearest neighbor distance). One of the most fascinating topics of quantized atomic motion in a laser field derives from optical dark states that can even occur in the simplest (two-level) atoms, where there are no magnetic sublevels and the polarization is irrelevant. In spite of the simplicity of this two-level atom case however, the more interesting cases occur in multilevel atoms where the internal magnetic states and external quantum states of atomic motion become truly entangled. Schrödinger called such states "the heart of quantum mechanics" because they led to puzzles such as his famous "cat" and the EPR paradox.

PACS numbers: 32.80.Pj

1. Introduction

In their early days, laser cooling and atom trapping were envisioned as techniques for producing a sample of nearly stationary atoms with negligible Doppler shifts that could be used for precision spectroscopy. More recently, the topic has evolved toward optical control of atomic motion in a broader sense, and has therefore exposed many new and interesting phenomena. The main topic of research in optical control of atomic motion is now no longer the lowest possible steady-state temperatures and the variety of cooling schemes that were of initial interest. Instead, the focus has shifted to the study of elementary processes, especially the quantum mechanical description of the atomic motion.

The uniquely complex character of this subject stems from the internal structure of atoms that can be exploited so beautifully to manipulate their interactions with light. This is accomplished using optical pumping and Raman transitions to optically pump atoms into desired internal states that determine the magnitude and nature of the electromagnetic forces on them. The quantum mechanical description of the atomic motion then means that the Hamiltonian must include

the kinetic energy of the atomic center-of-mass motion, and that the total wave functions must be composed of both internal and motional contributions.

2. Laser cooling

2.1. Classical view

From the beginning, theories of laser cooling recognized that dissipation required some irreversible or non-adiabatic behavior. In the extremely simplified but well-studied case of two-level atoms moving in a monochromatic standing wave field, the dissipation is produced by spontaneous emission that provides relaxation between the excited state $|e\rangle$ and the ground state $|g\rangle$ (in a two-level atom, the polarization is irrelevant) [1]. In the spirit of the dressed atom picture [2], the eigenstates of the Hamiltonian are intensity-dependent mixtures of $|g\rangle$ and $|e\rangle$, and atoms moving through an inhomogeneous optical field (e.g., a standing wave) must undergo periodic variation of their internal states to remain in eigenstates of the Hamiltonian. Without fast enough relaxation of the otherwise pure Rabi oscillations, the atoms generally are not in eigenstates.

The required relaxation from spontaneous emission has a rate $\gamma \equiv 1/\tau$, where τ is the excited state lifetime, and the spatial inhomogeneity of a standing wave optical field occurs on the scale of $\lambda/2\pi$. Thus atomic speeds comparable to $\lambda/2\pi\tau \equiv \gamma/k$ result in non-adiabatic response of moving atoms in the field variations they encounter. This can result in energy exchange with the field at each scattering event, of magnitude corresponding approximately to the fraction $v/(\gamma/k)$ of the light shift. For velocities $v \ll \gamma/k$, the internal states can follow the changing field seen by the moving atoms, and the rate of energy exchange is much smaller. For a laser field tuned below an atomic transition, the energy flow is from the atoms into the field, resulting in cooling of the atomic sample. When such laser cooling occurs in pairs of counterpropagating beams, it is called optical molasses, and there are many descriptions of this in terms of the different Doppler shifts seen by the moving atoms [3–5]. The non-adiabatic response, and subsequent energy loss, is then described as a viscous damping force whose nature can be calculated in several ways [1, 6, 7].

Real atoms have more than two levels, and relaxation to the local eigenstates of such atoms moving in an inhomogeneous optical field can be far more complicated. For example, in a three-dimensional (3D) light field that necessarily has polarization gradients, there can be several relaxation rates among the various Zeeman sublevels of the ground state, and these can be much slower than γ. Thus there can be significant energy exchange even at velocities much slower than γ/k, corresponding to laser cooling to much lower temperatures. Such polarization gradient cooling, and other types of related "Sisyphus" mechanisms that routinely cool atomic vapors to the μK regime, have been described in several places [8–12].

2.2. Quantum view

Up to now, the motion of atoms has been described in a completely classical way, assuming they had arbitrary position and momentum that could be known simultaneously. The mechanism of energy exchange in laser cooling, as well

as competition with and limits to that mechanism that determine the ultimate achievable temperatures, depend upon the location of the individual atoms in the spatially varying light field. Such a classical picture of atoms moving as point particles without regard to their overall wave-like character has been of great use, but when atoms are moving sufficiently slowly that their de Broglie wavelength precludes their localization to $\approx \lambda/2\pi$, these descriptions fail and a quantum mechanical description is required. Such conditions are routinely achieved in modern laser cooling experiments.

It becomes necessary to consider atomic position and motion as quantum mechanical variables, replete with wave packet spreading and non-commuting operators. A de Broglie wave field occupies allowed states of a region of space that may have a spatially varying potential that derives from the light shift and which defines modes of the field. These may be eigenstates in the optical potentials created by the laser fields. Laser cooling then becomes a process of optically pumping atoms to discrete quantum states of lower kinetic energy [13], dissipating the lost energy by fluorescence into the radiation field. In a standing wave, for example, the light shift produces an array of potential wells and the atoms' quantum states of motion are simply the bound states within these wells as shown in Fig. 1. Laser cooling is then the optical pumping to the lower states as shown [13].

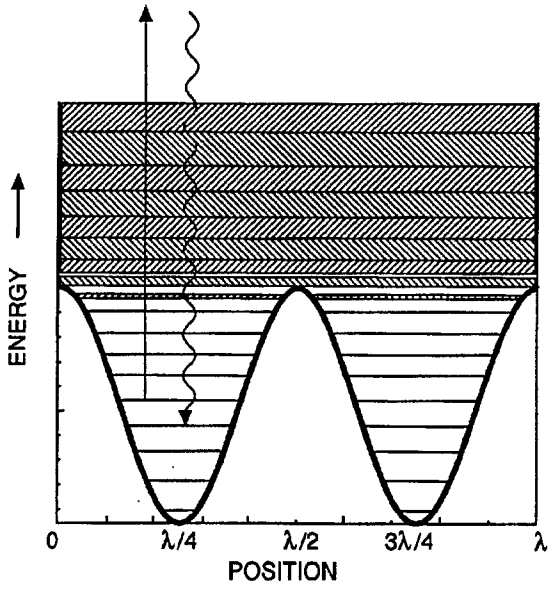

Fig. 1. Energy levels of atoms moving in the periodic potential of the light shift in a standing wave. There are discrete bound states deep in the wells that broaden at higher energy, and become bands separated by forbidden energies above the tops of the wells. Under conditions appropriate to laser cooling, optical pumping among these states favors populating the lowest ones as indicated schematically by the arrows (figure adapted from [13]).

In analogy with optics, occupation of particular modes of this de Broglie field can result in spatial or temporal interference, and then the entire field of atom interferometry emerges as a subset of this way of thinking. Atoms can only "interfere" if they occupy both the same internal and external states, and thus are truly indistinguishable. "Parts of an atom", i.e., atoms described by a superposition of eigenstates, certainly may have some overlap and can thus partially interfere. Of course, atoms at ordinary thermal velocities are distributed over thousands of quantum states of motion, so laser cooling is intimately involved in these studies. One important difference between this and the optical case arises because unlike photons, atoms are not all bosons. There will be cases where only a single atom can occupy a particular mode of the de Broglie wave field.

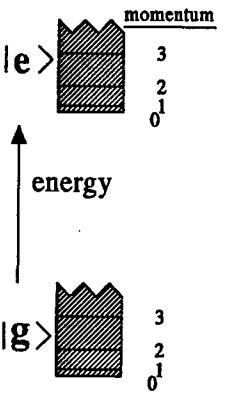

Fig. 2. Kinetic energies accessible to atoms moving freely (no spatially varying light shift) for both ground and excited states, with the integer momentum values marked as lines. All these KE states are doubly degenerate in 1D except for $p = 0$.

The quantum description of atomic motion requires that the energy of such motion be included in the Hamiltonian. Such a Hamiltonian will have eigenstates of not only the usual internal energy levels and the atom–laser interaction that connects them, but also of the kinetic energy (KE) operator $P^2/2M$. These eigenstates will therefore be labelled by quantum numbers of the atomic states as well as the center of mass momentum p. For example, an atom in the ground state, $|g;p\rangle$, has energy $E_g + p^2/2M$ which can take on a range of values. Figure 2 shows the continuum of KE values for both ground and excited states, with the integer momentum values marked as lines. All these KE states are doubly degenerate in 1D except for $p = 0$.

3. Shedding new light on dark states

3.1. Introduction to dark states

One of the most important requirements for successful experiments in de Broglie wave optics is the preservation of atomic coherence against destruction by spontaneous emission (SE). Recently there have been a few pioneering

experiments where SE has been carefully avoided by detuning the light frequency ω_ℓ so very far from atomic resonance ω_a that the rate of SE becomes negligibly small: only a few atoms are lost from the experiment because of SE. Thus atoms are kept "in the dark".

Using large values of $\delta \equiv \omega_\ell - \omega_a$ is not the only way to inhibit SE; a far more interesting way involves inherently "dark states", atomic states that cannot be excited by the light field. Some atomic states are trivially dark, that is, they cannot be excited because the light has the wrong frequency or polarization. The more interesting cases are superposition states created by coherent optical Raman coupling [14, 15]. A very special case are those superpositions whose excitable component vanishes exactly when their external (de Broglie wave) states are characterized by a particular momentum. Such velocity selective coherent population trapping (VSCPT) has been a subject of considerable interest since its first demonstration in 1988 [16–18]. VSCPT enables arbitrarily narrow momentum distributions and hence arbitrarily large delocalization for atoms in the dark states.

3.2. The two-level atom case

To see how the quantization of atomic motion allows the existence of such a velocity selective dark state, we consider the states of a two-level atom with single internal ground and excited levels, $|g;p\rangle$ and $|e;p\rangle$. Two ground eigenstates $|g;p\rangle$ and $|g;p'\rangle$ are generally not coupled to one another by an optical field except in certain cases. For example, in oppositely propagating light beams (1D) there can be absorption-stimulated emission cycles that connect $|g;p\rangle$ to itself or to $|g;p\pm 2\rangle$, depending on whether the stimulated emission is induced by the beam that excited the atom or by the other one (momentum is measured in units of $\hbar k$).

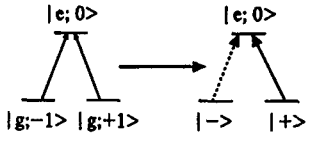

Fig. 3. Schematic diagram of transformation of eigenfunctions from the internal atomic states $|g;p\rangle$ coupled by Raman transitions to the coupled basis $|\pm\rangle$.

In the first case, the states of the atom and field are left unchanged, but the interaction shifts the internal atomic energy levels, thereby producing the light shift. In the second case, the initial and final KE of the atom differ by $\pm 4(p \pm 1)/2M$ (the energy of the light field is unchanged by the interaction), so energy conservation requires $p = \mp 1$. Thus energy conservation corresponds to Raman resonance between the distinct states $|g;-1\rangle$ and $|g;+1\rangle$, and is therefore velocity selective. The coupling of these two degenerate stationary states by the light field results in the new ground eigenstates of the (optical + KE) Hamiltonian given by (see Fig. 3)

$$|\pm\rangle \equiv \frac{|g;-1\rangle \pm |g;+1\rangle}{\sqrt{2}}. \tag{1}$$

Excitation of the states $|\pm\rangle$ given in Eq. (1) to $|e;0\rangle$ is proportional to the square of the radial matrix element

$$|\langle e;0|r|\pm\rangle|^2 = \frac{|\langle e;0|r|g;-1\rangle \pm \langle e;0|r|g;+1\rangle|^2}{2}, \tag{2}$$

and this vanishes for $|-\rangle$ because the two terms on the right side of Eq. (2) are equal since r does not operate on the external momentum of the atom (dashed line of Fig. 3). Excitation of $|\pm\rangle$ to $|e;\pm2\rangle$ is off resonance because its energy is higher by $4\hbar\omega_r \equiv 4\hbar^2k^2/2M$ so that the required frequency is higher than to $|e;0\rangle$. The detuning is thus $8\omega_r/\gamma \equiv 8\epsilon$ halfwidths, and for $\epsilon \approx 0.5$–1, this is large enough so that the excitation rate is small, making $|-\rangle$ quite dark. Excitation to any state of $p' \neq 0, \pm2$ violates conservation of momentum and is forbidden. Atoms are therefore optically pumped into the dark state $|-\rangle$ where they stay trapped, and since their momentum components are fixed, the result is VSCPT [17].

A useful view of this dark state arises by considering that its components $|g;\pm1\rangle$ have well defined momentum, and are therefore completely delocalized. Such oppositely travelling waves of the same frequency form a standing de Broglie wave. The fixed spatial phase of this wave relative to the optical standing wave results in the vanishing of the spatial integral of the dipole transition matrix element so that the state cannot be excited.

This view can also help to understand the consequences of p not exactly equal to ±1. In this case, the two components of the standing wave do not have exactly the same energy, and so their relative phase evolves at the rate of their energy difference. The de Broglie wave "walks" at a corresponding velocity, and has soon shifted its phase relative to the optical standing wave by $\pi/4$. Thus its transition matrix element no longer vanishes, and the "evolved" state is readily excited by the standing wave laser field.

3.3. Bragg reflection

A different view of VSCPT emerges by considering more carefully the motion of such dark state atoms in the spatially periodic field of oppositely propagating light beams [19]. As Fig. 4 shows, dark state atoms travelling with longitudinal

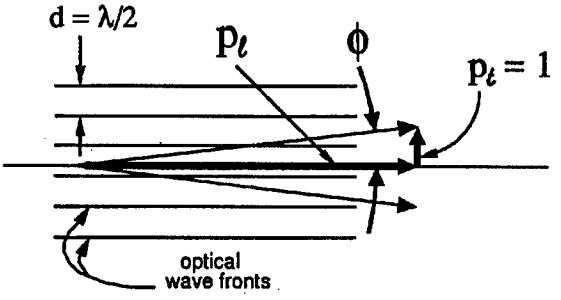

Fig. 4. The trajectory of an atom in the dark state makes an angle ϕ with the wave front planes. Its transverse component is one recoil.

momentum p_ℓ make an angle ϕ with the optical wave fronts, and their de Broglie wavelength is

$$\lambda_{\mathrm{dB}} = \frac{h}{\sqrt{p_\ell^2 + 1}} = \frac{2\pi}{k} \sin\phi \tag{3}$$

since $\sin\phi = 1/\sqrt{p_\ell^2 + 1}$ (momentum is in units of $\hbar k$). Thus

$$\lambda_{\mathrm{dB}} = 2d \sin\phi, \tag{4}$$

where $d \equiv \lambda/2$ is the spatial periodicity of the light field. Equation (4) is exactly the equation for Bragg diffraction, but its interpretation in this context is indeed *most astounding* [19]. Here the de Broglie "matter" wave is Bragg diffracted by the spatially periodic optical field: matter and field have been interchanged from the usual case of Bragg diffraction of an electromagnetic field by crystalline planes of atoms!

In retrospect, if we view ordinary Bragg diffraction as arising from multi--center scattering of radiation by atoms at each lattice site, then propagation of the diffracted wave can occur only in the preferred direction defined by Eq. (4). Such waves are the only ones not diffusively scattered by the lattice. The equivalent view of atoms in dark states is simply that the de Broglie wave fields propagate without scattering (i.e., no SE) in the light field only when the atoms are indeed in dark states [19]. Such an effect has recently been observed in metastable Ar atoms [20].

Such Bragg reflection has a rather simple intuitive explanation. In the absence of SE, atoms cannot exchange energy with the light field since its energy is unchanged by stimulated emission processes (the frequency is always ω_ℓ). Therefore atoms entering the light field with momentum p_t can leave with only $\pm p_t$. Their paths are thus either unaltered or Bragg reflected, and either process preserves coherence. Beam splitting simply leaves atoms in a superposition of degenerate states with $+p_t$ and $-p_t$.

3.4. High velocity dark states

The discussion above has focussed on the case of dark states composed of superpositions that arise from a two-photon coupling between two states whose momenta differ by ± 2. It is also possible to construct analogous dark states with $2n$-photon coupling between two states whose momenta differ by $\pm 2n$. Of course, their energies are larger, but as long as the components have equal energies, that is, their opposite momenta have equal magnitude, the states are stationary and remain dark. For $n = 2$, the two momentum states having $p = \pm 2$ have momenta that differ by 4, and so a four-photon Raman transition is required to conserve momentum, corresponding to a higher order process in VSCPT.

Experimentally we note that population always accumulates in the state $|-\rangle$ because it is dark, producing peaks in the momentum distribution at $p = \pm 1$. But there is also population accumulated in the analogous superposition states coupled by four photons that produce peaks in the momentum distribution at $p = \pm 2$, resulting in four peaks as shown in Fig. 5. Both of these long-lived states are populated by a random walk in momentum space, and each of them has a

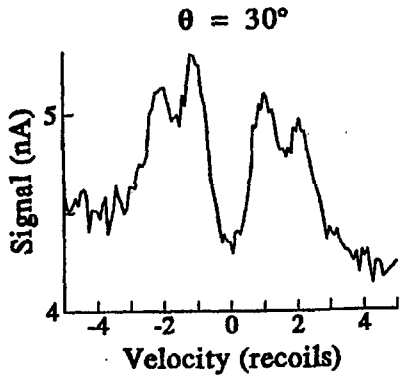

Fig. 5. Measured He* velocity distributions after 20 μs interaction time for $I = 1.6$ mW/cm^2 and zero detuning with counterpropagating beams linearly polarized at 30°. The four-peaked structure is quite evident.

long enough lifetime to be readily observable in an experiment with appropriate interaction time. Thus we see four very narrow (FWHM ≤ 1) peaks in the measured momentum distribution of Fig. 5 [21]. From the point of view of Bragg reflection as described above in Sec. 3.3 above, this simply corresponds to the next higher order, found by replacing the right hand side of Eq. (4) by $2nd\sin\phi$ with $n = 2$. This is the only example we know of using higher order non-linear optical effects to produce dark states and laser cooling.

4. Real (multilevel) atoms

4.1. The $J = 1 \Leftrightarrow 1$ transition

Real atoms have multiple internal levels that include the magnetic, hfs, and other sublevels, and thus the strength of their optical interactions depends on the light polarization. A particularly beautiful example of dark states appears in the $J = 1 \Leftrightarrow 1$ transition, where the optical selection rules associated with M_J produce an analog of the hypothetical state $|-\rangle$ that is perfectly dark [16–18].

When a single circularly polarized light beam drives a $J = 1 \Leftrightarrow 1$ transition with $\Delta M_J = +1$, the state $M_J = +1$ is dark, and similarly for $\Delta M_J = -1$ and $M_J = -1$ with the opposite circular polarization. (Choosing the z-axis parallel to the beam's $\boldsymbol{k}$ vector allows only $\Delta M = \pm 1$ transitions because the light has no electric field component parallel to $\boldsymbol{k}$.) Because the transition $M_J = 0 \rightarrow 0$ is forbidden by the selection rules, the $M_J = 0$ level is then emptied by optical pumping, and the only populated ground states are $M_J = \pm 1$ and the excited state $M_J = 0$, forming "Λ" system of levels.

The velocity-dependent dark state can be visualized by considering that a single beam travelling in the $+z$ direction excites the ground state $|M_J = -1; p-1\rangle$ only to a single excited state $|M_J = 0; p\rangle$ as shown in Fig. 6 (the excited state $|M_J = 0; p-2\rangle$ is not coupled by a beam travelling in the $+z$ direction). A beam of opposite circular polarization travelling in the opposite direction excites $|M_J = +1; p'+1\rangle$ only to a single excited state $|M_J = 0; p'\rangle$. The two excited

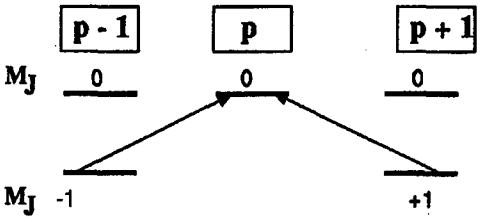

Fig. 6. The coupling between momentum states connected by oppositely circularly polarized light beams travelling in opposite directions. The internal atomic states are indicated by their M_J values, and in this $J = 1 \Leftrightarrow 1$ transition, they are entangled with the momentum states. The Λ system consists of the set of three levels coupled by the two arrows.

states are the same only for $p = p' = 0$, and the subsequent mixing of the ground states forms two new superposition states, as in Sec. 3.2. These states are given by

$$|\pm\rangle = \frac{|+1,+1\rangle \pm |-1,-1\rangle}{\sqrt{2}}, \tag{5}$$

where the quantum numbers in the kets are $|M_J, p\rangle$.

4.2. Entanglement

One of the most interesting aspects of dark state physics arises from the entanglement of motional and internal states that can be produced. The states represented in Eq. (5) are called entangled states because they satisfy the very special criterion that there exists no basis set in which the states could be written as a product of sums. This leads to the opportunity for fundamental studies at the heart of quantum mechanics, such as quantum communication, computing, cryptography, and teleportation.

Although there have been many recent studies of these topics using photons as the primary quantum objects, the use of atoms has many advantages. Atomic dark states have special advantages. First, the number state can be controlled with minimal doubt, unlike optical fields whose Fock states always have significant uncertainty. Perhaps more important, the number of Hilbert spaces, as well as their dimensionality, can each be larger than two.

As an illustration of how these entangled states could enable quantum computing, we consider the elementary functional unit of a quantum computer, the controlled NOT gate (CN). A two-qubit CN gate, which can be combined with rotations to enable any computational operation, can be realized directly using the states $|M_J, p\rangle$. By simply applying a focused optical Raman π-pulse to one of the two separated VSCPT beams, say $|+1,+1\rangle$, the following CN truth table results:

$A = \|-1,-1\rangle$	$\rightarrow$	$A' = \|-1,-1\rangle$
$B = \|+1,-1\rangle$	$\rightarrow$	$B' = \|+1,-1\rangle$
$C = \|+1,+1\rangle$	$\rightarrow$	$C' = \|-1,+1\rangle$
$D = \|-1,+1\rangle$	$\rightarrow$	$D' = \|+1,+1\rangle$

Clearly the value of p controls the inversion of M_J. This neutral atomic beam version is complementary to a quantum CN gate realized with trapped ions, while retaining the relatively high isolation from environmental decoherence (the momentum states are naturally very robust, and the internal states are composed entirely of ground levels).

Note that the Raman π-pulse converts the perfectly entangled state $(A + C)/\sqrt{2}$ into the product state $(A' + C')/\sqrt{2}$ $(= (A + D)/\sqrt{2})$, and vice versa. That is, the state $|-\rangle$ given in Eq. (5) is converted into

$$\frac{|M_J = -1\rangle \otimes (|p = +1\rangle + |p = -1\rangle)}{\sqrt{2}}. \tag{6}$$

Because the states A and C are orthogonal, overlapping them would produce interference fringes of visibility equal to zero because their superposition is a perfectly entangled state [22], whereas overlapping states A' with C' would produce fringes of visibility equal to unity because their sum can be written as a simple product as in Eq. (6).

5. Conclusions and summary

Advances in laser cooling have imposed a new view of atomic motion that constitutes de Broglie wave optics. Optical pumping of atoms among the momentum states accessible to these de Broglie waves shares many common features with optical pumping among internal atomic states. Especially interesting features arise when entangled superpositions of momentum and internal states result in dark states that can be readily observed because of their long lives.

This paper is not a report of work done solely by the author, but rather by his students and associates. The work described here was done principally by Marya Doery, Mark Widmer, Mary-Jo Bellanca, Wally Buell, Edgar Vredenbregt, and Tom Bergeman. The research was supported by the NSF and the ONR.

References

[1] J. Gordon, A. Ashkin, *Phys. Rev. A* **21,** 1606 (1980).

[2] C. Cohen-Tannoudji, S. Reynaud, *J. Phys. B* **10,** 345 (1977).

[3] D. Wineland, W. Itano, *Phys. Rev. A* **20,** 1521 (1979).

[4] J. Dalibard, W. Phillips, *Bull. Am. Phys. Soc.* **30,** 748 (1985).

[5] S. Chu, L. Hollberg, J. Bjorkholm, A. Cable, A. Ashkin, *Phys. Rev. Lett.* **55,** 48 (1985).

[6] H. Metcalf, P. van der Straten, *Phys. Rep.* **244,** 203 (1994).

[7] M. Doery, E. Vredenbregt, T. Bergeman, *Phys. Rev. A* **51,** 4881 (1995).

[8] P. Lett, R. Watts, C. Westbrook, W. Phillips, P. Gould, H. Metcalf, *Phys. Rev. Lett.* **61,** 169 (1988).

[9] J. Dalibard, C. Cohen-Tannoudji, *J. Opt. Soc. Am. B* **6,** 2023 (1989).

[10] P. Ungar, D. Weiss, E. Riis, S. Chu, *J. Opt. Soc. Am. B* **6,** 2058 (1989).

[11] C. Cohen-Tannoudji, W. Phillips, *Phys. Today* **43,** 33 (1990).

[12] G. Nienhuis, P. van der Straten, S.-Q. Shang, *Phys. Rev. A* **44,** 462 (1991).

[13] T. Bergeman, *Phys. Rev. A* **48**, R3425 (1993).

[14] E. Arimondo, G. Orriols, *Lett. Nuovo Cim.* **17**, 333 (1976).

[15] H. Gray, R. Whitley, C. Stroud, *Opt. Lett.* **3**, 218 (1978).

[16] A. Aspect, E. Arimondo, R. Kaiser, N. Vansteenkiste, C. Cohen-Tannoudji, *Phys. Rev. Lett.* **61**, 826 (1988).

[17] A. Aspect, E. Arimondo, R. Kaiser, N. Vansteenkiste, C. Cohen-Tannoudji, *J. Opt. Soc. Am. B* **6**, 2112 (1989).

[18] F. Bardou, J. Bouchard, O. Emile, A. Aspect, C. Cohen-Tannoudji, *Phys. Rev. Lett.* **72**, 203 (1994).

[19] H. Batelaan, S. Bernet, M. Oberthaler, E. Rasel, J. Schmiedmayer, A. Zeilinger, in: *Advances in Atomic, Molecular, and Optical Physics: Supplement Atom Interferometry*, Ed. P.R. Berman, Academic Press, to be published.

[20] S. Bernet, M. Oberthaler, R. Abfalterer, J. Schmiedmayer, A. Zeilinger, *Phys. Rev. Lett.* **77**, 5160 (1996).

[21] M. Widmer, M. Doery, M.-J. Bellanca, W. Buell, T. Bergeman, H. Metcalf, *Phys. Rev. A* **53**, 946 (1996).

[22] M. Scully, B.-G. Englert, H. Walther, *Nature* **351**, 111 (1991).

Vol. 93 (1998) *ACTA PHYSICA POLONICA A* No. 1

Proceedings of the International Conference "Quantum Optics IV", Jaszowiec, Poland, 1997

MEASUREMENT OF WAVE FIELDS

I.A. WALMSLEY, L. WAXER AND C. IACONIS

Institute of Optics, University of Rochester, Rochester, NY 14627, USA

Wave fields play a central role in both classical and quantum mechanics. Generally applicable methods for the characterization of (scalar) fields are outlined, and illustrated by experiment and simulation.

PACS numbers: 03.65.Bz, 42.50.Vk, 33.80.-b, 42.50.Dv

1. Introduction

Wave fields are the fundamental entities in both classical electrodynamics and quantum mechanics. The similarity of their governing dynamical equations suggests that similar strategies may be used to measure both classical and quantum fields. Indeed, numerous experiments in the recent past have demonstrated just this. But it is not this similarity alone that makes it important to consider their measurement within a single context, it is the very notion of manipulation of quantum systems (the idea of quantum state preparation or control) that demands it. Consider, for example the generation of a single photon "on demand", using the prescription, say, of Eberly and Law's "photon pistol" [1]. What does this mean, precisely? Nothing more than the specification of the quantum state of the field (a Fock state with eigenvalue unity) and a classical state of the field (the temporal mode in which the excitation is generated). Both pieces of information are necessary to appropriately specify what one means by the time of production of a photon. This problem resurfaces in all quantum measurement problems — one needs to know both the basis in which one is making the measurement and the degree of freedom (or the mode) for which the measurement is defined.

To the extent that quantum state measurement is the same as state preparation, it might be argued that there is no need to consider state measurement procedures separately. Of course, in practice most measurement schemes end up being of the demolition variety — one infers from the detected signal what the state must have been at the detector before a signal was registered. This is quite a different situation than the ideal envisioned by von Neumann. But this aside, the situation may perhaps be likened to one of quality control, if one may adopt the industrial metaphor used by the state engineers. That is, the consumer needs to determine whether she has been sold the quantum system that meets her needs, in the state that she ordered. Thus she needs both a classical and a quantum field measurement apparatus. Of course in practice one must order (and measure) an ensemble of identically prepared states, and then use the apparatus to determine

not only the quantum state and mode, but also the purity of the ensemble. Since presumably one would wish also to do an experiment with the purchased state, then the acquisition of two identical ensembles would, of course, be necessary, along with some "fair sampling" assumption consistent with good quality control.

2. General strategies for wave field measurement

2.1. Quantum and classical measurements

The quantities to be determined in the first instance, are, in the case of classical fields, the scalar optical field $E(x,t)$ (as a function of one of these variables only, at the moment) and in the case of quantum matter fields, the wave function $\Psi(x)$ (the dynamical dependence of this function being understood). In the case of the radiation field, the argument of the wave function is considered to be a field quadrature. In fact the measurements to be described can all be used to determine the purity of the state or the coherence of the field, in which case one seeks the density matrix (in position or momentum basis) or the two-point or two-time correlation function. We consider only fields or particles that are well localized, so that it is rather simple to define an ensemble for which the correlations may be evaluated. Thus the two-point correlation function for the electric field (taken to be time-stationary) can be defined as

$$\Gamma(x,x') = \ll E^*(x)E(x') \gg, \tag{1}$$

where the average is taken over a set of realizations of the experiment, repeated many times. This definition is analogous to the definition of the density matrix, which involves an average over all pure states that the system may potentially occupy. If one does not know a priori that the field is coherent or the state is pure, it is necessary to measure $\rho(x,x')$ or $\Gamma(x,x')$ and then to perform a test for coherence or purity. The test consists of assessing whether the function factorizes. That is, construct the parameter μ, defined as

$$0 \leq \mu = \frac{\int_{-\infty}^{+\infty} \mathrm{d}x \int_{-\infty}^{+\infty} \mathrm{d}x' |\rho(x,x')|^2}{\left[\int_{-\infty}^{+\infty} \mathrm{d}x \rho(x,x)\right]} \leq 1. \tag{2}$$

Then, if $\mu = 1$ the field is coherent, or the state is pure.

The similarity of the measurement problem in the case of (one-particle) quantum fields and the optical field arises not only because they obey similar dynamical equations, and can be represented by continuous complex functions of real variables, but also because they can be observed using only "square-law" type detectors*. A general measurement strategy for both can thus be worked out in the context of a strategy for either. We therefore consider the case of idealized linear quantum measurements. The analogous formulation for classical wave fields is related to the theory of optimal signal detection. There are two manipulations that one may perform on a quantum system; a unitary evolution $\widehat{U}_\theta$ where θ denotes a parameter, and a measurement $\widehat{\Pi}_A$, where A denotes the outcome of the measurement. This is defined by

*For THz pulses it is possible to measure the dynamical electric field directly, so that this analogy does not hold. In the optical regime, however, the situation is quite different.

$$\widehat{\Pi}_A = \int \mathrm{d}A' f(A|A')|A'\rangle\langle A'|, \tag{3}$$

where $f^2(A|A')$ is the conditional probability that the measurement will yield the outcome A if the input was definitely in state $|A'\rangle$.

According to Braginsky and Khalili [2] sequential measurements of two observables $\widehat{A}$ and $\widehat{A}'$ are defined as linear if their commutator is a complex number. In the case of a sequence of unitary transformations (labeled by the set of parameters $\{\theta_i\}$) and measurements of the set of observables $\left\{\widehat{A}_i\right\}$, the probability that the result will be a set of real numbers $\{A_i\}$ is

$$P(\{A_i\};\{\theta_j\}) = \mathrm{Tr}\Big(\prod_{i,j} \widehat{\Pi}_{A_i}\widehat{U}_{\theta_j}\widehat{\rho}\prod_{i,j}\widehat{\Pi}^{\dagger}_{A_i}\widehat{U}^{\dagger}_{\theta_j}\Big). \tag{4}$$

For a single, ontinuous degree of freedom, the probability may be written as an overlap integral of the density matrix (taken here in the position representation) as

$$P(\{A_i\};\{\theta_j\}) = \int_{-\infty}^{+\infty}\mathrm{d}x\int_{-\infty}^{+\infty}\mathrm{d}x'\rho(x,x')F(x,x';\{A_i\},\{\theta_j\}). \tag{5}$$

where the propensity function $F(x,x';\{A_i\},\{\theta_j\})$ depends on the meter and transformation parameters.

An entirely analogous expression may be derived for the photodetector signal at the output of a sequence of linear filters, at the input of which is an electric field specified by its correlation function ($\Gamma(x,x')$ for the case of time-stationary fields and filters, or $\Gamma(t,t')$ for space-shift invariant fields and filters). In this case the analog of a meter (used for making a measurement) is an amplitude filter, and that of a unitary evolution is a phase-only filter. Then, denoting the filter transfer function parameters by X_i and ϕ_j leads to

$$S(\{X_i\};\{\phi_j\}) = \int_{-\infty}^{+\infty}\mathrm{d}x\int_{-\infty}^{+\infty}\mathrm{d}x'\Gamma(x,x')F(x,x';\{X_i\},\{\phi_j\}). \tag{6}$$

We may ask what are the minimal conditions for reconstructing this correlation function or density matrix? It is clear that any measurement apparatus must be capable of completely exploring the two-dimensional space of these functions even if one only wishes to measure a one-dimensional electric field or wave function. The simplest methods, therefore, require two linear operations. These take two forms, either in series, or in parallel. If one considers both meters and unitary-transformers two-port devices (the field enters at one port and exits in a modified form at the other) then the in-series arrangements consist only of two-ports. Any in-parallel arrangement must, though, include a way to divide the input field into parts, and must therefore contain at least one ancillary four-port device, such as a beam-splitter. The unused input port of such devices plays an important role in many quantum measurement apparati, but none at all in classical measurements.

In-series measurements consist of a meter or a unitary transformation, followed by a meter, as shown in Fig. 1a. In the case of two meters in sequence, it

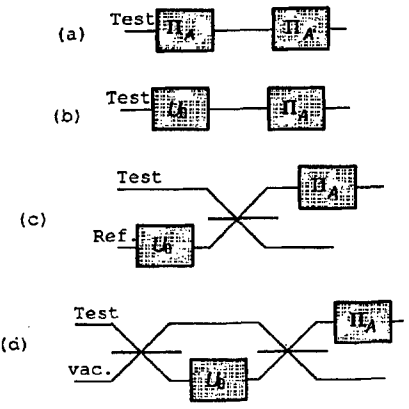

Fig. 1. The four minimal-operation in-series arrangements, and two in-parallel arrangements for field or state measurement for a single degree of freedom. Test denotes the unknown input field. $\widehat{\Pi}_A$ denotes a measurement and $\widehat{U}_\theta$ a unitary transformation of the field. (a) spectrographic (two-meter) (b) tomographic (unitary transform-meter) (c) test-plus reference. (d) self-referencing. In these figures "Ref" denotes a well-characterized reference field, and "vac" an empty input.

is straightforward to show that the meters must register complementary observables if the measured probability density is to be dependent on the phase of the density matrix. For the case of a unitary transformation and a meter, it is clear from Eq. (4) by cyclic permutation under the trace that the unitary operation must precede the meter, otherwise the probability density will be independent of the parameter characterizing the transformation.

The inversion method for these two schemes are quite different. The two-dimensional function returned by the two-meter method is a particular phase-space representation of the input state. If the first filter in the arrangement has a Gaussian conditional probability, and the second is precise (i.e. its conditional probability is a delta function) then the measured function is the Q-function, or its analog for a classical field. The inversion to the density matrix or correlation function is then via deconvolution. This class of measurement is termed spectrographic, since it involves characterizing the field by a spectrogram or a sonogram.

The method involving a unitary transform and a meter, shown in Fig. 1b, returns a set of one-dimensional positive functions (position or momentum distributions, for example) that depend also on the setting of the parameter(s) associated with the transformation. It is possible to invert this set of functions for any type of transformation [3], but it is particularly straightforward for transformations that are equivalent to dynamical evolution in a harmonic potential. In this case the transformation is characterized by a single parameter θ that ranges from $-\pi$ to $+\pi$. For a sufficiently large number of, say, position distributions, each with a different value of θ over this range, the discrete inverse Radon transform that is well known from computer-assisted tomography may be used to reconstruct the

Wigner distribution of the field [4]. From this function it is straightforward to obtain the density matrix via a Fourier transform. This class of measurement is therefore labeled tomographic.

The second class of measurement involves two filters placed in parallel channels at the output ports of a four-port. Or two filters simultaneously in the two input channels of a second four port, at one of whose output ports is a meter. Schematic illustrations of these are shown in Figs. 1c and d. Both of these classes of measurement are essentially interferometric, and determine phase by comparison with a second field. The difference is that the first type of apparati use a known reference field for comparison, whereas the second type are self-referencing.

For classical fields, it is well known that the real part of the correlation function is simply related to the fringe pattern observed in two-beam interferograms. Even so, interferometry is not commonly used in measurements for coherence, and it has not yet been applied at all to the measurement of the state of quantum matter waves. On the other hand, the optical balanced homodyne detector may be thought of as an interferometer, so that the technique of homodyne tomography for characterizing quantum optical fields can be considered as either an in-series (if one takes the detector to measure the quadrature amplitudes directly) or in-parallel devices.

An important point in interferometric measurements is that there is always a second input field, whether or not it is explicitly manipulated by the experimenter. For example, in test-plus-reference type interferometers, Fig. 1c, the two input ports of the four-port are occupied by the test and reference fields. But in the self-referencing type (Fig. 1d) the second input port sees only the vacuum or no-particle state. The presence of this field may or may not compromise the precision of the measurement, but its presence must always be taken into account.

2.2. Phase-space representations of in-series measurements

Spectrographic and tomographic measurements can be clearly distinguished by their phase-space representations. Such spaces can be defined for both quantum and classical fields, and are based on the notion of conjugate variables. For example, the quantum oscillator phase-space variables are position and momentum, which are complementary in the sense that the commutator of the corresponding observables is a complex number, and the variance of the two observables taken in any state of the oscillator is greater than or equal to $\hbar$. The phase-space of a classical field can be thought of as also involving two classically conjugate variables, corresponding to two representations of the field. In the case of the optical field, these might be position and wave vector or time and frequency. In both cases the products of the variances of these quantities for any field is greater than or equal to 2π according to Fourier's theorem — one may think of such Fourier pairs as "classically incompatible observables".

Thus for any complex field that is a function of a real variable, $\zeta(\chi)$, it is possible to define a Wigner representation of the correlation function of the field,

$$W(\xi,\eta) = \int_{-\infty}^{+\infty} \mathrm{d}\chi \mathrm{e}^{\mathrm{i}\chi\eta} \Gamma(\xi - \frac{\chi}{2}, \xi + \frac{\chi}{2}). \tag{7}$$

For example, a temporally localized optical field may be represented by a Wigner function of time and frequency in the chronocyclic phase space. This representation has all the analytic properties associated with the more familiar quantum Wigner function, including the property that it may be negative. Negativity in this context arises from the interference of classical waves rather than quantum waves, but nonetheless provides information about the coherence of the underlying field [5].

The output of spectrographic measurement apparati is a two-dimensional function of ξ and η (say, position and momentum, or time and frequency) that is related to the input field according to

$$P(\xi,\eta) = \int_{-\infty}^{+\infty} \mathrm{d}\xi' \int_{-\infty}^{+\infty} \mathrm{d}\eta' W(\xi',\eta') H(\xi-\xi',\eta-\eta'). \tag{8}$$

The function $H(\xi',\eta')$ is a phase-space "window" function through which one may gaze upon the input field. It is related to the propensity function defined by Eq. (5) by a transformation similar to Eq. (7). Since we assumed linear measurements (or filtering, in the case of classical fields) this function is a property of the apparatus alone. The window function occupies a minimum phase space area of $\hbar$ in the quantum case, or 2π in the classical case, but only attains this minimum when the first measurement is imprecise and the second precise. It is easy to see why this should be so from a simple example, say the measurement of a short optical pulse. In the frequency-resolved optical gating (FROG) spectrographic method the first meter is a spectrometer or frequency meter, and the second a fast shutter, or time gate. It is obvious that a precise initial measurement of frequency will discard all information about the arrival time of the field, and thus render the shutter useless. Thus intuitively one might expect that the optimum situation is arrived at if the spectral filter bandwidth is comparable to the pulse spectral width and the shutter opening is very rapid. This turns out to be the case[†].

A cartoon of a spectrographic window function is shown in Fig. 2a. It is a well-localized entity in both transform variables, and moves about the phase

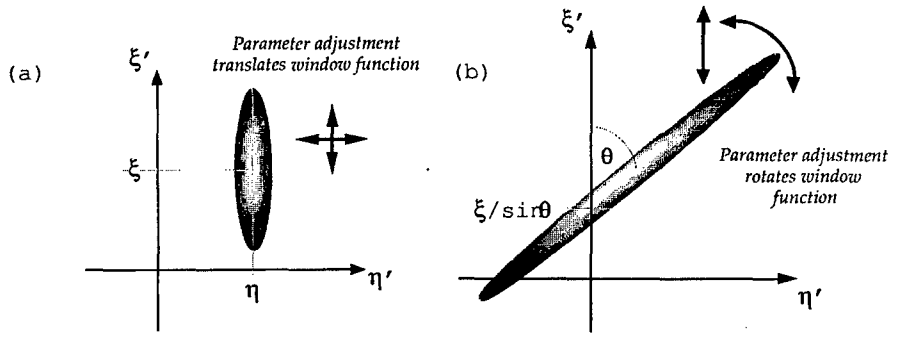

Fig. 2. Phase-space representations of window functions for in-series arrangements, (a) spectrographic. (b) tomographic.

[†]The formalism behind noninterferometric pulse characterization routines as well as an extensive list of references is given in Ref. [6].

space as the output variables ξ and η change, corresponding, in our example, to varying the time of opening of the shutter, and the tuning of the center of the spectrometer passband. These devices act as meters for the classical field in the sense that if one detects radiation having passed through the apparatus with a particular setting of these parameters, then one infers that the radiation contained that particular frequency during that particular time slot. The configuration space version of this situation has been discussed in connection with the measurement of spatially localized quantum wave functions by Raymer [7].

The output of tomographic measurement apparati are a set of one-dimensional functions of ξ that are parametrized by the transformation variable θ. In the case of harmonic tomography, these are related to the input field via

$$P(\xi;\theta) = \int_{-\infty}^{+\infty} \mathrm{d}\xi' \int_{-\infty}^{+\infty} \mathrm{d}\eta' W(\xi',\eta') T(\xi',\eta';\xi,\theta)\,. \tag{9}$$

The function $T(\xi',\eta';\xi,\theta)$ is also a phase-space window function, but has quite a different form than the spectrographic window function, as is shown in Fig. 2b. It rotates in the phase space as θ varies, and moves horizontally as ξ varies. Again it is possible to show that the function occupies a minimum area of phase space for precise measurements of ξ, in which case the window function becomes a delta function, and θ is the angle between $T(\xi',\eta';\xi,\theta) = \delta(\xi' \sin\theta - \eta' \cos\theta - \xi)$ and the ξ axis. Then the measured probability distributions are projections of the Wigner function representing the field onto a set of rotated $\xi - \eta$ axes. The principles of tomography for quantum systems based on these ideas has been reviewed extensively by several authors [8, 9].

2.3. Coherence-space representations of in-parallel measurements

Interferometric measurements are more easily visualized in the space in which the correlation function resides. We shall label this the "coherence space" of the field. This might be a two-dimensional configuration space, in the case of $\Gamma(x,x')$ for example, or the two-dimensional momentum or wave vector space that is occupied by its conjugate function $\tilde{\Gamma}(k,k')$. These are two representations of the same underlying entity, of course, analogous to the position and momentum representations of the density matrix of a quantum particle. The relationship between these two representations and the phase-space densities discussed in Sec. 2.2 follows straightforwardly from Eq. (7). The Wigner phase-space density is obtained by a Fourier transform of the density matrix or correlation function in the ξ representation, with respect to the difference of its two arguments. A second Fourier transform, this time with respect to the average of its two arguments, yields the η-space representation of the density matrix or correlation function. This may also be obtained by a second route in which the order of the Fourier transforms are inverted; the intermediate function in this case is the characteristic function of the Wigner distribution, which is known as the ambiguity function for classical fields.

There are two versions of the test-plus-reference interferometric measurement for quantum fields. In the first, a coherent-state field enters the reference port, after a phase shift characterized by the phase angle θ. A precise ξ measurement is made at the output ports. This leads to the method of optical homodyne tomography.

In the second method, a vacuum enters the second input port, and precise ξ and η measurements are made simultaneously at the two output ports. Since these are incompatible observables, this arrangement corresponds to a spectrographic type of measurement, as discussed by Stenholm [10].

Self-referencing methods in which one of the input ports sees a vacuum are different. These correspond to looking at the region of coherence space occupied by the field using a point-like window representing a precise measurement of the η or ξ observable, a unitary transformation, parametrized by a displacement by amount $\delta\xi$ of one part of the field with respect to the other, and a phase-shift θ. Because only a single observable is measured, there is no minimum area of phase space that the window function must occupy. The correlation function or density matrix can be constructed directly by a series of measurements of ξ for various values of $\delta\xi$ and two values of θ separated by $\pi/2$.

Given the direct access to the density matrix or correlation function that this class of measurement affords, one may question why it is not used more often when fields are to be characterized. The reason is that the unitary transformation and meter must be functions of the same observable, and it is rare that one is able to find both simple displacements and precise measurements in the same variable. For example, in the case of an ultrashort optical pulse, it is simple to displace the pulse in time — a delay line will do this — but impossible to measure the shape of the resulting temporal interference pattern, which contains beat frequencies as large as the optical frequency. On the other hand, it is easy to measure frequency precisely, but difficult to make a wavelength displacement of any significant magnitude.

3. Spectrography and tomography

3.1. Emission tomography for quantum state reconstruction in matter

The principles of tomography may be applied to the measurement of any material system in which the electronic and vibrational degrees of freedom are coupled. For systems in which the major mechanism for the damping of the electronic degree of freedom is radiation, tomographic reconstruction of the vibrational mode is accomplished from measurement of the spontaneous emission. An example of this is the reconstruction of the quantum state of the vibrational mode of a diatom in an excited electronic state from a measurement of its time-dependent fluorescence spectrum.

A molecule may be excited into nonclassical vibrational states, notably quadrature squeezed states [11] or classically distinguishable coherent superposition states [12, 13], by the application of a short optical pulse resonant with the electronic transition. Because the electronic and nuclear vibrational motions are coupled, a change in the electronic configuration causes a change in the nuclear configuration, so that when the molecule emits a photon and returns to the ground electronic state, as shown in Fig. 3, the wavelength of the emitted photon will depend on the location of the vibrational wave packet at the moment of emission. Thus the vibrational mode is allowed to evolve freely in a known potential for a certain time (this corresponds to the unitary evolution required for tomography) following which its position distribution is measured with a certain precision from the spectrum of spontaneous emission sampled at a given time [14].

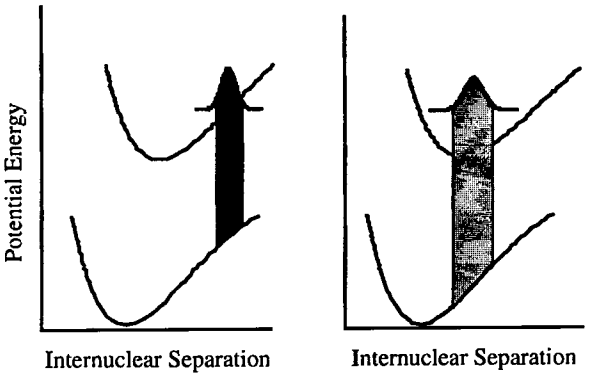

Fig. 3. Schematic illustration of the connection between quasi-instantaneous emission spectrum and wave packet position distribution for a molecular vibrational mode. A photon emitted by the molecule when the vibrational wave packet is at the outer turning point has a longer wavelength (black column) than one emitted when the packet is near the potential minimum (gray column).

These simple physical ideas may be put on a firmer footing using the notion of a time-dependent spectrum [15] based on an empirical scheme [16]. For example, in the case relevant to our experiments, the spontaneous radiation from a sample of molecules in the near-forward direction is sampled at some instant using a nonlinear-optical time gate, open for duration Γ^{-1} near a time T (which is referenced to the creation time of the wave packet by a preceding pump pulse). The spectrum of this temporal slice of fluorescence is then measured by a spectrometer with passband centered at frequency Ω, and with spectral resolution γ [16]. Thus the measured quantity is a two-parameter function $S(\Omega, T)$: the time-dependent spectrum of spontaneous emission,

$$S(\Omega,T) = K \sum_{n,m} \rho_{nm} \sum_{k} f_{kn} f_{km}^{*} \exp(-\mathrm{i}\nu_{nm}T) g(\Omega - \omega_{21}^{nk}) g(\Omega - \omega_{21}^{mk}), \quad (10)$$

where ρ_{nm} is the vibrational density matrix in the excited electronic state $|2\rangle$ and ν_{nm} is the difference of vibrational frequencies in this state. f_{kn} contains the details of the vibrational surfaces through the Franck–Condon factors. The unimportant constant K specifies the correct units of the spectrum. The function g is determined by the details of the time-gate and spectrometer response functions, and in our simple model is given by $g(\omega) = \exp\left[-\omega^2/(4\Gamma^2)\right]$. It can be shown that the time-dependent spectrum of Eq. (10) corresponds to projections of a rotated phase-space density of the vibrational mode in the excited electronic state, with the position mapped to emitted wavelength in a way that depends on the details of the vibrational potentials[‡] [14]. The phase-space density is a smoothed version of the Wigner function, since there is an inherent uncertainty in the emission frequency when a time-gate is used to sample the spectrum. For the case of harmonic vibrational potentials, the density can be obtained from the spectrum using the in-

[‡]The desired information can also be determined by photoelectron spectroscopy, see Ref. [17].

verse Radon transform [14]. But in general molecular vibrations are not harmonic, so different inversion methods must be used to implement tomography.

A small, easily invertable linear system can be developed from Eq. (10). A time series is obtained from the time-dependent spectrum by sampling. The time series is a sampling of the truncated spectrum defined $S'(\Omega,T) = S(\Omega,T)\times G(T;\tau)$ where $G(T;\tau)$ is a sampling window of length τ. The Fourier transform of this series with respect to T is

$$\widetilde{S}'(\Omega,\nu) = K\sum_{n,m}\rho_{nm}\sum_{k} f_{kn}f^{*}_{km}g(\Omega-\omega_{21}^{mk})g(\Omega-\omega_{21}^{nk})\widetilde{G}(\nu-\nu_{nm}). \qquad (11)$$

For a particular value of ν, chosen typically to lie near a maximum of $\widetilde{G}(\nu-\nu_{nm})$, there will be several ρ_{nm} which contribute to $\widetilde{S}'(\Omega,\nu)$. It is possible to resolve the contribution of each density matrix element to the time-series spectrum at frequency ν by forming a linear system consisting of a set of different time series, each associated with different values of the frequency filter setting, Ω. This system can then be inverted to find the particular contributing density matrix elements [18].

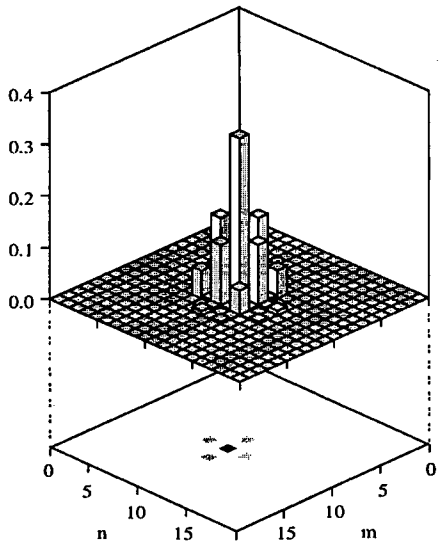

Fig. 4. Reconstruction of a classically distinguishable coherent superposition state for an anharmonic vibrational mode, from a simulated time-dependent emission spectrum, in the basis of eigenstates $|n\rangle, |m\rangle$ of the vibrational mode in the excited electronic state. The upper histogram represents the modulus of the density matrix elements and lower portion represents the errors between reconstructed and actual matrix elements.

To illustrate the efficacy of this method, Fig. 4 shows a simulated reconstruction of the reduced density matrix for a molecular vibration in the $A^1\Sigma_u^+$ state of the sodium dimer, measured by its fluorescence to the $X^1\Sigma_g^+$ state. The method is quite robust, and is capable of reconstructing a complicated mesoscopic Schrödinger-cat state, simulated by superposing two quasi-coherent-state wave

packets which are separated by one half a vibrational period. The mean vibrational quantum number of each wave packet was set at $\overline{n} = 9$, and about 8 states were populated around this quantum number. The temporal resolution was taken to be 20% of the classical vibrational period (310 fs), or $\Gamma = 0.0167\ \mathrm{fs}^{-1}$, and the total sampling time was $\tau = 23$ ps, corresponding to the one-quarter fractional revival period for this molecular state. In this case we used up to 13 different time scans (each corresponding to a particular value of Ω). In order to ensure a stable inversion, the values of Ω were chosen to be equally spaced across the fluorescence spectrum of the molecular wave packets (i.e. in wavelength, between 630 nm and 810 nm corresponding to the wave packet classical turning points).

3.2. Chronocyclic spectrography for classical ultrashort optical pulse shape reconstruction

Tomography has also been proposed as a method for the measurement of the (classical) electric field of an ultrashort optical pulse[§]. It has not yet been implemented experimentally, since, for technical reasons, it is much easier to make the measurements using a spectrographic method. The most widely studied of the spectrographic methods is FROG, but there are alternates, such as a version of Treacy's dynamic spectrogram known as temporal analysis of spectral components or TASC.

These two techniques measure two different types of spectrogram: based on either resolving the spectrum of temporally filtered components, as in FROG [20–23], or time-resolving each component of the pulse's spectrum as in TASC [24, 25] or other methods [26]. The two permutations of spectrometer and time-gate make up the two simplest experimental arrangements for spectrographic measurement of pulsed optical fields.

The dynamic spectrogram was shown by Chilla and Martinez [25] to possess a simple phase retrieval algorithm in the limit of precise frequency measurements. A better estimate of the input pulse field, using an iterative phase-retrieval algorithm, is available if the measurement is imprecise, however, and the full temporal dependence of each spectral component is measured.

Our experimental demonstration of TASC measured the output of a conventional Kerr-lens modelocked Ti:sapphire laser operating at 808.5 nm, producing pulses 80–90 fs in duration, with a spectral FWHM of 11.8 nm. The pulses passed through an optical isolator before being measured. This type of source has also been measured using FROG [27].

The apparatus, shown schematically in Fig. 5a was a modified Michelson interferometer, in one arm of which was a quasi-zero-dispersion grating spectrometer, with adjustable passband center frequency ω_c. In the reference arm, the input pulse was reflected by a corner cube and a plane mirror. The corner cube was moveable to provide the variable temporal delay τ. These two pulses are combined in a non-collinear geometry onto a 300-μm-thick nonlinear crystal, resulting in second-harmonic generation (SHG) which is detected by a photomultiplier tube (PMT). The nonlinear optical interaction of SHG forms the time gate for the

[§]For an introduction to pulse shape measurement methods see Ref. [19].

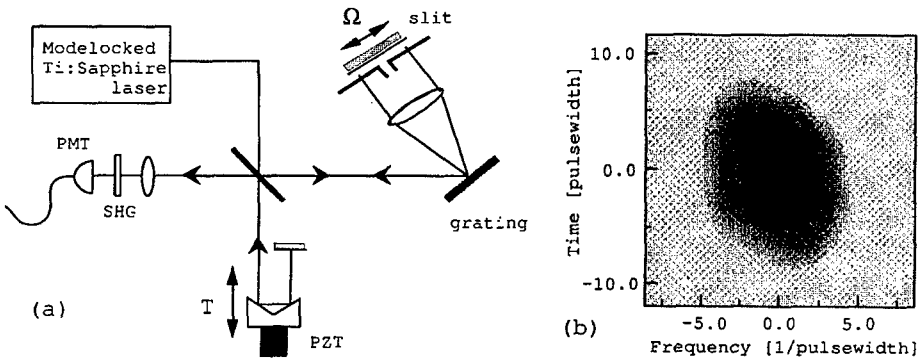

Fig. 5. (a) Apparatus for the characterization of an ultrashort optical pulse via TASC. (See text for description.) (b) Experimentally measured spectrogram measured using the apparatus of (a).

spectrally filtered pulse from the other arm. The spectrogram is obtained from the resulting cross-correlations, which are recorded as a function of Ω and T.

Figure 5b shows the spectrogram recorded with spectrometer resolution of one-tenth the spectral bandwidth of the input pulse. The spectrogram displays a slight negative chirp, arising primarily from the residual chirp in the spectral filter combined with the pulse's phase structure due to the dispersion of the optical isolator. This intuitive spectrographic representation of the pulse is a feature that TASC shares with polarization-gate-FROG, which uses a third-order nonlinearity.

The extraction of the input spectral field $\widetilde{E}_{\text{in}}(\omega)$ from the TASC spectrogram involves a two-dimensional phase retrieval problem, which is well known to yield unique solutions [20]. We apply an iterative algorithm based on the method of generalized projection similar to that of FROG [28] to perform the two-dimensional phase retrieval [24].

The amplitude and phase of the pulse that are reconstructed from the sonogram exhibit the correct phase structure expected from the passage of a nominally 80 fs transform-limited pulse from the Ti:sapphire laser through the dispersive optical isolator.

4. Interferometry

4.1. Self-referencing interferometry for characterizing the spatial coherence of classical optical fields

It is well known that the real part of $\Gamma(x, x')$ is simply related to the fringe pattern observed in two-beam interferograms. Despite this, interferometric measurements have been sparingly applied to the measurement of fields with an arbitrary correlation function [29–34].

It is possible, however, to construct an interferometer capable of measuring the space-shift variant two-point correlation function for fields at a remote plane with arbitrary spatial coherence in a simple, accurate and efficient manner [35].

The apparatus consists of a Sagnac interferometer, shown in Fig. 6a, consisting of a polarization-insensitive nominally 50/50 beamsplitter and two mirrors.

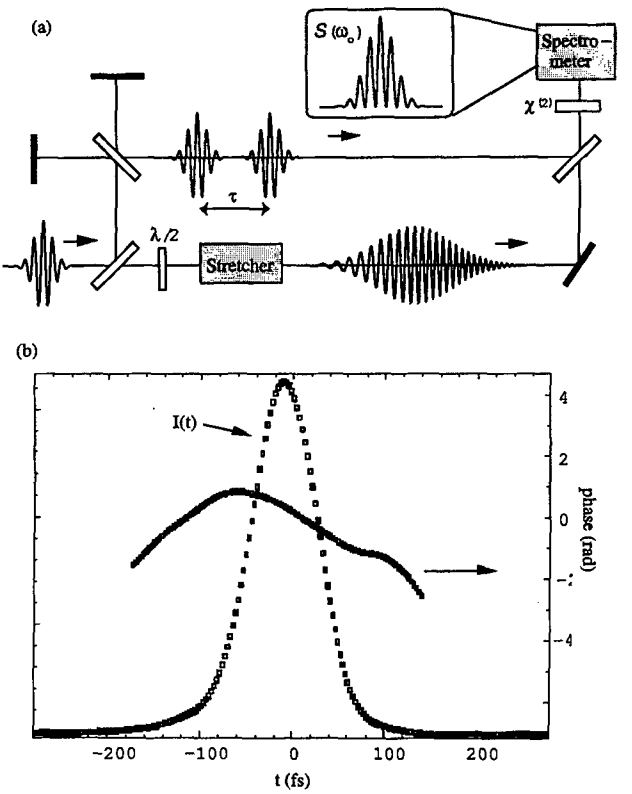

Fig. 6. (a) Sagnac interferometer for the measurement of the two-point correlation function of a time-stationary optical field. (See text for description.) (b) Magnitude of the experimentally measured correlation function for a filamentary broad-area laser diode.

A glass block mounted on a rotation stage is located in the common path allowing the Sagnac to be operated as a lateral shearing interferometer for both transverse coordinates. Also in the common-path region are first-order quarter- and half-wave plates that are used for quadrature selection. The object fields are imaged onto a detector array by a lens, which must be placed after the interferometer so that phase structure due to the imaging optics does not appear in the measured interferograms¶. The field exiting the input port of the beamsplitter is sent to a detector array. This arrangement ensures that both clockwise (cw) and counter-clockwise (ccw) fields experience one reflection from and one transmission through the beamsplitter, nulling the effect of deviations from 50% transmission and allowing for polarization insensitive orientation of the beamsplitter. The shear

¶If the shear is not introduced in the object space of the imaging system, then the interferograms exhibit tilt-like fringes perpendicular to the direction of shear that arise from the spherical phase front that is imposed on the field by the lenses.

is varied from 0 to 1 (as a fraction of the full field) in equal steps. The resulting data consists of an array of numbers representing the measured intensity.

The two quadratures of $\Gamma(x, x')$ are determined by the following procedure. The quarter- and half-wave plates are oriented such that their fast axes are parallel to the object field polarization. In this orientation both cw and ccw fields travel equal optical path lengths. The intensity at the detector array is

$$I_{\mathrm{det}}(y; s) = \Gamma(y + \frac{s}{2}, y + \frac{s}{2}) + \Gamma(y - \frac{s}{2}, y - \frac{s}{2}) + 2\mathrm{Re}\Gamma(y + \frac{s}{2}, y - \frac{s}{2}), \quad (12)$$

where y is the position on the detector array, equal to the object field coordinate x multiplied by the image magnification, and s is the shear. Measurement of $I_{\mathrm{det}}(\mathrm{y;s})$ for all s directly yields a sample of $\mathrm{Re}\Gamma(x, x')$ by subtracting out the individual intensities. Measurement of $\mathrm{Im}\Gamma(x, x')$ is accomplished by rotating the half-wave plate by 45 degrees so that the cw and ccw propagating fields experience different path lengths.

Measurement of two spatially separated Gaussian beams that were superposed with either fixed phases or random phases show that the two-point correlation function can be reconstructed quite reliably, and the integral degree of coherence μ, defined in Eq. (4), evaluated. Note that μ provides a simple measure of beam quality, although a different one than the more usual M^2 parameter. It does not specify how close the beam is to a Gaussian, as does the latter value, but rather, whether it is possible in principle (although not of course necessarily in practice) to find an optical system that will produce a beam of size equal to the diffraction limited spot size of a Gaussian beam.

We have used this technique to examine filamentation in the output of broad--area semiconductor lasers; an important problem for the design of high power lasers of this type. Figure 6b shows the correlation function for the output of an edge-emitting, AlGaAs, buried-heterostructure-type Fabry–Perot laser. The laser was operated about two times above threshold. The intensity at the output facet at this current was a four-peaked pattern, each peak centered at x_i $(i = 1 \div 4)$, corresponding to four filaments being above threshold. The correlation function reveals, however, that these filaments are not all coherent with one another. Evidence for this is that the correlation function is close to zero in the regions near (x_3, x_i) $(i = 1, 2, 4)$. The implication of this is that there exists no optical system that can transform this beam to a diffraction limited spot containing all of the laser's output power. Also, it shows that the filamentation of the laser beam is not necessarily due to a single mechanism. One might expect, for example, that if self-focusing-induced modulation instability were responsible for the filamentation then the degree of coherence of the filaments might depend only on $x_i - x_j$.

4.2. Self-referencing interferometry for characterizing classical ultrashort optical pulses

Interferometric characterization of ultrashort optical pulses has been performed primarily using the test-plus-reference geometry, in either the time domain [36], or the frequency domain, in which guise it is known as spectral interferometry [37–39].

Although some self-referencing methods have been developed for time-domain measurements, including the classic interferometric autocorrelation [40], and other methods [26] these either provide only partial phase information or require unreasonably precise temporal measurement. Precise spectral measurements are possible, though, and spectral shearing interferometry (SSI) [41, 42] is a self-referencing interferometric method that takes advantage of the direct phase retrieval routine offered by interferometry. It does require, however, shifting the two spectra with respect to one another by several hundred GHz. This can be done quite simply using upconversion.

The spectral interferogram of two pulses that are identical in all respects with the exception that they are shifted (sheared) in frequency with respect to one another, is given by the frequency domain analog of Eq. (12)

$$S(\omega_0) = \left|\widetilde{E}(\omega_0)\right|^2 + \left|\widetilde{E}(\omega_0+\delta\omega)\right|^2 + 2\left|\widetilde{E}(\omega_0)\widetilde{E}(\omega_0+\delta\omega)\right| \times \cos\left(\phi_\omega(\omega_0+\delta\omega) - \phi_\omega(\omega_0) + \omega_0\tau\right), \tag{13}$$

where τ is the temporal delay between the two replicas.

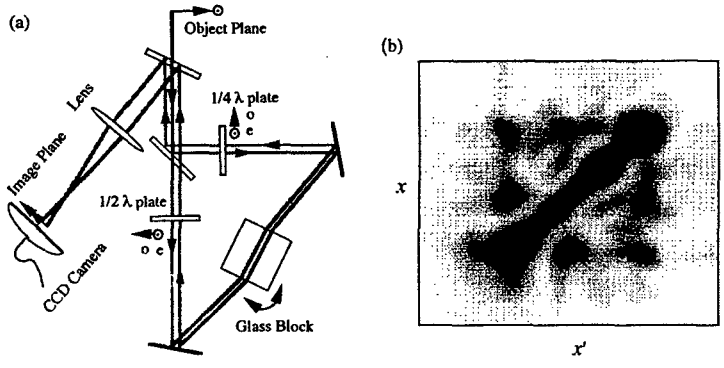

Fig. 7. (a) Upconversion spectral shearing interferometer for measuring the field of ultrashort optical pulses. (b) Phase and amplitude of an 80 fs-duration pulse from a modelocked laser measured using SSI.

Our apparatus for generating such a pair is shown in Fig. 7a. A portion of the pulse to be characterized is split off and directed through a Michelson interferometer. The output from the Michelson is a pair of test pulses separated in time by delay τ. This pair of pulses is mixed with a stretched replica of the input pulse in a type-II nonlinear crystal (250 μm BBO). In the limit of large dispersion, the stretched pulse stretcher is highly chirped with each frequency occurring at a different time. Since the pulses in the test pair are delayed with respect to one another by τ, each is upconverted with a different spectral slice of the stretched pulse. For a stretched Gaussian pulse of temporal duration T and spectral width Ω, the spectral shear between the upconverted pair of test pulses is $\delta\omega = \tau\Omega/T$. It is necessary that $T \gg \tau$ so that the frequency of the chirped pulse does not change over the duration of an individual unstretched test pulse. The resultant spectral interferogram is recorded by a spectrometer.

The phase reconstruction routine follows a procedure introduced by Takeda et al. [43]. The recorded spectral interferogram is Fourier transformed with respect to ω, and all features at times near to and less than $t = 0$ are discarded. The remaining signal for positive t is inverse transformed. After subtracting the carrier frequency term $\omega_0\tau$ from the resulting phase distribution we are left with the relative phase, $\phi_\omega(\omega_0 + \delta\omega) - \phi_\omega(\omega_0)$, between each pair of frequency components separated by $\delta\omega$. (In the limit of small $\delta\omega$ this is approximately the group delay at ω_0.)

Using the above apparatus and inversion procedure we reconstructed the amplitude and phase of the pulses output from a Ti:sapphire oscillator. The test pulses leaving the Michelson arrangement are separated by roughly 4 ps. The dispersed pulse is stretched to 25 ps, roughly a factor of 300, such that a spectral shear of 16% of the total pulse bandwidth is achieved and upconversion of the test pulses with "continuous-wave slices" of the stretched pulse is assured. The reconstructed pulse amplitude and phase in the time domain is shown in Fig. 7b.

4.3. Self-referencing interferometry for characterizing atomic wave functions

Shearing interferometry can also be used to measure the transverse component of the wave function of the center of mass degree of freedom of an atom moving in free space. Freyberger et al. [44] have recently proposed a method quite similar to that described for optical fields in Sec. 4.1. Here we discuss an alternate approach that makes use of shearing in momentum space rather than in configuration space [45].

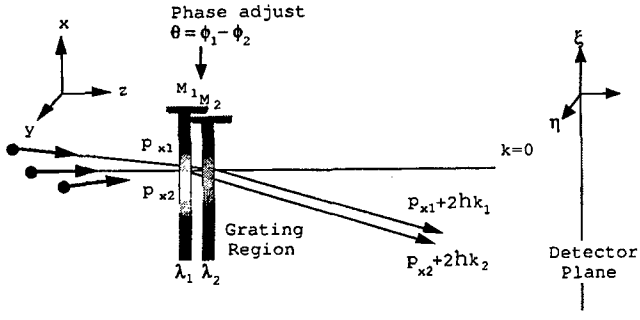

Fig. 8. Double-grating lateral shearing interferometer for measuring the density matrix of the transverse coordinate of free atoms. The λ_i's are the wavelengths of the two standing-wave light field diffraction gratings, whose relative phases are adjusted using the mirrors M_i. Monoenergetic atoms with different transverse momenta area scattered into the same direction $(p_{xi} + 2\hbar k_i)$ and detected in the far-field at ξ.

The set up is sketched in Fig. 8. It consists of a beam of atoms, width Δx in their ground electronic states, with reasonable collimation, propagating in the z-direction. It is incident upon two quasi-monochromatic standing wave light fields with wave vectors in the $\pm x$ directions. The fields differ in their wavelength, and one has a phase adjustment that allows the nodes of the standing wave to be

shifted through one half wavelength. An array of hot-wire or other atom detectors is situated in the far-field of the apparatus.

If the standing light waves are strongly detuned from the atomic resonance, and the gratings, width ϵ_i, are taken to be thin, and if the two gratings are closely spaced, so that there is no lateral spreading of the beam within the grating region due to scattering or diffraction, then the wave function of the beam immediately to the right of the second grating is

$$\Psi(x, z = \epsilon_1 + \epsilon_2) = \Psi_+(x, 0) = T_1(x)T_2(x)\Psi(x, 0), \tag{14}$$

where $T_i(x)$ is the grating (spatial) response function. Of course, the atom also accumulates a phase $\Phi_i = E\tau_i/\hbar$, where τ_i is the approximate time taken for the atom to traverse the grating.

If the beam is then allowed to propagate in free space then the wave function $\Psi(\xi, z)$ at the detector plane, in the far-field of the gratings, is proportional to the Fourier transform of the wave function immediately after the gratings. The detected signal in the vicinity of the first-order scattered beam is approximately

$$S_1(\xi) = |A_{10}|^2 \left\{ \widetilde{\rho}\left(\frac{k\xi}{z} - 2k_1, \frac{k\xi}{z} - 2k_1\right)^2 + \widetilde{\rho}\left(\frac{k\xi}{z} - 2k_2, \frac{k\xi}{z} - 2k_2\right)^2 \right.$$

$$\left. +2\mathrm{Re}\left[e^{(\phi_2 - \phi_1)} \widetilde{\rho}\left(\frac{k\xi}{z} - 2k_1, \frac{k\xi}{z} - 2k_2\right)\right]\right\}. \tag{15}$$

This part of the signal depends on the momentum space correlation function of the initial state, and from it the momentum representation of the initial density matrix can be reconstructed, even for mixed states. The requirement of well-separated first-order diffraction sets a lower bound on the wave functions that can plausibly be reconstructed using this technique. In particular the scattering light beams ought to satisfy $k_1, k_2 > 2\pi/\Delta x$.

A procedure for the complete reconstruction of this quantity follows from Eq. (15), and is quite analogous to that described in Sec. 4.2 for the optical field. The two quadratures of the density matrix are measured by adjusting the phase between the two gratings to be first 0 then $\pi/2$. Simple estimates indicate that this method should be experimentally feasible for sodium atoms moving at about 10 m/s, and having a divergence of less than 2.5 mrads, using two laser beams tuned near the D lines, that may be detuned from one another by about 50 nm while maintaining a relatively constant Rabi frequency.

5. Interferometric spectrography

5.1. Test-plus-reference interferometry for quantum state reconstruction of ultrashort optical pulses

As an example of the importance of both classical and quantum field measurements we discuss in this section a method for measuring the multimode quantum state of a pulsed quantum optical field. The single mode problem has been solved using optical homodyne tomography, (OHT) [4] and partial reconstruction has been developed for the two-mode problem [46]. As Raymer has shown [48], a

complete state reconstruction for even the two-mode problem using OHT is unpleasantly cumbersome. However, it is possible to reconstruct the Q-function of a multimode field using a simple multi-detector apparatus, and using a much simpler arrangement [48].

Consider a balanced test-plus-reference spectral interferometer, into which the quantum (test) pulse and a classical (reference or local oscillator (LO)) pulse, duration τ_p, enter. The spectra of the radiation at the two output ports of the beamsplitter are detected by two multichannel detector arrays, and the difference photocount numbers N_{ω_i} are taken channel by channel from the array outputs. The discrete Fourier transform of the N_{ω_i} is taken to yield a set of complex numbers N_{t_i} [49]. The real and imaginary parts of this set of numbers are realizations of the two quadratures of a set of temporal modes of the field, each displaced by a time $i\tau_p$ from the reference pulse. This procedure is followed on each shot, and the statistics of the set N_{t_i} constructed. Then it can be shown that the probability distribution of these numbers scaled by the LO field amplitude is proportional to the joint Q-function for the set of temporal modes

$$P([N_{t_i}]) = Q\left(\left[X_{t_i} = \mathrm{Re}\frac{N_{t_i}}{2E}; Y_{t_i} = \mathrm{Im}\frac{N_{t_i}}{2E}\right]\right), \tag{16}$$

where X_{t_i} and Y_{t_i} are the in-phase and in-quadrature field amplitudes for mode t_i. Note that the single or two mode statistics can be obtained by simply tracing over the remaining modes. The total number of modes on which information is simultaneously obtained is equal to the number of pixels (or resolution elements) of the multichannel detectors.

Note that the spectral interferogram is sensitive only to the modulus of the delay of the LO pulse from the test pulse. Thus there is an uncertainty as to whether the detected photons came from a temporal mode that arrived at the detector before the LO pulse or after it. This is analogous to the case in heterodyne detection in which the measurement space is increased to include the image modes of the test field. Shapiro and Wagner [50] have shown that this is equivalent to making a joint measurement of the two quadratures of the signal mode simultaneously provided the image mode is in the vacuum, so that measurement of the multimode Wigner function of the test field is not possible.

6. Conclusions

The similarity of detectors and dynamic equations for both quantum matter waves and classical optical fields allows techniques developed for the characterization of one to be easily translated to the characterization of the other. We have illustrated this by several experimental and numerical examples. Note that both characterization procedures are necessary when measuring the state of a quantum field, since then one must first characterize the classical mode function in which the quantum system exists. The important and emerging problem of quantum state engineering in both matter and radiation will no doubt benefit from the ability to measure fields of all types, although new methods need to be developed to tackle the multimode problem in matter. Given the recent activity and progress in this field, it is likely that such techniques will be available in the near future.

This work was supported by the National Science Foundation.

References

[1] J.H. Eberly, C.K. Law, *Acta Phys. Pol. A* **93,** (1998).

[2] V.B. Braginsky, F.Ya. Khalili, *Quantum Measurement*, Cambridge University Press, Cambridge (NY) 1992.

[3] U. Leonhardt, M.G. Raymer, *Phys. Rev. Lett.* **76,** 1989 (1996).

[4] D.T. Smithey, M. Beck, J. Cooper, M.G. Raymer, *Phys. Scr. T* **48,** 35 (1993).

[5] K. Wodkiewicz, private communication.

[6] I.A. Walmsley, V. Wong, *J. Opt. Soc. Am. B* **13,** 2453 (1996).

[7] M.G. Raymer, *Am. J. Phys.* **62,** 10 (1994).

[8] W. Vogel, D.-G. Welsch, *Lectures on Quantum Optics*, Akademie Verlag, Berlin/VCH Publishing Inc., New York 1994.

[9] U. Leonhardt, *Measuring the Quantum State of Light*, Cambridge University Press, Cambridge 1997.

[10] S. Stenholm, *Ann. Phys. (New York)* **218,** 233 (1980).

[11] A. V. Vinogradov, J. Janszky, *Phys. Rev. Lett.* **64,** 2771 (1990).

[12] J. Janszky, A.V. Vinogradov, I.A. Walmsley, J. Mostowski, *Phys. Rev. A* **50,** 1777 (1994).

[13] I.A. Walmsley, M.G. Raymer, *Phys. Rev. A* **52,** 681 (1995).

[14] T.J. Dunn, I.A. Walmsley, S. Mukamel, *Phys. Rev. Lett.* **74,** 884 (1995).

[15] J.H. Eberly, K. Wodkiewicz, *J. Opt. Soc. Am.* **67,** 2591 (1979).

[16] P. Kowalczyk, C. Radzewicz, J. Mostowski, I.A. Walmsley, *Phys. Rev. A* **42,** 5622 (1990).

[17] A. Assion, M. Geisler, J. Helbing, V. Seyfried, T. Baumert, *Phys. Rev. A* **54,** R4605 (1996).

[18] L. Waxer, I.A. Walmsley, W. Vogel, *Phys. Rev. A* **56,** R3491 (1997).

[19] I. Walmsley, R. Trebino, *Opt. Photonics News* **7,** 23 (1996).

[20] D.J. Kane, R. Trebino, *IEEE J. Quantum Electron.* **29,** 571 (1993).

[21] J.-P. Foing, J.-P. Likforman, M. Joffre, A. Migus, *IEEE J. Quantum Electron.* **28,** 2285 (1992).

[22] S.P. LeBlanc, R. Sauerbrey, *Opt. Commun.* **111,** 297 (1994).

[23] J.-K. Rhee, T.S. Sosnowski, A.-C. Tien, T.B. Norris, in: *Conf. Lasers and Electro--Optics, Baltimore (MD), 1995*, OSA, Washington (DC) 1995, paper CPD39.

[24] V. Wong, I.A. Walmsley, *J. Opt. Soc. Am. B* **14,** 944 (1997).

[25] J.L.A. Chilla, O.E. Martinez, *IEEE J. Quantum Electron.* **27,** 1228 (1991).

[26] K.C. Chu, J.P. Heritage, R.S. Grant, K.X. Liu, A. Dienes, W.E. White, A. Sullivan, *Opt. Lett.* **20,** 904 (1995).

[27] K.W. DeLong, R. Trebino, J. Hunter, W.E. White, *J. Opt. Soc, Am. B* **11,** 2206 (1994).

[28] K.W. DeLong, D.N. Fittinghoff, R. Trebino, B. Kohler, K. Wilson, *Opt. Lett.* **19,** 2152 (1994).

[29] D. Kohler, L. Mandel, *J. Opt. Soc. Am.* **63,** 126 (1972).

[30] P. DeSantis, F. Gori, G. Guattari, C. Palma, J.M. Webster, *J. Photo. Sc.* **33,** 197 (1985).

[31] N. Streibl, *Opt. Commun.* **49,** 6 (1984).

[32] K. Ichikawa, A.W. Lohmann, M. Takeda, *Appl. Opt.* **27,** 3433 (1988).

[33] K.H. Brenner, A.W. Lohmann, *Opt. Commun.* **42,** 310 (1982).

[34] K. Creath, in: *Progress in Optics XXVI,* Ed. E. Wolf, Elsevier, Amsterdam 1988, p. 349.

[35] C. Iaconis, I.A. Walmsley, *Opt. Lett.* **21,** 1783 (1996).

[36] J.E. Rothenberg, D. Grischkowsky, *Opt. Lett.* **12,** 99 (1987).

[37] E. Fung, E.S. Yeung, *Analytical Chem.* **67,** 1913 (1995).

[38] L. Lepetit, G. Cheriaux, M. Joffre, *J. Opt. Soc. Am B* **12,** 2467 (1995).

[39] D.N. Fittinghof, J.L. Bowie, J.N. Sweetser, R.J. Jennings, M.A. Krumbügel, K.W. Delong, R. Trebino, I.A. Walmsley, *Opt. Lett.* **21,** 884 (1996).

[40] J.C. Diels, E.W. VanStryland, D. Gold, in: *Proc. First Intern. Conf. on Picosecond Phenomena,* Eds. C.V. Shank, E.P. Ippen, S.L. Shapiro, Springer, New York 1978, p. 117.

[41] V.A. Zubov, T.I. Kuznetsova, *Laser Physics* **2,** 73 (1992).

[42] V. Wong, I.A. Walmsley, *Opt. Lett.* **19,** 287 (1994).

[43] M. Takeda, H. Ina, S. Kobayashi, *J. Opt. Soc. Am.* **72,** 156 (1982).

[44] M. Freyberger, S. Kienle, V. Yakovlev, *Phys. Rev. A* **56,** 195 (1997).

[45] I.A. Walmsley, N.P. Bigelow, submitted for publication.

[46] D.F. McAlister, M.G. Raymer, *Phys. Rev. A* **55,** R1609 (1996).

[47] M.G. Raymer, M. Beck, D.F. McAlister, *Phys. Rev. Lett.* **72,** 1137 (1994).

[48] I.A. Walmsley, C. Iaconis, R. Trebino, in: *Ultrafast Phenomena X,* Eds. P. Barbara, J. Fujimoto, Springer, New York 1996, p. 169.

[49] M.G. Raymer, J. Cooper, M. Beck, *Phys. Rev. A* **48,** 4617 (1993).

[50] J.H. Shapiro, S.S. Wagner, *IEEE J. Quantum Electron.* **QE-20,** 803 (1984).

Vol. 93 (1998) ACTA PHYSICA POLONICA A No. 1

Proceedings of the International Conference "Quantum Optics IV", Jaszowiec, Poland, 1997

CHAOS ASSISTED TUNNELING AND NONSPREADING WAVE PACKETS

J. ZAKRZEWSKI

Instytut Fizyki im. Mariana Smoluchowskiego, Uniwersytet Jagielloński
Reymonta 4, 30-059 Kraków*, Poland

D. DELANDE

Laboratoire Kastler-Brossel, Tour 12, Etage 1, Université Pierre et Marie Curie
4 Place Jussieu, 75-005 Paris, France

AND A. BUCHLEITNER

Max-Planck-Institut für Quantenoptik
Hans-Kopfermann-Str. 1, 85748 Garching, Germany

Consider an initial state lying on a primary resonance island. The state may tunnel into the chaotic sea surrounding it and further escape to infinity via chaotic diffusion. Properties of transport in such a situation are studied on an exemplary system — the hydrogen atom driven by microwaves. We show that the combination of tunneling followed by chaotic diffusion leads to peculiar large scale fluctuations of the AC Stark shift and ionization rates. An appropriate random matrix model describes accurately these statistical properties.

PACS numbers: 05.45.+b, 32.80.Rm, 42.50.Hz

1. Introduction

Typical textbook cases of tunneling (in one-dimensional systems) consider quantum transport in situations when the classical transport between regions of space separated by e.g. potential barriers is forbidden. In multidimensional systems, the situation becomes complicated. Classically, in two-dimensions, Kolmogorov–Arnold–Moser (KAM) [1] tori provide strictly impenetrable borders for transport separating the phase space into distinct regions of classical motion†. When the classical phase space is of the mixed type — partially chaotic and partially

*Permanent address.

†In higher-dimensional systems, classical Arnold diffusion provides another mechanism of classical transport, a process which is, however, typically very slow [1].

regular — composed of a chaotic sea and regular islands embedded in it, the classical transport between the islands and the sea is forbidden. Semiclassically, one can associate wave functions with distinct regions of phase space [2], the residual coupling between them will be due to quantum tunneling process. One can then consider the tunneling between two islands mediated by the classical transport in the chaotic sea surrounding them.

Interestingly, this chaos assisted tunneling mechanism possesses unique features typically absent in the standard "barrier" tunneling of quantum mechanics, such as a great sensitivity to the variation of external parameters manifesting itself in fluctuations of observable quantities. Previous works considered mainly model one-dimensional time dependent systems [3–5] or model two-dimensional autonomous systems [6–9]. A similar problem in the scattering case has also been discussed on a kicked model system [10].

We shall consider here a different situation, motivated by the physics of atoms ionized by external strong electromagnetic radiation. We discuss the single tunneling process out of the stable island followed by the chaotic diffusion process which eventually leads to ionization. The example studied, a hydrogen atom placed in the microwave field of circular polarization, is realistic and experimentally accessible.

Firstly we review the properties of states localized on stable primary islands — the so-called nonspreading wave packets. Later we concentrate on the properties of the decay of wave packet states showing, by comparison to a statistical model, that their mechanism of ionization is indeed due to chaos assisted tunneling process. The reader interested in details should consult the original papers [11–15].

2. Nonspreading wave packets in periodically driven systems

Consider a one-dimensional system described by the Hamiltonian $H_0(I)$ where I is the principal action (we denote by φ the angle conjugate to I). The frequency of the classical motion $\omega_{\rm cl}(I) = \partial H_0/\partial I$ is a function of the action and, therefore of the energy E. Now let us perturb the system by a time-periodic potential $V = v(I,\varphi)\cos(\omega t)$. If, for a given E, $\omega_{\rm cl}$ is vastly different from the external frequency ω, the perturbation is nonresonant and affects only weakly the motion. The situation is drastically different in the case of a resonance, i.e. when $n\omega_{\rm cl} = m\omega$ with n, m being low integers [1]. A resonant exchange of energy can take place, the system becomes strongly perturbed by V. Consider the simplest case of $1:1$ resonance, i.e. when $\omega_{\rm cl} \approx \omega$. The Hamiltonian of the perturbed system can be (locally in energy) represented by the Hamiltonian of a pendulum with a pair of stable and unstable fixed points (periodic orbits of period $2\pi/\omega$) [1].

While in the unperturbed system two initially close points (I_1, φ_1) and (I_2, φ_2) in the phase space tend to separate in angle from one another (since $\omega_{\rm cl}(I_1) \neq \omega_{\rm cl}(I_2)$) it may no longer be so for the perturbed motion. Inside the island surrounding the stable fixed point, the classical motion is restricted to tori surrounding the fixed point, the classical motion becomes locked to the external driving frequency.

Consider now a wave packet constructed for the unperturbed system. It will disperse following the fate of classical trajectories. By contrast, a wave packet placed inside the resonance island of the perturbed system *will not* disperse re-

maining in the vicinity of the fixed point at every period of the external driving (following the corresponding periodic trajectory at all times).

Quantum mechanics of periodically perturbed systems tells us, by Floquet theorem [16], that the eigenstates of the system, the so-called quasi-energy states, are time periodic. If the classical island is large enough to support quantum states, some of the Floquet states must be localized inside the island. As exact solutions of the Schrödinger equation, they regain their shape every period and remain localized in the same region. Thus a quantum representation of the non-dispersive wave packet is simply a well chosen Floquet eigenstate.

First examples of Floquet states with such interesting properties were studied for model systems [17] and termed flotons. In an independent work, the non-dispersive wave packets have been semiclassically constructed for the hydrogen atom driven by a circularly polarized microwaves (CPM) [18]. Similarly such objects have been found for linearly polarized microwaves (LPM) [19] and identified with single Floquet eigenstates. For CPM this identification has been carried out in [11]. Let us mention also that the pendulum analysis in LPM case was also done [20]. Such a pendulum approach gives an excellent semiclassical prediction for the quasienergies of wave packet Floquet states.

For a hydrogen atom in CPM the situation is even simpler if not generic. In the frame rotating with the CPM field, the Hamiltonian becomes time independent

$$H = \frac{p^2}{2} - \frac{1}{r} + Fx - \omega \ell_z , \tag{1}$$

with ℓ_z the angular momentum operator. Atomic units are used throughout the paper.

At the center of the principal resonance island between the Kepler and the microwave frequency, a periodic orbit exists in the lab frame whose period exactly matches the period of the microwave. It corresponds to a fixed point of the motion in the rotating frame. It is possible to find the region of microwave fields when the point is stable [18], the semiclassical quantization based on a harmonic approximation around the fixed point yields accurate prediction for their energies [11]. Moreover, the wave packet is a coherent superposition of circular Rydberg states with a Gaussian-like distribution of the corresponding overlaps centered around the principal quantum number $n_0 = \omega^{-1/3}$. Note that n_0 is not necessarily an integer.

Due to the scaling properties of the Coulomb problem, the classical dynamics depends only on the scaled microwave amplitude $F_0 = Fn_0^4 = F\omega^{-4/3}$ which is the ratio of the microwave amplitude to the Coulomb field of the nucleus on the unperturbed n_0 circular orbit. The fixed point remains stable up to $F_0 \approx 0.11$, i.e. fields which are strong enough to ionize a typical atomic state in few microwave periods [21]. In fact a significant ionization of a typical initial atomic state occurs already at $F_0 \approx 0.03$ during few tens of microwave periods. Yet the lifetime against ionization of the wave packet states may well exceed million microwave periods! [12]. This is precise because these Floquet states are strongly localized on the stable island and classically forbidden to ionize. The spontaneous emission lifetime for the wave packets is exceedingly long [22], orders of magnitude longer than their lifetime against the ionization. Thus the ionization process is a

dominant mechanism of the decay of wave packet states, the unusual properties of this decay are reviewed in the next section.

3. Chaos assisted tunneling as a mechanism for ionization

Using the expansion of Eq. (1) in the Sturmian basis combined with complex rotation technique and Lanczos diagonalization routine we are able to calculate exactly the quasienergy spectrum of the problem (for details and further references see [12, 15]). The resulting Hamiltonian matrix is complex symmetric and yields eigenvalues of the form $\epsilon_i = E_i - \mathrm{i}\Gamma_i/2$. For a bound state the imaginary part vanishes and E_i is simply the energy of the state. For resonances, E_i yields the energy position of the resonance while the corresponding Γ_i is the resonance width. Excellent semiclassical prediction for the real part of the energy [11] allows us to extract only few eigenvalues (from matrices of a typical rank of 50000) around the semiclassical value, the wave packet state is then identified by its large dipole moment ($\approx n_0^2$) in the rotating frame.

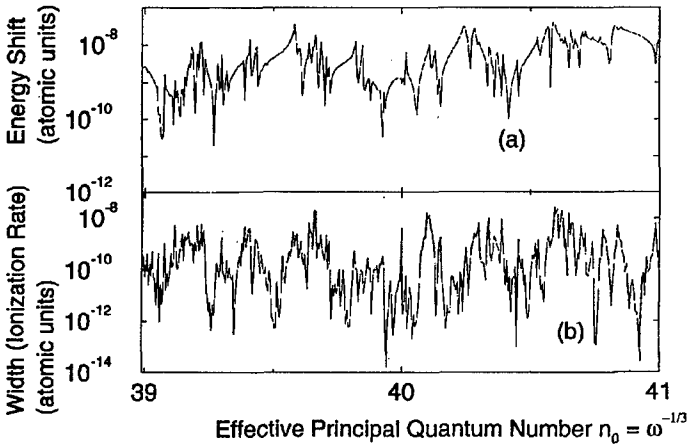

Fig. 1. Typical fluctuations of the width (ionization rate) (b) and the energy shift (a) (with respect to its unperturbed position) of the non-spreading wave packet of a hydrogen atom in CPM. The data presented are obtained for small variations of the effective principal quantum number n_0 around 40, a scaled microwave electric field $F_0 = Fn_0^4 = 0.0426$ and a microwave frequency $\omega = 1/n_0^3$. To present both plots on the logarithmic scale, preferred to show the fluctuations over several orders of magnitude, we plot the absolute value of the shift rather than the shift itself.

The typical *deviations* of the exact resonance position from the semiclassical prediction and the *ionization rates* obtained are presented in Fig. 1. Observe the large scale fluctuations of both quantities over several orders of magnitude for small changes of the frequency (typically of the order of 1 part in 1000). These fluctuations — although perfectly deterministic — look completely random and are strongly reminiscent of the universal conductance fluctuations observed in mesoscopic systems [23]. Indeed, the ionization width measures the rate at which

an electron initially localized close to the stable resonant trajectory ionizes, i.e. escapes to infinity. In other words, the ionization width directly measures the conductance of the atomic system from the initial point to infinity. In a quantum language, the ionization width is due to the coupling (via tunnel effect) between the localized wave packet and states lying in the chaotic sea surrounding it. While the energy of the wave packet is a smooth function of the parameters F and ω, the energies of the chaotic states display a complicated behavior characterized by level repulsion and strong avoided crossings. By chance, it may happen that — for specific values of the parameters — there is a quasi-degeneracy between the wave packet eigenstate and a chaotic state. There, the two states are more efficiently coupled by tunneling and the ionization width of the wave packet eigenstate increases. This is the very origin of the observed fluctuations. Simultaneously, the repulsion between the two states should slightly modify the energy (real part of the complex eigenvalue) of the wave packet state leading to fluctuations of the AC Stark shift.

To describe the fluctuations *quantitatively* we calculate the statistical distributions of the ionization widths $P(w)$ and of the energy shifts $P(s)$ and compare them with a simple statistical model [15]. The idea is to consider the wave packet eigenstate as coupled randomly with a set of chaotic states (described by random matrix theory [24]) themselves randomly coupled to the atomic continuum. For the detailed description of the model we refer the reader to [15]. In short the random realization of the Hamiltonian takes the form

$$\mathcal{H} = \begin{pmatrix} E_0 & \sigma V^{\mathrm{T}} \\ \sigma V & H_0 - \mathrm{i}\gamma W W^{\mathrm{T}} \end{pmatrix}, \tag{2}$$

where V is a random vector (whose components are Gaussian distributed random numbers) coupling a regular (wave packet) state with energy E_0 to N chaotic states (eigenstates of H_0). The strength of the coupling is determined by σ. To model H_0 we use the standard assumption that H_0 pertains to the Gaussian orthogonal ensemble and generate H_0 accordingly [24]. The decay of chaotic states is due to a non-Hermitian part $-\mathrm{i}\gamma W W^{\mathrm{T}}$ with strength determined by γ. W itself is a random vector for a single channel decay [25]. The variance of the Gaussian distribution used to generate H_0 and the dimension of the matrix N determine the mean level spacing Δ of the model. The two physically relevant, independent parameters are γ/Δ and σ/Δ. In the perturbative regime ($\gamma/\Delta, \sigma/\Delta \ll 1$) one may obtain analytically [15] the predictions for the distribution of shifts (of the regular state energy from the unperturbed value E_0) $P(s)$ and that for the widths $P(w)$. Alternatively, as done here, one may find both distributions numerically by averaging over several realizations of random Hamiltonian Eq. (2). A comparison of the obtained distributions with data obtained for the real system — the hydrogen atom in CPM — allows us to extract the values of the physical parameters: σ/Δ — the coupling between the regular and chaotic states (the tunneling rate) and γ/Δ — the strength of the decay of chaotic states (the chaotic ionization rate). An example of such a fit is presented in Fig. 2. Typically around 1000 data points are taken around some mean value of n_0 and F_0.

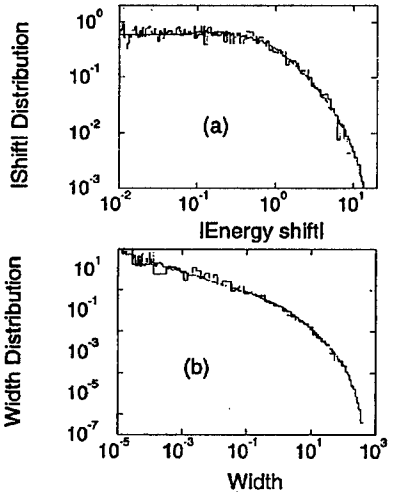

Fig. 2. The AC Stark shift distribution (a) and the width distribution (b) obtained from the data, part of which is shown in Fig. 1. Both distributions are shown in double logarithmic scale to better visualize the behavior over a range of shift and width values. Since AC Stark shift may be both positive and negative we show the distribution of the modulus. Large bin histograms correspond to hydrogen atom in circularly polarized microwaves, small bins to a fitted random model. Both distributions show the dominance of algebraic tail behavior followed by an exponential cut-off.

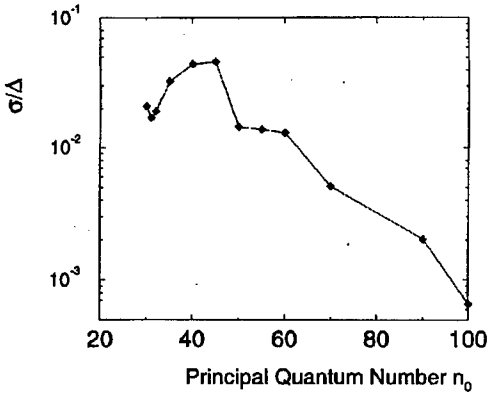

Fig. 3. The tunneling rate σ/Δ as a function of the effective quantum number $n_0 \propto 1/\hbar$ for a fixed classical dynamics, $F_0 = 0.0426$. Note the exponential decrease for sufficiently high n_0 (vertical scale is logarithmic).

Taking several stretches of data corresponding to different mean n_0 and the same F_0 one can test the $\hbar$ dependence of the tunneling rate and the ionization rate. The effective $\hbar$ in our problem is inversely proportional to n_0. It turns out that γ/Δ, the chaotic ionization rate, is only weakly dependent on n_0. This is

understandable — the ionization of chaotic states originates from the classical diffusion. However, as depicted in Fig. 3, σ/Δ, i.e., the tunneling rate decays exponentially with n_0 to a good accuracy. Writing the tunneling rate as $\sigma/\Delta \propto \exp(-S/\hbar) \propto \exp(-Sn_0)$ we can extract by a straight line fit, the tunneling action value $S = 0.06 \pm 0.01$. This exponential behavior is a strong evidence of the tunneling mechanism of the ionization.

4. Conclusions

We have provided a numerical evidence for a novel mechanism of ionization — chaos assisted tunneling — by studying a realistic and experimentally accessible example — a hydrogen atom driven by circularly polarized microwaves. It turns out that both the widths and AC Stark shifts of nonspreading wave packet states exhibit large scale fluctuations. We analyse these fluctuations quantitatively using an appropriately defined random matrix model. The model allows us to separate the ionization into two stages: tunneling from a stable island into the surrounding chaotic sea (which shows the typical exponential dependence on $\hbar$) and the chaotic diffusion process (weakly dependent on $\hbar$) which leads to further excitation and finally ionization.

Acknowledgments

CPU time on a Cray C98 computer has been provided by IDRIS. Laboratoire Kastler Brossel de l'Université Pierre et Marie Curie et de l'Ecole Normale Supérieure is unité associée 18 du CNRS. J.Z. acknowledges support of the Committee for Scientific Research (Poland) under project No. 2P03B 03810. The additional support under the bilateral collaboration scheme (J.Z. and D.D.) of the French Embassy in Poland, no. 76209 and the Programme International de Coopération Scientifique (CNRS) no. 408 is appreciated.

References

[1] A.J. Lichtenberg, M.A. Liberman, *Regular and Chaotic Dynamics*, Springer-Verlag, New York 1992.

[2] I.C. Percival, *J. Phys. B* **6**, L229 (1973).

[3] W.A. Lin, L.E. Ballentine, *Phys. Rev. Lett.* **65**, 2927 (1990); *Phys. Rev. A* **45**, 3637 (1992).

[4] F. Grossmann, T. Dittrich, P. Jung, P. Hänggi, *Phys. Rev. Lett.* **67**, 516 (1991); *Z. Phys. B* **84**, 315 (1991); *J. Stat. Phys.* **70**, 229 (1993).

[5] J. Plata, J.M. Gomez Llorente, *J. Phys. A* **25**, L303 (1992).

[6] O. Bohigas, S. Tomsovic, D. Ullmo, *Phys. Rep.* **223**, 43 (1993).

[7] O. Bohigas, D. Boosé, R. Egydio de Carvalho, V. Marvulle, *Nucl. Phys. A* **560**, 197 (1993).

[8] S. Tomsovic, D. Ullmo, *Phys. Rev. E* **50**, 145 (1994).

[9] F. Leyvraz, D. Ullmo, *J. Phys. A* **29**, 2529 (1996).

[10] P. Gerwinski, P. Šeba, *Phys. Rev. E* **50**, 3615 (1994).

[11] D. Delande, J. Zakrzewski, A. Buchleitner, *Europhys. Lett.* **32**, 107 (1995).

[12] J. Zakrzewski, D. Delande, A. Buchleitner, *Phys. Rev. Lett.* **75**, 4015 (1995).

[13] J. Zakrzewski, A. Buchleitner, D. Delande, *Z. Phys. B* **103**, 115 (1997).

[14] J. Zakrzewski, D. Delande, *J. Phys. B, Atom. Mol. Opt. Phys.* **30**, L87 (1997).

[15] J. Zakrzewski, D. Delande, A. Buchleitner, unpublished.

[16] J.H. Shirley, *Phys. Rev.* **138**, B979 (1965).

[17] J. Henkel, M. Holthaus, *Phys. Rev. A* **45**, 1978 (1992); M. Holthaus, *Chaos Solitons Fractals* **5**, 1143 (1995).

[18] I. Białynicki-Birula, M. Kaliński, J.H. Eberly, *Phys. Rev. Lett.* **73**, 1777 (1994).

[19] A. Buchleitner, thèse de doctorat, Université Pierre et Marie Curie, Paris 1993, unpublished; D. Delande, A. Buchleitner, *Adv. At. Mol. Opt. Phys.* **35**, 85 (1994); A. Buchleitner, D. Delande, *Chaos Solitons Fractals* **5**, 1125 (1995); *Phys. Rev. Lett.* **75**, 1487 (1995).

[20] L. Sirko, P.M. Koch, *Appl. Phys. B* **60**, 195 (1995).

[21] J. Zakrzewski, R. Gębarowski, D. Delande, *Phys. Rev. A* **54**, 691 (1996).

[22] Z. Białynicka-Birula, I. Białynicki-Birula, submitted to *Phys. Rev. A*; K. Hornberger, A. Buchleitner, submitted to *Phys. Rev. Lett.*

[23] S. Washburn, R. Webb, *Adv. Phys.* **35**, 375 (1986); D. Mailly, M. Sanquer, *J. Phys. I (France)* **2**, 357 (1992); P.A. Lee, A.D. Stone, *Phys. Rev. Lett.* **55**, 1622 (1985).

[24] O. Bohigas, in: *Chaos and Quantum Physics*, Eds. M.-J. Giannoni, A. Voros, J. Zinn-Justin, Les Houches Summer School, Session LII, North-Holland, Amsterdam 1991, p. 87.

[25] F. Haake, F. Izrailev, N. Lehmann, D. Saher, H.-J. Sommers, *Z. Phys. B* **88**, 359 (1992).

Vol. 93 (1998) ACTA PHYSICA POLONICA A No. 1

Proceedings of the International Conference "Quantum Optics IV", Jaszowiec, Poland, 1997

QUEST FOR GHZ STATES

M. Żukowski[a,b], A. Zeilinger[a],
M.A. Horne[c], and H. Weinfurter[a]

[a]Institut für Experimentalphysik, Universität Innsbruck, 6020 Innsbruck, Austria
[b]Institute of Theoretical Physics and Astrophysics
Gdańsk Uniwersity, 80-952 Gdańsk, Poland
[c]Stonehill College, North Easton, Massachusetts 02357, USA

The premises of the Einstein–Podolsky–Rosen argument for their claim that quantum mechanics is an incomplete theory are inconsistent when applied to three-particle systems in entangled Greenberger–Horne–Zeilinger states. However, thus far there is no experimental confirmation for existence of such states. We propose a technique to obtain Greenberger–Horne–Zeilinger states which rests upon an observation that when a single particle from two independent entangled pairs is detected in a manner such that it is impossible to determine from which pair the single came, the remaining three particles become entangled.

PACS numbers: 03.65.Bz, 42.50.Dv, 89.70.+c

1. Introduction

The premises of the Einstein–Podolsky–Rosen (EPR) argument [1] to show incompleteness of quantum mechanics are inconsistent when applied to maximally entangled states of at least three particles. Take a Greenberger–Horne–Zeilinger (GHZ) state of three particles which are on their way to three spatially separated observers (Fig. 1) [2]. Imagine that the relevant degrees of freedom for the local measurements are described by

$$|\psi(3)\rangle = \frac{1}{\sqrt{2}}\left(|a\rangle|b\rangle|c\rangle + |a'\rangle|b'\rangle|c'\rangle\right), \tag{1}$$

where $\langle x|x'\rangle = 0$ ($x = a, b, c$, and kets denoted by one letter pertain to one of the particles). The three observers A, B and C (spatially separated) measure the observables: $\widehat{A}(\phi_A)$, $\widehat{B}(\phi_B)$, $\widehat{C}(\phi_C)$, defined by

$$\widehat{X}(\phi_X) = |+,\phi_X\rangle\langle+,\phi_X| - |-,\phi_X\rangle\langle-,\phi_X| \tag{2}$$

and

$$|\pm,\phi_X\rangle = \frac{1}{\sqrt{2}}\left(\pm\mathrm{i}|x'\rangle + \exp\left(\mathrm{i}\phi_X\right)|x\rangle\right), \tag{3}$$

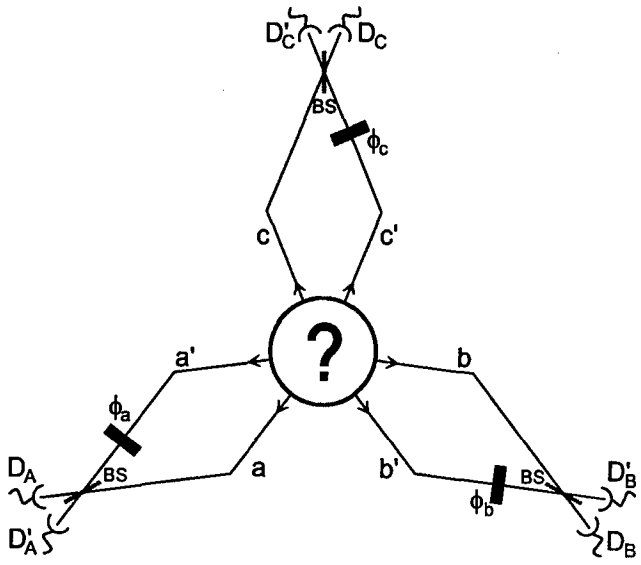

Fig. 1. Three-particle beam-entanglement GHZ interferometer [2]. Three particles in state (1) enter the arrangement. Adjustable phase shifters provide a change of the relative phase of the state components by $\phi_A + \phi_B + \phi_C$. Consequently the threefold coincident count rate in, say, detectors D_A, D_B, and D_C will oscillate sinusoidally when the phase is varied. The detection events are spatially separated.

where $X = A, B, C$. The quantum prediction for the expectation value of the product of the three local observables is given by

$$E(\phi_A, \phi_B, \phi_C) = \langle\psi|\widehat{A}(\phi_A)\widehat{B}(\phi_B)\widehat{C}(\phi_C)|\psi\rangle = \sin(\phi_A + \phi_B + \phi_C). \tag{4}$$

The EPR program, when applied to the above process, should be based first on the establishment of the elements of reality for the system. The EPR definition of an element of reality reads: *if, without in any way disturbing a system, we can predict with certainty (i.e., with probability equal to unity) the values of a physical quantity, then there exist an element of physical reality corresponding to this physical quantity.* The EPR argument continues now with the following steps. One establishes that quantum mechanics predicts for the studied system perfect correlations. This occurs in the present case when $\phi_A + \phi_B + \phi_C = \pi/2 + k\pi$ (that is, when $\sin(\pi/2 + k\pi) = \pm 1$). E.g., for the settings $\phi_A = \pi/2$, $\phi_B = 0$ and $\phi_C = 0$ whatever may be the results of local measurements of the observables, for say the particles belonging to the i-th triple (the ensemble of all such triples is represented by the quantum state $|\psi(3)\rangle$), they have to satisfy

$$A_i(\pi/2)B_i(0)C_i(0) = 1, \tag{5}$$

where $X_i(\phi)$ is the value of a local measurement of the observable $\widehat{X}(\phi)$ that *would have been* obtained for the i-th particle triple if the setting of the measuring device *had* been as indicated, i.e. ϕ. Note that relativistic causality demands that $X_i(\phi)$ depends solely on the local parameter. Equation (5) clearly indicates that we can

predict with certainty the result of measuring the observable pertaining to one of the particles (say c) by choosing to measure suitable observables for the other two. As the two first acts of measurement are spatially separated from the third particle, EPR argue that they cannot cause any real change in it. Hence the value $C_i(0)$ is an element of physical reality.

However, *had* the local apparatus settings been different one *would have had*, e.g.

$$A_i(0)B_i(0)C_i(\pi/2) = 1. \tag{6}$$

We can repeat the argument, establishing now the value of the element of reality $C_i(\pi/2)$. Hence two noncommuting observables $\widehat{C}(\pi/2)$ and $\widehat{C}(0)$ are endowed with elements of reality (i.e. their values are predetermined). Since such statement is prohibited by quantum mechanics therefore it cannot be a complete theory!

However, for the *three*-particle state one can consider also two other similar situations and establish that quantum mechanical predictions imply that the elements of reality must satisfy

$$A_i(0)B_i(0)C_i(\pi/2) = 1 \tag{7}$$

and

$$A_i(\pi/2)B_i(\pi/2)C_i(\pi/2) = -1. \tag{8}$$

The allowed values for the elements of reality are equal, by definition, to the eigenvalues of the respective observables, i.e. they are ± 1. If one multiples the left hand sides of Eqs. (5–8), and simply notices that all elements of reality appear in such a product twice, the result is, surprisingly, 1, whereas, the product of right hand sides gives -1. Thus the EPR program breaks down at the very outset, as their definition of the elements of reality (via the perfect correlations, and locality) is void. We have a "Bell theorem without inequalities" [2]. One can summarize the above story by yet another *counterfactual* statement (precisely on such type of statements the EPR argument is based on): had EPR known about GHZ states they might never have written their paper or, at least, they might have written it very differently.

Due to imperfections of laboratory devices, one cannot expect perfect correlations to occur. Thus, any test of local realism based on the GHZ correlations has to resort to some Bell-type inequalities. The simplest (ad hoc) algebraic form leading to a Bell-like inequality seems to be the one based upon the following algebraic identity:

$$A_i(\phi'_A)B_i(\phi_B)C_i(\phi_C) + A_i(\phi_A)B_i(\phi_B)C_i(\phi'_C) + A_i(\phi_A)B_i(\phi'_B)C_i(\phi_C)$$
$$-A_i(\phi'_A)B_i(\phi'_B)C_i(\phi'_C) = \pm 2, \tag{9}$$

which must be always satisfied if $X_i(\phi_X) = \pm 1$. Thus the average values for local realistic [3] predictions for the products of the local results should fulfill

$$-2 \leq E(\phi'_A, \phi_B, \phi_C) + E(\phi_A, \phi_B, \phi'_C) + E(\phi_A, \phi'_B, \phi_C)$$
$$-E(\phi'_A, \phi'_B, \phi'_C) \leq 2. \tag{10}$$

The maximal violation of this inequality, by a factor of 2, is obtained if we put into it the quantum prediction with the previously discussed settings: $\phi_X = 0$, $\phi'_X = \pi/2$.

In a real experiment one cannot expect the three-particle interference fringes to be of 100% visibility (V) and therefore one expects the correlation function to be $V\sin(\phi_A+\phi_B+\phi_C)$ [4]. Therefore, the critical value of the visibility to violate the Bell inequality is $V_{\rm crit}=50\%$ (i.e. much lower than the threshold for the two-particle Bell-type experiment).

2. Experiment

While it would be interesting to experimentally exhibit the correlations present in a three-particle entanglement, no experimentally tested procedure exists for preparing the necessary state. The natural source of three-particle entanglements, three-photon positonium annihilation, is a rare event, and the polarizations of the γ rays are difficult to measure. Also one could think of a higher order spontaneous down-conversion process involving cubic nonlinearity in crystal's polarizability. However, both processes share (almost) complete unpredictability of the directions of emission (this makes the count rates very low). Since 1989, many other sources were proposed but thus far no experiment has been performed [5].

We wish to propose a possibly realizable, relatively simple procedure for generating three-particle entanglement out of only *two* pairs of entangled photons [6]. One can generate these states by interfering photon pairs produced by two independent spontaneous parametric frequency down-conversion (PDC) sources. The product of two two-particle states can be projected, by a measurement upon one of the four particles, in such a way that the resulting collapse leads to a three-particle GHZ-state. As the PDC sources are endowed with high angular correlation of the emissions, this feature is also present in our compound source (what, despite relatively low probability of simultaneous emissions from two independent sources, should contribute to tolerable count rates).

Yurke and Stoler [7] were first to suggest that interfering particles from independent sources may give rise to non-classical Bell-EPR correlations. Interference between particles produced by independent sources is observable only if the origin of the particles cannot be inferred anymore [8]. This necessitates that either the coincidence detection or the generation of the particles is done with a time resolution shorter than their coherence times [9]. Here we shall employ the second alternative.

Consider the arrangement of Fig. 2. Two independent PDC sources each emit a pair of particles in a beam entangled state (type-I phase matching) [10] and, by chance, these emissions are nearly simultaneous. Suppose for example that the states of the pairs are

$$\frac{1}{\sqrt{2}}\left(|a\rangle|d\rangle+|a'\rangle|c'\rangle\right) \tag{11}$$

from source A, and

$$\frac{1}{\sqrt{2}}\left(|d'\rangle|b'\rangle+|c\rangle|b\rangle\right) \tag{12}$$

from source B (the letters represent beams taken by the photons in Fig. 2, all beams have the same polarization) [10]. The beams d and d' are mixed by a 50–50 beamsplitter, behind which are two detectors $D_{\rm T}$ (trigger) and $D'_{\rm T}$.

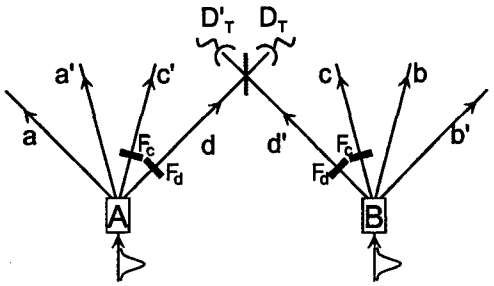

Fig. 2. A three-particle beam-entanglement source. Short pulses of duration ΔT stimulate two independent two-particle sources, A and B, to each emit a pair of beam-entangled particles. The state of the pair from A [B] is given by Eq. (11) [(12)]. Suppose that the trigger detector, D_{T}, registers a single particle and the other three particles are eventually found to have been in beams a or a', b or b', and in c or c', respectively. If the trigger particle came from A via transmission at the beam splitter, BS, its sibling must be in beam a and the pair from B must be in beams b and c. If the trigger particle came from B via reflection at BS, its sibling must be in beam b' and the pair from A must be in beams a' and c'. Narrow filters, F_c and F_d, of widths much narrower than the pulse spectrum make the source of the trigger particle essentially unknowable (see text). Consequently, the state of the other three particles is the entanglement of Eq. (13).

Suppose that one and only one of these four particles is detected by D_{T}, no particle is detected at D'_{T}, and the other six beams illuminate the three-particle interferometer [2] of Fig. 1. Because of the beamsplitter, the trigger particle could have come from either source A or B. If it came from A, its companion must be in beam a, and the pair from B must be in beams b and c. Thus, the state of the triple of remaining particles is $|a\rangle|b\rangle|c\rangle$. If on the other hand the trigger particle came from source B, its companion must be in beam b' and the pair from A must be in beams a' and c'. Thus, if the trigger particle came from B, the state of the remaining triple is $|a'\rangle|b'\rangle|c'\rangle$.

Now, if the procedure of emission and selection of the four photons is such that one *cannot ever know, not even in principle*, which source produced the trigger event, then the other photons, as they enter the interferometer of Fig. 1, will be in a superposition of the two three-particle states mentioned above, i.e. in the GHZ state

$$\frac{1}{\sqrt{2}}\left(|a\rangle|b\rangle|c\rangle+\mathrm{e}^{\mathrm{i}\phi}|a'\rangle|b'\rangle|c'\rangle\right), \tag{13}$$

where the relative phase ϕ depends on the positions of various elements of the full setup.

For the *coherent* superposition of state (13) to form one must erase *all* ways by which one might in principle identify true pairs. We assume that the two sources are pumped by one pulsed laser and emitting down converted radiation of a degenerate frequency. All three remaining photons (after the trigger event) are fed into three spatially separated interferometers (see, Fig. 1). The detection

station B observes the radiation coming from beams b and b', station A from beams a and a', whereas the station C collects the radiation from c and c'. In all beams we have filters of the same central frequency (half of the pump frequency). However, the widths of the filters may differ.

Suppose that the three photons and the trigger one are detected coincidently (within a few nanosecond window), one in each detection stations A, B and C, and the fourth at D_{T}. Clearly the photons at the first two stations came from the crystals bearing the same name as the station. But the origins of the photon at D_{T} and C are unclear. In such a case one could, in principle, determine that photon detected at D_{T} came from crystal A (B) by noting the near simultaneity of the detection of photon D_{T} and one of the photons at B or A (this is due to the property of the PDC radiation: the detection times of a pair are extremely well correlated). To ensure that the source of photons is unknowable, we propose that the two crystals should be pumped by pulses of durations around $\tau \approx 100$ fsec, and that the trigger should be detected behind a narrow filter whose inverse of the bandwidth (coherence time) exceeds τ. If one of the members of a PDC pair passes such a filter the temporal correlation with its companion spreads to around τ. Thereby placing suitable filters prevents identification of the trigger photon and its partner by comparison of their arrival times. However, if the detections at C and either A or B are strictly time correlated one still concludes that the photons came from one crystal. One can again remedy this by putting filters of coherence time exceeding τ in beams c and c'. Now, the which-way information is completely erased. Please note that due to the pulsed nature of the pump (i.e. its non-monochromaticity) the complementary feature which could in principle betray the origin of particles at D_{T} and C, namely the frequency correlation, is more fuzzy than the frequency resolution imposed by the filters. We can expect high visibility of three-particle fringes.

With a more quantitative description we now shall estimate the visibility of the three-particle fringes. The following assumptions will be made: (i) the probability of a multiple emission from a single PDC is low; (ii) the pulse is not too short, i.e., the nonmonochromaticity of the pulse will not blur too much the strong angular correlation of the emissions (due to the effective energy and momentum conservation within the crystal). Thus, the photons can be described as emitted in specified, very well-defined directions.

The state of the photon *pair* emerging from the source A (plus the filter system) can therefore be approximated by

$$|\Psi^A\rangle = |\psi_{ad}\rangle + |\psi_{a'c'}\rangle = \int \mathrm{d}\omega_1 \mathrm{d}\omega_2 \mathrm{d}\omega_0 \Delta(\omega_0 - \omega_1 - \omega_2) g(\omega_0)$$
$$\times \left(f_a(\omega_1) f_d(\omega_2) |\omega_1; a\rangle |\omega_2; d\rangle + f_{a'}(\omega_1) f_{c'}(\omega_2) |\omega_1; a'\rangle |\omega_2; c'\rangle \right), \qquad (14)$$

where, e.g., the ket $|\omega, e\rangle$ describes a single photon of frequency ω in the beam e, the function g represents the spectral content of the pulse, and f_e is the transmission function of the filter in the beam e. The function Δ is sharply peaked at the origin and describes the phase-matching condition. One can approximate it by the Dirac delta. Similar structure has the ket describing the pair of photons coming from the other source, $|\psi_B\rangle$.

If one introduces objects [9] like, e.g. $|t;b\rangle = (1/\sqrt{2\pi})\int \mathrm{d}\omega \mathrm{e}^{\mathrm{i}\omega t}|\omega;b\rangle$, the amplitude, e.g., to detect a photon at time $t_{x'}$ by a detector monitoring the beam x' and another one at time $t_{y'}$ by a counter in the beam y', provided the initial photon state was, say, $|\psi_{xy}\rangle$, can be written as $A_{xy}(t_{x'},t_{y'}) = (\langle t_{x'};x'|\langle t_{y'};y'|)|\psi_{xy}\rangle$. The elementary amplitudes of the interferometric process have now a simple, intuitively appealing, form $A_{xy}(t_x,t_y) = (1/\sqrt{2\pi})\int \mathrm{d}tG(t)F_x(t_x-t)F_b(t_y-t))$, where the functions denoted by capitals are the Fourier transforms: $F(t) = (1/\sqrt{2\pi}) \times \int \mathrm{d}\omega \mathrm{e}^{\mathrm{i}\omega t} f(\omega)$.

The amplitude of the three-photon interference at, say, detectors D_A, D_C and D_B (detector D_X registers photons in state $|+,\phi_X\rangle$), at times t_A, t_B and t_C, under the condition that the trigger photon fired at t_T, is proportional to

$$A_{ad}(t_A,t_\mathrm{T})A_{cb}(t_C,t_B) + \mathrm{e}^{\mathrm{i}\phi}\mathrm{e}^{\mathrm{i}(\phi_a+\phi+b\phi_c)}A_{b'd'}(t_B,t_\mathrm{T})A_{a'c'}(t_A,t_C), \tag{15}$$

where ϕ_i, $i=a,b,c$ is the local phase shift in the given beam. To get the overall probability of the process one has to integrate the square of the modulus of the amplitude over the detection times (the time resolution of the detectors is of the order of nanoseconds, which is much longer than the coherence times, thus due to our earlier assumptions the integration over time can be extended to infinity).

Now, if one assumes that the filters in beams leading to a single detector station are identical, that the functions have the following structure: $F_f(t) = \mathrm{e}^{-\mathrm{i}\frac{1}{2}\omega_\mathrm{P}t}|F(t)|$, $G(t) = \mathrm{e}^{-\omega_\mathrm{P}t}|G(t)|$, where ω_p is the central frequency of the pulse, then the maximal visibility of the three-particle interference can be written as

$$V(3) = \frac{\int \mathrm{d}^4t|A_{ad}(t_A,t_\mathrm{T})A_{bc}(t_B,t_C)A_{b'd'}(t_B,t_\mathrm{T})A_{a'c'}(t_A,t_C)|}{\int \mathrm{d}^4t|A_{ad}(t_A,t_\mathrm{T})A_{bc}(t_B,t_C)|^2}, \tag{16}$$

where $\mathrm{d}^4t = \mathrm{d}t_A\mathrm{d}t_B\mathrm{d}t_C\mathrm{d}t_\mathrm{T}$.

If one specifies, for simplicity, all the functions as Gaussians, $\exp\left[-\frac{(\omega-\Omega)}{2\sigma^2}\right]$, where Ω is the mid frequency and σ the width, the formula for the visibility reads

$$V(3) = \left(\frac{2\sigma_\mathrm{p}^2}{2\sigma_\mathrm{p}^2 + \sigma_A^2\sigma_C^2/(\sigma_\mathrm{p}^2+\sigma_A^2+\sigma_C^2) + \sigma_A^2\sigma_T^2/(\sigma_\mathrm{p}^2+\sigma_A^2+\sigma_T^2)}\right)^{1/2}, \tag{17}$$

where σ_p is the spectral width of the pulse, σ_f, $f=A,B,C$, is the width of the filter, and we assume that $\sigma_A = \sigma_B$. If one removes the filters A and B, the formula simplifies to

$$V(3) = \left(\frac{2\sigma_\mathrm{p}^2}{2\sigma_\mathrm{p}^2+\sigma_C^2+\sigma_T^2}\right)^{\frac{1}{2}}. \tag{18}$$

Therefore, narrow filters in paths a, a' and b, b' are not necessary to obtain high visibility. The other filters should be always sufficiently narrow.

3. Prospects

Currently realizable values of $\sigma_f \approx 1$ nm for filter widths and $\sigma_\mathrm{p} \approx 5$ nm for pulse spectral width yield $V(3) \approx 97\%$. This is well above the required 50%, and therefore there is much room before the imperfections of the actual equipment force down the visibility below this crucial figure. It is worthwhile to add that

our current set-up for pulsed two-source down conversion (producing polarization entanglements [11]) gives about 10^{-2} s^{-1} fourfold coincidences, but with wider filters.

The principal aim of the experiment will be to show the existence of GHZ states. However, one also may view it as yet another attempt for a test against local realism. At the present moment plenty of "loophopes" seem to be present in our proposal if one wishes to view it in this way. However, if one attempts to interpret experimental observations in a local realistic way, one must notice that while the filters select photons, one could in principle detect all of them by using a suitably sophisticated dispersive optical element. The other complications are less important. For example, the trigger detector may fire if (a) only one down conversion occurred, (b) two down conversions occurred in one crystal. Case (a) can be rejected, two of the detector stations will show no counts. Case (b) can also be rejected, station D_A or D_B will exhibit no counts.

The laboratory realization of three-particle entanglement will open the door to many novel quantum phenomena and applications. These may include, not only the demonstration of GHZ correlations, but also: (a) generalization of two-particle phenomena (e.g. illumination of a tritter [12] with three entangled particles), (b) demonstration of *entangled entanglement* [13], (c) multiparticle quantum communication schemes (see, e.g. [14]).

One can for example link the ideas (b) and (c) and notice that the use of GHZ states (1) makes possible generation of a cryptographic key in such a way that it can be controlled by a third operator who decides whether to activate the key or not. Imagine that Alice, Bob and Cecil observe GHZ correlations. The protocol of key establishment between Alice and Bob is exactly the same as the one proposed by Ekert [15] for standard two-particle EPR-Bell correlations. However, depending on the measurement result at the station of Cecil, Alice and Bob share different two photon entangled states. Say that Cecil's observable is given by (3) with $\phi_C = \pi/2$. Then depending on the local result that he obtains the state shared by Alice and Bob is either $|\psi(2+)\rangle = (1/\sqrt{2})\,(|a\rangle|b\rangle + |a'\rangle|b'\rangle)$ or $|\psi(2-)\rangle = (1/\sqrt{2})\,(|a\rangle|b\rangle - |a'\rangle|b'\rangle)$, and therefore he holds the key to their key. Without the information on his results all that Alice and Bob share is just useless. However, once Cecil has communicated his results to Alice and Bob, the key they now can establish is also perfectly secret to him. The Third Man can control the key distribution but not the secret communication once he allows it!

This work was supported by the Austrian Fonds zur Förderung der wissenschaftl. Forschung (S6502). M. Żukowski acknowledges partial support of the University of Gdańsk research grant No. BW-5400-5-0306-7, and of the 1996/97 Austrian–Polish scientific-technological collaboration program No. 22 (Quantum communication and quantum information). H.W. is supported by the APART-fellowship of the Austrian Academy of Science.

References

[1] A. Einstein, B. Podolsky, N. Rosen, *Phys. Rev.* **47,** 777 (1935).

[2] D.M. Greenberger, M. Horne, A. Zeilinger, in: *Bell's Theorem, Quantum Theory, and Conceptions of the Universe*, Ed. M. Kafados, Kluwer, Dordrecht 1989; D.M. Greenberger, M.A. Horne, A. Shimony, A. Zeilinger, *Am. J. Phys.* **58,** 1131 (1990); N.D. Mermin, *Phys. Today*, June 1990, p. 9.

[3] J.S. Bell, *Physics* **1,** 195 (1965).

[4] M. Żukowski, *Phys. Lett. A* **177,** 290 (1993).

[5] For example, K. Wódkiewicz, L.-W. Wang, J.H. Eberly, *Phys. Rev. A* **47,** 3280 (1993); J.I. Cirac, P. Zoller, *Phys. Rev. A* **50,** R2799 (1994); S. Haroche, *Ann. N. Y. Acad. Sci.* **755,** 73 (1995); T. Sleator, H. Weinfurter, *Ann. N. Y. Acad. Sci.* **755,** 646 (1995); F. Laloë, *Current Science* **68,** 1026 (1995); C.C. Gerry, *Phys. Rev. A* **53,** 2857 (1996); T. Pfau, C. Kurtsiefer, J. Mlynek, *Quantum Semiclass. Opt.* **8,** 665 (1996).

[6] A. Zeilinger, in: *15 th Intern. Conf. Atomic Physics (ICAP)*, Ed. J. Walraven, Amsterdam 1996; A. Zeilinger, M.A. Horne, H. Weinfurter, M. Żukowski, *Phys. Rev. Lett.* **78,** 3031 (1997).

[7] B. Yurke, D. Stoler, *Phys. Rev. Lett.* **68,** 1251 (1992); *Phys. Rev. A* **46,** 2229 (1992).

[8] M. Żukowski, A. Zeilinger, M.A. Horne, A. Ekert, *Phys. Rev. Lett.* **71,** 4287 (1993).

[9] M. Żukowski, A. Zeilinger, H. Weinfurter, *Ann. N. Y. Acad. Science* **755,** 91 (1995).

[10] M.A. Horne, A. Shimony, A. Zeilinger, *Phys. Rev. Lett.* **62,** 2209 (1989); J.G. Rarity, P.R. Tapster, *Phys. Rev. Lett.* **64,** 2495 (1990).

[11] P.G. Kwiat, K. Mattle, H. Weinfurter, A. Zeilinger, *Phys. Rev. Lett.* **75,** 4337 (1995).

[12] A. Zeilinger, M. Żukowski, M.A. Horne, H.J. Bernstein, D.M. Greenberger, in: *Quantum Interferometry*, Eds. F. DeMartini, A. Zeilinger, World Scientific, Singapore 1994, p. 159; M. Żukowski, A. Zeilinger, M.A. Horne, *Phys. Rev. A* **55,** 2564 (1997).

[13] G. Krenn, A. Zeilinger, *Phys. Rev. A* **54,** 1793 (1996).

[14] C.H. Bennett, *Phys. Today*, Oct. 1995, p. 24.

[15] A.K. Ekert, *Phys. Rev. Lett* **67,** 661 (1991).

Vol. 93 (1998) ACTA PHYSICA POLONICA A No. 1

Proceedings of the International Conference "Quantum Optics IV", Jaszowiec, Poland, 1997

INTERFEROMETRY AND DISSIPATIVE OPTICS WITH ATOMS

P. SZRIFTGISER*, D. GUÉRY-ODELIN, P. DESBIOLLES, J. DALIBARD

Laboratoire Kastler Brossel, 24 rue Lhomond, 75005 Paris, France

M. ARNDT

Institut für Experimentalphysik der Universität Innsbruck
Technikerstr. 25, 6020 Innsbruck, Austria

AND A. STEANE

Clarendon Laboratory, Oxford, OX13PU, United Kingdom

We have designed a gravitational cavity for ultra-cold atoms using an atomic mirror made from an evanescent laser wave. By a temporal variation of the evanescent wave intensity, we have realized various atom optics components such as temporal slits and phase modulators. We have also designed an atom interferometer using this cavity which proves that the coherence of the de Broglie waves can be preserved during the bounce of the atoms on the mirror. Finally we show that an efficient cooling of the atoms inside the cavity can be achieved using a Sisyphus process during the bounce.

PACS numbers: 03.75.Dg, 32.80.Pj, 42.50.Vk

1. Introduction

In textbook presentations of quantum mechanics, a central argument for the validity of the theory is the equivalence of the behavior of material particles and light in a given interferometric setup, such as a Young slit or a Bragg diffraction experiment. From this equivalence we deduce the wave nature of particles, the optical wavelength being replaced by the de Broglie wavelength in the expressions for the fringe spacing or the diffraction angles.

The central point of this paper is to address the directly related question: are there situations where atoms and photons will give qualitatively different results in a given interference experiment? For steady-state problems the answer is negative since equal wavelength for light and matter will produce equal diffraction patterns. On the contrary, for time dependent problems, the dispersion relation

*Present address: Laboratoire de Spectroscopie Hertzienne de Lille, Bâtiment P5, 59655 Villeneuve d'Ascq, France.

enters into play and it becomes possible to investigate the nature of the interfering or diffracting objects.

Consider for example the following "Gedanken" experiment where a quasi--monochromatic wave packet is incident on a chopper (Fig. 1). The chopper is opened only for two short periods of duration τ and one looks for the signal on a detector located after the chopper. Is there any interference observable on this detector? In the case of photons propagating in vacuum, the answer is negative since the two wave packets will not spread and they will never overlap. On the contrary, for nonrelativistic material particles, the dispersion relation is not linear and the spreading of the two wave packets may be large enough so that they overlap onto the detector: an interference signal may be observed.

Fig. 1. (a) A quasi-monochromatic wave packet is incident onto a chopper which is opened for two short periods. (b) For matter waves the spreading of the two wave packets may lead to interferences in the signal recorded by the detector. This is not possible for light waves propagating in a non dispersive medium.

We present in this paper experiments performed with cesium atoms and addressing this class of time-dependent problems in quantum mechanics. We first describe the basic tool which allows us to chop and modulate atomic de Broglie waves, i.e. the atomic mirror (Sec. 2). We then present an observation of the time-diffraction phenomenon mentioned above (Sec. 3). In Sec. 4 we show that it is indeed possible to observe interferences between de Broglie waves by letting two wave packets spread and overlap. We then describe in Sec. 5 a phase modulator for atomic de Broglie waves. Finally we present in Sec. 6 a side experiment showing that an evanescent wave mirror can also provide an efficient cooling of the bouncing atoms using a Sisyphus process.

2. The atomic mirror

The key element for all the experiments presented in this paper is an atomic mirror formed by an evanescent light wave extending from a glass surface into the vacuum [1, 2]. The electric field in this wave gives rise to a potential for the atom which is simply the light shift of the atomic ground state

$$U = \hbar\Omega^2/4\delta, \qquad \text{for } |\delta| \gg \Omega, \tag{1}$$

$\Omega = dE/2\hbar$ is the Rabi frequency *in the evanescent wave*, proportional to the electric field amplitude E and the atomic dipole moment d; $\delta = \omega_L - \omega_A$ is the detuning between the laser frequency ω_L and the atomic resonance frequency ω_A. The electric field falls off with a distance z into the vacuum as $\exp(-\kappa z)$, where

the characteristic distance $\kappa^{-1} \approx 0.19$ μm. The potential is repulsive at positive detunings providing thus the desired mirror.

The prism surface is concave, with a radius of curvature 2 cm. The evanescent wave (EW) has a circular Gaussian profile, with $1/e^2$ radius $w = 300$ μm. It is formed using the total internal reflection of a laser with intensity $I = 100$ mW, with a linear polarization in the reflection plane; it is blue-detuned by $\delta/2\pi =$ 1 to 10 GHz from the resonance line $6s_{1/2}, F = 4 \leftrightarrow 6p_{3/2}, F = 5$. The EW therefore creates a potential barrier along the z-vertical direction $U(x, y, z) \propto I \exp[-2(x^2 + y^2)/w^2] \exp(-2\kappa z)/\delta$. The incident atomic velocity on the mirror is $v_i = 25$ cm/s, corresponding to a free fall of 3 mm (see below). The EW mirror is switched on and off by an acousto-optic modulator used in the zeroth order, triggered by a quartz-stabilized function generator. The switching time is ≈ 0.5 μs, similar to the atomic bouncing time $1/\kappa v_i \approx 1$ μs.

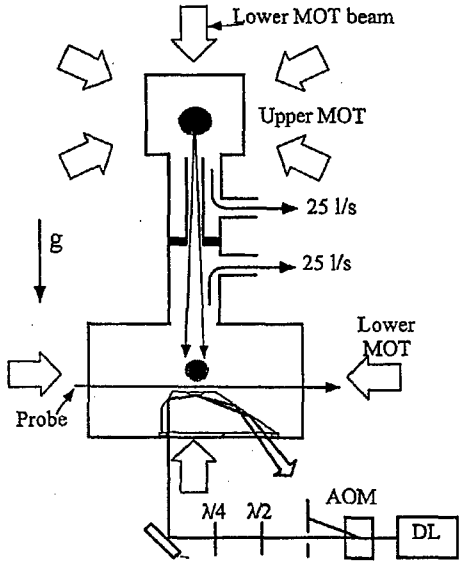

Fig. 2. Experimental setup. Atoms are captured in the upper MOT from a cesium vapor, and transferred to the lower MOT in a high vacuum cell. They are then cooled and dropped into the evanescent wave mirror, which is formed using light produced by a diode laser and which may be time modulated by an acousto-optic modulator.

Our vacuum system is based on two glass cubes of side 10 cm, one positioned 70 cm above the other (see Fig. 2). Each is evacuated by a 25 l/s ion pump, and they are connected through a narrow glass tube (ϕ9 mm, length 140 mm) to allow differential pumping. This system allows us to produce a good vacuum in the lower cell ($\leq 3 \times 10^{-9}$ mbar) while having sufficient vapor pressure of cesium in the upper cell (6×10^{-8} mbar) to load a magneto-optical trap (MOT) there in a short time.

The experimental cycle begins by loading 3×10^8 atoms into the MOT in the upper cell during 1 second. The collected atoms are then cooled to 5 μK in optical

molasses: the laser intensity is switched to 1 mW/cm^2 per beam, the magnetic field gradient is cut and the detuning δ between the laser and atomic frequencies is ramped to $\delta = -9\Gamma$, where $\Gamma = 2\pi \times 5.3$ MHz is the FWHM of the atomic resonance. The trap light is then switched far from the atomic resonance, and the atoms fall into the lower chamber.

After a free fall time of 365 ms, a MOT in the lower cell is switched on for 100 ms. The overall transfer efficiency is about 20%, so this provides 6×10^7 atoms each 1.4 seconds, with a lower trap lifetime $\approx$ 12 s. Once the atoms are caught in the lower MOT, they are compressed to a density 5×10^{10} cm^{-3} by reducing the laser intensity in the MOT to 0.5 mW/cm^2 at $\delta = -3\Gamma$ during 3 ms, and then cooled to 3.6 μK at $\delta = -9\Gamma$ in optical molasses during 20 ms. The center of the lower MOT is located 3 mm above the surface of the prism where the EW forms the mirror. The atoms are then dropped and hit the mirror $\approx$ 25 ms later; multiple bounces have been observed in this gravitational cavity [3].

3. Temporal diffraction of de Broglie waves

When a beam of particles with a well-defined energy is chopped into a short pulse, the outcoming energy distribution is broadened according to the time-energy uncertainty relation. This effect is very well known for photons and it is at the basis of spectroscopy with ultra-short pulses of light. For matter waves, the phenomenon of diffraction by a time slit has been studied theoretically by several authors [4].

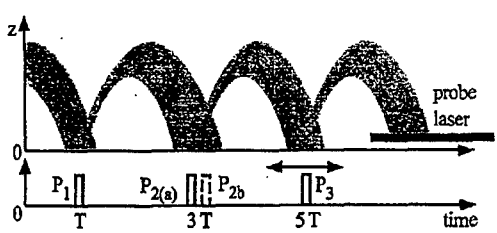

Fig. 3. A cold atomic cloud is released above a mirror formed by an evanescent laser wave. The mirror intensity I (lower curve) is chopped for two short pulses P_1 and P_2. The energy distribution is probed using a time-of-flight method, by measuring the number of atoms bouncing on a third pulse P_3 whose temporal position is scanned. By replacing P_2 by two pulses P_{2a} and P_{2b} (dashed line), we realize the temporal equivalent of a Young slit interferometer.

To investigate experimentally this effect [5], we start at $t = 0$ with the atomic cloud from the MOT released above the atomic mirror. We first select atoms with a well-defined total (kinetic+potential) energy using a sequence of two bounces (Fig. 3), generated by chopping the atomic mirror on for two short pulses P_1 and P_2; these pulses are respectively centered at time $T = 25$ ms and $3T$, with a variable width τ. From classical mechanics, one would expect after P_2 a triangular energy distribution centered on $E_0 = mg^2T^2/2 = h \times 10$ MHz (m is the atomic mass and $g = 9.81$ m/s^2), with a full width at half maximum (FWHM) $\Delta E_{\rm cl} = E_0\tau/T$. This prediction has to be compared with the typical width $\Delta E_{\rm Qu} = h/\tau$ of the

sine-shape energy distribution obtained after the diffraction of a monoenergetic beam by the pulse P_2. The range at which diffraction phenomenons become predominant corresponds to $\Delta E_{\mathrm{Qu}} \geq \Delta E_{\mathrm{cl}}$, leading to $\tau \leq 50\ \mu$s.

The energy distribution after P_2 is determined by a time-of-flight technique, by measuring the number of atoms bouncing on a third pulse P_3, whose temporal position is scanned around $5T$.

The width of P_3 is also τ, so that the broadening of the energy distribution in the measurement process remains small. The number of atoms which can perform this sequence of three bounces varies as τ^2 in the classical region ($\tau > 50\ \mu$s) and as τ^3 in the quantum region, provided P_3 is centered on $5T$. To increase this number, we have used for P_1, P_2 and P_3 a grating of pulses instead of a single pulse. The separation between two consecutive pulses of the grating ranges from 400 μs for $\tau \leq 40\ \mu$s, up to 1200 μs for $\tau = 100\ \mu$s; it is chosen large enough so that there is no overlap between the various patterns going through the time slits. The number of atoms per shot for $\tau = 40\ \mu$s is ≈ 40 for the optimal position of the grating of pulses P_3.

In order to detect those atoms, we have measured the fluorescence induced by a weak resonant probe beam using a cooled photomultiplier. Each atom scatters $\approx 10^4$ photons, among which 10 are detected on average, due to the detection solid angle and to the photomultiplier sensitivity. The signal therefore constitutes in a bunch of $40 \times 10 = 400$ photons, distributed over the duration (4 ms) of the detection window. The stray light is responsible for a similar background signal (10^5 detected photons/s). We note that this detection scheme was possible thanks to the double cell system, which guarantees that the Cs vapor pressure is low in the prism region and that the resonant scattering from this vapor remains small enough.

A typical time-of-flight spectrum is presented in Fig. 4a for $\tau = 30\ \mu$s. It gives the fluorescence induced by the probe laser as the temporal position of P_3 is

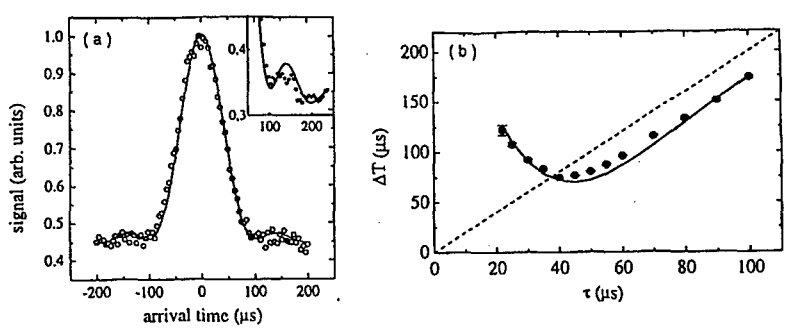

Fig. 4. (a) Circles — experimental time-of-flight signal for a pulse duration $\tau = 30\ \mu$s; continuous line — theoretical prediction using the temporal version of the Huygens–Fresnel principle. Inset — magnification of the side band signal. (b) • and continuous line — experimental and theoretical FWHM ΔT of the time-of-flight signals, as a function of the pulse width τ. Dotted line — classical prediction $\Delta T = 2\tau$.

scanned. Each of the 90 points of this figure has been averaged 170 times so that the total acquisition time for such a plot is 7 hours. We have repeated this experiment for various τ and we have plotted in Fig. 4b the corresponding FWHM ΔT. For large τ, we find that ΔT increases with τ as expected from classical mechanics. When τ decreases, ΔT passes through a minimum and increases again, as expected from the time-energy uncertainty relation. The error bars shown in Fig. 4b indicate the statistical fluctuations of ΔT in a series of measurements. We have also plotted in Fig. 4b the result of a theoretical analysis based on the path integral approach, which is well suited for this Fresnel-like diffraction problem.

In addition to the existence of a minimum width ΔT, which is a direct consequence of the time-uncertainty relation, there are two other signatures of the temporal diffraction phenomenon in the set of data presented here. First, side bands appear on the time-of-flight data of Fig. 4a (see in particular the inset, in which the data have been averaged 850 times and smoothed over every 3 consecutive data points). Because of the convolution of the signal with the detecting pulse P_3, they are not as visible as in spatial diffraction experiments (see e.g. [6] for neutron diffraction). Second, for large τ, the width ΔT is found to be smaller by ≈ 10 μs than the classical prediction (broken line in Fig. 4b). This originates from the temporal equivalent, on each side of P_2, of the well-known edge diffraction phenomenon [7].

4. A temporal Young slit interferometer for atoms

The time-diffracted atomic wave packet produced in the experiment described above can now be used as a source for an interferometry experiment. In this purpose we have designed a temporal Young slit interferometer by splitting P_2 into two pulses P_{2a} and P_{2b} separated by a variable duration τ'. This is an analog for de Broglie waves of the Sillitto–Wykes photon experiment [8]†. The interference occurs between the paths $P_1 - P_{2a} - P_3$ and $P_1 - P_{2b} - P_3$, as in a Young double slit experiment [10]. Figure 5a presents the time-of-flight distribution obtained with $\tau' = 40$ μs. The measured interference profile between the paths $P_1 - P_{2a} - P_3$ and $P_1 - P_{2b} - P_3$ is in good agreement with the one calculated using the path integral approach, shown in a continuous line, which takes into account the finite width of the temporal slits.

The relative phase between the two arms of this interferometer can be easily scanned by changing the effective height of the mirror for P_{2b}, with respect to the mirror height for P_{2a}. This is done by changing the mirror intensity I by a quantity δI during the pulse P_{2b}, which displaces the atom turning point by

$$\delta z = (2\kappa)^{-1}\delta I/I, \tag{2}$$

and modifies the path length of $P_1 - P_{2b} - P_3$ by $2\delta z$. A phase shift of π between the two paths is obtained for $\delta z = \Lambda_{dB}/4$, where $\Lambda_{dB} = h/mgT = 12$ nm is the de Broglie wavelength of the atoms incident on the mirror. In our experimental condition, this corresponds to $\delta I/I = 0.03$. The interference profile obtained in this situation is shown in Fig. 5b. As expected, the central fringe then corresponds to a destructive interference.

† The extension of Ref. [8] to neutrons has been discussed theoretically in Ref. [9].

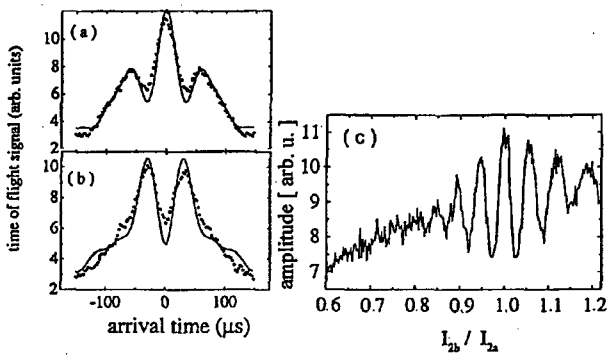

Fig. 5. Experimental (•) and calculated (continuous line) time-of-flight signals obtained in a temporal Young-slit configuration, in which the pulse P_2 is split into two pulses P_{2a} and P_{2b} separated by a duration $\tau' = 40$ μs. (a) Equal mirror intensity for P_{2a} and P_{2b}. (b) Phase shift of π between the two paths of the interferometer, obtained experimentally using a 3% reduction of the evanescent wave intensity during P_{2b}. (c) Amplitude of the central fringe of the temporal Young-slit interferometer as a function of the evanescent wave intensity I_{2b} during the pulse P_{2b}. The intensity I_{2a} during the pulse P_{2a} is constant. The maxima correspond to a path difference between the two arms multiple of $\Lambda_{dB}/2 = 6$ nm.

Finally, Fig. 5c gives the interference signal obtained with the detecting pulse P_3 set on the central fringe ($t = 5T$), when the intensity for P_{2b} is scanned. Several extrema are visible and each maximum corresponds to constructive interference which occurs when the turning point in P_{2b} is displaced by a multiple of $\Lambda_{dB}/2$. The reduction of the contrast as δI increases is due to the dispersion in Λ_{dB} resulting from the use of a sequence of several pulses for P_1, P_2, P_3. Also the van der Waals interaction between the bouncing atoms and the dielectric modifies the simple prediction (2), so that the phase shift actually varies with the distance between the turning point of the atomic trajectory and the dielectric surface. It therefore depends on the atomic transverse position in the Gaussian evanescent wave. This latter experiment can be used for a measurement of the van der Waals interaction between the atom and the dielectric surface[‡], by analyzing precisely the variation of the phase difference between the two paths, as the turning point of P_{2b} gets closer to the dielectric.

5. Phase modulation of matter waves

Atomic mirrors with evanescent waves can be used in a way which is richer than simply blocking and unblocking an atomic beam. For instance by modulating the evanescent wave intensity, we can mimic a vibrating mirror. When atoms prepared in a state of well-defined total energy are reflected from such a vibrating mirror, the associated matter waves are phase modulated. The resulting beam

[‡]A meaurement of this van der Waals interaction using an atomic mirror is reported in Ref. [11].

then consists of a "carrier" plus various side bands corresponding to de Broglie waves propagating at different velocities [12].

To observe such a phenomenon [13], we prepare as before cesium atoms in the magneto-optical trap of the lower chamber and we release them. They form a cold "beam", moving vertically downwards. They are velocity-selected using a sequence of two short pulses of the EW intensity (Fig. 6a). Each pulse has a duration $\tau = 0.4$ ms and their centers are separated by $T = 52$ ms, with the first pulse centered $T/2 = 26$ ms after the atoms have been released from the MOT. The velocity distribution which is thus selected is triangular, centered at $v_i = gT/2 = 25.5$ cm/s, with a width (HWHM) $\Delta v = g\Delta T/4 = 0.098$ cm/s. Note that this value of τ is large enough for a classical reasoning to be valid; in other words the time diffraction phenomenon described in Sec. 3 is negligible in these conditions.

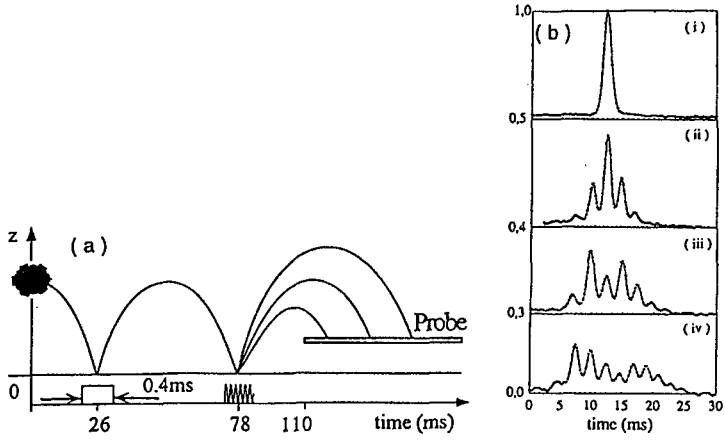

Fig. 6. Phase modulation of de Broglie waves (a) Atoms with a well-defined energy are selected using a two-pulse technique. The modulation of the EW during the second pulse introduces sidebands onto the de Broglie waves. These are detected by their time of flight to a probe beam introduced after the second pulse. (b) Time-of-flight signals. (i) Non-modulated potential; (ii)–(iv) modulated potential, with frequency $\nu = 950$ kHz (ii), 880 kHz (iii), and 800 kHz (iv).

The atomic kinetic energy is $E/h = 10.42 \pm 0.03$ MHz at the mirror surface. During the second pulse, the amplitude of the light field is modulated at a chosen frequency between 0 and 2 MHz. The presence of several frequency components in the reflected atomic beam is deduced by recording the time taken for the beam to rise and then fall back down to a fixed "probe" height in the earth's gravitational field. Since the matter waves' group velocity (at any given height) depends on their frequency, the negative-order side bands arrive first at the probe, followed by the carrier, followed by the positive side bands. The presence of these side bands clearly demonstrates the quantum nature of the phenomenon, since they could not appear in the reflection of a classical point-like particle on a modulated potential.

They demonstrate also a direct transfer of a precisely synthesised r.f. frequency onto the atomic motion.

The time-of-flight (TOF) signal shown in Fig. 6b(i) was obtained with a non-modulated mirror ($\epsilon = 0$). It represents the average of 1000 shots, with $\approx$ 4000 atoms contributing per shot. The TOF spectra 6b(ii–iv) were obtained with various modulation frequencies ν with a modulation depth $\epsilon = 0.82$. We have measured from these spectra the positions t_n of the side bands, from which we derive the corresponding energy transfers. These agree with the theoretical predictions. From our measurements, we deduce $h/Mg^2 = 3.14 \pm 0.02 \times 10^{-11}$ s^3, to be compared with the expected value 3.120×10^{-11} s^3, using the local $g = 9.81$ m/s^2 in Paris.

This device opens up new possibilities for precision experiments in atom optics, in complement to current gratings and slits, since one can take advantage of the fact that frequency and time intervals can be produced more accurately than distance intervals. This feature is now basic to high precision methods in photon optics, such as frequency chains using electro-optics modulators. In neutron optics, direct frequency transfer can be achieved by reflection of a neutron beam off a crystal lattice vibrating at one of its resonant frequencies [14, 15]. For atoms or molecules, most experiments [16] using precise r.f. techniques have relied on the presence of a narrow resonant transition between internal states of the system. By contrast, in our experiment and in a recent experiment performed in Innsbruck [17], demonstrating a frequency shifter for atomic matter waves as a generalization of an acousto-optic shifter for photons, the internal structure of the atom plays no role in defining the modulating frequency, and the latter can be varied continuously.

6. Dissipation with atomic mirrors

We have seen that the ability to vary in time the intensity of the evanescent mirror enables us to manipulate the motion of the reflected atoms. Pursuing this theme, we have performed further experiments in which the mirror is used to accelerate or decelerate reflected atoms in a controlled way, thus enabling the atomic trajectories to be focussed [18]. All such experiments are conservative, and so do not permit the brightness of the atomic beams to be increased. Equivalently, the phase space density of the atoms is conserved. However, atomic mirrors, unlike their photonic equivalents, can also provide dissipation. Using a spontaneous emission process during the reflection of the atoms, one can take advantage of the Sisyphus cooling mechanism to reduce their kinetic energy much below the incident one. This idea was first proposed in Ref. [19] and later on investigated theoretically in detail in Ref. [20]. The atomic ground level has to involve at least two states which experience a different and spatially dependent light shift by the evanescent wave. A spontaneous Raman transition from the most shifted state to the other one may occur during the bouncing process, which leads to a reduction of the atomic kinetic energy.

A first experimental evidence for such a cooling process was reported in Ref. [21]. A thermal atomic beam was sent at grazing incidence onto an atomic mirror, and a non-specular reflected beam was observed, corresponding to a decrease in the atomic kinetic energy due to the Sisyphus process. A good agreement

between the experimental results and a simple theoretical model was obtained concerning the average energy loss. We report here on an observation of this cooling process for our laser cooled atoms dropped at normal incidence onto the evanescent wave mirror (for more details, see also [22]).

We model the cesium atoms as a three-level system, with an unstable excited state e and two stable ground states. These two states correspond to the hyperfine ground levels ($6s_{1/2}, F_g = 3$ and $F_g = 4$) of the cesium atom separated by $\Delta = 2\pi \times 9.193$ GHz. The excited state corresponds to the level $6p_{3/2}$, whose hyperfine structure can be neglected since it is small compared with the laser detunings chosen in the experiment.

The interaction between the atom and the evanescent wave gives rise to a potential which depends on the ground state

$$U_3(z) = \frac{\hbar\Omega_0^2}{4\delta} \exp(-2\kappa z), \tag{3}$$

$$U_4(z) = \frac{\hbar\Omega_0^2}{4(\delta+\Delta)} \exp(-2\kappa z) = \frac{\delta}{\delta+\Delta} U_3(z), \tag{4}$$

where $\delta = \omega_L - \omega_3$ is the detuning between the laser frequency and the atomic resonance corresponding to the transition $6s_{1/2}, F_g = 3 \leftrightarrow 6p_{3/2}$. The potential $U_4(z)$ is proportional to $U_3(z)$, but weaker.

Consider an atom in state $F_g = 3$ with kinetic energy $E_i = mv_0^2/2$ entering into the wave. It experiences the repulsive potential, so that its kinetic energy decreases, whereas its potential energy increases. If we choose the intensity and the detuning such that the spontaneous emission probability per bounce is much smaller than unity, the spontaneous emission process, if it occurs, will preferentially take place in the vicinity of the classical turning point z_0, given by $E_i = U_3(z_0)$. The atom may then fall back to either one of the two ground states.

If it ends up in $F_g = 3$, it will continue its way, without being perturbed, if we neglect the atomic recoil during absorption and emission. However, the atom may also fall into $F_g = 4$. While the kinetic energy remains constant during this transition, the atom now experiences the potential $U_4(z)$ which is weaker than $U_3(z)$. After the bounce, the atomic kinetic energy $E_f = mv_f^2/2$ is thus smaller than the initial one [19, 20]. The loss of potential energy is maximal when the scattering process occurs at z_0. The final energy in this case is given by

$$E_f^{\min} = E_i \frac{\delta}{\delta+\Delta}. \tag{5}$$

The atoms are prepared in the MOT located 3 mm above the prism as described above. We then block the repumping laser at a time referred to as $t = 0$ in the following. Consequently almost all atoms are optically pumped into the $F_g = 3$ ground state in which they no longer interact with the light and fall under the influence of gravity. At $t = 6$ ms, we also block the main lasers resonant with the $F_g = 4 \leftrightarrow F_e = 5$ transition.

If the Sisyphus transition occurs, it changes the velocity of the reflected atoms. We analyze the energy distribution of these atoms by a TOF starting at $t = 43$ ms (Fig. 7). We record the absorption of a horizontal probe laser beam resonant with the $F_g = 4 \leftrightarrow F_e = 5$ transition. The probe is centered 450 μm

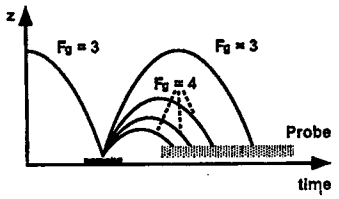

Fig. 7. A fraction of ground state ($F_g = 3$) atoms bouncing on the mirror can undergo a Sisyphus transition towards $F_g = 4$ in the evanescent wave. The energy loss results in a shorter arrival time in the probe beam.

above the evanescent wave mirror. It may be mixed with a repumping beam $F_g = 3 \leftrightarrow F_e = 4$, so that we can choose between the detection of atoms either in $F_g = 4$ or in both hyperfine states. We can therefore determine the proportion of atoms undergoing the Sisyphus transition.

Figure 8a gives a typical atomic TOF curve. It shows the probe absorption as a function of time t. The bouncing period for atoms in state $F_g = 3$, which undergo a specular reflection, is 53 ms. These atoms cross the probe laser mixed with the repumping beam at $t = 83$ ms. Atoms undergoing a Sisyphus transition loose energy during the reflection and leave the mirror at a smaller velocity and with a shorter bouncing period. They arrive first at the detection laser and they give rise to a corresponding broad peak of low height, whose maximum is located around the arrival time $t_{Sis} = 53$ ms. The signal was recorded using a mirror detuning of $\delta = 2\pi \times 3000$ MHz and a repumping laser was introduced in the probe beam so that both ground hyperfine levels were detected.

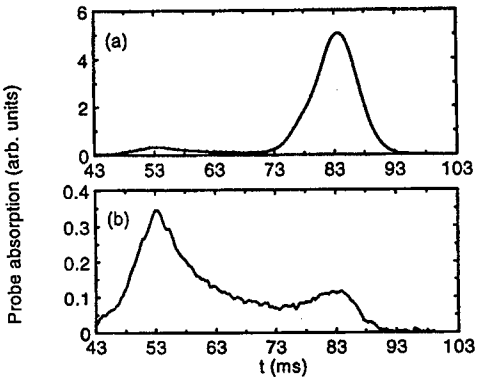

Fig. 8. TOF signals showing a Sisyphus cooling in a single bounce: (a) The atoms are detected both in $F_g = 3$ and $F_g = 4$ using a probe beam including a repumping laser. The slowed atoms arrive first (peak centred at $t_{Sis} = 53$ ms) followed by the uncooled atoms (peak centred at $t = 83$ ms). (b) Same experiment without a rempumping beam in the probe; only the cooled atoms (in $F_g = 4$) are detected.

In order to prove that this signal corresponds to atoms undergoing a Sisyphus process, we repeated the measurement detecting only atoms in the state $F_g = 4$, i.e. without repumping laser. The result is presented in Fig. 8b. The peak previously detected at 83 ms, which corresponds to atoms in state $F_g = 3$, nearly disappears, whereas the earlier observed signal is unchanged. The atoms corresponding to this broad peak maximum at t_{Sis} are thus in state $F_g = 4$.

This elementary Sisyphus process is a convenient tool to accumulate a large number of atoms in a restricted domain of space, increasing therefore the quantum degeneracy of the gas. As pointed out in Ref. [19] and [21], and as shown experimentally very recently in Ref. [23], the repetition of such processes, alternated with repumping phases transferring the atoms back to $F_g = 3$, should lead to an atomic gas with a kinetic energy of a few recoil energies $\hbar^2 k^2/2m$ only, where $\hbar k$ is the momentum of a single photon.

This Sisyphus process can also be used to populate efficiently the ground state of a potential confining the atoms in the vicinity of the dielectric prism, achieving thus a quasi bidimensional gas [24–26]. This could provide an efficient way to prepare a 2D gas with a high quantum degeneracy.

We acknowledge stimulating discussions and general encouragement from the E.N.S. laser cooling group. M.A. acknowledges financial support by the Alexander von Humboldt Foundation. This work has been partially supported by DRET, CNRS, Collège de France, DRED and the T.M.R. program of the European Community (contract FMRX-CT960002).

References

[1] R.J. Cook, R.K. Hill, *Opt. Commun.* **43,** 258 (1982).

[2] V.I. Balykin, V.S. Letokhov, Yu.B. Ovchinnikov, A.I. Sidorov, *Sov. Phys. JETP Lett.* **45,** 353 (1987); *Phys. Rev. Lett.* **60,** 2137 (1988).

[3] C.G. Aminoff, A. Steane, P. Bouyer, P. Desbiolles, J. Dalibard, C. Cohen-Tannoudji, *Phys. Rev. Lett.* **71,** 3083 (1993).

[4] M. Moshinski, *Phys. Rev.* **88,** 625 (1952); A.S. Gerasimov, M.V. Kazarnovskii, *Sov. Phys. JETP* **44,** 892 (1976); J. Felber, G. Müller, R. Gälher, R. Golub, *Physica B* **162,** 191 (1990); A. Zeilinger, C. Brukner, unpublished.

[5] P. Szriftgiser, D. Guéry-Odelin, M. Arndt, J. Dalibard, *Phys. Rev. Lett.* **77,** 4 (1996).

[6] R. Gähler, A. Zeilinger, *Am. J. Phys.* **59,** 316 (1991).

[7] M. Born, E. Wolf, *Principles of Optics*, 6th ed., Pergamon, New York 1980, p. 433.

[8] R.M. Sillitto, C. Wykes, *Phys. Lett. A* **39,** 333 (1972).

[9] H.R. Brown, J. Summhammer, R.E. Callaghan, P. Kaloyerou, *Phys. Lett. A* **163,** 21 (1992).

[10] O. Carnal, J. Mlynek, *Phys. Rev. Lett.* **21,** 2689 (1991); F. Shimizu, K. Shimizu, H. Takuma, *Phys. Rev. A* **46,** R17 (1992).

[11] A. Landragin, J.-Y. Courtois, G. Labeyrie, N. Vansteenkiste, C.I. Westbrook, A. Aspect, *Phys. Rev. Lett.* **77,** 1464 (1996).

[12] C. Henkel, A.M. Steane, R. Kaiser, J. Dalibard, *J. Phys. II (France)* **4,** 1877 (1994).

[13] A. Steane, P. Szriftgiser, P. Desbiolles, J. Dalibard, *Phys. Rev. Lett.* **74,** 4972 (1995).

[14] W.A. Hamilton, A.G. Klein, G.I. Opat, P.A. Timmins, *Phys. Rev. Lett.* **58,** 2770 (1987).

[15] J. Felber, Ph.D., Technischen Universität, Munich 1994, unpublished; J. Felber, R. Gähler, C. Rausch, R. Golub, *Phys. Rev. A* **53,** 319 (1996).

[16] *Atom Interferometry,* Ed. P. Berman, Academic Press, New York 1996 and references therein.

[17] S. Bernet, M. Oberthaler, R. Abfalterer, J. Schmiedmayer, A. Zeilinger, *Phys. Rev. Lett.* **77,** 5160 (1996).

[18] M. Arndt, P. Szriftgiser, J. Dalibard, A. Steane, *Phys. Rev. A* **53,** 3369 (1996).

[19] K. Helmerson, S. Rolston, L. Goldner, W.D. Phillips, poster at the *Workshop on Optics and Interferometry with Atoms,* Insel Reichenau (Germany) 1992, unpublished; *Quantum Electronics and Laser Science Conference,* 1993, OSA Technical Digest Series, Vol. 12, O.S.A., Washington DC 1993, p. 209.

[20] J. Söding, R. Grimm, Yu.B. Ovchinnikov, *Opt. Commun.* **119,** 652 (1995).

[21] Yu.B. Ovchinnikov, D.V. Laryushin, V.I. Balykin, V.S. Letokhov, *JETP Lett.* **62,** 113 (1995).

[22] P. Desbiolles, M. Arndt, P. Szriftgiser, J. Dalibard, *Phys. Rev. A* **54,** 4292 (1996).

[23] Yu.B. Ovchinnikov, I. Manek, R. Grimm, unpublished.

[24] P. Desbiolles, J. Dalibard, *Opt. Commun.* **132,** 540 (1996).

[25] M. Reynolds, J. Walraven, private communication (November 1994).

[26] T. Pfau, J. Mlynek, *OSA Trends in Optics and Photonics Series on Bose–Einstein Condensation* **7,** 33 (1996).

Vol. 93 (1998) ACTA PHYSICA POLONICA A No. 1

Proceedings of the International Conference "Quantum Optics IV", Jaszowiec, Poland, 1997

LOW ENERGY EXCITATION SPECTRA OF TRAPPED BOSE CONDENSATES

L. You[a], W. Hoston[b], M. Lewenstein[c] and M. Marinescu[a]

[a]School of Physics, Georgia Institute of Technology, Atlanta, GA 30332-0430, USA
[b]Institute for Theoretical Atomic and Molecular Physics
Harvard-Smithsonian Center for Astrophysics
60 Garden Street, MS 14, Cambridge, Massachusetts 02138, USA
[c]Commissariat à l'Energie Atomique, DSM/DRECAM/SPAM
Centre d'Etudes de Saclay
91191 Gif-sur-Yvette, France

We discuss our numerical studies of the low energy excitations of trapped Bose condensates using a Bogoliubov–Hartree treatment. In the zero temperature limit, the lowest few excitation frequencies calculated within the Bogoliubov approximation agree well with the experimental data. Finite temperature results obtained using the Popov approximation display qualitative differences from the experimental data close to the critical temperature region. Details of our numerical approach are presented and comparison with other results is discussed.

PACS numbers: 03.75.Fi, 67.90.+z

1. Introduction

A little over two years ago a new phase of research was entered by experimentalists pursuing research in the Bose–Einstein condensation (BEC). Built upon cumulative research advances in laser cooling and trapping [1] and in evaporative cooling [2], BEC was first observed in ^{87}Rb by a collaboration at JILA [3]. Shortly thereafter, a group at Rice University reported apparent evidence of quantum degeneracy with ^{7}Li [4], and a group at MIT developed techniques for rapid production of large condensates containing about a million ^{23}Na atoms [5]. Tremendous progress has been made in the past two years: many single particle properties of trapped condensates have been measured; direct non-destructive optical imaging techniques have been developed [6]; several of the low-lying collective excitation modes have been detected [7, 8]. Recently, the macroscopic coherence properties of the condensate were displayed in a spectacular fashion with the demonstration of interference between two condensates [9], and the suppression of the collisional losses from the inelastic collisions [10] due to the multi-particle correlations. Rudimentary atom lasers with pulsed output couplers have also been reported [9, 11], and the sound velocities of the condensate have been measured [12].

The theoretical description of these experimental systems has also been an active field. Particular interest has been focused on the calculation of excitation spectra for condensates. In the zero temperature limit, the Bogoliubov–de Gennes equations that govern the wave functions for quasi-particles have been studied by several groups [13, 14]. An (analytic) asymptotic expression for the eigenfrequencies valid in the Thomas–Fermi/hydrodynamic limit was first presented by Stringari [15]. A variational approach was developed in Ref. [16]. A dynamical variational approach was also applied by Pérez-García et al. [17]. More recent studies can be found in Refs. [18–21]. All of these studies describe the condensate within a mean-field approximation with excitations corresponding to the poles of the single particle Green function. Multi-particle excitations and related correlation effects have not been carefully addressed yet, although an atomic structure approach based on the Hartree–Fock, random phase approximation, and configuration interaction approach as presented in [22], can be used to study such correlation effects by including multi-excitation configurations [23]. The finite temperature mean-field Bogoliubov–Hartree (BH) approach to the collective excitations involves a great deal of numerical effort and only limited results are available at the moment [24]. A detailed comparison with the experimental data [8] is yet to be performed.

In this paper we present the numerical procedure we have developed for the study of low energy excitations of trapped Bose condensates [25]. The paper is organized as follows. We start by giving an overview of the field theoretical description of the condensate. In Sec. 3 we follow with an outline of the numerical procedures we have developed. The results and discussions are given in Sec. 4. Finally, we conclude in Sec. 5.

2. Bogoliubov–Hartree theory

Several versions of the Bogoliubov–Hartree theory exist in the literature [26] but we closely follow the approach of Ref. [25], which is based on the linearization of the 2nd-quantized Hamiltonian around a *coherent state* (or a c-number) of the atomic fields. This approach fixes the overall phase (by breaking the global U(1) gauge invariance) of the mean atomic fields and keeps quadratic terms of the small quantum fluctuations (around this coherent state) in the Hamiltonian. For trapped systems, these quantum fluctuations cause the initial fixed phase of the atom field to diffuse, which can be understood mathematically as due to the degeneracy of the zero mode in the quasi-particle excitation spectra. For a detailed discussion of the zero mode, see Ref. [27]. Recently approaches which conserve the number of particles (and therefore do not fix the phase) have been presented [28].

The second quantized Hamiltonian for a system of N spinless bosonic atoms trapped in a potential $V_t(r)$ is given by [25, 26]

$$\mathcal{H} = \int \mathrm{d}r \widehat{\Psi}^\dagger(r) \left[-\frac{\hbar^2}{2M}\nabla^2 + V_t(r) - \mu \right] \widehat{\Psi}(r)$$

$$+ \frac{u_0}{2} \int \mathrm{d}r \, \widehat{\Psi}^\dagger(r)\widehat{\Psi}^\dagger(r)\widehat{\Psi}(r)\widehat{\Psi}(r), \qquad (2.1)$$

where $\widehat{\Psi}(r)$ and $\widehat{\Psi}^\dagger(r)$ are atomic (bosonic) annihilation and creation fields, $u_0 = 4\pi\hbar^2 a_{sc}/M$, with M being the atomic mass, and a_{sc} — the scattering length of the atom–atom interaction. This Hamiltonian in fact describes the free energy since the chemical potential μ is used to guarantee the conservation of the average of the total number of atoms $\widehat{N} = \int dr\, \widehat{\Psi}^\dagger(r)\widehat{\Psi}(r)$. The aim of the BH approach is to describe the single particle excitations of the system in terms of non-interacting quasiparticles. Mathematically we try to cast the Hamiltonian (2.1) into the form

$$\mathcal{H} \to \sum_{n\neq 0} \hbar\widetilde{\omega}_n \widetilde{g}_n^\dagger \widetilde{g}_n + (n = 0 \text{ zero mode part } \alpha\widehat{P}^2/2), \tag{2.2}$$

where $\widetilde{g}_n^\dagger$ ($\widetilde{g}_n$) are the quasiparticle creation (annihilation) operators which satisfy the standard bosonic commutation relations and the quasiparticle index, $n = 0, 1, 2, \ldots$, labels the positive eigenfrequencies $\widetilde{\omega}_n$ arranged in ascending order. Therefore, the density matrix for quasiparticles at equilibrium is described by the Bose–Einstein distribution

$$\widehat{\rho} = \frac{1}{Z}\exp\left(-\beta\sum_{n\neq 0}\hbar\widetilde{\omega}_n\widetilde{g}_n^\dagger\widetilde{g}_n + \ldots\right), \tag{2.3}$$

where $\widetilde{\omega}_n$ depend on the chemical potential μ and Z is the partition function.

At zero temperature the BH approach takes its simplest form, the Bogoliubov approximation, which starts with the assumption

$$\widehat{\Psi}(r) = \sqrt{N_0}\psi_0(r) + \delta\widehat{\Psi}(r), \tag{2.4}$$

where the c-number condensate wave function $\psi_0(r)$ is assumed to be real (without loss of generality) and normalized such that $\int dr|\psi_0(r)|^2 = 1$, and N_0 is the number of particles in the condensate. In Eq. (2.4), $\delta\widehat{\Psi}(r)$ denotes the quantum fluctuation which obeys the same standard bosonic commutation relations as $\widehat{\Psi}(r)$. We substitute Eq. (2.4) into Eq. (2.1) and neglect both 3-rd and 4-th order fluctuation terms. The linear fluctuation terms are vanishing provided that $\psi_0(r)$ satisfies the nonlinear Schrödinger equation (NLSE), i.e.

$$[\mathcal{L} + u_0\rho_0]\,\psi_0(r) = 0, \tag{2.5}$$

where we have defined $\mathcal{L} \equiv -\frac{\hbar^2\nabla^2}{2M} + V_t(r) - \mu$, and the condensate density $\rho_0(r) \equiv N_0|\psi_0(r)|^2$. The resulting linearized effective Hamiltonian

$$\mathcal{H}_{\text{eff}} = \int dr\delta\widehat{\Psi}^\dagger(r)\mathcal{L}\delta\widehat{\Psi}(r) + \frac{1}{2}Nu_0\int dr\psi_0^2(r)$$

$$\times\left[\delta\widehat{\Psi}^\dagger(r)\delta\widehat{\Psi}^\dagger(r) + \text{h.c.} + 4\delta\widehat{\Psi}^\dagger(r)\delta\widehat{\Psi}(r)\right], \tag{2.6}$$

may be diagonalized in the representation of the quasiparticle annihilation operators

$$\widetilde{g}_k = \int dr\left[U_k(r)\delta\widehat{\Psi}(r) + V_k(r)\delta\widehat{\Psi}^\dagger(r)\right], \tag{2.7}$$

for $k = 1, 2, 3, \ldots$ and their Hermitian conjugates, a quasiparticle creation operators $\widetilde{g}_k^\dagger$. The $U_k(r)$ and $V_k(r)$ are the mode functions of the quasiparticles which

have to be determined. To determine the functions $U_n(r)$ and $V_n(r)$ (for $n \neq 0$) we solve $[\tilde{g}_n, \mathcal{H}] = \hbar\tilde{\omega}_n\tilde{g}_n$, which is equivalent to the coupled Bogoliubov–de Gennes equations

$$[\mathcal{L} + 2u_0\rho_0(r)]\,U_n(r) - u_0\Delta_0^*(r)V_n(r) = \hbar\tilde{\omega}_n U_n(r),$$

$$[\mathcal{L} + 2u_0\rho_0(r)]\,V_n(r) - u_0\Delta_0(r)U_n(r) = -\hbar\tilde{\omega}_n V_n(r), \tag{2.8}$$

where $\Delta_0(r) = N_0\psi_0^2(r)$. There is a time-reversal symmetry associated with (2.8). If the set $\{U_n(r), V_n(r)\}$ constitutes a solution for energy $+\hbar\tilde{\omega}_n$ then the set $\{V_n^*(r), U_n^*(r)\}$ is also a solution but for energy $-\hbar\tilde{\omega}_n$ [26]. All of the non-zero eigenvalues are thus paired and real. To have $\tilde{g}_k$ and $\tilde{g}_k^\dagger$ fulfill bosonic commutation relations, $[\tilde{g}_k, \tilde{g}_{k'}^\dagger] = \delta_{kk'}$, $[\tilde{g}_k, \tilde{g}_{k'}] = 0$, the mode functions have to obey the *orthonormality* condition [26],

$$\int \mathrm{d}r\,[U_k(r)U_{k'}^*(r) - V_k(r)V_{k'}^*(r)] = \delta_{kk'},$$

$$\int \mathrm{d}r\,[U_k(r)V_{k'}(r) - V_k(r)U_{k'}(r)] = 0. \tag{2.9}$$

The presence of a zero mode solution to Eq. (2.8) requires the introduction of the momentum operator $\hat{P}$, defined according to [27] as,

$$\hat{P} = \int \mathrm{d}r\psi_0(r)\left[\delta\hat{\Psi}(r) + \delta\hat{\Psi}^\dagger(r)\right]. \tag{2.10}$$

The zero mode and the above associated momentum operator describe *collective motion without restoring force* of the condensate [29]. Therefore, $\hat{P}$ commutes with all $\tilde{g}_k$, and $\tilde{g}_k^\dagger$ operators, i.e., $\int \mathrm{d}r\psi_0(r)[U_k(r) - V_k(r)] = 0$ for $k \neq 0$. The conjugate "position" operator is defined as

$$\hat{Q} = \mathrm{i}\int \mathrm{d}r\Phi_0(r)\left[\delta\hat{\Psi}(r) - \delta\hat{\Psi}^\dagger(r)\right], \tag{2.11}$$

and it has to satisfy $[\hat{Q}, \hat{P}] = \mathrm{i}$, $[Q, \tilde{g}_k] = 0$ (for $k \neq 0$), and $[\hat{Q}, \mathcal{H}_{\mathrm{eff}}] = \mathrm{i}\alpha\hat{P}$ [27]. Thus, we obtain

$$2\int \mathrm{d}r\Phi_0(r)\psi_0(r) = 1,$$

$$\int \mathrm{d}r\Phi_0(r)[U_k(r) + V_k(r)] = 0, \qquad \text{for } k \neq 0, \tag{2.12}$$

and

$$[\mathcal{L} + 3u_0\rho_0(r)]\Phi_0(r) = \alpha\psi_0(r), \tag{2.13}$$

which has a unique solution, since the operator on the lhs of Eq. (2.13) is clearly positive-definite. The coefficient α is related to the rate of change of the condensate phase. The annihilation operator for the zero mode is $\tilde{g}_0 = (\hat{P} - \mathrm{i}\hat{Q})/\sqrt{2}$. Its associated mode functions are given by

$$U_0(r) = [\psi_0(r) + \Phi_0(r)]/\sqrt{2},$$

$$V_0(r) = [\psi_0(r) - \Phi_0(r)]/\sqrt{2}. \tag{2.14}$$

The total atomic field can now be expanded as

$$\hat{\Psi}(r) = \sum_{k=0}^{\infty} \left[U_k(r)\tilde{g}_k - V_k(r)\tilde{g}_k^\dagger \right], \tag{2.15}$$

assuming the validity of the linearization approximation. Since the mean value of $\hat{\Psi}(r)$ is $\sqrt{N_0}\psi_0(r)$, this can happen if and only if the system is in the coherent state $|\sqrt{N_0}\rangle$ of all the quasiparticle operators $\tilde{g}_k|\sqrt{N_0}\rangle = z_k|\sqrt{N_0}\rangle$, such that

$$\sum_{k=0}^{\infty}[z_k U_k(r) - z_k^* V_k(r)] = \sqrt{N_0}\psi_0(r). \tag{2.16}$$

The above condition implies that $z_k = \sqrt{N_0}\int \mathrm{d}r\psi_0(r)[U_k(r)+V_k(r)]$ and $z_k^* = z_k$.

In addition to the collective excitation frequencies $\tilde{\omega}_n$, several other quantities are of potential interest. The total energy of the system (at $T = 0$, the ground state) of trapped atoms is given by

$$\mathcal{E}_0 = N_0\mu + \mathcal{H}_0 = N_0\mu - u_0 \int \mathrm{d}r\rho_0^2(r)/2, \tag{2.17}$$

which may be measured as the total release energy by turning off the trapping potential [30]. The depletion of the condensate (caused by the inter-atomic interactions) at zero temperature is [31],

$$N'(T=0) = \int \mathrm{d}r \sum_{n>0} |V_n(r)|^2. \tag{2.18}$$

For $T \neq 0$, a self-consistent Bogoliubov–Hartree approach is usually adopted. Within the present notation, we have to take into account the neglected 3rd and 4th order terms of $\delta\Psi(r)$ and $\delta\Psi^\dagger(r)$ and reduce these terms to quadratic operator terms using a decorrelation approximation [26]. The resulting equations will then be slightly different from those used for the zero temperature studies. First the condensate wave function $\sqrt{N_0}\psi_0(r)$ cannot in general be assumed to be real. In fact, the analogue to the NLSE are two coupled equations

$$\begin{aligned}
&[\mathcal{L} + u_0(\rho_0 + 2\rho')]\psi_0(r) + u_0\Delta'(r)\psi_0^*(r) = 0,\\
&[\mathcal{L} + u_0(\rho_0 + 2\rho')]\psi_0^*(r) + u_0\Delta'^*(r)\psi_0(r) = 0.
\end{aligned} \tag{2.19}$$

Similarly modifications to Eqs. (28) lead to

$$\begin{aligned}
&[\mathcal{L} + 2u_0\rho(r)]\,U_n(r) - u_0\Delta^*(r)V_n(r) = \hbar\tilde{\omega}_n U_n(r),\\
&[\mathcal{L} + 2u_0\rho(r)]\,V_n(r) - u_0\Delta(r)U_n(r) = -\hbar\tilde{\omega}_n V_n(r),
\end{aligned} \tag{2.20}$$

where we have used the notations

$$\begin{aligned}
&\rho(r) = \rho_0(r) + \rho'(r), \quad \rho'(r) = \sum_{n\geq 0}\left[N_n|U_n(r)|^2 + (N_n+1)|V_n(r)|^2\right],\\
&\Delta(r) = \Delta_0(r) + \Delta'(r), \quad \Delta'(r) = -\sum_{n\geq 0}(2N_n+1)U_n^*(r)V_n(r),
\end{aligned} \tag{2.21}$$

where

$$N_{n\neq 0} = \langle g_n^\dagger g_n\rangle = \frac{1}{\mathrm{e}^{\beta\hbar\tilde{\omega}_n} - 1}, \qquad \beta = 1/kT, \tag{2.22}$$

is the Bose–Einstein distribution. We also obtain

$$\mathcal{E}_0 = N_0\mu - u_0 \int \mathrm{d}r\rho_0(r)[\rho_0(r)/2 + \Delta'(r) + 2\rho'(r)],$$

$$N'(T) = \int \mathrm{d}r\rho'(r). \tag{2.23}$$

Self-consistent solutions to the above Eqs. (2.19) and (2.20) can be obtained through an iterative scheme. We note that the BH approximation as outlined here is a conserving approximation, but it leads to an energy gap in the excitation spectra [26]. Generally, one expects the low energy excitations for an interacting Bose gas to be gapless since the zero mode will always be present in a U(1) symmetry-breaking approach [26, 27]. A commonly adopted approximation to enforce gapless excitation solutions is by setting $\Delta' = 0$ in Eqs. (2.19) and (2.20). Such an approach is called the Popov approximation. It is gapless but this is not a conserving approximation. However, it has allowed preliminary numerical studies of finite temperature excitation spectra [24]. Recently a U(1) symmetric approach has also been developed. It is a conserving gapless formalism [28].

To study numerically the trapped Bose gas within the BH approach, one may solve first the NLSE (2.5) or (2.19) for ψ_0 and then proceed to solve the Bogoliubov–de Gennes equations (2.8) or (2.20) for U_n and V_n. For non-zero temperatures, self-consistency is enforced by iteration. The details of our numerical approach are discussed in the following section.

3. The numerical approach

In this section we outline the details of our numerical approach to solve the equations of the BH theory. We present the details of the calculation technique for the zero temperature limit since it is in this limit that most of our results have been obtained. A generalization to non-zero temperature calculations is straightforward. Several groups have studied the zero temperature problem [13, 22, 24, 32]. Our work relies on a basis expansion method that we have developed [25]. Since most of the experimental traps can be well approximated at their minima by a harmonic potential, $V_t(r) = \frac{1}{2}M(\omega_x^2x^2 + \omega_y^2y^2 + \omega_z^2z^2)$ [3–5], we use a harmonic oscillator basis. The basis is composed of product states of three separate one-dimensional harmonic oscillators, $\phi_n(r) = \phi_{n_x}(x)\phi_{n_y}(y)\phi_{n_z}(z)$. All frequencies (energy terms) are scaled in units of the smallest trap frequency, $\omega = \min(\omega_x, \omega_y, \omega_z)$, and the three coordinates (x, y, z) are scaled to their ground state sizes (a_x, a_y, a_z), where $a_{x,y,z} = \sqrt{\hbar/2M\omega_{x,y,z}}$. We also scale the scattering length a_{sc} to $a = \sqrt{\hbar/2M\omega}$. In these units the atom–atom interaction coupling takes the dimensionless form $N_0u_0 \to 8\pi N_0 a_{\mathrm{sc}}\sqrt{\omega_x\omega_y\omega_z}$.

Given a basis, one can write the condensate wave function (for $T = 0$) as $\psi_0(r) = \sum_n a_n\phi_n(r)$. Equations (2.5) and (2.8) can be rewritten in terms of their matrix representation

$$\mathcal{L} \to \mathcal{L}_{nn'} = \int \mathrm{d}r\phi_n^*(r)\mathcal{L}\phi_{n'}(r) = (\omega_n^{(0)} - \mu)\delta_{nn'}, \tag{3.1}$$

$$N_0u_0|\psi_0(r)|^2 \to D_{nn'} = \sum_m\sum_{m'} a_m^*a_{m'}I_{nmn'm'}, \tag{3.2}$$

where

$$I_{nmn'm'} = \int \mathrm{d}r \phi_n^*(r)\phi_m^*(r)\phi_{m'}(r)\phi_{n'}(r), \tag{3.3}$$

with $\omega_n^{(0)} \equiv n_x\omega_x + n_y\omega_y + n_z\omega_z$.

The NLSE (2.5) can now be written as a matrix eigenproblem

$$(\omega_n^{(0)}\delta_{nn'} + N_0 u_0 D_{nn'})a_{n'} = \mu_n \delta_{nn'} a_{n'}. \tag{3.4}$$

The Bogoliubov–de Gennes equations (2.8) can also be expressed similarly in terms of $D_{nn'}$ and $\mathcal{L}_{nn'}$.

We find an approximate solution to Eq. (3.4) by taking a finite subset of the basis functions (N_{tot}) and solving iteratively the above equation for μ_n and a_n. The proper choice of the subset is dictated by the relevant symmetries of the problem. One also has to prove that the number of states within the subset basis is sufficient to obtain a reasonable numerical solution. This is most easily done by checking the change in the "final" answers as a function of the number of basis states used. The iterative procedure is as follows. An initial guess a_n^{old} is used to generate the matrix $D_{nn'}$. The eigenvalues and eigenvectors of this matrix are found numerically and the eigenvector corresponding to the lowest eigenvalue, a_n^{eigen}, is used to update the input vector according to the rule

$$a_n^{\mathrm{new}} = \overline{c}[(1-\eta)a_n^{\mathrm{eigen}} + \eta a_n^{\mathrm{old}}], \tag{3.5}$$

where typically $\eta \in [0,1)$ is fixed for relatively weak interacting case, and adjusted step by step (by-section) for other values of N_0u_0. The coefficient $\overline{c}$ ensures proper normalization. Then the vector a_n^{new} is used as the new input for generating the $D_{nn'}$ and the steps are repeated. If the procedure converges to a fixed point, $a_n^{\mathrm{new}} = a_n^{\mathrm{old}}$, this point is a solution of Eq. (3.4). The lowest eigenvalue corresponds to the chemical potential μ. The rate of convergence clearly depends on the value of η chosen as well as the initial guess for the a_n. We have achieved convergence to a fixed point for a wide range of coupling strengths Nu_0 by using an appropriate η. The initial guess $a_n^{(0)}$ was also varied with the parameter Nu_0. For moderate values of this parameter, the noninteracting ground state was chosen as the initial guess. For larger values of N_0u_0 one can neglect the kinetic energy term in the NLSE [15, 18], often referred as the Thomas–Fermi approximation (TFA). In this limit, the condensate wave function becomes the mirror image of the trapping potential,

$$\psi_0(r) \propto \sqrt{\mu - V_t(r)}\theta[\mu - V_t(r)], \tag{3.6}$$

where $\theta(x)$ is the step function, and μ is determined from the normalization condition. The solution (3.6) was found to provide a better starting point for the algorithm for large values of N_0u_0.

The solution for the NLSE (3.4) is used to solve Eq. (2.8) for $U_n(r)$, $V_n(r)$, and $\hbar\widetilde{\omega}_n$. For calculations of experimental interest, the computational effort is bottle-necked at the evaluation of the $D_{nn'}$ matrices. In using this approach, two issues must be addressed: (1) a practical method of ordering the basis must be found, i.e., a mapping $n_x, n_y, n_z \rightarrow n$; (2) an efficient method of storing and evaluating the integrals $I_{nmn'm'}$ must be identified.

Without loss of generality, we can assume all (U_k, V_k) to be real. By introducing the sums and differences as

$$S_k(r) = U_k(r) + V_k(r),$$

$$D_k(r) = U_k(r) - V_k(r). \tag{3.7}$$

Equation (2.8) may be rewritten in a decoupled form [21] as

$$(\mathcal{L} + 3Nu_0\psi_0^2)(\mathcal{L} + Nu_0\psi_0^2)S_k(r) = (\hbar\widetilde{\omega}_k)^2 S_k(r),$$

$$(\mathcal{L} + Nu_0\psi_0^2)(\mathcal{L} + 3Nu_0\psi_0^2)D_k(r) = (\hbar\widetilde{\omega}_k)^2 D_k(r). \tag{3.8}$$

The latest form will reduce the size of the numerical computation.

The above equation yields the spectrum of quasiparticle excitations as the eigenvalues of the product operator of $\mathcal{L} + 3Nu_0\psi_0^2(r)$ and $\mathcal{L} + Nu_0\psi_0^2(r)$. Mathematically, $S_k(r)$ and $D_k(r)$ correspond to the left- and right-eigenvectors of the non-Hermitian product operator (although individual operators $\mathcal{L} + Nu_0\psi_0^2$ and $\mathcal{L} + 3Nu_0\psi_0^2$ are Hermitian, they do not commute). In the TFA and working in the classical phase space (r, p) with $E_p = p^2/2M$, we can easily find the excitation spectra as

$$\widetilde{\omega}(p, r) = \sqrt{(E_p + V_t - \mu + Nu_0\psi_0^2)(E_p + V_t - \mu + 3Nu_0\psi_0^2)}$$

$$\approx \begin{cases} \sqrt{E_p(E_p + 2\mu - 2V_t)} \propto p, & \theta(\mu - V_t), \\ E_p + V_t - \mu, & \theta(V_t - \mu), \end{cases} \tag{3.9}$$

where $\theta(\mu - V_t)$ is the step function, and the region specified by $\theta(\mu - V_t)$ is the inner region of the condensate with phonon-like low energy collective excitations, while the second line of $\theta(V_t - \mu)$ corresponds to the outer region with no condensate mean-field, where the excitations in phase space are particle-like.

We can also understand the mathematical reason for introduction of the conjugate wave function Φ_0 described by Eq. (2.13). By putting $\widetilde{\omega}_0 = 0$ in Eq. (3.8), one may see that $S_0(r) \propto \psi_0(r)$ is a solution, and in general we have $[\mathcal{L} + 3Nu_0\psi_0^2(r)]\, D_0(r) \propto \psi_0(r)$, which corresponds to $D_0(r) \propto \Phi_0$. A general misleading of the previous works was to consider the trivial solution of $D_0(r) = 0$ which corresponds to the Goldstone mode of $U_0 = V_0 = \psi_0(r)$.

3.1. Ordering of the basis states

We choose to order the basis states such that if $n \leq n'$ then $E_n = (n_x\omega_x + n_y\omega_y + n_z\omega_z) \leq E_{n'} = (n'_x\omega_x + n'_y\omega_y + n'_z\omega_z)$. Within the degeneracy manifolds of E_n eigenvalue, the states are sorted by (1) increasing order of the largest of the three 1D indices ($n_{\max} = \max(n_x, n_y, n_z)$); (2) increasing order of the second largest of the three 1D indices ($n_{\mathrm{mid}} = \mathrm{sum}(n_x, n_y, n_z) - \max(n_x, n_y, n_z) - \min(n_x, n_y, n_z)$); (3) increasing in the n_x index. This sorting indexes the basis states in ascending order of energy using a single integer n index.

In numerical computations we further decompose the states into eight sectors since the parity along each of the three coordinates (x, y, z) are good quantum numbers [14]. The resulting parity sectors consists of (even x, even y, even z), (odd x, even y, even z), (even x, odd y, odd z), etc. Then the numerical diagonalization may be performed in each of the sectors, provided that the mean

field potential profiles due to $\rho_0(x,y,z), \rho'(x,y,z), \Delta_0(x,y,z)$, and $\Delta'(x,y,z)$ are symmetric, which is indeed the case of the ground state of the NLSE (3.4). This numerical strategy will reduce eight times the size of the problem, since the NLSE (2.5) and the Bogoliubov–de Gennes equations (2.8) may be solved independently in each of the parity sectors. The total computation effort is then determined by the summation of all the $I_{nmn'm'}$ terms in the $D_{nn'}$ expression Eq. (3.2). One may easily see that to compute all N_{tot}^2 matrix elements would, at least, require N_{tot}^4 operations, since computing each of these matrix elements requires a summation over N_{tot}^2 terms (matrix diagonalization scales with a lower power of N_{tot} and we focus on leading order behavior). To perform self-consistent calculations such as those required by the Popov approximation, each iterative loop demands N_{tot}^4-order calculations. Therefore this repartition of the total basis, into the 8 distinct parity sectors, has some clear advantages.

3.2. Indexing the I_{ijkl}

The evaluation of the basis coupling matrix elements $I_{nmn'm'}$ is also an extremely intensive numerically effort. Since in total there are N_{tot}^4 elements, we mention that the evaluation may lead to a memory management problem too. Various approaches have been developed [13, 25, 32]. The most common one is based on the fast Gaussian quadrature algorithms. Analytic formulas are not very useful since their numerical evaluation takes longer than a direct quadrature computation. We note that, using the harmonic oscillator basis, there is an efficient scheme for ordering the $I_{nmn'm'}$ that allows for both a compact storage as well as efficient addressing and searching.

For a harmonic oscillator basis representation the matrix elements I_{ijkl} are a direct product of three one-dimensional matrix elements,

$$I_{ijkl} = I^{1\text{D}}_{i_x j_x k_x l_x} I^{1\text{D}}_{i_y j_y k_y l_y} I^{1\text{D}}_{i_z j_z k_z l_z}. \tag{3.10}$$

Further, the symmetry properties (to be discussed later) of the one-dimensional matrix elements $I^{1\text{D}}$ are, obviously, the same and the values of the matrix elements are related to each other by a scaling constant. This allows the full matrix element to be calculated from a single set of $I^{1\text{D}}$ elements.

The stored values of $I^{1\text{D}}$ must be ordered and indexed. Because all harmonic oscillator basis functions ϕ_h are real, any permutation of the indices will refer to elements with equal values. Therefore, we assume that each element to be indexed by four integers $h_1 \geq h_2 \geq h_3 \geq h_4 \geq 0$. Written in this way, the $I^{1\text{D}}_{i_1 j_1 k_1 l_1}$ elements may be mapped into a one-dimensional array labeled by an single integer index "ind",

$$I^{1\text{D}}_{h_1 h_2 h_3 h_4} \longrightarrow I^{1\text{D}}_{\text{ind}}. \tag{3.11}$$

This mapping is most easily explained by considering a simple case of an object with two indices, I_{ab} for $a \geq b \geq 0$. For a given value of a, there are

$$\sum_{b=0}^{a} b = \frac{1}{2} a(a+1) \tag{3.12}$$

elements preceding the next $a+1$ elements which correspond to the possible values of b. We associate with the original two indices a single number $a, b \rightarrow$

$\frac{1}{2}a(a+1)+b \quad (0 \le b \le a)$. Generalizing this procedure to higher numbers of indices is straightforward. For the case of $I^{1D}_{h_1h_2h_3h_4}$ with $h_1 \ge h_2 \ge h_3 \ge h_4 \ge 0$ one finds

$$h_1h_2h_3h_4 \to \text{ind} = \frac{1}{4!}h_1(h_1+1)(h_1+2)(h_1+3) + \frac{1}{3!}h_2(h_2+1)(h_2+2) + \frac{1}{2!}h_3(h_3+1) + h_4. \tag{3.13}$$

The use of this indexing procedure allows us to store economically all of the matrix elements needed for our computations.

3.3. Evaluation of $I^{1D}_{h_1h_2h_3h_4}$

The wave function for a 1D-harmonic oscillator, of fundamental frequency ω, in the coordinate representation is given by

$$\phi_n(x) = (2^n n!)^{-\frac{1}{2}} \left(\frac{1}{2\pi a^2}\right)^{\frac{1}{4}} \exp\left(-\frac{x^2}{4a^2}\right) H_n\left(\frac{x}{\sqrt{2}a}\right), \tag{3.14}$$

where $a = \sqrt{\hbar/2M\omega}$ is the size of the ground state. Then we have

$$I^{1D}_{h_1h_2h_3h_4} = (2^{h_1+h_2+h_3+h_4}h_1!h_2!h_3!h_4!)^{-\frac{1}{2}} \frac{1}{2\pi a^2}\int_{-\infty}^{\infty} dx \times \exp\left(-\frac{x^2}{a^2}\right) H_{h_1}\left(\frac{x}{\sqrt{2}a}\right) H_{h_2}\left(\frac{x}{\sqrt{2}a}\right) H_{h_3}\left(\frac{x}{\sqrt{2}a}\right) H_{h_4}\left(\frac{x}{\sqrt{2}a}\right)$$

$$= \frac{1}{a}\left[(2^{h_1+h_2+h_3+h_4}h_1!h_2!h_3!h_4!)^{-\frac{1}{2}} \frac{\sqrt{2}}{2\pi} M_{h_1h_2h_3h_4}\right], \tag{3.15}$$

where

$$M_{h_1h_2h_3h_4} = \int_{-\infty}^{\infty} dy \exp(-2y^2) H_{h_1}(y) H_{h_2}(y) H_{h_3}(y) H_{h_4}(y). \tag{3.16}$$

We note that the quantity inside the square bracket in the rhs of Eq. (3.15) is dimensionless and independent of the frequency of the harmonic oscillator. The $M_{h_1h_2h_3h_4}$ integrals may be easily evaluated with the help of the generating function of the Hermite polynomials, i.e.,

$$e^{-s^2+2sy} \equiv \sum_{h_1}^{\infty} H_{h_1}(y)\frac{s^{h_1}}{h_1!}, \tag{3.17}$$

and so

$$\sum_{h_1,h_2,h_3,h_4=0}^{\infty} M_{h_1h_2h_3h_4}\frac{s^{h_1}}{h_1!}\frac{t^{h_2}}{h_2!}\frac{\mu^{h_3}}{h_3!}\frac{\nu^{h_4}}{h_4!}$$

$$= \int_{-\infty}^{\infty} dy e^{-2y^2} e^{-s^2+2sy} e^{-t^2+2ty} e^{-\mu^2+\mu y} e^{-\nu^2+2\nu y}$$

$$= \sqrt{\frac{\pi}{2}} \exp\left[\frac{(s+t+\mu+\nu)^2}{2}\right]. \tag{3.18}$$

Then, the $M_{h_1h_2h_3h_4}$ are found to be the coefficients of the Taylor expansion of the rhs of Eq. (3.18). Alternatively, numerical quadratures can be developed to evaluate (3.16) [32]. Also, another equivalent analytical expression exists,

$$M_{h_1h_2h_3h_4} \equiv h_1!h_2! \sum_{t=0}^{\min(h_1,h_2)} \frac{2^t}{t!(h_1-t)!(h_2-t)!}$$

$$\times \frac{1}{\pi} 2^{\bar{k}-\frac{1}{2}} \Gamma\left[\bar{k}-(h_1+h_2-2t)+\frac{1}{2}\right] \Gamma\left[\bar{k}-h_3+\frac{1}{2}\right] \Gamma\left[\bar{k}-h_4+\frac{1}{2}\right], \quad (3.19)$$

for $h_1+h_2+h_3+h_4 = 2k = 2\bar{k}+2t$, and zero otherwise (when $h_1+h_2+h_3+h_4 =$ odd number) [33].

3.4. From $I^{1D}_{nmn'm'}$ to I^{1D}_{eee} and I^{1D}_{eoo}

The above approach was initially implemented for the calculation of low energy excitations within a mean-field Bogoliubov approximation [25]. At $T = 0$, only a linear computation (one loop) of the Bogoliubov–de Gennes equations was needed. To study the properties of the excitation spectra at a finite temperature (e.g. with the Popov approximation), we are forced to develop new methods for more efficient evaluation of the matrix elements given in Eq. (3.2). After dividing the basis into 8 parity sectors, it became clear that there is indeed a systematic way of reducing the overall computational effort for one loop from N^4_{tot}-order to N^3_{tot}-order. We outline this approach in this subsection.

As we mentioned earlier, in a harmonic oscillator trap, quasiparticle states have well defined parities with respect to their (x, y, z) coordinates. This can be used to accomplish more efficient evaluation of the matrix elements of the type $D_{nn'}$, Eq. (3.2), i.e. of the following types of integrals:

$$\sum_m \sum_{m'} a^*_m a_{m'} \int \mathrm{d}r \phi^*_m(r)[\rho_0(r), \rho'(r), \Delta_0(r), \Delta'(r)]\phi_{m'}(r). \quad (3.20)$$

At thermal equilibrium, the converged solutions for $\psi_0(r)$ and $(U_k(r), V_k(r))$ will necessarily result in parity symmetric functions for $\rho_0(r), \rho'(r), \Delta_0(r), \Delta'(r)$. Therefore, these functions themselves can be expanded into one particular 8 parity basis sector: the (even x, even y, even z) basis set. As an example, we formally write

$$\rho(r) = \sum_n b_n \phi_n(r), \quad (3.21)$$

where ϕ_n are the complete symmetric basis set. Suppose that the expansion parameters b_n are known, then the calculation of matrix elements as given in Eq. (3.20) will involve products of three ϕ_n functions

$$\sum_n b_n \int \mathrm{d}r \phi^*_m(r)\phi_n(r)\phi_{m'}(r), \quad (3.22)$$

which contain only three Hermite polynomials. We denote the corresponding terms as $I_{mnm'}$ ($I^{1D}_{mnm'}$) and the reduced integral involving products of the Hermite polynomial as $M_{mnm'}$ (compare with $M_{nmn'm'}$ defined in (3.16)). The $M_{mnm'}$ is given by the following identity [33]:

$$\int_{-\infty}^{\infty} \mathrm{d}y \exp\left(-\frac{1}{\gamma}y^2\right) H_{h_1}(y)H_{h_2}(y)H_{h_3}(y) = \sqrt{\gamma}\left(-\frac{z}{2}\right)^{-k} \Gamma\left[k+\frac{1}{2}\right]$$

$$\times \sum_{t=0}^{\min(h_1,h_2)} \frac{(-h_1)_t(-h_2)_t z^t}{t!(\frac{1}{2}-k)_t} F\left(2t-h_1-h_2,-h_3;\frac{1}{2}-k+t;z\right), \quad (3.23)$$

for $\gamma = 2/3$ and $h_1 + h_2 + h_3 = 2k$ (even), where $z = [2(1-\gamma)]^{-1}$, and $(m)_t \equiv \frac{(m+t-1)!}{(m-1)!}$ are the Pochhammer symbols. For the case $h_1 + h_2 + h_3 =$ odd numbers we have $M_{h_1h_2h_3} = 0$. The above calculation (3.22) is now a simple summation of $N_{\rm tot}$ terms (instead of a double summation of $N_{\rm tot}^2$ terms as in Eq. (3.2)). Therefore, the computation of all matrix elements requires only $N_{\rm tot}^3$ operations. Only two distinct possibilities exist for nonzero values of $M_{h_1h_2h_3}$: (1) all indices are even; (2) one index is even and the other two are odd. We denote them as $M_{\rm eee}$ and $M_{\rm eoo}$ respectively, and they can be ordered into a one-dimensional array in a manner similar to that detailed in Sec. 3.2.

One question remains: how do we find the expansion coefficients b_n and what is the associated computational effort? If one writes explicitly the form of expansion (3.21) for any generic term in $\rho_0(r), \rho'(r), \Delta_0(r)$, or $\Delta'(r)$, then one may see that these quantities involve terms proportional to $\psi_0^2(r)$ or $|U_k(r)|^2$ and $|V_k(r)|^2$. We assume that $\psi_0(r)$, $U_k(r)$, and $V_k(r)$ are written as $\sum_n a_n\phi_n(r)$ (these are just the solutions for condensate or quasiparticle states in any of the 8 parity sector basis sets). Then we have

$$\sum_n b_n\phi_n(r) = \sum_m \sum_{m'} a_m^* a_{m'} \phi_m^*(r)\phi_{m'}(r), \quad (3.24)$$

which allows the following expression for b_n coefficients:

$$b_n = \sum_m \sum_{m'} a_m^* a_{m'} I_{nmm'}. \quad (3.25)$$

The above operation is again of the $N_{\rm tot}^3$-order for all the expansion coefficients b_n, and the matrix elements $\int dr\phi_m^*(r)\phi_n^*(r)\phi_{m'}(r)$ are exactly of the same type as those needed in Eq. (3.22), i.e. they can all be reduced to terms involving $M_{\rm eee}$ and $M_{\rm eoo}$. Therefore, by first expanding terms such as $\rho_0(r), \rho'(r), \Delta_0(r), \Delta'(r)$ in the appropriate basis given their parity, the calculation for the density matrix elements of the type $D_{nn'}$ has been reduced from the $N_{\rm tot}^4$-order to the $2N_{\rm tot}^3$-order (one $N_{\rm tot}^3$-order from calculating the expansion coefficients b_n, as in Eq. (3.25), and another $N_{\rm tot}^3$-order from computing the matrix elements for the expanded form, as in Eq. (3.22)).

We want to emphasize that this technique, of reducing a calculation involving $I_{nmn'm'}$ to one involving only $I_{mnm'}$, is also applicable when the ground state $\psi_0(r)$ (and thus $\rho_0(r), \rho'(r), \Delta_0(r), \Delta'(r)$) have different symmetries, as one might expect to occur in the case of vortex states. It even applies when there is no explicit symmetry. In such a case, one may use the complete set of basis states which includes all 8 different parity sectors.

3.5. Construction of the angular momentum states

The preceding subsections have outlined an approach which is efficient for finding the low energy excitations for a trapped Bose gas [25]. Although we have repartitioned the basis states into parity sectors for three coordinates (x, y, z),

no other special symmetries of a given trap have been used. In practice, most of the current magnetic traps used in BEC experiments have cylindrical symmetry. For such traps the angular momentum projection along the symmetric z-axis, $\widehat{L}_z$, is conserved. For $L_z \neq 0$ there is a double degeneracy according to the sign of L_z. Using the harmonic oscillator eigenfunctions as our expansion basis, the reconstruction of the $\widehat{L}_z$ eigenstates is a straightforward task [34], which will be discussed below.

For a cylindrical trap with $\omega_x = \omega_y \equiv \omega_r$ (radial trapping frequency), we can characterize the quasiparticle states according to (1) their energy $\widetilde{\omega}_n$; (2) their angular momentum projection L_z; and, (3) an integer indexing the sequence within a degenerate $\widetilde{\omega}_n$ and L_z manifold. We notice that the states (U_{ki}, V_{ki}) for $i = 1, \ldots, n_d$ correspond to the same energy $\widetilde{\omega}_k$ and so are any linear combinations of them (since the Bogoliubov–de Gennes equations, Eqs. (2.8) and (2.20), are linear). Thus, the eigenstates of $\widehat{L}_z$ into the n_d-degenerate manifold may be constructed as a linear combination, i.e. $U_{kL_z} = \sum c_i U_{ki}$ (and similarly for V_{ki}). The appropriate coefficients c_i are given by the following system of equations:

$$\sum_i \langle U_{ki'}|\widehat{L}_z|U_{ki}\rangle c_i = L_z \sum_i \langle U_{ki'}|U_{ki}\rangle c_i. \tag{3.26}$$

The summation on the rhs is due to the non-orthogonality of the U_{ki} functions. This is a generalized matrix eigenvalue problem. The matrix elements involved may be easily evaluated using a product of harmonic oscillator basis denoted by $|n_x\rangle|n_y\rangle|n_z\rangle$. Let us assume that

$$|U_{ki}\rangle = \sum_{n_x,n_y,n_z} a^{ki}_{n_x,n_y,n_z}|n_x\rangle|n_y\rangle|n_z\rangle. \tag{3.27}$$

Using the creation (annihilation) operators $\widehat{a}_x^\dagger, \widehat{a}_y^\dagger, \widehat{a}_z^\dagger$, $(\widehat{a}_x, \widehat{a}_y, \widehat{a}_z)$ for the harmonic oscillator basis states $|n_x\rangle, |n_y\rangle, |n_z\rangle$ and the relations,

$$\begin{aligned}
&\widehat{L}_z = \mathrm{i}\hbar(\widehat{a}_x\widehat{a}_y^\dagger - \widehat{a}_x^\dagger a_y), \quad a_q|n_q\rangle = \sqrt{n_q}|n_q - 1\rangle, \qquad q = x, y, z,\\
&a_q^\dagger|n_q\rangle = \sqrt{n_q + 1}|n_q + 1\rangle, \qquad q = x, y, z,
\end{aligned} \tag{3.28}$$

we find

$$\begin{aligned}
&\langle U_{ki'}|\widehat{L}_z|U_{ki}\rangle = \mathrm{i}\hbar \sum_{n'_x,n'_y,n'_z} \sum_{n_x,n_y,n_z} a^{ki'*}_{n'_x,n'_y,n_z} a^{ki}_{n_x,n_y,n_z}\\
&\langle n'_x|\langle n'_y|(\widehat{a}_x\widehat{a}_y^\dagger - \widehat{a}_x^\dagger\widehat{a}_y)|n_x\rangle|n_y\rangle = \mathrm{i}\hbar \sum_{n_x,n_y,n_z} \Big[a^{ki'*}_{n_x-1,n_y+1,n_z} a^{ki}_{n_x,n_y,n_z}\\
&\quad \times\sqrt{n_x(n_y+1)} - a^{ki'*}_{n_x+1,n_y-1,n_z} a^{ki}_{n_x,n_y,n_z}\sqrt{(n_x+1)n_y}\Big],
\end{aligned} \tag{3.29}$$

and

$$\begin{aligned}
\langle U_{ki'}|U_{ki}\rangle &= \sum_{n'_x,n'_y,n'_z} \sum_{n_x,n_y,n_z} a^{ki'*}_{n'_x,n'_y,n'_z} a^{ki}_{n_x,n_y,n_z} \delta_{n_x n'_x}\delta_{n_y n'_y}\delta_{n_z n'_z}\\
&= \sum_{n_x,n_y,n_z} a^{ki'*}_{n_x,n_y,n_z} a^{ki}_{n_x,n_y,n_z}.
\end{aligned} \tag{3.30}$$

Similar techniques may be used in the case of a spherically symmetric harmonic trap to find the quasiparticle states for the angular momentum operators $\widehat{L}^2 = \widehat{L}_x^2 + \widehat{L}_y^2 + \widehat{L}_z^2$. In this case the eigenstates of $\widehat{L}^2$ and $\widehat{L}_z$ must be of a spherical harmonics type, Y_{LL_z}.

4. Results and discussions

We incorporated the above ideas into a numerical program and use it in the study of interacting trapped Bose gases within the standard mean-field BH approximation. In our ongoing efforts, we have solved the BH equations for the excitations of condensates in various types of traps. Some of the results are discussed here.

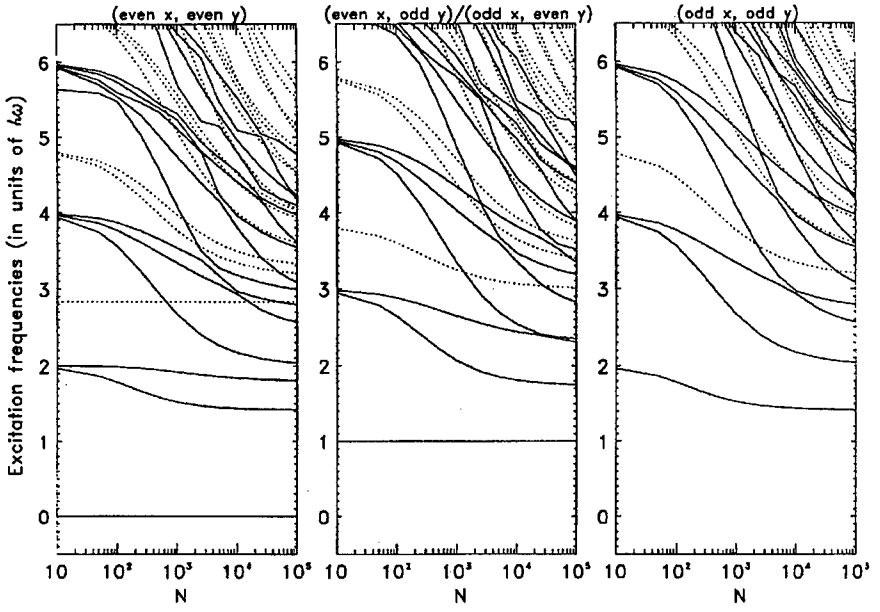

Fig. 1. The calculated dependence of quasiparticle excitation frequencies on the number of condensed atoms for the JILA TOP trap with $(\omega_x : \omega_y : \omega_z) = (1 : 1 : \sqrt{8})$ (129 Hz), for ^{87}Rb atoms with $a_{sc} = 5.2$ nm. The three separate panels are for the 4 separate parity sectors in x and y coordinates respectively: first panel for (even x, even y); second panel for (even x, odd y) [same as (odd x, even y)]; third panel for (odd x, odd y). The even z parity states are plotted with solid lines while odd parity z states are plotted with dashed lines.

We note that our quasiparticles represent elementary excitations of the quantum noise $\delta\Psi(r)$ $(\delta\Psi^\dagger(r))$, while in the current experimental investigations the quasiparticle excitations are created by using microwave pulses or trapping potential perturbations [7].

For the solution of the NLSE (2.5), we typically use up to 10,000 states with the highest energy states corresponding to $E_{\max} > 50\hbar\omega$ for the JILA TOP trap

and $E_{\max} > 200\hbar\omega$ for the MIT cloverleaf trap. Here we only present results for the TOP trap with $\omega_x = \omega_y = \omega_z/\sqrt{8}$. For the zero-temperature calculations, the same number of basis states were used for Eq. (2.8), therefore, higher excitations, closer to $E_{\max}$, are not well represented. For finite temperature calculations within the Popov approximation, we have used fewer basis states for Eq. (2.20), in order to make the calculation possible on a personal workstation. We limited the calculations to a range of parameter where the convergence of the solution is ensured.

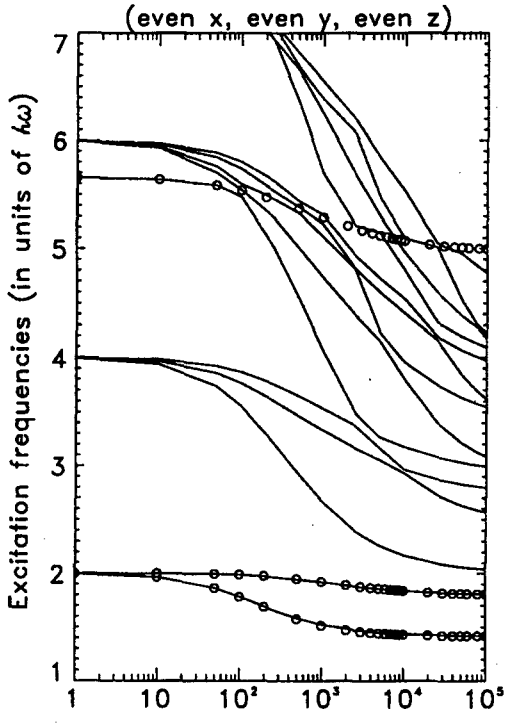

Fig. 2. The first panel of Fig. 1 for even z. The open circles highlight our data points for the three shape oscillation modes of Ref. [17].

The typical dependence of the excitation spectrum on the number of condensed atoms is shown in Fig. 1 calculated in the 8 separate parity sectors. The characterization of the angular momentum operator $\widehat{L}_z$ is a straightforward task usually involving only two energy degenerate states. All $L_z = \pm(2m+1)$ states (i.e. odd angular momentum projection states) are obtained simply from the doubly degenerate states of the (odd x, even y) and (odd y, even x) sectors (of the same, z parity). All states in the middle panel are doubly degenerated. This symmetry between the x and y basis sets requires us to solve only Eqs. (2.8) and (2.20) within the (odd x, even y) sector (for both odd and even z parity). The even angular

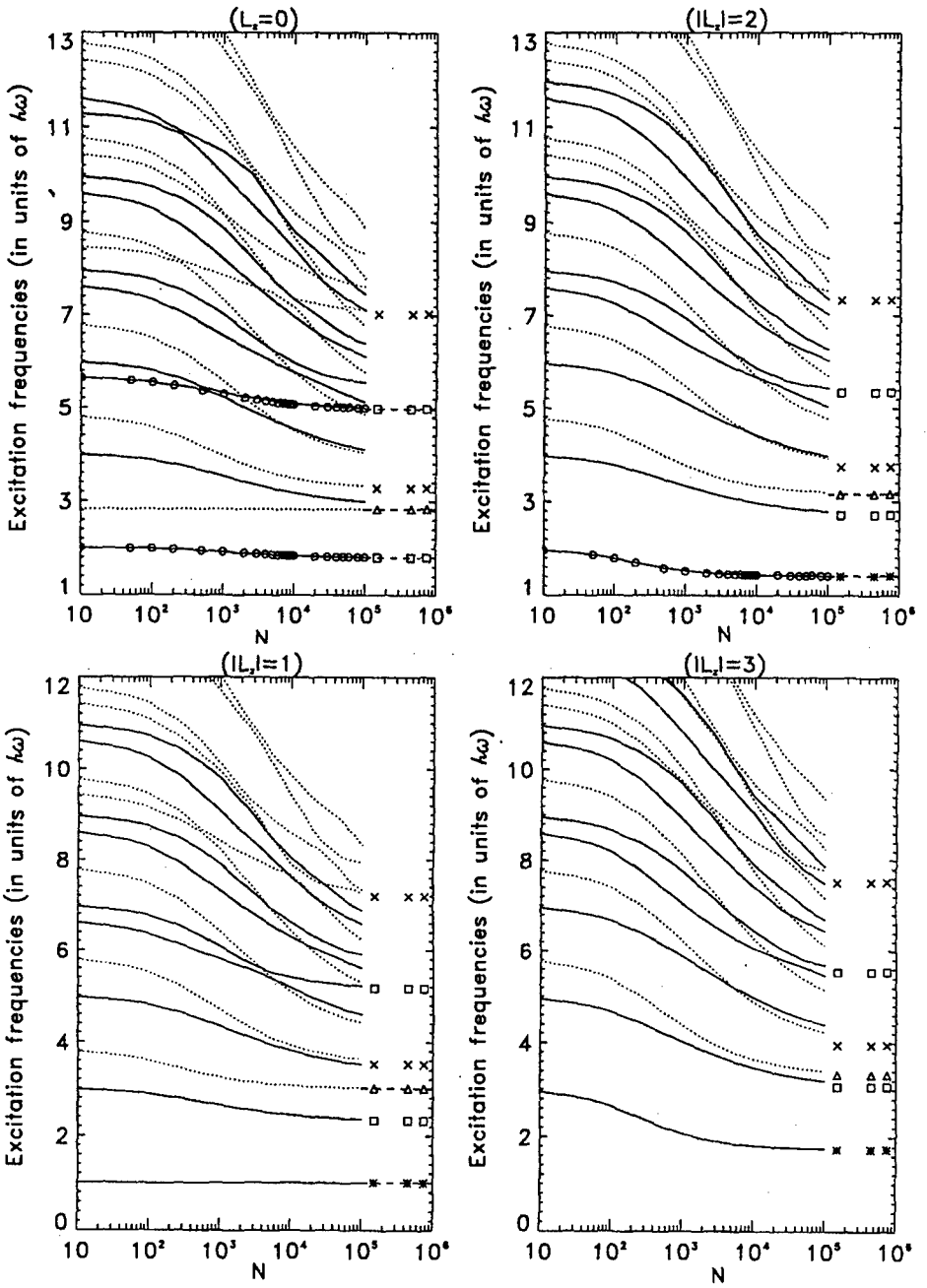

Fig. 3. The same curves as in Fig. 1, now characterized by their L_z quantum numbers. The open circles denote the three shape oscillation modes from Ref. [17]. The dashed lines in the asymptotic limit, $N = 10^5 \div 10^6$, are the results based on Ref. [16]. The asterisks, triangles, squares, and X's denote, respectively, the $n = 0, 1, 2, 3$ modes in the asymptotic limit of Ref. [19].

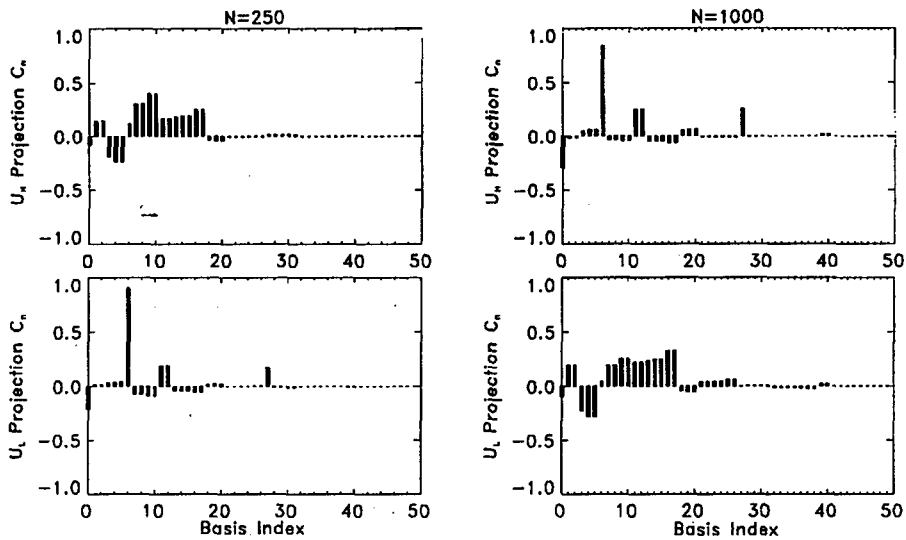

Fig. 4. Plots of the expansion coefficients of the mode function U for two modes at $N = 250$ and $N = 1000$. These modes participate in the lowest energy possible crossing of the $L_z = 0$ curves. The higher energy modes are shown across the top and the lower energy modes are shown across the bottom. It is interesting to note that the level crossing actually occurs at $N \approx 655$. At this point, our numerical diagonalization results in the energy difference of ≈ 0.001.

momentum states, $L_z = \pm(2m)$, are formed by the linear combinations of the solutions for (even x, even y) and (odd x, odd y) sectors (i.e. states in the first and third panel). In particular, all $L_z = 0$ states are within the (even x, even y) sector. For every state in the (odd x, odd y) sector there is always an energy degenerate counterpart in the (even x, even y) sector. Together they form a nonzero even $\pm L_z$ pair of states. In this plot, we have connected the calculated points assuming no crossing between states with the same symmetries.

In the first panel of this Fig. 1, there are two curves with constant excitation frequencies. The lowest curve, for $\tilde{\omega} = 0$, corresponds to the Goldstone mode associated with the U(1) symmetry breaking. The higher one, at $\tilde{\omega} = \sqrt{8}$, is the small amplitude center of mass motion of the rigid cloud in the z-direction. Similarly, in the middle panel, the doubly degenerate state for $\tilde{\omega} = 1$ corresponds to the small amplitude center of mass oscillation in the x and y axes.

Three of the independent shape oscillations have been measured experimentally [7, 8] and discussed extensively using various analytic approaches [15, 17–20]. In Fig. 2 we compare our calculations with the results of Ref. [17]. In Fig. 3 we show the dependence of the quasiparticle eigenfrequencies on N for $L_z = 0, \pm 1, \pm 2$, and ± 3. The open circles denote the three shape oscillation modes from Ref. [17]. The dot lines in the asymptotic limit, $N = 10^5 \div 10^6$, are obtained using the Stringari results [15]. The asterisks, triangles, squares, and X's denote the $n = 0, 1, 2, 3$ modes, respectively, obtained in the asymptotic limit of Refs. [19, 20].

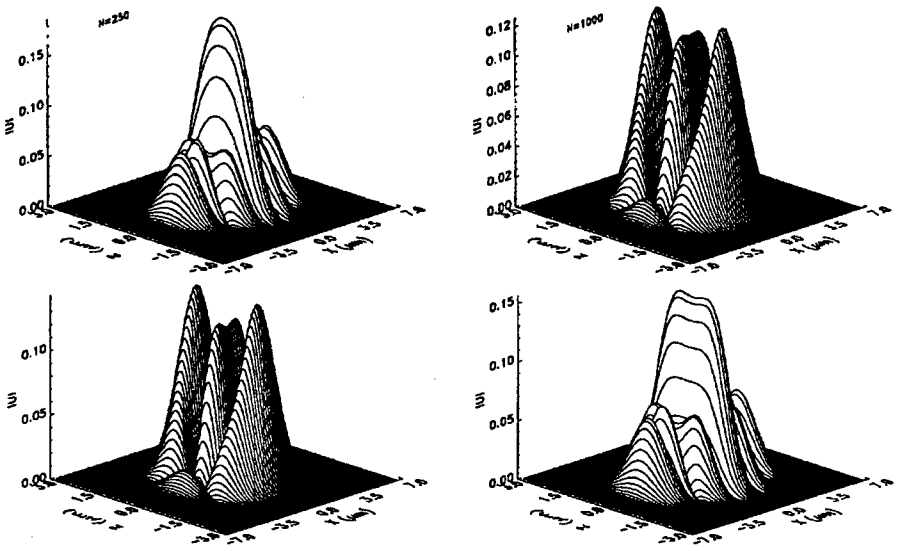

Fig. 5. The mode functions $|U(x,0,z)|$ for the modes of Fig. 4.

Our numerical evaluation agrees well in the asymptotic limit with the analytical results of [15, 17–20].

In Figs. 1, 2, and 3, all crossings between curves of different z parity are allowed. For curves with the same z parity, we have connected the calculated points assuming that there are no crossings between them. This may not be always true. Let consider a possible crossing for the lower energy curves with $L_z = 0$ from Fig. 3. Any of these curves represents one of the shape oscillations Ref. [17] and, therefore, they should maintain their symmetry through any value of N. In Fig. 4, for values of $N = 250$ and $N = 1000$ on either side of the possible crossing, we show projections of the mode function $U(r)$ onto the (even x, even y, even z) basis for each of the two curves involved. This may suggest that a crossing point exists in this range of value of N. To firmly determine if this crossing indeed exists one has to perform detailed numerical computations at exactly the crossing points (minimum distance points between the two energy curves for avoided crossings). We have performed such a study of the crossing shown in Fig. 4. Figure 5 presents the shape of $|U(z, y = 0, z)|$ for the same values of N. These figures indicate the existence of a crossing between these two curves. In our initial studies [25] this crossing was identified as an avoided crossing based on the fact that these two quasiparticle energy levels belong to the same symmetry manifold. Recent semiclassical studies of quasiparticle motion in trapped condensates have revealed rich chaotic dynamics underlining these complicated level crossings and avoided crossings [35].

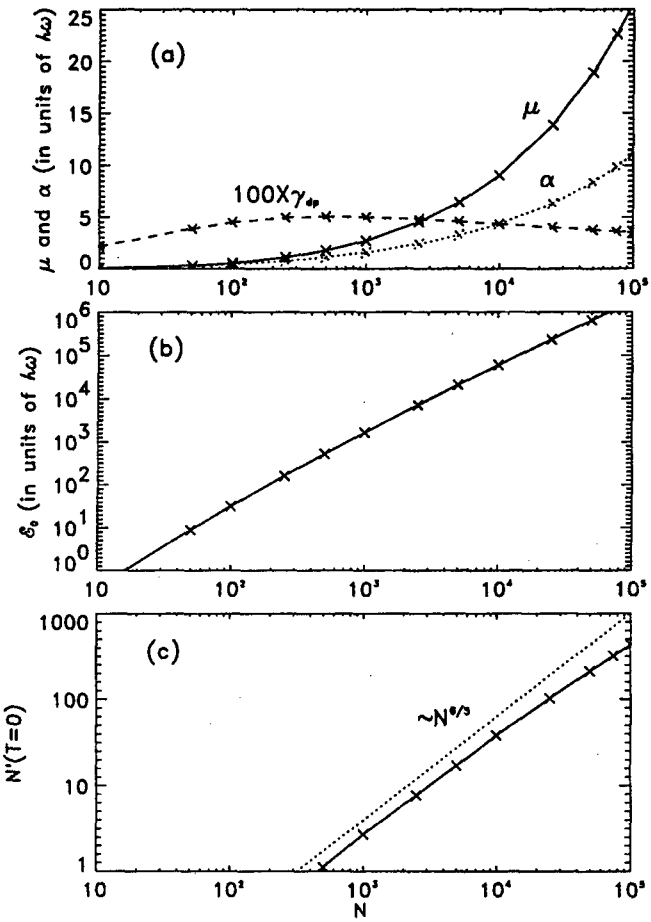

Fig. 6. Zero temperature results for (a) the chemical potential μ and the dephasing parameter α, (b) total ground state energy, and (c) number of the noncondensate particle. The crosses denote the calculated data points.

In Fig. 6 various zero temperature results are plotted as a function of N. Figure 6a presents the chemical potential, μ, the dephasing parameter, α, as well as the dephasing rate, $\gamma_{\rm dp} = \alpha/\sqrt{N_0}$ as a function of N. In the TFA both μ and α scale as $N^{2/5}$, while $\gamma_{\rm dp}$ scales as $N^{-1/10}$. It is interesting to note that before $\gamma_{\rm dp}$ reaches its asymptotic scaling behavior it passes through a maximum. Figure 6b presents the total ground state energy as a function of N. Figure 6c presents the number of noncondensed particles in the zero temperature limit as a function of N. The condensate depletion is a good measure of the effect of interparticle interaction. As a percentage, only a very small fraction of the atoms are noncondensed. In the asymptotic limit $N'(T=0)$ scales approximately as $N^{6/5}$, as indicated with the dashed line. This is consistent with the empirical results of Ref. [31] as well as the semiclassical results of Ref. [36]. The projection, z_k, of the condensate wave function

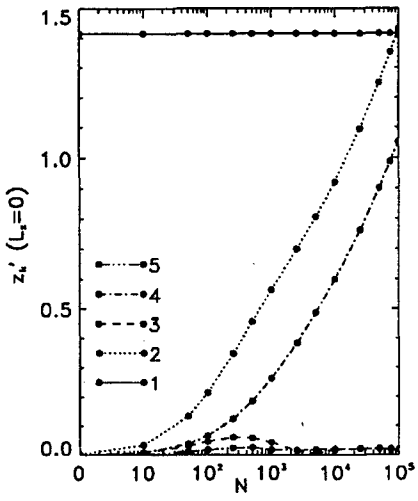

Fig. 7. The projections of the condensation wave function onto the various $L_z = 0$ mode functions. The lists are indexed by an integer denoting in increasing order (the weakly interacting limit) the quasiparticle modes within the $L_z = 0$ symmetry.

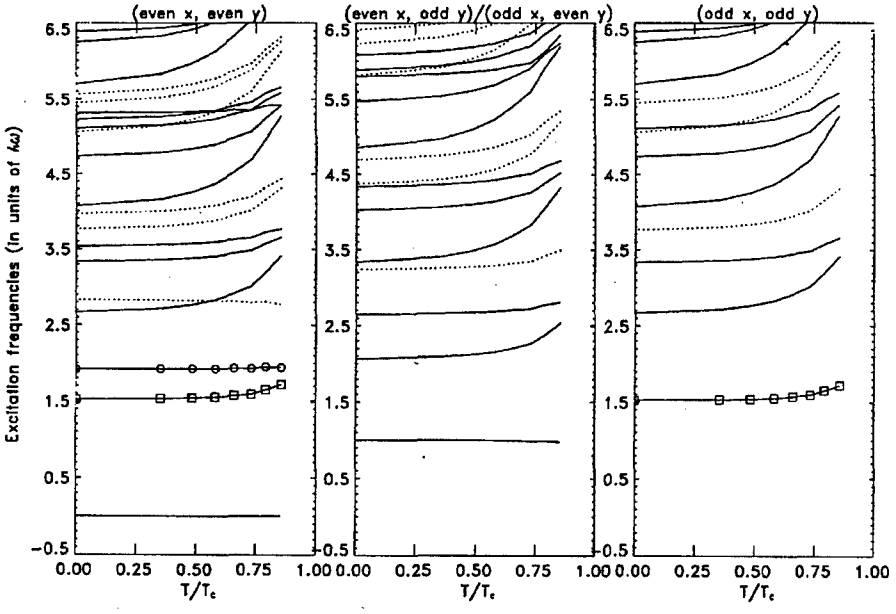

Fig. 8. The calculated dependence of quasiparticle excitation frequencies on the temperature T, within the Popov approximation for $N = 1000$. The open circles represent the results for $L_z = 0$ modes while the squares represent the results for $L_z = \pm 2$ modes.

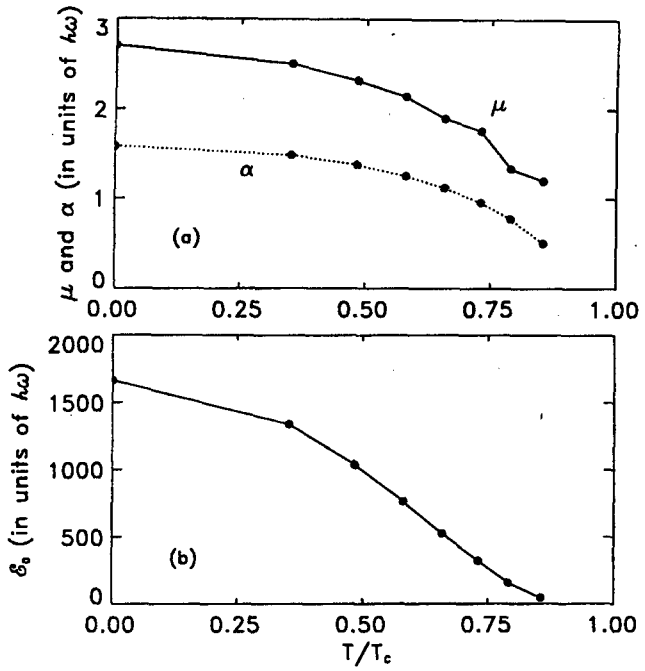

Fig. 9. The temperature dependent results for (a) the chemical potential and the dephasing, and (b) the ground state energy computed within the Popov approximation for $N = 1000$ atoms. The filled circles denote the calculated data points.

onto the quasiparticle mode functions (U_k, V_k) (see Eq. (2.16)), is plotted in Fig. 7 only for k corresponding to the $L_z = 0$ quasiparticles since the ground state condensate wave function $\psi_0(r)$ has the $L_z = 0$ symmetry.

In Figs. 8, 9, and 10, we plot our preliminary results for finite temperature calculations within the Popov approximation for the JILA TOP trap with $N = 1000$ atoms. The trap and atomic parameters are the same as in the previous zero temperature results. Figure 8 is arranged in a similar fashion as Fig. 1 except now we plot the dependence of the excitation spectra on the temperature T, which is determined from the self-consistent Popov calculation by specifying both N_0 and N. We denote with T_c the ideal Bose gas condensation temperature for the same trap parameters and number of atoms (in our case it is equal to $13.3\hbar\omega/k$). Even with the limited basis set of functions used, the highest temperature point computed is very close to T_c. For $N_0 = 0.125N$ the temperature is given approximately by $T/T_c \propto (1 - 0.125)^{1/3} \approx 0.9565$. The open circles and squares are used to highlight the shape oscillations recently studied experimentally [7, 8] but they do not represent experimental data points. We can see that when T is close to T_c, the overall trends of the temperature dependence of the two excitation frequencies are similar to those measured in Ref. [8], although $N = 1000$ atoms is significantly smaller than the total number of atoms involved in the experiment. However, close

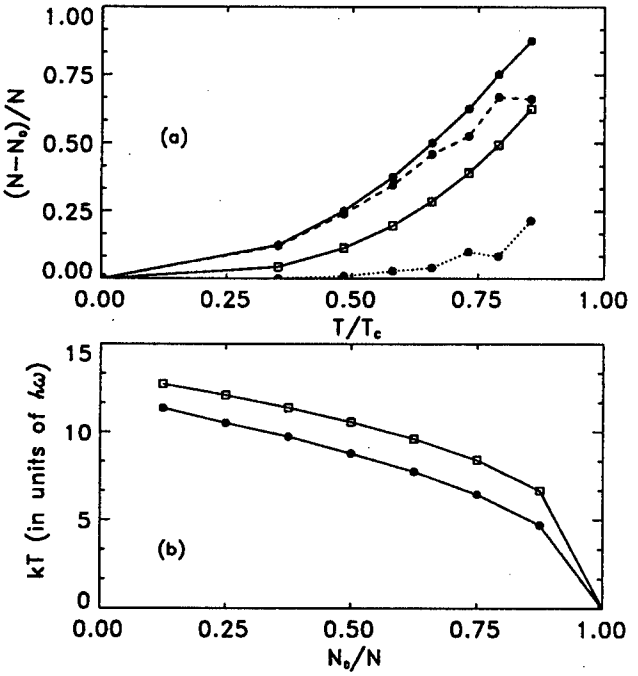

Fig. 10. (a) The depleted fraction as a function of the computed temperature within the Popov approximation. (b) The temperature as a function of the condensate fraction within the Popov approximation. Calculations were performed for $N = 1000$ atoms. The filled circles denote the calculated data points and the open squares represent the results for a trapped ideal Bose gas: $N_0/N = 1 - (T/T_c)^3$.

to the transition temperature, our calculations do not produce any rapid changes of the excitation frequencies. This is in disagreement with the variations observed in recent experiments and is the subject of our continued study.

Figure 9 presents: (a) the temperature dependence of the chemical potential, μ, and the dephasing parameter, α, and (b) the ground state energy of the condensate.

In Fig. 10a the solid line with filled circles shows the fraction of noncondensed atoms, $N'/N = (N-N_0)/N$, plotted against the computed temperature. The filled circles denote the computed data points. The dashed line represents the fraction as given by our numerical solution using a basis of states satisfying $E_{\max} \leq 50\hbar\omega$. The dotted line represents the difference between the two curves. We are confident that the size of the basis adopted here is suitable to describe the present system, of course, increasing the total number of atoms, the interaction strength, or the temperature would require a larger basis set. Figure 10b presents the computed temperature of the condensed gas plotted against the fraction of condensate atoms.

We note that the computed temperature is always lower than that of the ideal Bose gas prediction, $N_0/N = 1 - (T/T_c)^3$. This is consistent with the observation of lowering the condensation temperature T_c from Ref. [39].

5. Conclusions

We conclude the following:

(1) At zero temperature, results of the quasiparticle excitation spectra from the mean field Bogoliubov approximation calculations agree well with the experimental data. Many approximate analytical approaches [15, 17–20] also produce excellent predictions for various quasiparticle excitation frequencies in the Thomas–Fermi limit.

(2) For finite temperatures, we have presented a self-consistent mean field Bogoliubov–Hartree calculation within the Popov approximation. Our preliminary calculations indicate that more detailed studies are needed in order to explain the recently measured finite temperature excitation results [8].

Acknowledgments

We would like to acknowledge many enlightening conversations with Drs. Y. Castin, M. Edwards, B. Forrey and T.A.B. Kennedy. This work is supported by the U.S. Office of Naval Research grant No. 14-97-1-0633. L.Y. also wants to acknowledge the support of NSF grant INT. 9722745. The work of W.H. is supported by the National Science Foundation through a grant for the Institute for Theoretical Atomic and Molecular Physics at Harvard University and Smithsonian Astrophysical Observatory.

References

[1] See the special issue *Laser Cooling and Trapping of Atoms, J. Opt. Soc. Am. B* **6** (1989), Eds. S. Chu, C.E. Wieman; and the review articles in the section of "Advances in Laser Cooling and Trapping of Atoms; Atom Optics", *Proc. 14th Int. Conf. on Atomic Physics*, Eds. D.J. Wineland, C.E. Wieman, S.J. Smith, AIP Press, New York 1995.

[2] J.M. Doyle, J.C. Sandberg, I.A. Yu, C.L. Cesar, D. Kleppner, T.J. Greytak, *Phys. Rev. Lett.* **67**, 603 (1991); O.J. Luiten, M.W. Reynolds, J.T.M. Walraven, *Phys. Rev. A* **53**, 381 (1996); W. Ketterle, N.J. Van Druten, *Adv. Atom. Mol., Opt. Phys.* **37**, 181 (1996).

[3] M.H. Anderson, J.R. Ensher, M.R. Matthews, C.E. Wieman, E.A. Cornell, *Science* **269**, 198 (1995).

[4] C.C. Bradley, C.A. Sackett, J.J. Tollett, R.G. Hulet, *Phys. Rev. Lett.* **75**, 1687 (1995).

[5] K.B. Davis, M.-O. Mewes, M.R. Andrews, N.J. van Druten, D.S. Durfee, D.M. Kurn, W. Ketterle, *Phys. Rev. Lett.* **75**, 3969 (1995).

[6] M.R. Andrews, M.-O. Mewes, N.J. van Druten, D.S. Durfee, D.M. Kurn, W. Ketterle, *Science* **273**, 84 (1996).

[7] D.S. Jin, J.R. Ensher, M.R. Matthews, C.E. Wieman, E.A. Cornell, *Phys. Rev. Lett.* **77**, 420 (1996); M.-O. Mewes, M.R. Andrews, N.J. van Druten, D.M. Kurn, D.S. Durfee, C.G. Townsend, W. Ketterle, *ibid.* **77**, 988 (1996).

[8] D.S. Jin, M.R. Matthews, J.R. Ensher, C.E. Wieman, E.A. Cornell, *Phys. Rev. Lett.* **78**, 764 (1997).

[9] M.R. Andrews, C.G. Townsend, H.-J. Miesner, D.S. Durfee, D.M. Kurn, W. Ketterle, *Science* **275**, 637 (1997).

[10] E. Burt, R.W. Ghrist, C.J. Myatt. M. Holland, E.A. Cornell, C.E. Wieman, *Phys. Rev. Lett.* **79**, 337 (1997).

[11] M.-O. Mewes, M.R. Andrews, D.M. Kurn, D.S. Durfee, C.G. Townsend, W. Ketterle, *Phys. Rev. Lett.* **78**, 582 (1997).

[12] M.R. Andrews, D.M. Kurn, H.-J. Miesner, D.S. Durfee, C.G. Townsend, S. Inouye, W. Ketterle, *Phys. Rev. Lett.* **79**, 553 (1997).

[13] M. Edwards, P.A. Ruprecht, K. Burnett, R.J. Dodd, C.W. Clark, *Phys. Rev. Lett.* **77**, 1671 (1996).

[14] K.G. Singh, D.S. Rokhsar, *Phys. Rev. Lett.* **77**, 1667 (1996).

[15] S. Stringari, *Phys. Rev. Lett.* **77**, 2360 (1996).

[16] A.L. Fetter, *Phys. Rev. A* **53**, 4245 (1996); *Czech. J. Phys.*, accepted for publication.

[17] V.M. Pérez-García, H. Michinel, J.I. Cirac, M. Lewenstein, P. Zoller, *Phys. Rev. Lett.* **77**, 5230 (1996).

[18] Yu. Kagan, E.L. Surkov, G.V. Shlyapnikov, *Phys. Rev. A* **54**, R1753 (1996); Y. Castin, R. Dum, *Phys. Rev. Lett.* **77**, 5315 (1996); A. Griffin, W.C. Wu, S. Stringari, *Phys. Rev. Lett.* **78**, 1838 (1997).

[19] P. Öhberg, E.L. Surkov, I. Tittonen, S. Stenholm, M. Wilkens, G.V. Shlyapnikov, submitted to *Phys. Rev. A*, 1997.

[20] A.L. Fetter, D. Rokhsar, *Phys. Rev. A*, in press.

[21] M. Marinescu, A.F. Starace, *Phys. Rev. A* **56**, 570 (1997).

[22] B.D. Esry, *Phys. Rev. A* **55**, 1147 (1997).

[23] B.D. Esry, C. Green, private communication.

[24] D.A.W. Hutchinson, E. Zaremba, A. Griffin, *Phys. Rev. Lett.* **78**, 1842 (1997); M. Edwards, private communication.

[25] L. You, W. Hoston, M. Lewenstein, *Phys. Rev. A* **55**, R1581 (1997).

[26] A.L. Fetter, J.D. Walecka, *Quantum Theory of Many-Particle Systems*, McGraw-Hill, New York 1971; A.L. Fetter, *Ann. Phys. (NY)* **70**, 67 (1972); A. Griffin, *Phys. Rev. B* **53**, 9341 (1996).

[27] M. Lewenstein, L. You, *Phys. Rev. Lett.* **77**, 3489 (1996); A. Imamoğlu, M. Lewenstein, L. You, *Phys. Rev. Lett.* **78**, 2511 (1997); P. Villain, M. Lewenstein, R. Dum, Y. Castin, L. You, A. Imamoğlu, T.A.B. Kennedy, *J. Mil. Opt.*, in press.

[28] Y. Castin, R. Dum, *Phys. Rev. Lett.* **79**, 3553 (1997); C.W. Gardiner, *Phys. Rev. A* **56**, 1414 (1997).

[29] J.-P. Blaizot, G. Ripka, *Quantum Theory of Finite Systems*, MIT Press, Cambridge MA 1986.

[30] M. Holland, D.S. Jin, M.L. Chiofalo, J. Cooper, unpublished.

[31] J. Javanainen, *Phys. Rev. A* **54**, 3722 (1996).

[32] R.J. Dodd, *J. Res. Natl. Inst. Stand. Technol.* **101**, 545 (1996); M. Edwards, R.J. Dodd, C.W. Clark, K. Burnett, *ibid.* **101**, 553 (1996).

[33] I.W. Busbridge, *J. London Math. Soc.* **23**, 135 (1948).

[34] C. Cohen-Tannoudji, B. Diu, L. Laloë, *Quantum Mechanics*, Vols. 1 and 2, Wiley, New York 1997.

[35] M. Fliesser, A. Csordás, R. Graham, P. Szépfalusy, preprint, cond-mat/9707122; M. Fliesser, A. Csordás, P. Szépfalusy, R. Graham, preprint, cond-mat/9706002.

[36] F. Dalfovo, S. Giorgini, M. Guilleumas, L. Pitaevskii, S. Stringari, cond-mat/9705240, preprint.

[37] J.R. Ensher, D.S. Jin, M.R. Matthews, C.E. Wieman, E.A. Cornell, *Phys. Rev. Lett.* **77**, 4984 (1996).

Vol. 93 (1998) *ACTA PHYSICA POLONICA A* No. 1

Proceedings of the International Conference "Quantum Optics IV", Jaszowiec, Poland, 1997

FEMTOSECOND LIGHT WAVE PACKETS

C. RADZEWICZ

Institute of Experimental Physics, Warsaw University, Hoża 69, 00-681 Warsaw, Poland

M. TRIPPENBACH, Y.B. BAND

Department of Chemistry and Physics, Ben-Gurion University, Beer Sheva, Israel

AND J.S. KRASINSKI

Center for Laser and Photonics Research, Oklahoma State University
Stillwater, OK, 74078, USA

We analyze propagation of ultra short light pulses in a transparent, dispersive, nonlinear medium. A general formula for femtosecond wave packet evolution is developed and applied to specific problems. Theoretical and experimental results for wave packet distortion by lenses, wave packet rotation in birefringent media and group velocity matching in sum frequency generation are presented. Numerical results for splitting of femtosecond wave packets in dispersive Kerr media are also presented.

PACS numbers: 42.65.Jx, 42.65.Re

1. Introduction

Developments in laser mode-locking techniques during the last decade led to generation of pulses as short as 7.5 fs (1 fs = 10^{-15} s) directly from Ti:sapphire laser [1]. By employing pulse compression techniques one can achieve even shorter pulses with the current record at less than 5 fs level [2, 3]. Progress in this field has been very fast, especially in the 70-ties and 80-ties, as illustrated in Fig. 1 which presents the history of ultra short pulse generation in the last 25 years. Originally, the most common femtosecond systems were based on organic dyes as laser materials, however with an advent of fs Ti:sapphire lasers [4] in the early 90-ties a solid state technology is available. Currently, systems operating at 20–30 fs range are routine and commercial systems with sub-20 fs capabilities are on the market.

A femtosecond light pulse propagating in a given medium can be visualized as a wave packet of electro-magnetic radiation that moves with its group velocity and at the same time changes its shape due to the interaction with the medium. We find the wave packet picture appealing and we will use the wave packet language throughout this paper. One of the simplest experiments with femtosecond light pulses involves propagation of such wave packets through a transparent medium,

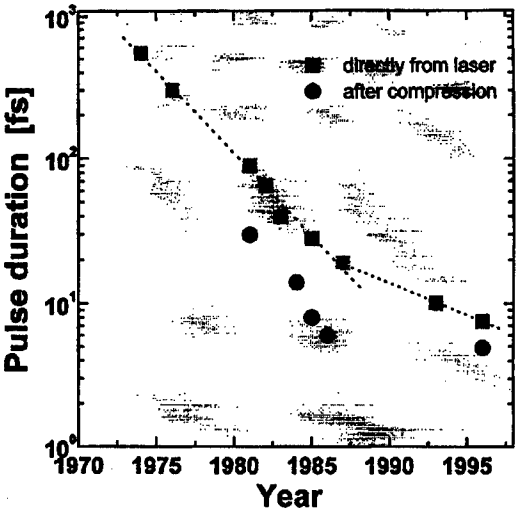

Fig. 1. A history of ultra short light pulse generation. Pulse duration available directly from lasers and after compression are shown.

for example an optical window made of glass. Such experiments are omnipresent. They are performed every day in ultra fast optics laboratories, often without a conscious thought on the experimentalist part, whenever an ultrashort light pulse has to be delivered from the laser system to the sample and, on its way, passes through a lens or a glass cell window. Since the result of many experiments with ultra short light pulses, especially in a nonlinear regime, strongly depends on the details of the pulse such as its time and/or spatial properties it is quite important to understand what happens to such a pulse on its way from the laser system to the sample. When considering propagation of a low intensity monochromatic light beam in a dielectric one only has to account for its index of refraction which modifies the diffraction of the beam by changing the propagation constant with respect to that for vacuum. What makes the propagation of femtosecond pulses different? First, by the virtue of their brevity, the femtosecond pulses have broad spectrum. Because of that, a significant pulse shaping is observed whenever they propagate in a dispersive medium. Second, the peak intensity can be quite high even with a moderate pulse energy and average power. Therefore 3-rd order processes (allowed in a medium of any symmetry) cannot be neglected. For instance, intensity dependent refraction index gives rise to self-phase modulation and self-focusing which influence the spectrum of the pulse and its spatio-temporal characteristics, respectively. It is a well-known phenomenon leading, among other things, to formation of optical solitons in fibers [5, 6] and white light continuum generation [7]. As is often the case in nonlinear problems, three phenomena: diffraction, dispersion and self-focusing are entangled; one can study their effects separately only in a limited number of cases when one of them dominates. However, in most cases numerical methods have to be employed as a method of solution. This paper is organized as follows. In Sec. 2 we present a general form of the propagation equation for a fem-

tosecond wave packet in a transparent, dispersive and nonlinear medium. Section 3 provides examples of the wave packet shaping effects in a linear regime — both theoretical and experimental data are provided. In Sec. 4 we analyze nonlinear propagation regime and present the results of numerical calculations illustrating a complex wave packet evolution.

2. Propagation equation

We start by representing the scalar electric field $E(r,t)$ of the light wave packet as an integral of its Fourier components

$$E(r,t) = \frac{1}{(2\pi)^3}\int \mathrm{d}^3k\widetilde{E}(k)\exp\{[k\cdot r-\omega(k)t]\}, \tag{1}$$

each characterized by its amplitude $\widetilde{E}(k)$, wave vector k and frequency $\omega(k)$. Out of four variables, i.e. frequency and three components of the wave vector that describe each Fourier component, only three are independent because of the dispersion relation $\omega=\omega(k)$. Next we represent the field amplitude as a product of a slowly varying envelope (SVE) and a phase factor

$$E(r,t) = A(r,t)\exp\{\mathrm{i}[k_0\cdot r-\omega(k_0)t]\}, \tag{2}$$

where we assumed that the wave vectors are grouped around a central value k_0 and correspondingly the frequencies form a band around the central frequency $\omega_0=\omega(k_0)$. This leads to the propagation equation for slowly varying envelope [8–11]

$$\frac{\partial A(r,t)}{\partial z} = \frac{1}{(2\pi)^3}\int_{-\infty}^{+\infty}\mathrm{d}^3kA(k,\omega)(\mathrm{i}[k-k_0]\cdot s_0)$$
$$\times\exp\{\mathrm{i}[(k-k_0)\cdot r-(\omega-\omega_0)t]\}+\mathrm{i}\gamma_{nl}|A|^2A. \tag{3}$$

In the last equation a unit length vector $s_0=k_0/|k_0|$ assumed to be in the direction of z coordinate has been introduced. An additional term $\mathrm{i}\gamma_{nl}|A|^2A$ has also been added. It describes the effect of the 3-rd order nonlinearity (Kerr type nonlinearity) of the medium. The integral over k_z can be replaced by an integral over ω when the dispersion relation is taken into account:

$$k_z=\sqrt{\omega^2n^2(\omega,s)/c^2-k_x^2-k_y^2},$$

where n is the index of refraction and $s=k/|k|$. This particular form of expression for n allows application of this approach to both isotropic and anisotropic media. Since no assumptions about the form of $A(r,t)$ have been made Eq. (3) is exact. A partial differential equation for $A(r,t)$ can also be obtained by using Eq. (3). This is done by expanding k_z in powers of k_x, k_y and $(\omega-\omega_0)$ and replacing these variables with $\mathrm{i}\partial/\partial x$, $\mathrm{i}\partial/\partial y$ and $-\mathrm{i}\partial/\partial t$, respectively. Keeping terms up to the second order gives for a uniaxial birefringent medium [11]

$$\frac{\partial A}{\partial z} = -\beta_1\frac{\partial A}{\partial t}+\frac{\mathrm{i}}{2}\beta_2\frac{\partial^2A}{\partial t^2}+\gamma_x\frac{\partial A}{\partial x}+\mathrm{i}\gamma_{tx}\frac{\partial^2A}{\partial t\partial x}$$
$$+\frac{\mathrm{i}}{2}\gamma_{xx}\frac{\partial^2A}{\partial x^2}+\frac{\mathrm{i}}{2}\gamma_{yy}\frac{\partial^2A}{\partial y^2}+\mathrm{i}\gamma_{nl}|A|^2A. \tag{4}$$

The coefficients $\beta_1 = 1/v_g = \partial k/\partial\omega$ and $\beta_2 = \partial\beta_1/\partial\omega$ describe the effects of group velocity and group velocity dispersion, respectively, γ_{xx} and γ_{yy} are responsible for the diffraction of the wave packet, γ_x reflects beam walk-off in a birefringent medium while γ_{tx} was found to be responsible for the rotation of the wave packet [9]. It is worth mentioning that the coefficients γ_x and γ_{tx} vanish for isotropic medium. One can easily generalize Eq. (4) by adding higher order terms. For the sake of clarity we will not do it here but rather refer an interested reader to the original papers [8–11]. Either of the two equations (Eq. (3) or the expanded version of Eq. (4)) can be numerically integrated. It should be pointed out that Eq. (4) is an approximation of Eq. (3) and in order to make them totally equivalent one would have to include terms of all orders into Eq. (4). This clearly is not a practical approach. We found however that in all cases studied, the results of either approach are almost identical if the terms up to 3-rd order are included into Eq. (4). Before we present the results of such integration let us consider some simpler cases.

3. Linear propagation: 1-D and 3-D effects

First, let us analyze Eq. (4) in a 1-dimensional case. Assume that $A(r,t) = A(z,t)$. This is the case whenever light propagates in a single mode optical fiber or the laser beam properties are such that it can be modeled as a one-dimensional plane wave. In this case all derivatives with respect to x and y vanish and we are left with a well-known nonlinear Schrödinger equation of the following form:

$$\frac{\partial A}{\partial z} = -\beta_1 \frac{\partial A}{\partial t} + \frac{\mathrm{i}}{2}\beta_2 \frac{\partial^2 A}{\partial t^2} + \mathrm{i}\gamma_{\mathrm{nl}}|A|^2 A. \tag{5}$$

This equation is easy to solve if we keep only the first term on the right side. One can verify that any function $A(z,t)$ that has a form $A(z, z/v_g)$ constitutes a proper solution. This means that in the lowest order approximation a 1-dimensional wave packet can be of any shape and it propagates without distortions with the speed equal to the group velocity in a given medium. It may seem to be a trivial statement, which it is, but a one with significant consequences in many experiments. We will illustrate this with two examples.

The first example of the havoc that the group velocity can play with an experiment is a wave packet distortion by lenses. It has been recognized quite a long time ago that the difference between phase and group velocities can lead to significant effects upon propagation of femtosecond pulses through lenses [12–13]. If a collimated beam, i.e. a flat wave packet, is focused with a chromatic lens then the phase surfaces behind the lens are spherical but the shape of the wave packet is not. In the UV-visible range the group velocity is smaller than the phase velocity for optical glasses. Because the wave packet propagates through more glass in the center of the beam where the lens is the thickest it accumulates more group delay than phase delay there while at the edges of the lens the two delays are almost equal. As a result the wave packet behind the lens is distorted; its central part lags behind the edges. This in turn causes that the intensity of light in the focus no longer follows the intensity time profile of the input pulse because different radial zones of the wave packet contribute to it at different times. It is important to be able to measure this distortion, especially for complex lenses such

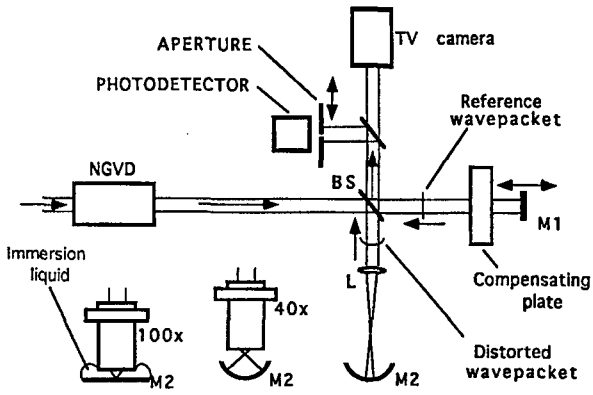

Fig. 2. An experimental set-up used to measure wave packet distortion by lenses. NGVD is a negative group velocity dispersion prismatic line. L is the tested lens. The TV camera has been used to align the interferometer.

as microscope objectives for which direct calculations may be quite difficult and which are commonly used in applications such as two-photon microscopy [14]. We have designed an interferometric method to measure the wave packet distortion in lenses [15]. The experimental set-up is shown in Fig. 2. The main part of the system is a modified Michelson interferometer with one arm serving as a reference arm and the other arm including the tested lens L. A collimated beam from a femtosecond Ti:sapphire laser was used as an input beam. Its diameter was big enough to fill the aperture of the lens. As indicated in the figure, at the output of the interferometer a flat reference wave packet interferes with a wave packet distorted by a double passage through the lens. The interference fringes are visible only in the regions where the two wave packets overlap for a given delay defined by the position of the mirror $M1$. As this mirror is scanned the fringes appear and disappear in different radial zones of the output beam. A detector placed behind a small pinhole was used to measure the fringe visibility at different distances from the beam center. For any given position of the pinhole we measured the delay corresponding to maximum fringe visibility and thus found the shape (we assume cylindrical symmetry) of the distorted wave packet. An example of the results is presented in Fig. 3. It shows the relative group delay as a function of the radial position on a $40\times$ microscope objective. As one can see the parts of the wave packet propagating close to the edges of the lens are advanced by more than 30 fs with respect to the center of the wave packet. We found it quite amusing that an addition of a cover glass (170 μm thick) between the lens and the curved mirror $M2$ significantly improved the performance of the objective. Apparently the objective has been designed to work with the cover glass!

As a second example, consider a frequency mixing experiment with femtosecond laser pulses. A crystal with $\chi^{(2)}$ nonlinearity is illuminated by two collinear ultra short laser pulses with frequencies ω_1 and ω_2 and a sum frequency at $\omega_3 = \omega_1 + \omega_2$ is generated. Since the three frequencies involved in the process are quite different, the group velocities of the corresponding pulses are differ-

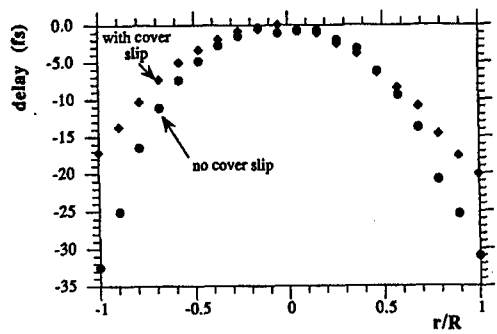

Fig. 3. Wave packet distortion by 40×, 0.65 NA Olympus microscope objective. Relative delays for different radial zones of the wave packet are shown.

ent, too. This has a detrimental effect on the sum frequency generation process. If $\omega_1 \neq \omega_2$ then $\nu_g(\omega_1) \neq \nu_g(\omega_2)$ in a dispersive medium. As a result the two input pulses propagate with different speeds. This limits the range over which the input pulses overlap which in turn limits the efficiency of the process. In addition, the output pulse at ω_3 propagates at yet another (and usually very different) speed. As a result, the output pulse is longer than the input pulses because contributions from different slices of the crystal arrive at the output face at different times. The latter effect remains even in the case of second harmonic generation (SHG) when a single femtosecond pulse is used to produce another pulse at twice the input frequency. The problem of group velocity mismatch could be significantly alleviated if a frequency mixing scheme which ensures both phase matching (PM) and group velocity matching (GVM) could be found. We found that this can be actually achieved in some cases when type I non-collinear sum frequency generation scheme is applied [16, 17].

Figure 4 illustrates the basic idea. In the UV-visible range the group velocity in nonlinear crystals decreases with increasing frequency and thus the sum frequency pulse at ω_3 lags behind the driving pulses at ω_1 and ω_2. Therefore with a suitable choice of the angles ψ_1 and ψ_2 the projections of $\boldsymbol{\nu}_{g1}$, $\boldsymbol{\nu}_{g2}$ and $\boldsymbol{\nu}_{g3}$ on $\boldsymbol{k}_3$ can be made equal. This means that the three pulses have the same components of the group velocity along the propagation direction and they do not separate as they propagate. It is not obvious that group velocity matching and phase matching can be achieved in a given crystal for given wavelengths of the input pulses. Whether this is possible or not depends on dispersion properties of the particular nonlinear birefringent crystal selected. Figure 5 shows the results of numerical calculations for β-barium borate (BBO) crystal in the range of fundamental wavelengths corresponding to the tunability range of Ti:sapphire femtosecond oscillator. Two processes have been considered: non-collinear type I SHG ($\omega + \omega \rightarrow 2\omega$) and non-collinear type I third harmonic generation (THG) ($\omega + 2\omega \rightarrow 3\omega$). The two cases are quite different. For SHG the problem involves solving two equations (phase matching condition and group velocity matching condition) for two variables $\psi = \psi_1 = \psi_2$ and Θ (Θ is an angle between $\boldsymbol{k}_3$ and the optic axis of the crystal) and the solutions are exact if they exist. In the case of THG there are

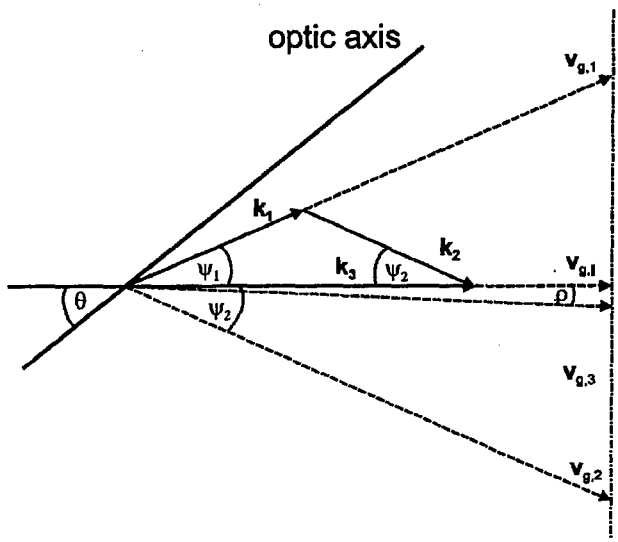

Fig. 4. A schematic diagram of non-collinear phase matching and group velocity matching scheme for sum frequency generation. The angles ψ_1 and ψ_2 are chosen so that the components of the group velocity of all three waves along the k vector of the output signal are equal. Θ is the phase matching angle.

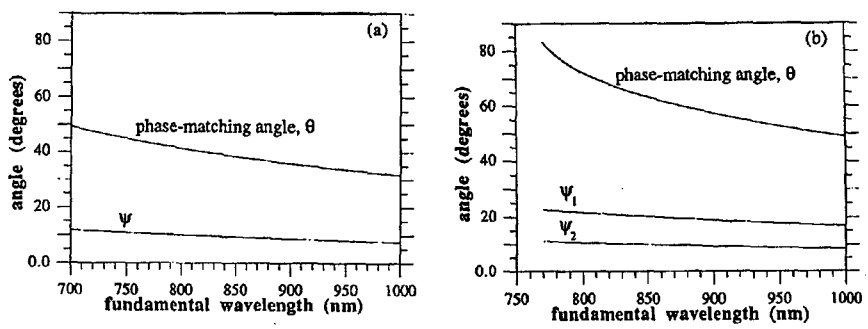

Fig. 5. (a) Phase-matching angle Θ and angle ψ for SHG in BBO versus wavelength. (b) Phase-matching angle Θ and angles ψ_1 and ψ_2 for THG in BBO versus wavelength. Note that for THG group velocity matching is possible only for wavelengths longer than 740 nm.

3 variables ψ_1, ψ_2, and Θ and only two equations. Phase matching condition has to be fulfilled but then group velocity matching is not exact. However, the results of numerical calculations indicate that the residual group velocity mismatch in our scheme can be as small as one percent of that for a standard collinear THG case. As one can see in Fig. 5 PM and GVM conditions can be achieved for SHG in BBO over an entire tuning range of Ti:sapphire laser. Similarly exact PM and approximate GVM are possible for THG process in a somewhat smaller range of wavelengths.

In order to see the effect of GVM on frequency mixing with femtosecond pulses we have numerically integrated the nonlinear equations for the amplitudes of the three fields

$$\frac{\partial A_1}{\partial z} + \frac{\beta_{21}}{2}\frac{\partial^2 A_1}{\partial t^2} = -\frac{i\omega_1}{n_1}\chi A_3 A_2^*,$$

$$\frac{\partial A_2}{\partial z} + \Delta\beta_{12}\frac{\partial A_2}{\partial t} + \frac{\beta_{22}}{2}\frac{\partial^2 A_2}{\partial t^2} = -\frac{i\omega_2}{n_2}\chi A_3 A_1^*,$$

$$\frac{\partial A_3}{\partial z} + \Delta\beta_{13}\frac{\partial A_3}{\partial t} + \frac{\beta_{23}}{2}\frac{\partial^2 A_3}{\partial t^2} = -\frac{i\omega_3}{n_3}\chi A_1 A_2, \tag{6}$$

where A_i is the amplitude, ω_i — the frequency, n_i — the refraction index of the i-th field and $\beta_{2i} = \partial^2 k_i/\partial\omega^2$. A reference frame moving with the group velocity of the ω_1 pulse is used and $\Delta\beta_{1i} = 1/\nu_{gi} - 1/\nu_{g1}$ for $i = 2, 3$.

The results of the integration are shown in Fig. 6. One can clearly see that for reasonable experimental conditions the effect of group velocity mismatch is not negligible. Second harmonic pulses in a GVM non-collinear scheme can be significantly shorter than those achievable in a standard collinear scheme.

This has been verified in an experiment performed with approximately 30 fs long pulses from a Ti:sapphire laser and a 0.5 mm long BBO crystal. The second harmonic has been generated using two different approaches: a standard collinear

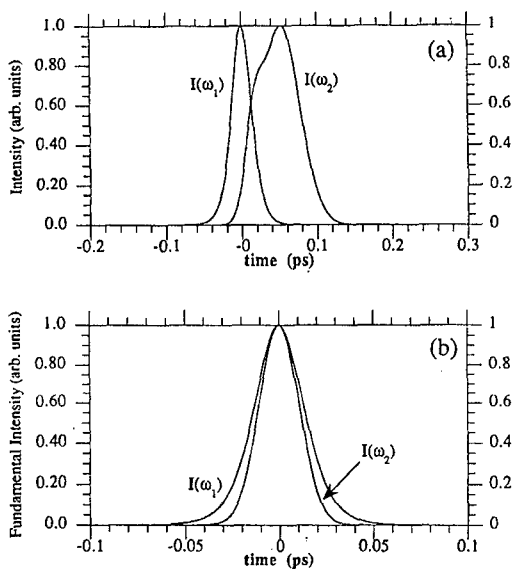

Fig. 6. Numerical results for SHG in a 0.5 mm thick BBO crystal. Input pulse duration is 30 fs and input wavelength 800 nm, (a) shows fundamental and second harmonic pulses for collinear geometry while (b) shows the same data for non-collinear (GVM) scheme. Note that in (b) the second harmonic pulse is shorter than the laser pulse.

SHG and a non-collinear GVM SHG. In each case the duration of the second harmonic pulse has been measured by intensity cross-correlation with the input laser pulse. Results of the cross-correlation measurements are shown in Fig. 7. For the standard collinear scheme the output pulse duration is almost twice of that for the laser pulse. At the same time the results show that for the GVM scheme second harmonic pulses that are shorter than the input laser pulses, can be achieved. This is not surprising since in an ideal case of SHG without saturation one should expect the second harmonic pulse to be shorter than the input pulse by a factor of $\sqrt{2}$.

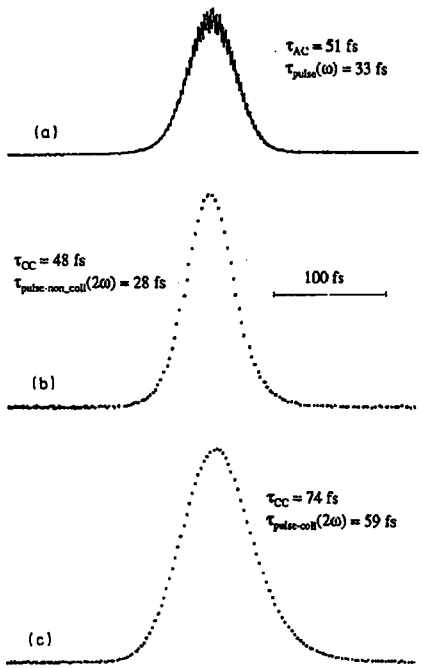

Fig. 7. Experimental results for (a) the auto-correlation of the fundamental pulse, (b) the cross-correlation of the fundamental with the SH pulse in the non-collinear experiment, and (c) the cross-correlation of the fundamental pulse with the SH pulse in the collinear experiment.

As a final example of linear propagation effects let us consider a femtosecond wave packet propagating in a birefringent dispersive medium. If the light propagates as an extraordinary wave then the terms γ_x and γ_{tx} in Eq. (4) are non-zero. While the first one means that the Poynting vector in such a medium is not parallel to the wave vector (a fact known for at least a century) the existence and meaning of the second one have been found and explained only recently [8, 9]. Numerical integration of Eq. (4) shows that because of this term the wave packet, which is tightly focused when it enters an uniaxial birefringent crystal, rotates around the axis that is perpendicular to the plane defined by optic axis of the crystal and the $\boldsymbol{k}$ vector. The effect can be explained in a way very similar to that employed to explain the wave packet distortion by lenses. Because of the tight focusing the ex-

panding beam contains wave vectors that form different angles with the optic axis of the crystal. Since, for an extraordinary wave, the index of refraction depends on this angle, both phase and group velocities are also functions of the same angle. What is even more important, the difference between phase velocity and group velocity varies as a function of this angle. As a result, one side of the wave packet lags more behind the phase fronts than the other side which leads to the wave packet rotation. If such a pulse is recollimated after it exits the crystal, it will look skewed — while the phase fronts will be perpendicular to the direction of propagation, the wave packet itself will be not, simply because the difference between phase and group delays will be different at its opposite sides. The theoretical predictions for the wave packet rotation have been verified experimentally in a set-up [18] similar to the one shown in Fig. 2. The set-up has been modified to include two identical 1:1 telescopes, one in each arm. Two 1 mm thick rutile crystals have been placed, one at the focus of each telescope. The wave packets propagating in the crystals experience rotation as described above. We have placed the crystals in both arms to cancel all the distortions of the wave packets that are not due to the rotation in the crystal. However the crystals were set in such a way that the two wave packets experienced rotation in opposite directions and thus did not overlap perfectly in space. By recording the fringe visibility at different positions in the output beam versus the delay between two arms of the interferometer we were able to measure the wave packet rotation.

The results of the experiment (points) are compared to the theoretically calculated wave packet rotation (line) in Fig. 8. It is clear that our model for wave packet rotation is at least adequate as indicated by the agreement of its predictions with the experimental results.

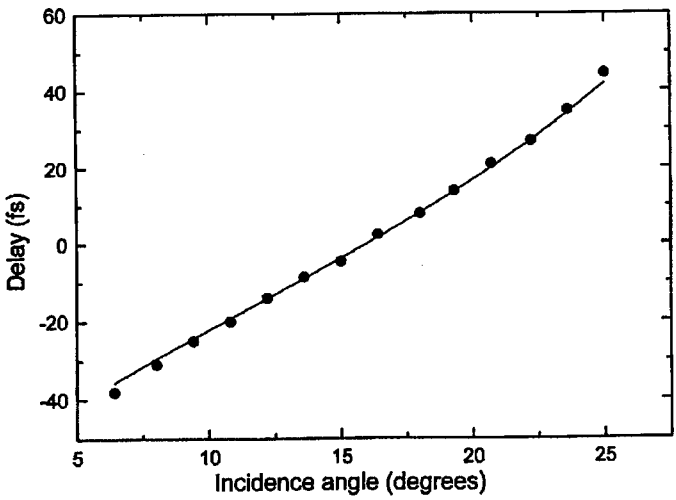

Fig. 8. Measured (dots) and calculated (line) wave packet rotation in rutile crystal.

To complete our analysis of the linear propagation we should briefly mention the effects of the group velocity dispersion. When the group velocity dispersion term $-(\mathrm{i}/2)\beta_2\partial^2 A/\partial t^2$ is also included into the analysis of Eq. (5) the pulse shape does not remain constant during propagation. Instead, because different Fourier components of the pulse experience different group delays, the result is a pulse with varying shape and time dependent frequency. In this approximation the light frequency varies linearly with time and thus the pulse is said to have a linear chirp. The effect can be quite severe. For instance, a 25 fs long Fourier limited pulse at 630 nm doubles its duration upon propagation through 10 mm of fused silica. The reshaping of femtosecond pulses due to propagation in dispersive media means that in any given experiment we cannot take the pulse duration for granted. Even if we verify that the pulse is short when it exits the laser system, it can be quite longer when it interacts with our sample simply because there was some glass on the way from the laser to the interaction region! An addition of higher order dispersion terms leads to even more significant pulse reshaping and a nonlinear chirp.

4. Nonlinear propagation

Let us start again with 1-dimensional case. The nonlinear term $\mathrm{i}\gamma_{\mathrm{nl}}|A|^2A$ in Eq. (5) describes the effect of intensity dependent index of refraction $n(A) = n_0 + \gamma_{\mathrm{nl}}|A|^2$. This introduces a time dependent phase and nonlinear chirp without affecting the pulse shape. As a result, new frequencies are generated and the pulse spectrum broadened. Spectrum broadening in Kerr media can be combined with a group velocity dispersion to produce pulses that are significantly shorter than the original laser pulses in a technique called pulse compression [19]. When both group velocity dispersion and Kerr nonlinearity terms are included the net result depends on the signs of β_2 and γ_{nl} coefficients. If the two terms have the same sign the chirp due to dispersion and the one due to Kerr nonlinearity have the same sign, too. As a result the pulse experiences reshaping and a combined chirp. On the other hand, if $\mathrm{sgn}(\beta_2) = -\mathrm{sgn}(\gamma_{\mathrm{nl}})$ then there exist stable solutions of the propagation equation [5]. Such solutions are called optical solitons. Because they can propagate over long distances in optical fibers without changes in shape they are of particular interest to engineers designing optical communication systems. In one of the experiments in this field picosecond pulses have been propagated in a fiber of length 1.8×10^{11} m, i.e. further than from the Earth to the Sun [20].

In a 3-D case the interplay between dispersion and nonlinearity is augmented by an additional effect, namely a competition between diffraction and self-focusing. While the first tends to increase the transverse dimensions of the wave packet, the latter does exactly the opposite. It has been known for at least 30 years [21] that for long pulses the ultimate fate of a beam propagating in a Kerr medium is determined by its power P. For $P < P_{\mathrm{c}}$ (P_{c} is called critical power and depends on the medium properties only) diffraction wins and the beam defocuses. If, however, $P > P_{\mathrm{c}}$ self-focusing prevails and catastrophic beam collapse is observed. This is not true for femtosecond pulses. As has been pointed out by several groups [22–25] in this case one has to take into account dispersion effects as well. Because of that the wave packet with a power higher than the critical power does not collapse;

instead it undergoes a complex evolution both in time and space. In order to illustrate this evolution let us turn back to Eq. (4).

For a wave packet that is Gaussian both in time and transverse spatial distribution propagating in an isotropic medium, it is convenient to rewrite Eq. (4) in a slightly different form [11]

$$\frac{\partial A}{\partial z} = -\beta_1 \frac{\partial A}{\partial t} - \mathrm{i}\frac{\tau_0^2}{L_{\mathrm{ds}}}\frac{\partial^2 A}{\partial t^2} + \mathrm{i}\frac{w_0^2}{L_{\mathrm{df}}}\left(\frac{\partial^2 A}{\partial x^2} + \frac{\partial^2 A}{\partial y^2}\right) + \mathrm{i}\frac{1}{|A_0|^2 L_{\mathrm{nl}}}|A|^2 A, \tag{7}$$

where three new parameters all of length dimension have been introduced: dispersion length $L_{\mathrm{ds}} = \tau_0^2/\beta_2$, diffraction length $L_{\mathrm{df}} = \gamma_{xx} w_0^2/2 = \pi w_0^2/\lambda_0$, and nonlinear length $L_{\mathrm{nl}} = \left(\gamma_{\mathrm{nl}}|A_0^2|\right)^{-1}$ with τ_0, w_0, and A_0 being the duration, transverse size, and amplitude of the wave packet, respectively. The advantage of such scaling is that it provides three parameters that can be easily compared to each other which in turn enables one to evaluate the strength of the three phenomena they represent (the smaller the coefficient the more important the corresponding term in Eq. (7). The meaning of these parameters is as follows: L_{ds} is a distance

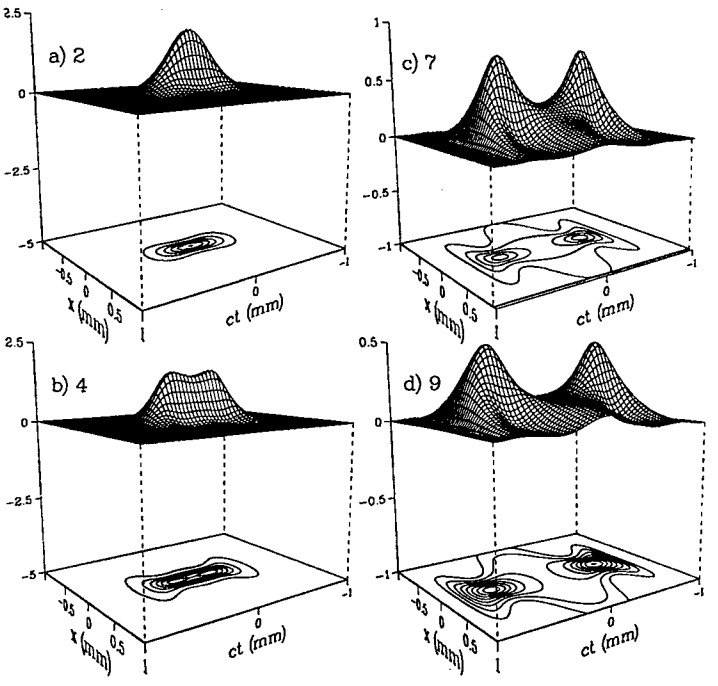

Fig. 9. Numerical results for nonlinear propagation of a wave packet in fused silica. Numbers in each figure indicate the distance that the wave packet has propagated inside the medium.

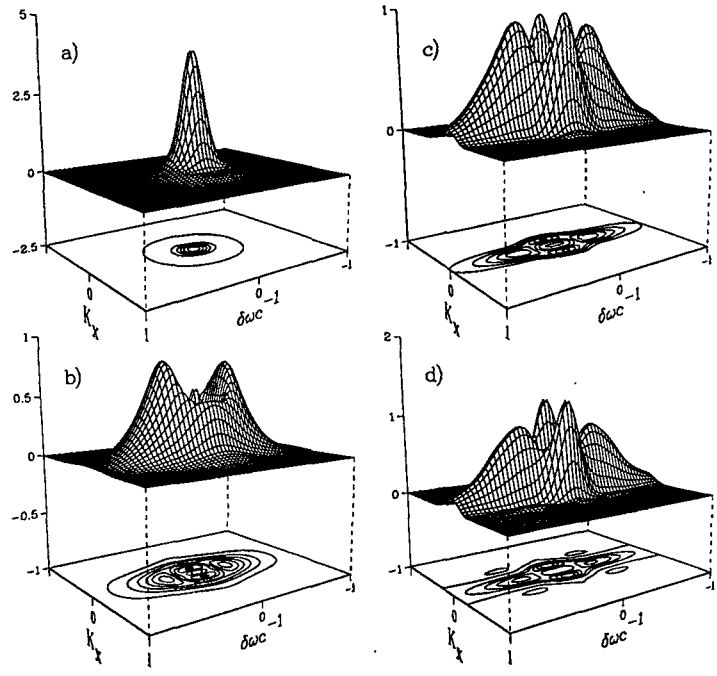

Fig. 10. Spatio-temporal spectrum of the wave packets shown in Fig. 9. K_x is the spatial frequency in the x direction.

which takes the pulse to double its duration because of the medium dispersion, $L_{\rm df}$ is the distance required for the pulse to double its area as a result of diffraction, and $L_{\rm nl}$ is the self-focusing distance. For transparent media the inequality $L_{\rm ds} \gg L_{\rm nl}, L_{\rm df}$ typically holds. It means that the dispersion effects constitute only a small correction to the basic wave packet evolution defined by diffraction and self-focusing. However, the results of integration of Eq. (7) show that, small as it is, the dispersion plays a crucial role in propagation of a femtosecond wave packet. An example of the wave packet evolution obtained by direct integration of Eq. (3) is shown in Fig. 9 (the results were very similar when Eq. (7) with 3-rd order terms included was integrated). In this particular case it was assumed that the wave packet size in the y direction is much larger than its size in the x direction. This not only made the computation simpler but also enabled us to present the results as a 3-D graphs. The following parameters have been assumed: material — fused silica ($L_{\rm ds} = 240$ mm), pulse duration — 66 fs, pulse wavelength — 800 nm, beam size — 32 μm ($L_{\rm df} = 4$ mm), pulse intensity — 70 GW/cm^2 ($L_{\rm nl} = 2$ mm). The power of the beam is about $2.2P_{\rm c}$. A long pulse of this power would self-focus and collapse. However the femtosecond wave packet considered here displays a quite different behavior. It starts to self-focus as indicated by the elongated shape in Fig. 9a but then the process is arrested and the pulse splits into two pulses as shown in Figs. 9c and d. It is instructive to look at the spatio-temporal spectrum of the wave packet shown in Fig. 10. Starting from a smooth Guassian shape the

spectrum evolves through a "Mexican hat" structure (Fig. 10c) and then develops three spatial lobes. The central lobe (around $k_x = 0$) contains two peaks in the frequency distribution, one at the frequencies lower than the input pulse frequency and another which is shifted towards higher frequencies. The two side lobes have broad spectra centered at the input pulse frequency. The results depend, as one might expect for a nonlinear problem, on a particular choice of parameters, for example the sign and magnitude of the β_2 coefficient, but from the numerical integration results some general conclusions about the role of the dispersion can be drawn. For the case illustrated in Figs. 9 and 10 the process starts with the self-focusing. The self-focusing is the strongest at $ct = 0$ (Fig. 9a) simply because the intensity is the highest there. Thus the intensity at the center of the wave packet increases rapidly and so does the width of spectrum due to self-phase modulation. Once the spectrum is broad enough the dispersion shifts lower frequencies towards the head of the pulse and higher frequencies towards its tail. This lowers the intensity at the center of the wave packet and prevents it from a collapse. At the same time the part of the wave packet that has been focused strongly diffracts to form the side lobes in the spectrum as discussed above. The pulse splitting shown in Fig. 9 has been recently observed in an experiment [26].

In conclusion, we have analyzed some aspects of linear and nonlinear propagation of femtosecond light wave packets in transparent, dispersive nonlinear media. In particular, we have shown the effects of group velocity on propagation of such wave packets through lenses, wave packet rotation in birefringent media and sum frequency generation without group velocity mismatch. Numerical results showing wave packet splitting were also presented.

References

[1] L. Xu, Ch. Spielmann, F. Krausz, R. Szipocs, *Opt. Lett.* **21,** 1259 (1996).

[2] M. Nisoli, S. De Silvestri, O. Svelto, R. Szipocs, F. Ferencz, Ch. Spielmann, S. Sartania, F. Krausz, *Opt. Lett.* **22,** 522 (1997).

[3] A. Baltuska, Z. Wei, M.S. Pshenichnikov, D.A. Wiersma, *Opt. Lett.* **22,** 102 (1997).

[4] D.E. Spence, P.N. Kean, W. Sibbet, *Opt. Lett.* **16,** 42 (1991).

[5] V.E. Zakharov, A.B. Shabat, *Sov. Phys. JETP* **34,** 62 (1970).

[6] L.F. Mollenauer, R.H. Stolrn, J.P. Gordon, *Phys. Rev. Lett.* **45,** 1095 (1980).

[7] For example: *The Supercontinuum Laser Source*, Ed. R.R. Alfano, Springer-Verlag, New York 1989.

[8] Y.B. Band, M. Trippenbach, *Phys. Rev. Lett.* **76,** 1457 (1996).

[9] M. Trippenbach, Y.B. Band, *J. Opt. Soc. Am. B* **13,** 1403 (1996).

[10] M. Trippenbach, T.C. Scott, Y.B. Band, *Opt. Lett.* **22,** 579 (1997).

[11] M. Trippenbach, Y.B. Band, *Phys. Rev. A* **56,** 1 (1997).

[12] H. Staerk, J. Ihlemann, A. Hembold, *Laser Optoelectronic* **20,** 6 (1988).

[13] Z. Bor, *Opt. Lett.* **14,** 119 (1989).

[14] P.F. Curley, A.I. Ferguson, J.G. White, W.B. Amos, *Optical Quantum Electron.* **24,** 851 (1992).

[15] C. Radzewicz, M.J. la Grone, J.S. Krasinski, *Opt. Commun.* **126,** 185 (1996).

[16] C. Radzewicz, Y.B. Band, G.W. Pearson, J.S. Krasinski, *Opt. Commun.* **117,** 295 (1995).

[17] Y.B. Band, M. Trippenbach, C. Radzewicz, J.S. Krasinski, *J. Nonlinear Opt. Phys. Mater.* **5,** 477 (1996).

[18] C. Radzewicz, J.S. Krasinski, M.J. la Grone, M. Trippenbach, Y.B. Band, *J. Opt. Soc. Am. B* **14,** 420 (1997).

[19] C.V. Shank, R.L. Fork, R. Yen, R.H. Stolen, W.J. Tomlinson, *Appl. Phys. Lett.* **40,** 761 (1982).

[20] M. Nakazawa, K. Suzuki, E. Yamada, H. Kubota, Y. Kimura, in: *Proc. Conf. on Fiber Communications (OFC'93)*, Opt. Soc. Am., Washigton (D.C.) 1993, WC1.

[21] Y.R. Shen, *The Principles of Nonlinear Optics*, John Wiley & Sons, New York 1984.

[22] D. Strickland, P.B. Corkum, *Proc. Soc. Photo-Opt. Instrum. Engl.* **1413,** 54 (1991).

[23] P. Chernev, V. Petrov, *Opt. Lett.* **17,** 172 (1992).

[24] J.E. Rothenberg, *Opt. Lett.* **17,** 172 (1992).

[25] G.G. Luther, A.C. Newell, J.V. Moloney, E.M. Wright, *Opt. Lett.* **19,** 789 (1994).

[26] J.K. Ranka, R.W. Schirmer, A.L. Gaeta. *Phys. Rev. Lett.* **77,** 3783 (1996).

Manuscripts, preferably in English (though papers in German and French are acceptable), should comply with the following rules:

Submission of a manuscript indicates a tacit understanding that the paper is not actively under consideration for publication elsewhere; that its publication has been approved by all coauthors; that the manuscript accepted for publication will not be published elsewhere without the consent of the Editor.

All contributions submitted will be refereed. It is the right of Editorial Committee to accept or to reject contributions. The Editorial Board does not return the manuscripts of rejected papers.

1. Manuscripts, in duplicate, should be sent to the Editor of Acta Physica Polonica A, Al. Lotników 32/46, 02-668 Warszawa, Poland. A file with source code of the paper on a diskette (all DOS or 1.44 MB Mac) or sent by e-mail to Internet address appol@ifpan.edu.pl – preferably in the plain TEX format, although other TEX formats, MS Word, ChiWriter or unformatted ASCII codes are also acceptable – will substantially speed up the processing.

2. The author's name, initials, affiliation, and address should be given.

3. The manuscript should be as concise as possible with a short abstract in English. In the case of French and German manuscripts also the title in English should be added. Just below the abstract the PACS Index numbers should be typed.

4. The manuscript, including the abstract, references, and captions should be neatly typed in double spacing, on a good quality paper with ample margins. Poor reproductions are unacceptable as originals. Unclear or excessive handwritten insertions are not acceptable. Badly arranged manuscripts will be returned.

5. A covering letter, signed by one of the authors, requesting publication should accompany the paper.

6. Equations should be neatly typed or written in ink, punctuated and aligned to bring out their structure, and numbered on the right.

7. One should avoid detailed derivations of mathematical expressions and formulae. It is generally sufficient to indicate the method of treatment and the final results.

8. Figures should be submitted in two sets. The originals must be drawn in Indian ink on good-quality tracing paper, completely ready for reproduction. High-quality computer graphics are acceptable. Photographs must be on heavy--weight glossy white paper. The maximum space available for figure is 12 cm x 17 cm and drawings should not exceed the size of 30 cm x 42 cm. Preffered reduction of figures is 1:2 and the maximum allowed reduction is 1:4. The amount of writing in the figures should be kept to a minimum. All figures must be numbered and bear the name of the author of the paper. Figure captions as well as tables should be submitted on separate sheets of paper.

9. References should be given on a separate sheets and conform to the conventions used in Acta Physica Polonica. Abbreviations should follow conventions of Physics Abstracts (Science Abstracts, Series A). No comments or remarks should be made in the references.

10. A Guide to Authors of Papers in Acta Physica Polonica can be found in *Acta Phys. Pol. A* **92**, 1211 (1997) or in www at http:/info.ifpan.edu.pl.

ACTA PHYSICA POLONICA A
Volume 93 — Number 1

Proceedings of the International Conference "Quantum Optics IV" Jaszowiec, Poland, 1997